Printable 2d Material Optoelectronics and Photonics

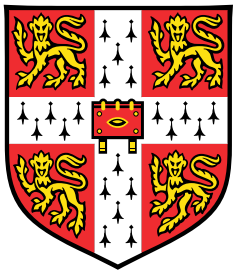

Guohua Hu

Supervisor: Dr Tawfique Hasan

Department of Engineering
University of Cambridge

This dissertation is submitted for the degree of
Doctor of Philosophy

St John's College November 2017

Declaration

I hereby declare that except where specific reference is made to the work of others, the contents of this dissertation are original and have not been submitted in whole or in part for consideration for any other degree or qualification in this, or any other university. This dissertation is my own work and contains nothing which is the outcome of work done in collaboration with others, except as specified in the text and Acknowledgements. This dissertation contains fewer than 65,000 words including appendices, bibliography, footnotes, tables and equations and has fewer than 150 figures.

Guohua Hu
November 2017

Acknowledgements

I would like to take this opportunity to express my gratitude to those who offered me help and support.

Foremost, I am grateful to my supervisor Dr Tawfique Hasan. I joined in Tawfique's research group, the Hybrid Nanomaterials Engineering, with barely no knowledge of solution processing and printing of graphene and its related 2d materials. With his guidance, I gradually developed the knowledge and understanding on my doctoral work, and a great interest in this field of research. With his support, I had the opportunities to work with lab colleagues and collaborators on so many exciting projects, and publish my work on peer-review journals and conferences. His own passion and enthusiasm towards work and research have also inspired me to work hard with passion and enthusiasm.

I wish to thank my lab colleagues at the Hybrid Nanomaterials Engineering. Special thanks go to Dr Richard Howe. He has offered me a lot of help, trainings and many valuable suggestions on my doctoral work. I would like to thank Tom Albrow-Owen, Leonard Ng, Zongyin Yang and Tien-Chun Wu for their help with my work. I would also like to thank the colleagues and staff from the Cambridge Graphene Centre, the CAPE and the Nanoscience Centre.

I have been working closely with many international collaborators on many exciting projects. I express my sincere thanks to them: Prof Meng Zhang at the Beihang University; Dr Rob Woodward and Dr Edmund Kelleher at the Imperial College London; Prof Zhipei Sun at the Aalto University; Ayaz Ali and Prof Yang Xu at the Zhejiang University; Dr Sumita Santra at the Indian Institute of Technology; Dr David Dodoo-Arhin at the University of Ghana; and Chris Jones at the Novalia Ltd.

I thank my parents and my sister for giving me spiritual support. In the end, I express my gratitude to China Scholarship Council, Cambridge Overseas Trust and St John's College for the PhD funding support.

Abstract

Graphene and structurally similar 2-dimensional (2d) materials such as transition metal dichalcogenides (TMDs) and black phosphorus (BP) hold enormous potential for the next generation optoelectronics and photonics. Pairing 2d materials with printing is an emerging cost-effective large-scale device fabrication strategy. However, the current inks are far from ideal to support reproducible device fabrication. In addition, the instability of BP in ambient limits its applications.

In this thesis, I present formulation of 2d material inks for inkjet printing for optoelectronic and photonic applications. To begin with, I produce mono- and few-layer 2d material flakes *via* ultrasonic assisted liquid phase exfoliation. This allows one-step formulation of a polymer stabilised graphene ink. For TMDs and BP, I design a binary solvent carrier for binder-free ink formulation. I show that these 2d material inks have optimal fluidic properties, drying dynamics and interaction with substrates for spatially uniform, highly controllable and print-to-print consistent large-scale printing on untreated substrates. In particular, the rapid ink drying at low temperatures leads to minimal oxidation of BP during ambient printing; the printed BP with passivation retains a stability over one month. On this basis, the printed graphene is employed as active sensing layer in CMOS integrated humidity sensors and as counter-electrodes in dye-sensitised solar cells, while the printed TMDs and BP are used to develop nonlinear photonic devices (*i.e.* saturable absorbers for femtosecond pulsed laser generation) and visible to near-infrared photodetectors (*e.g.* MoS_2 and BP/graphene/silicon hybrid photodetectors).

Beyond inkjet printing, I present an ink formulation of commercial graphene nanoplatelets for roll-to-roll flexographic press ($\sim$100 m min^{-1} printing speed). This allows hundreds of conductive electronic circuits to be printed in a minute for capacitive touchpads.

Though I investigate only graphene, TMDs and BP, the ink formulation strategies can be effortlessly transferred to other 2d materials such as boron nitride, MXenes and mica. In addition to the demonstrated applications, printing of 2d materials can be potentially exploited to fabricate devices such as transistors, light emitters, energy storage conversion, and biosensors. This significantly expands the prospect of printable 2d material optoelectronics and photonics.

Publications

Peer-reviewed journal articles

[1] **G. Hu**, T. Albrow-Owen, X. Jin, A. Ali, Y. Hu, R. C. T. Howe, K. Shehzad, Z. Yang, X. Zhu, R. I. Woodward, T-C. Wu, H. Jussila, J-B., P. Peng, P. Tan, Z. Sun, E. J. R. Kelleher, M. Zhang, Y. Xu and T. Hasan, Black phosphorus ink formulation for inkjet printing of optoelectronics and photonics, **Nature Communications** 8, 278 (2017).

[2] S. Santra, **G. Hu** (co-first author), R. C. T. Howe, A. D. Luca, S. Z. Ali, S. K. Ray, F. Udrea, J. W. Gardner, P. K. Guha and T. Hasan, CMOS integration of graphene for humidity sensing, **Scientific Reports** 5, 17374 (2015).

[3] M. Zhang, **G. Hu** (co-first author), G. Hu, R. C. T. Howe, L. Chen, Z. Zheng and T. Hasan, Yb- and Er-doped fiber laser Q-switched with a broadband WS_2 saturable absorber, **Scientific Reports** 5, 17482 (2015).

[4] J. Wang, S. Lin, X. Liang, M. Wang, P. Yan, **G. Hu**, T. Albrow-Owen, S. Ruan, Z. Sun and T. Hasan, High-energy and efficient Raman soliton generation tunable from 1.98 to 2.29 μm in an all-silica-fiber thulium laser system, **Optics Letters** 42, 3518-3521 (2017).

[5] H. Jussila, T. Albrow-Owen, H. Yang, **G. Hu**, S. Aksimsek, N. Granqvist, H. Lipsanen, R. C. T. Howe, Z. Sun and T. Hasan, New approach for thickness determination of solution-deposited graphene thin films, **ACS Omega** 2, 2630 (2017).

[6] M. Chernysheva, A. Bednyakova, M. Al Araimi, R. C. T. Howe, **G. Hu**, T. Hasan, A. Gambetta, G. Galzerano, M. Rümmeli and A. Rozhin, Double-wall carbon nanotube hybrid mode-locker in Tm-doped fibre laser: A novel mechanism for robust bound-state solitons generation, **Scientific Reports** 7, 44314 (2017).

[7] D. Dodoo-Arhin, R. C. T. Howe, **G. Hu**, P. Hiralal, G. Amaratunga, A. Bello, Y. Xua and T. Hasan, Inkjet-printed graphene electrodes for dye-sensitized solar cells, **Carbon** 105, 33-41(2016).

[8] J. Wang, X. Liang, **G. Hu**, Z. Zheng, S. Lin, D. Ouyang, X. Wu, P. Yan, S. Ruan, Z. Sun and T. Hasan, 152 fs nanotube-mode-locked thulium-doped all-fiber laser, **Scientific Reports** 6, 28885 (2016).

[9] S. Xu, F. Wang, C. Zhu, Y. Meng, Y. Liu, W. Liu, J. Tang, K. Liu, **G. Hu**, R. C. T. Howe, T. Hasan, R. Zhang, Y. Shi, Y. Xu, Ultrafast nonlinear photoresponse of single-wall carbon nanotubes: A broadband degenerate invest igation, **Nanoscale** 8, 9304-9309 (2016).

[10] R. C. T. Howe, R. I. Woodward, **G. Hu**, Z. Yang, E. J. R. Kelleher and T. Hasan, Surfactant-aided exfoliation of molybdenum disulphide for ultrafast pulse generation through edge-state saturable absorption, **Physica Status Solidi (B)** 5, 911–917 (2016).

[11] R. I. Woodward, R. C. T. Howe, **G. Hu**, F. Torrisi, M. Zhang, T. Hasan and E. J. R. Kelleher, Few-layer MoS_2 saturable absorbers for short-pulse laser technology: Current status and future perspectives (*invited paper*), **Photonics Research** 3, A30-A42 (2015).
*Awarded as a best paper of 2016 by the journal

[12] R. I. Woodward, R. C. T. Howe, T. H. Runcorn, **G. Hu**, F. Torrisi, E. J. R. Kelleher and T. Hasan, Wideband saturable absorption in few-layer molybdenum diselenide ($MoSe_2$) for Q-switching Yb-, Er- and Tm-doped fiber lasers, **Optics Express** 23, 20051-20061 (2015).

[13] M. Zhang, R. C. T. Howe, R. I. Woodward, E. J. R. Kelleher, F. Torrisi, **G. Hu**, S. V. Popov, J. R. Taylor and T. Hasan, Solution processed MoS_2-PVA composite for sub-bandgap mode-locking of a wideband tunable ultrafast er:fiber laser, **Nano Research** 8, 1522-1534 (2015).
*Awarded as a best paper of 2017 by the journal

[14] R. I. Woodward, E. J. R. Kelleher, R. C. T. Howe, **G. Hu**, F. Torrisi, T. Hasan, S. V. Popov and J. R. Taylor, Tunable Q-switched fiber laser based on saturable edge-state absorption in few-layer molybdenum disulfide (MoS_2), **Optics Express** 22, 31113-31122 (2014).

Book

[1] L. W. T. Ng, R. C. T. Howe, **G. Hu**, X. Zhu, Z. Yang, C. Jones and T. Hasan, Functional Inks and Printing of Graphene and Related 2D Materials: Technology, Formulation and Applications (*invited book*), Springer, submitted (2017).

Patent

[1] **G. Hu**, R. C. T. Howe, Z. Yang, L. Ng, C. Jones, K. Stone and T. Hasan, Nanoplatelet dispersions, methods for their production and uses thereof, WO2017013263 A1 (2017).

Conference presentations

Invited talk

[1] **G. Hu** and T. Hasan, Using solvents for composites, functional inks and soft lithography patterns of 2D materials, NPO Conference, Sochi, Russia (2017).

Contributed oral presentations

[1] X. Jin, **G. Hu**, M. Zhang, Y. Hu, T. Albrow-Owen, R. C. T. Howe, T-C. Wu, X. Zhu, Z. Zheng and T. Hasan, Long term stable black phosphorus saturable absorber for mode-locked fiber laser, CLEO, San Jose, USA (2017).

[2] **G. Hu**, R. C. T. Howe, Z. Yang, T. Albrow-Owen, M. Zhang and T. Hasan, Inkjet printing of treatment free, highly uniform functional TMD inks on versatile substrates, 2016 MRS Fall Meeting, Boston, USA (2016).

[3] **G. Hu**, R. C. T. Howe, Z. Yang and T. Hasan, Low temperature processable, functional inks of TMDs for inkjet printing, IoP Printing and Graphics Science Student Conference, London, UK (2016).

[4] R. C. T. Howe, **G. Hu**, Z. Yang, C. Jones and T. Hasan, Graphene inks for industrial-scale flexo printing, IoP Printing and Graphics Science Student Conference, London, UK (2016).

[5] G. Hu, M. Zhang, L. Chen, X. Zhu, **G. Hu**, R. C. T. Howe, X. Zhao, Z. Zheng and T. Hasan, Q-switched pulse generation in Yb- and Er-doped fiber laser with WS_2 saturable absorber, CLEO, San Jose, USA (2015).

[6] G. Hu, M. Zhang, L. Chen, X. Zhu, **G. Hu**, R. C. T. Howe, X. Zhao, Z. Zheng and T. Hasan, Q-switched Yb-doped fiber laser with WS_2 saturable absorber, CLEO-PR, Busan, Korea (2015).

Conference proceedings

[1] X. Jin, **G. Hu**, M. Zhang, Y. Hu, T. Albrow-Owen, R. C. T. Howe, T-C. Wu, X. Zhu, Z. Zheng and T. Hasan, Long term stable black phosphorus saturable absorber for mode-locked fiber laser, CLEO, SW4K.1 (2017).

[2] R. C. T. Howe, **G. Hu**, Z. Yang and T. Hasan, Functional inks of graphene, metal dichalcogenides and black phosphorus for photonics and (opto)electronics, Proceedings of SPIE, 95530R (2015).

[3] G. Hu, M. Zhang, L. Chen, X. Zhu, **G. Hu**, R. C. T. Howe, X. Zhao, Z. Zheng and T. Hasan, Q-switched pulse generation in Yb- and Er-doped fiber laser with WS_2 saturable absorber, CLEO, FM3G.5 (2015).

[4] G. Hu, M. Zhang, L. Chen, X. Zhu, **G. Hu**, R. C. T. Howe, X. Zhao, Z. Zheng and T. Hasan, Q-switched Yb-doped fiber laser with WS_2 saturable absorber, CLEO-PR, 25A3_4 (2015).

[5] M. Chernysheva, C. Mou, R. C. T. Howe, **G. Hu**, T. Hasan, S. Turitsyn and A. Rozhin, Soliton molecules generation in DWCNT mode-locked thulium-doped fibre laser, CLEO/ Europe, CF_P_6 (2015).

Posters

[1] **G. Hu**, Z. Yang, T. Albrow-Owen, R. C. T. Howe, M. Zhang and T. Hasan, Inkjet printing of black phosphorus, 2016 MRS Fall Meeting, Boston, USA (2016).

[2] **G. Hu**, R. C. T. Howe, Z. Yang and T. Hasan, Low temperature inks of 2-dimensional crystals for inkjet printing, International Winterschool on Electron ic Properties of Novel Materials, Kirchberg in Tirol, Austria (2015).

[3] R. C. T. Howe, R. I. Woodward, **G. Hu**, F. Torrisi, M. Zhang, S. V. Popov, J.R. Taylor, E. J. R. Kelleher and T. Hasan, Solution-processed MoS_2 for broadband ultrafast optical pulse generation at sub-bandgap photon energies, International Winterschool on Electronic Properties of Novel Materials, Kirchb erg in Tirol, Austria (2015).

[4] M. Chernysheva, C. Mou, R. C. T. Howe, **G. Hu**, T. Hasan, S. Turitsyn and A. Rozhin, Soliton molecules generation in DWCNT mode-locked thulium-doped fibre laser, CLEO/ Europe, Munich, Germany (2015).

[5] S. Santra, **G. Hu**, A. D. Luca, S. Z. Ali, T. Hasan, S. K. Ray, J. W. Gardner, F. Udrea and P. K. Guha, Inkjet printed graphene on CMOS MEMS devices for NO_2 detection, ICMAT2015 IUMRS-ICA2015, Singapore (2015).

[6] D. Dodoo-Arhin, R. C. T. Howe, **G. Hu**, N. Jiao, P. Hiralal, G. Amaratunga, A. Bello, Y. Xu and T. Hasan, Graphene Ink-Based Natural Dye Sensitized Solar Cells, 5th Chem-On-Tubes Conference, Riva del Garda, Italy (2014).

[7] D. Dodoo-Arhin, R. C. T. Howe, **G. Hu**, N. Jiao, P. Hiralal, G. Amaratunga, A. Bello, Y. Xu and T. Hasan, Graphene Ink-Based Natural Dye Sensitized Solar Cells, MAT4ENERGY conference, Grenoble, France (2014).
*Awarded 1^{st} gold prize

[8] D. Dodoo-Arhin, R. C. T. Howe, **G. Hu**, N. Jiao, P. Hiralal, G. Amaratunga and T. Hasan, Graphene Ink-Based Natural Dye Sensitized Solar Cells, E-MRS Spring Meeting, Lille, France (2014).

Table of contents

List of figures **xiv**

List of tables **xvii**

List of abbreviations and symbols **xviii**

1 Introduction **1**
1.1 Project background 1
1.2 Project motivation 2
1.3 Structure of the thesis 3

2 Structures, properties and applications of 2d materials **5**
2.1 The 2d material family 5
2.2 Graphene 7
2.3 Transition metal dichalcogenides (TMDs) 13
2.4 Black phosphorus 17
2.5 Other 2d materials 19
2.5.1 Hexagonal boron nitride 19
2.5.2 MXenes 21
2.5.3 Mica 22
2.5.4 Oxides 23
2.5.5 Metal halides 23
2.6 Summary 24

3 Solution processing of 2d materials **25**
3.1 Production method overview 25
3.2 Solution processing methods 29
3.2.1 Exfoliation based on ion intercalation and exchange 30
3.2.2 Liquid phase exfoliation 32

3.3 Ultrasonic-assisted liquid phase exfoliation (UALPE) . . . 34
3.3.1 Exfoliation in pure solvents . . . 34
3.3.2 Exfoliation using surfactants . . . 37
3.3.3 Centrifugation processing principles . . . 39
3.4 Material characterisations . . . 41
3.4.1 Optical absorption spectroscopy . . . 41
3.4.2 Microscopy characterisations . . . 43
3.4.3 Raman spectroscopy . . . 45
3.5 Summary . . . 48

4 Ink systems and graphics printing technologies 49
4.1 Ink systems and formulation . . . 50
4.1.1 Ink composition . . . 50
4.1.2 Ink formulation processing . . . 52
4.1.3 Ink rheology . . . 53
4.2 Graphics printing technologies . . . 55
4.2.1 Flexographic printing . . . 55
4.2.2 Gravure printing . . . 57
4.2.3 Screen printing . . . 57
4.2.4 Inkjet printing . . . 58
4.3 Inkjet printing principles . . . 60
4.3.1 Stable droplet jetting . . . 60
4.3.2 Droplet impact and spreading . . . 62
4.3.3 Coffee ring effect . . . 65
4.4 Inkjet printing of 2d materials . . . 67
4.4.1 Current 2d material ink formulations . . . 67
4.4.2 Applications of current 2d material inks . . . 70
4.4.3 Challenges for the current ink formulations . . . 72
4.5 Summary . . . 75

5 Formulation of inkjet-printable graphene ink and its applications 76
5.1 UALPE production of graphene . . . 77
5.1.1 Exfoliation in pure solvents . . . 77
5.1.2 Exfoliation with surfactants . . . 78
5.2 Large-scale spatially uniform inkjet printing . . . 83
5.2.1 Graphene ink properties and printing parameters . . . 83
5.2.2 Printing characteristics . . . 85

5.2.3 Electrical properties of inkjet-printed graphene 87
5.3 CMOS integrated graphene humidity sensors 89
5.3.1 CMOS device design 90
5.3.2 Sensor fabrication with active graphene-PVP sensing layer 91
5.3.3 Humidity sensing 92
5.3.4 Sensing mechanism 95
5.4 Graphene based dye-sensitised solar cells 95
5.4.1 Natural dyes 97
5.4.2 Inkjet-printed graphene counter-electrode based solar cells 98
5.5 Summary 100

6 TMD ink formulation for large-scale printing of photonics and optoelectronics 102
6.1 UALPE production of TMDs 103
6.1.1 Dispersion production 103
6.1.2 Determination of optical absorption coefficient 105
6.1.3 Characterisations of the exfoliated TMD flakes 106
6.2 Large-scale spatially uniform inkjet printing of TMDs 109
6.2.1 Inkjet printing with IPA/PVP inks 109
6.2.2 Inkjet printing with IPA/2-butanol inks 111
6.3 Inkjet-printed TMD saturable absorbers 118
6.4 Inkjet-printed TMD photodetectors 122
6.5 Summary 124

7 Inkjet printing of black phosphorus for stable optoelectronics and photonics 126
7.1 UALPE production of black phosphorus 127
7.1.1 Dispersion production 127
7.1.2 Characterisations on black phosphorus flake size 128
7.1.3 Raman spectroscopy 130
7.1.4 Discussion on stability against oxidation 131
7.2 Inkjet printing and passivation of black phosphorus 133
7.2.1 Ink formulation 133
7.2.2 Large-scale spatially uniform inkjet printing 135
7.2.3 Passivation of inkjet-printed black phosphorus 139
7.3 Inkjet-printed black phosphorus saturable absorbers 141
7.4 Black phosphorus/graphene/silicon photodetectors 144
7.5 Summary 148

8 Functional inks of commercial graphene nanoplatelets for high-speed printing 149
8.1 Formulating commercial graphene nanoplatelet inks 150
8.2 Use of GNP inks as additive for conductive inks 154
8.3 Use of GNP inks as additive for nanocomposites 158
8.4 High-loading ink formulation of other 2d materials 159
8.5 Summary 161

9 Conclusions and outlook 162
9.1 2d material inks 162
9.2 Printable applications 164
9.3 Outlook 166

References 167

List of figures

2.1 Electromagnetic spectrum of 2d materials 6
2.2 Graphene and its chemical and electronic structures 8
2.3 Applications of graphene 11
2.4 Chemical and energy band structures, and properties of TMDs 14
2.5 Applications of TMDs 16
2.6 Structures, properties and applications of black phosphorus 18
2.7 Structures, properties and applications of *h*-BN 20
2.8 Exfoliation of MAX phases for MXene production 22
2.9 Chemical structure of mica 23

3.1 Common production methods of graphene 26
3.2 Production of 2d materials *via* micro-mechanical cleavage 27
3.3 Production of 2d materials *via* chemical vapour deposition 28
3.4 Production of 2d materials *via* solution processing 30
3.5 Solution processing based on ion intercalation 31
3.6 Solution processing based on liquid phase exfoliation 33
3.7 Ultrasonic-assisted liquid phase exfoliation 35
3.8 Centrifugation processing principles 39
3.9 Optical absorption spectroscopy of 2d material dispersions 42
3.10 Microscopy characterisations of 2d materials 44
3.11 Raman spectroscopy of 2d materials 46

4.1 Dispersal of pigment particles for ink formulation 52
4.2 Ink rheological properties and characterisation 54
4.3 Schematic figures for flexographic, gravure and screen printing 56
4.4 Schematic figures for inkjet printing 59
4.5 High-speed micrographs of droplet jetting 60
4.6 Droplet jetting defined by Reynolds and Weber numbers 61

4.7 Droplet impact and spreading on substrate 62
4.8 Morphology of printed lines 63
4.9 Droplet impinging and merging 64
4.10 Coffee ring effect 66
4.11 Suppression of the coffee ring effect *via* Marangoni flow 67
4.12 Inkjet printing with current 2d material inks 69
4.13 Inkjet-printable applications of current inks 71
4.14 Challenges for current 2d material inks for inkjet printing 73

5.1 Graphene production in pure organic solvents 78
5.2 Graphene production with ionic surfactants 79
5.3 Graphene production with polyvinylpyrrolidone 80
5.4 AFM characterisation of the exfoliated graphene 82
5.5 Raman characterisation of the exfoliated graphene 83
5.6 Droplet jetting of the graphene ink 84
5.7 Inkjet printing and printing characteristics of the graphene ink 86
5.8 Percolation model of printed graphene-PVP film 87
5.9 Sheet resistance of printed graphene 89
5.10 CMOS device design 90
5.11 CMOS integrated graphene humidity sensors 92
5.12 Humidity sensing of the CMOS integrated graphene sensors 93
5.13 Sensing reproducibilities of the CMOS integrated graphene sensors 94
5.14 Typical structure of dye-sensitised solar cells 96
5.15 Graphene counter-electrode based dye-sensitised solar cells 99

6.1 TMD dispersions and optical absorbance spectra 104
6.2 Determination of MoS_2 optical absorption coefficient 106
6.3 AFM characterisation of the exfoliated TMD flakes 107
6.4 Raman spectroscopy of the exfoliated TMD flakes 108
6.5 Inkjet printing of the TMD IPA/PVP inks 110
6.6 Formulation of the TMD IPA/2-butanol inks 113
6.7 Stability of the TMD IPA/2-butanol inks against sedimentation 114
6.8 Jetting and printed morphologies of the TMD IPA/2-butanol inks 115
6.9 Inkjet printing of the TMD IPA/2-butanol inks 116
6.10 Inkjet printing characteristics of the TMD IPA/2-butanol inks 118
6.11 Schematic figure for Z-scan set-up 119
6.12 Spatial optical absorption of the inkjet-printed TMD saturable absorbers . . 120

6.13 Mode-locking with the inkjet-printed TMD saturable absorbers 121
6.14 Inkjet-printed MoS_2 photodetectors 123
6.15 Inkjet-printed WS_2 and $MoSe_2$ photodetectors 124

7.1 Black phosphorus production *via* UALPE 128
7.2 AFM characterisation of black phosphorus 129
7.3 Raman spectroscopy of black phosphorus 131
7.4 Oxidation investigation of black phosphorus *via* Raman spectroscopy . . . 132
7.5 Formulation of black phosphorus ink 134
7.6 Black phosphorus ink stability against sedimentation and oxidation 135
7.7 Inkjet printing of black phosphorus 136
7.8 Characteristics of the inkjet-printed black phosphorus 137
7.9 Oxidation condition of the inkjet-printed black phosphorus 138
7.10 Passivation of the inkjet-printed black phosphorus 139
7.11 Raman spectroscopy of the passivated inkjet-printed black phosphorus . . . 141
7.12 Inkjet-printable black phosphorus saturable absorbers 142
7.13 Graphene/silicon Schottky junction photodetectors (Gr/Si) 145
7.14 Black phosphorus integrated Gr/Si photodetectors 146
7.15 Photodetection of the black phosphorus integrated Gr/Si photodetectors . . 146
7.16 Operation stability of the black phosphorus integrated Gr/Si photodetector . 147

8.1 SEM micrograph of commercial graphene nanoplatelets (GNPs) 151
8.2 Ink carrier design for the GNP inks 152
8.3 Formulated GNP inks and the rheological properties 153
8.4 Printed GNP films and electrical properties 153
8.5 Physical properties of the GNP/carbon inks 155
8.6 Mayer bar coated GNP/carbon films and their electrical properties 155
8.7 Printing pattern for printing trial on commercial flexographic press 156
8.8 Printing trial and printed capacitive touchpads 157
8.9 GNP based nanocomposite systems 158
8.10 High-loading inks of other 2d materials 160

List of tables

2.1 Bandgap of common semiconducting TMDs 15

4.1 Typical ink composition and viscosity for graphics printing technologies . . 50
4.2 Printing features of graphics printing technologies 55
4.3 Current inkjet-printable 2d material inks and their applications 68
4.4 Inverse Ohnesorge number of current 2d material inks 72

5.1 Concentration of the as-produced graphene dispersions 81
5.2 Photoelectrical parameters of the graphene based dye-sensitised solar cells . 100

6.1 Concentration of the as-produced TMD dispersions 104
6.2 Optical absorption coefficient values of TMDs 106
6.3 Inverse Ohnesorge number of alcohols and the TMD IPA/2-butanol inks . . 112
6.4 Average optical absorption properties of the inkjet-printed TMD SAs 120

7.1 Black phosphorus oxidation ratio analysis *via* Raman spectroscopy 132
7.2 Mode-locked fibre lasers using black phosphorus SAs 143
7.3 Photodetectors based on black phosphorus 147

8.1 Specific surface area of commercial graphene nanoplatelets 150

List of abbreviations and symbols

Roman Symbols

a	Inkjet nozzle diameter
A	Optical absorbance
C	Concentration
d	Flake diameter
d^*	Interflake distance
D	Droplet spacing
D_0	Deposited droplet diameter
ΔG_{mix}	Gibbs free energy of mixing
ΔH_{mix}	Enthalpy of mixing
$D_{\text{impinging}}$	Droplet impinging distance
ΔS_{mix}	Entropy of mixing
e	Charge on an electron
E	Optical extinction
FF	Fill factor
FoM	Figure of merit
F_{cen}	Centrifugation force
F_{fric}	Friction force

h	Planck's constant
I_{sat}	Saturation intensity
J_{sc}	Short circuit current density
l	Optical path length
L	Flake characteristic dimensional length
m	Mass
n_c	Number of charge carriers per unit area
N	Number of atomic layers
Oh	Ohnesorge number
P_{in}	Incident light power
r	Flake size (*i.e.* thickness and lateral dimension)
R_0	Radius of a deposited ink droplet
R_1	Radius of a printed line with uniform edges
R_d	Hansen solubility parameter distance
R_{drop}	Radius of a falling ink droplet
Re	Reynolds number
RH	Relative humidity
R_p	Photoresponsivity of photodetectors
R_{rad}	Centrifugation rotor rotation radius
R_s	Sheet resistance
t	Flake/film thickness
T	Optical transmittance
V_{drop}	Volume and radius of a falling ink droplet
V_{oc}	Open circuit voltage

We	Weber number
X	Density of percolating objects
X_0	Critical density of percolating objects
Z	Inverse Ohnesorge number

Greek Symbols

α_{d}	Optical modulation depth
α_{λ}	Absorption coefficient at a wavelength λ
α_{l}	Optical linear absorption
α_{ns}	Optical non-saturable absorption
δ_{D}	Dispersive Hansen solubility parameter
δ_{H}	Hydrogen bonding Hansen solubility parameter
δ_{P}	Polar Hansen solubility parameter
η	Viscosity
η_{eff}	Light-to-electrical energy efficiency
ξ	Line-edge roughness
γ	Surface tension
γ_{2d}	Surface energy of 2d material
γ_{s}	Surface energy of solvent
λ	Wavelength
μ_{c}	Carrier mobility
ν	Volume fraction
ν_0	Critical volume fraction
ω	Centrifugation rotor angular velocity
ρ	Density of ink/dispersion

σ	Optical scattering
σ_e	Electrical conductivity
σ_{op}	Optical conductivity
τ	Temperature
υ	Ink droplet jetting velocity
υ_{cen}	Centrifugation flake velocity

Solvents, compounds, and chemical abbreviations

BP	Black phosphorus
CB	Chlorobenzene
CHP	N-Cyclohexyl-2-pyrrolidone
CNT	Carbon nanotube
DMF	Dimethylformamide
EC	Ethyl cellulose
EG	Ethylene glycol
FTO	Fluorine-doped tin oxide
GNP	Graphene nanoplatelet
h-BN	Hexagonal boron nitride
HMDS	Bis(trimethylsilyl)amine
IPA	Isopropanol
ITO	Indium tin oxide
MoS_2	Molybdenum disulfide
$MoSe_2$	Molybdenum diselenide
MXenes	Transition metal carbides and carbonitrides
Na-CMC	Sodium carboxymethylcellulose

NC	Nitrocellulose
NMP	N-Methyl-2-pyrrolidone
PANI	Polyaniline
PDMS	Polydimethylsiloxane
PEDOT:PSS	Poly(3,4-ethylenedioxythiophene)-poly(styrenesulfonate)
PEN	Polyethylene naphthalate
PET	Polyethylene terephthalate
PI	Polyimide
Plasdone S-630	Copolymer of N-vinyl-2-pyrrolidone and vinyl acetate
PMMA	Polymethyl methacrylate
PQT-12	Poly[5,50-bis(3-dodecyl-2-thienyl)-2,20-bithiophene]
PS1	1-pyrenesulfonic acid sodium salt
PVA	Polyvinyl alcohol
PVP	Polyvinyl pyrrolidone
SC	Sodium cholate
SDBS	Sodium dodecylbenzene sulphonate
SDC	Sodium deoxycholate
s-TMD	Semiconducting transition metal dichalcogenide
TIPS_PEN	6,13-bis((triisopropylsilylethynyl) pentacene
TMD	Transition metal dichalcogenide
WS_2	Tungsten disulfide
WSe_2	Tungsten diselenide

Acronyms / Abbreviations

2d	2-dimensional

AFM	Atomic force microscopy
CE	Counter-electrode
CIJ	Continuous inkjet
CMC	Critical micelle concentration
CMOS	Complementary metal-oxide semiconductor
CVD	Chemical vapour deposition
DGU	Density gradient ultracentrifugation
DOD	Drop-on-demand inkjet
DSSC	Dye sensitised solar cell
FET	Field effect transistor
FWHM	Full width at half maximum
HOMO	Highest occupied molecular orbital
HSP	Hansen solubility parameter
IDE	Interdigitated electrode
IR	Infrared
LPE	Liquid phase exfoliation
LUMO	Lowest unoccupied molecular orbital
MC	Micro-mechanical cleavage
MEMS	Micro electromechanical system
NIR	Near-infrared
PCB	Printed circuit board
PL	Photoluminescence
R2R	Roll-to-roll
RFID	Radio-frequency identification

RF	Radio frequency
ROM	Read-only memory
RZS	Rate zonal separation ultracentrifugation
SA	Saturable absorber
SBS	Sedimentation based separation ultracentrifugation
SEM	Scanning electron microscopy
SESAM	Semiconductor saturable absorber mirror
TEM	Transmission electron microscopy
TGA	Thermogravimetric analysis
UALPE	Ultrasonic-assisted liquid phase exfoliation
UV	Ultraviolet
vdW	van der Waals

Chapter 1

Introduction

1.1 Project background

2-dimensional (2d) materials are atomically thin mono- and few-layer planar crystal nanosheets, where the atoms are covalently bonded in-plane and are weakly stacked by van der Waals (vdW) forces out-of-plane. The counterpart bulk crystals are termed as layered crystals [1–3]. There are many 2d materials. Archetypes include graphene, transition metal dichalcogenides (TMDs), black phosphorus (BP), hexagonal boron nitride (*h*-BN), and transition metal carbides and carbonitrides (MXenes) [1]. Unlike other functional material groups, the 2d material family exhibits a wide spectrum of distinct and complementary *e.g.* electronic, optoelectronic and photonic properties [4–8]. 2d materials are therefore promising for the next generation optoelectronics and photonics [5, 7, 9, 10], as well as energy storage and conversion [11, 12] and biomedicines [13, 14]. A great advance towards scalable applications is the development of solution processing methods for low-cost mass production of 2d materials [1, 15]. Importantly, the solution-processed 2d material dispersions are readily adaptable to graphics printing technologies for device fabrication [16–18].

Graphics printing technologies such as inkjet, screen, and roll-to-roll (R2R) flexographic and gravure are widely used in printing of documents, magazines, newspapers and packing materials [19, 20]. In recent years, there is a growing interest in incorporating functional materials into the inks for device fabrication [21–25]. Inkjet printing is of particular interest due to its non-contact, mask-less, high-resolution (sub-100 μm) digital "writing" capabilities. This is time and cost saving, especially when prototyping [23, 24]. Thus-far, a number of functional materials have been investigated for this purpose, including metallic nanoparticles [26], organic semiconductors [27, 28] and carbon materials (*e.g.* carbon black, carbon nanotubes) [29–31]. Printing allows additive patterning of these materials on rigid and flexible, conformable substrates [19, 20], enabling low-cost, large-scale device fabrication,

without the need for the conventional expensive vacuum deposition used in silicon based technologies [32, 33]. An additive patterning process supports successively deposition of different, multiple functional materials for device construction, leading to a high-level integration and a low fabrication complexity. Already, there are many demonstrations of printable applications, for instance inkjet-printed smart packaging systems [34], gravure-printed wireless power transmitters [35] and flexographic-printed paper based chipless RFID tags [36]. The printed devices, however, show limitations mostly due to poor performance, chemical instability or high production cost of the exploited functional materials [18, 24, 37]. For instance, printed organic transistors and logic integrated circuits exhibit an extremely low mobility (typically <1 $cm^2V^{-1}s^{-1}$), while their chemical instability prevents long-term device operation lifetime. With superior material properties, 2d materials are a promising alternative material platform that are potentially more advantageous for printable applications.

In 2012 Torrisi *et al.* first demonstrated inkjet printing of graphene produced from ultrasonic-assisted liquid phase exfoliation (UALPE) for transistor fabrication [37]. The printed graphene transistors exhibited a carrier mobility of up to 95 $cm^2V^{-1}s^{-1}$ with an I_{ON}/I_{OFF} (*i.e.* the ratio of currents in the ON- and OFF-state of the transistor) of $\sim$10. The carrier mobility is far greater than that of organic transistors. Since then, the field of 2d material printing has been gaining a huge momentum, with a rapid progress in ink formulation and device fabrication, though not yet optimised [38, 39]. Besides graphene, other 2d materials have also been successfully adapted to printing, for instance TMDs [40–42] and *h*-BN [42]. Developing from printing with the as-produced dispersions, ink formulations are now beginning to emerge not only for inkjet but also for screen [43, 44], flexographic [45] and gravure printing [46]. These formulations may comprise surfactants or polymer binders for improved ink concentration, fluidic properties and printed morphologies [39, 43–58]. Besides transistors [37, 42, 48], 2d materials have been also demonstrated in much broader printable applications, for example, in conductive electrodes, interconnects and circuits [44, 46, 51, 54, 57], photodetectors [40, 41, 48], sensors [49, 57, 58], and energy storage and conversion devices [45, 59].

1.2 Project motivation

The aim of my doctoral work is to develop functional inks of 2d materials and explore them in developing printable applications, in particular optoelectronics and photonics. The 2d materials I have investigated include graphene, TMDs and BP produced *via* UALPE, a solution processing method. The key printing technology I have employed is inkjet printing.

Though there is a rapid progress in inkjet printing of 2d materials, proceeding studies show that the current inks (typically the as-produced UALPE dispersions, or in some cases the formulations with surfactants and polymer binders) are far from ideal [48]. For the UALPE dispersions, their fluidic properties, drying dynamics and interaction with substrates are not optimal, leading to unstable jetting of ink droplets, poor wetting of the substrates, and the formation of "coffee rings" [60, 61]. As a result, inkjet printing cannot give a spatially uniform deposition of 2d materials, making it challenging to achieve reproducible device fabrication. This prevents large-scale device printing. Other challenges include such as low concentration, long drying times, and/or incompatibility with substrates. For the other formulations, though the inks may show improved printing results, post-printing treatment is usually required to remove the surfactants and polymers since unlike solvents they form integral parts of the printed 2d materials and hence, compromise the functionalities of the 2d materials [46, 48, 50, 51, 54]. This is usually done by high temperature (*e.g.* $>$400°C) annealing, problematic for flexible devices using polymeric substrates. Therefore, aiming to achieve large-scale device printing, a significantly improved ink formulation is desired, which is the major target of my doctoral work.

Beyond inkjet printing, high-speed printing is more appealing in terms of scalability [20, 62]. For instance, flexographic has a printing speed of up to 500 m min^{-1}, much higher than that of inkjet printing (typically 10 m min^{-1}) [20, 62]. This can lead to a much more efficient device fabrication. Correspondingly, flexographic printing requires certain physical ink properties, for instance a loading of $>$10 wt.% (*i.e.* 100 gL^{-1}) and a viscosity of $>$50 mPa·s [62]. To expand the scope of 2d material printing, formulation of high-speed printable inks is necessary. The UALPE dispersions present challenges in doing so with a concentration of $<$1 gL^{-1}. Such a low concentration means that formulating 1 L of flexographic-printable ink would use over 100 L of UALPE dispersions. In this context, using commercially available nanoplatelets is more suitable for scalable ink formulation. It also offers the convenience of tuning the ink composition and ink physical properties. Therefore, I also focus on ink formulation of commercial graphene nanoplatelets for high-speed printing.

1.3 Structure of the thesis

Besides this introduction chapter, this PhD thesis contains 8 further chapters, including a literature review on printing of 2d materials for optoelectronics and photonics (Chapter 2, 3 and 4), my detailed doctoral work (Chapter 5, 6, 7 and 8), and conclusions and outlook (Chapter 9).

For literature review, I begin with an introduction of 2d materials on their structures, properties and applications in Chapter 2, with the focus on graphene, TMDs and BP. I then describe the diverse production methods of 2d materials and the related material characterisation techniques in Chapter 3, in particular the fundamentals of UALPE. Finally, I discuss the ink systems and the printing technologies in Chapter 4. Inkjet printing is the main topic of this chapter, covering its working mechanisms, and the thus-far progress and challenges on 2d material printing.

In Chapter 5, 6 and 7, I look at inkjet-printable ink formulation of 2d materials produced *via* UALPE, and the printable 2d material applications. In Chapter 5, I elaborate my work on graphene production, ink formulation and inkjet printing. More specifically, I develop a polymer stabilised alcohol based ink formulation of graphene, *i.e.* a graphene isopropanol (IPA)/polyvinylpyrrolidone (PVP) ink, that is well-suited to print onto a range of untreated substrates for large-scale spatially uniform material deposition. I then discuss exploiting the inkjet-printed graphene in applications. These include integrating the inkjet-printed graphene onto CMOS platform for humidity sensors, and making use of the inkjet-printed graphene as counter-electrodes for dye-sensitised solar cells (DSSCs). In the further two chapters, I describe my work on TMDs (Chapter 6) and BP (Chapter 7). For TMDs, I study three types of semiconducting TMDs: molybdenum disulfide (MoS_2), tungsten disulfide (WS_2) and molybdenum diselenide ($MoSe_2$). I design a binary alcohol carrier (*i.e.* a mixture of IPA and 2-butanol) for ink formulation of these three TMDs and BP. This binder-free binary alcohol ink formulation is capable of achieving optimal ink fluidic properties, wetting of a range of substrates without substrate surface treatment, and suppression of the coffee ring effect by induced recirculating Marangoni flow. In addition, I present a methodology to seek the optimal inkjet printing parameters for a spatially uniform morphology of the printed patterns. On this basis, I focus on the development of printable optoelectronics and photonics, including photodetectors saturable absorbers (SAs). In Chapter 8, however, I look at ink formulation using commercial graphene nanoplatelets for high-speed printing technologies (*e.g.* R2R flexographic printing). This formulation yields high-loading inks that can be used as stand-alone highly conductive inks, as additives to polymer nanocomposite systems, and as additives to other functional ink systems. A graphene/carbon hybrid ink is developed for commercial R2R flexographic press, allowing hundreds of conductive electronic circuits for capacitive touchpad devices printed within one minute.

In the end, I conclude the thesis in Chapter 9 with a summarise of my doctoral work, and an outlook of the potential and future opportunities for printable 2d material applications.

Chapter 2

Structures, properties and applications of 2d materials

2.1 The 2d material family

Graphite naturally occurs in metamorphic geology. The use of graphite dates back to the *Neolithic* age when our ancient ancestors used it for ceramic decoration [63]. It was latter used in areas such as refractories due to its physical stabilities [64]. This soft rock was found constructed with a layered laminar structure and easy to delaminate into thin sheets. This particular property led to a widespread use as lubricant. Scientific research on this laminar structure was gradually established, leading to fundamental understandings and eventually experimental demonstrations of atomically thin nanosheets [1]. Thermally reduced graphitic oxide (*i.e.* compound of carbon, oxygen and hydrogen in variable ratios) with a highly layered structure was first reported in 1859 [65], while few-layer graphite flakes were first imaged in 1948 and subsequently even monolayers [66], which was termed as "graphene" in 1987 [67]. The major concern on graphene was that whether such monolayers could exist independently against thermal fluctuations [68]. It was in 2004 that graphene was finally conclusively demonstrated by Novoselov *et al.*, who produced it by repeatedly cleaving graphite with adhesive tape [2, 3]. This method is now widely known as micro-mechanical cleavage (MC) and is colloquially termed as the "scotch-tape" method.

Since then many other crystals that share a similar layered structure with graphite have been extensively studied, commonly referred to as layered crystals. Archetype examples include transition metal dichalcogenides (TMDs) that occur in nature [6], black phosphorus (BP) that is synthesised from other phosphorus allotropes [69], and hexagonal boron nitride (*h*-BN) that is produced *via* chemical synthesis [70]. The term "layered" is used to highlight

the crystal structure where one or few atom thick planar layers are bound into a stack with strong in-plane covalent bonds and weak out-of-plane van der Waals (vdW) forces [1–3, 5]. These two forces differ in the mechanical strength, allowing exfoliation of the layered crystals into few-layers and even monolayers. Because of the atomic thickness, these are termed as 2-dimensional (2d) materials [1–3, 5].

The research on the other 2d materials shared a long history with graphene. However, the renaissance of interest in this field was not until more recently. For instance, the optical absorption features of exfoliated molybdenum disulfide (MoS_2) [71] were initially reported by R. Frindt and A. Yoffe in 1963, and monolayer MoS_2 was reported as early as in 1986 [72], but the interest in MoS_2 or TMDs in general was restored only in 2011 when Radisavljevic *et al.* demonstrated monolayer MoS_2 based transistors with an I_{ON}/I_{OFF} exceeding 10^8 [73].

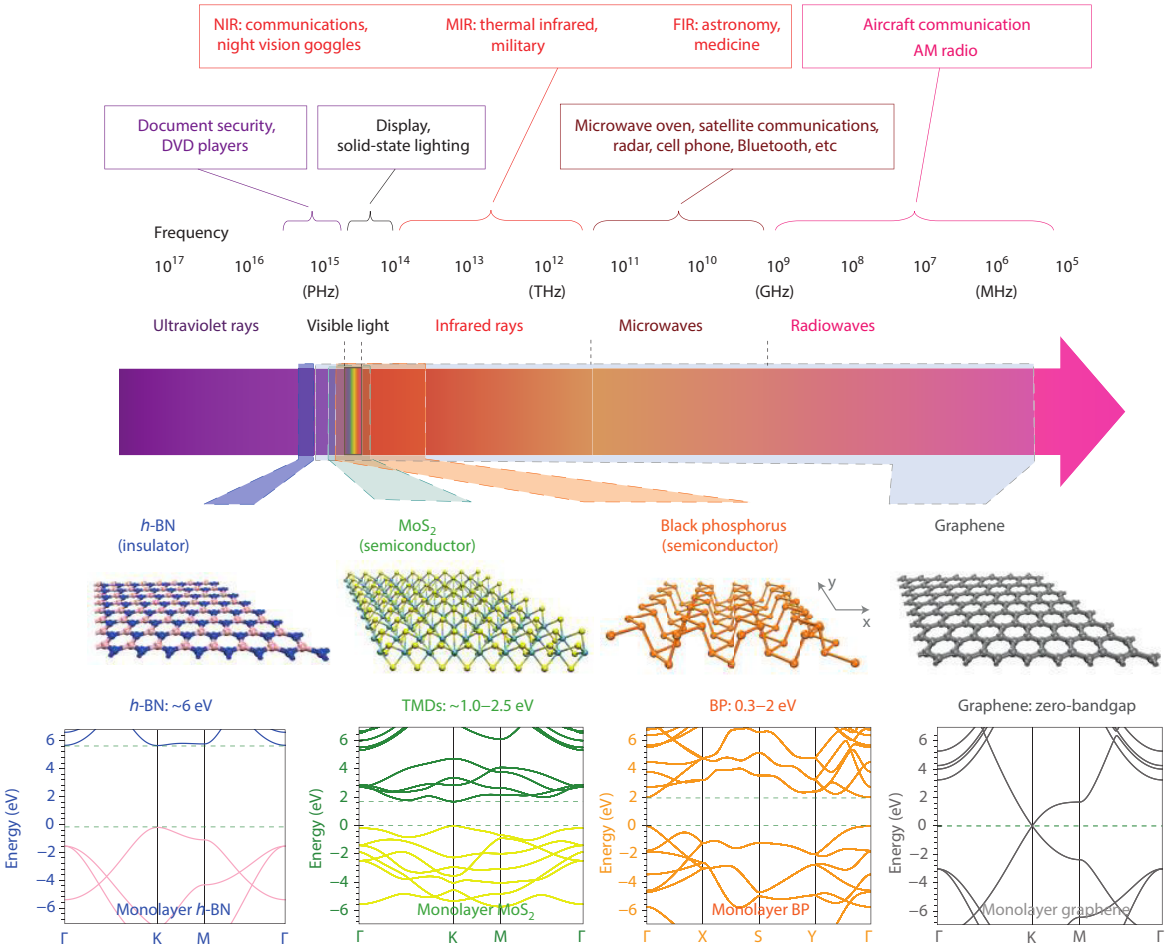

Fig. 2.1 Electromagnetic spectrum of 2d materials and their applications [4].

Similar to MoS_2, although BP was first successfully synthesised from white phosphorus in 1914 [74], it regained the significant attention as a new 2d material in 2014 [69].

2d materials typically can be directly exfoliated from the bulk. However, in some cases, 2d materials can only be artificially produced [1]. A prime example is transition metal carbides and carbonitrides (MXenes) such as Ti_3C_2 and Ti_3CN that are produced by selectively etching away the interlayer metal atoms from the corresponding bulk [75, 76].

This diversity amongst the 2d material family illustrates a broad spectrum of distinct and complementary optoelectronic properties, enabling a wide range of applications; Fig. 2.1 [4–6, 17, 75, 77, 78]. For graphene, the combination of atomic thickness, high transparency and high conductivity of graphene is promising for flexible transparent conductors, while its high carrier mobility in addition to the zero-bandgap can be exploited in high-frequency applications [4, 5, 9, 77, 79]. TMDs (*e.g.* MoS_2) and BP exhibit sizeable, layer-dependent bandgap spanning the visible to near-infrared (NIR) range [4–6], attracting tremendous attention for electronics such as thin-film transistors [42, 69, 73], and optoelectronics such as photodetectors and light emitters [80–82]. *h*-BN is an insulating 2d material with a bandgap of $\sim$6 eV. This can be exploited for ultraviolet (UV) light emission [83]. The atomically smooth surface and the absence of dangling bonds make *h*-BN an ideal dielectric substrate for other 2d materials in a wide variety of device applications [84]. The extent of applications of 2d materials go well beyond optoelectronics and photonics, ranging from composites, sensors, energy storage and conversion, to biomedicines. For instance, MXenes (*e.g.* Ti_3C_2 and Ti_3CN) exhibit interesting electrochemical properties to work as electrodes in batteries and supercapacitors [75, 76, 85, 86].

I next discuss the structures, properties and applications of graphene (Section 2.2), TMDs (Section 2.3) and BP (Section 2.4) that have been investigated in my doctoral work, as well as other common 2d materials such as *h*-BN (Section 2.5.1) and MXenes (Section 2.5.2).

2.2 Graphene

Graphene is atomically thin planar carbon sheet, as shown in Fig. 2.2(a,b), where the flakes were prepared by MC. Figure 2.2(c,d) schematically illustrate the honeycomb hexagonal lattice of graphene. Each of the carbon atoms is covalently bonded with three other carbon atoms and as such three of its four valence electrons are taken to form a chemical bond to the nearest neighbour electrons. The fourth electron, however, is left free to migrate through the graphene lattice [9, 87]. These freely migrating fourth electrons lead to an exceptionally high carrier concentration (n_c) in graphene [9, 87]. A value exceeding 10^{14} cm^{-2} was reported by Ye *et al.* [88].

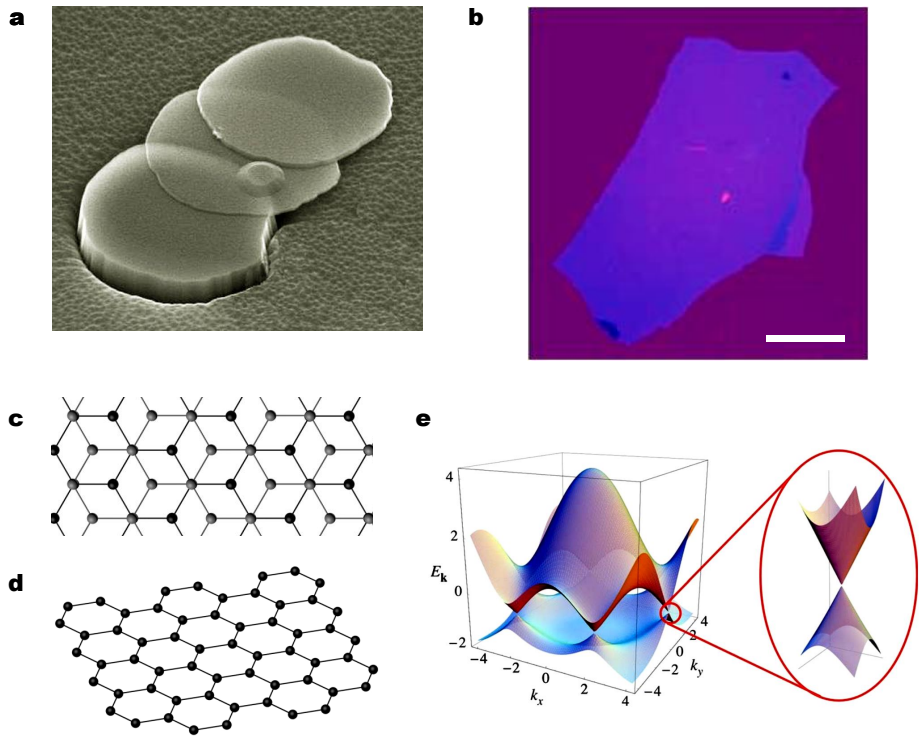

Fig. 2.2 (a) SEM micrograph of 10 nm thick graphene flakes produced *via* MC, source Condensed Matter Group, University of Manchester; (b) Optical micrograph of a 3 nm thick graphene flake, scale bar 20 µm [2]; (c) Top-view of stacked graphene layers, and (d) side-view of monolayer graphene; (e) Electronic dispersion in graphene honeycomb lattice [87].

Figure 2.2(e) depicts the dispersion of electrons in graphene. The forth free migrating electron corresponds to the low energies close to the Fermi energy. As this electron may be subjected to a spin-up or spin-down state, the valence band is completely filled, and the conduction band is completely empty. Meanwhile, this electron is subjected to the periodic potential of the graphene honeycomb lattice, giving rise to degeneracies in the valence and conduction bands of graphene. This means that the valence and conduction bands touch but do not overlap at the Dirac point of the Fermi energy. As a result, graphene has a zero-bandgap [9, 87].

This band structure defines the unique optoelectronic properties of graphene [5, 9, 87]. At the degenerate regions, the electrons are dispersed linearly and isotopically as massless Dirac fermions. Graphene therefore exhibits an exceptionally high carrier mobility (μ_c). For example, a mobility over 10^6 $cm^2v^{-1}s^{-1}$ was observed in epitaxial graphene nanoribbons [89]. This is about 1,000 times greater than that of silicon. The zero-bandgap nature of graphene enables a good electrical conductivity, with its sheet resistance (R_s) of mono- and few-layer

graphene derived according to the relation:

$$R_s = (n_c \mu_c e N)^{-1} \tag{2.1}$$

where N is the number of layers, e is the charge on an electron [5]. For ideal intrinsic graphene, $n_c \mu_c e$ assumes a constant value of $4e^2/h$ (where h is the Planck constant) [9, 87], giving R_s as 6 kΩ/□. In practice, however, graphene samples typically expect a much smaller calculated R_s according to Eq. 2.1, for instance ∼135 Ω/□ for MC graphene [5, 90]. Typical monolayer chemical vapour deposition (CVD) grown graphene expects a R_s as low as 30 Ω/□ with typical n_c of 10^{12}-10^{13} cm^{-2} and typical μ_c of 1,000-20,000 $cm^2v^{-1}s^{-1}$ [5]. Also, the sheet resistance can be tuned, for example, by controlling the layer numbers or by using electric field or chemical doping [91, 92].

The linearly dispersed electrons define that the optical transmittance of graphene is independent on the frequency of incident light in the visible to IR region [9, 87, 93]. Theoretically, monolayer graphene is highly transparent, absorbing 2.3% of the incident light, which has been experimentally observed from suspended graphene samples [93]. In addition, graphene only reflects <0.1% of the incident light [93]. With such low reflectance between layers, the optical absorption of few-layer graphene is therefore proportional to the graphene layer number, *i.e.* with each additional graphene layer increasing the absorption by 2.3% [93]. Under strong illumination, graphene additionally exhibits nonlinear absorption properties, where the absorption saturates, a phenomenon observed in many semiconductors [94, 95].

With an atomically thin layered structure, graphene has a large specific surface area, with a theoretical value of 2,630 m^2g^{-1} [96]. Graphene is mechanically strong, with a measured breaking strength of up to 42 N/m (100 times that of steel) [97], and a measured Young's modulus of ∼1 TPa (5 times that of steel) [97]. This makes graphene a promising filler material to enhance the strength of polymer-based nanocomposites. An addition of 1 wt% of graphene in nanocomposites was reported to offer an improvement to the Young's modulus by ∼80% [98]. Due to the strong mechanical properties, graphene exhibits a high bending stiffness such that the electronic properties do not substantially change upon stretching [99, 100]. The thermal conductivity of graphene is also exceptional with a measured conductivity for a suspended sample of up to ∼5,000 $Wm^{-1}K^{-1}$ at room temperature (compared to *e.g.* silver 429 $Wm^{-1}K^{-1}$) [101]. As such, graphene is a promising filler for thermal conductive nanocomposites.

These above properties offer unusual opportunities for applications. One is in transparent conductors, taking the advantages of the high optical transparency and the electrical conductivity of graphene. The sheet resistance (R_s) of a conductive thin film can be defined by its

electrical conductivity (σ_e) *via*:

$$R_s = (\sigma_e t)^{-1} \tag{2.2}$$

where t is the film thickness. The transmittance (T) can be defined by the optical conductivity (σ_{op}) *via* [102]:

$$T = (1 + \frac{Z_0}{2}\sigma_{op} t)^{-2} \tag{2.3}$$

where Z_0 is the impedance of free space and has a value of 377 Ω [102]. The relationship between R_s and T can then be defined as:

$$T = (1 + \frac{Z_0}{2R_s}\frac{\sigma_e}{\sigma_{op}})^{-2} \tag{2.4}$$

Therefore, the ratio of σ_e to σ_{op} can be used as figure of merit (*FoM*) for transparent conductors:

$$\frac{\sigma_e}{\sigma_{op}} = \frac{188.5}{R_s(T^{-1/2} - 1)} \tag{2.5}$$

The minimum industry standard of *FoM* is 35 (R_s = 100 Ω/□, T = 90%) [102]. CVD graphene with a low R_s and a high transparency has emerged as a promising candidate in replacement of the current transparent conductor technologies (*e.g.* indium tin oxide: ITO, silver nanowires and carbon nanotubes: CNTs) [5, 102–104]. Indeed, Bae *et al.* demonstrated a 30 inch CVD graphene transparent conductor with R_s of 125 Ω/□ at T of 97.4% [105]. The R_s could be further decreased to 30 Ω/□ at 90% [105]. This gives a *FoM* of up to 116, easily surpassing the industry standard. As a transparent conductor, graphene offers an additional advantage of flexibility. It is capable of sustaining a strain of ∼25% without breaking [5, 97]. The current incumbent, ITO, is a brittle material with a crack onset strain of only ∼1-1.5%, restricting the development of next generation flexible devices [5, 102, 104]. Proof-of-concept graphene flexible transparent conductor based applications have already been reported (*e.g.* Fig. 2.3(a)), for example, in touch screens, photovoltaics and light emitting devices [5, 105, 106]. Transparent graphene films fabricated by other methods (*e.g.* spray coating, rod coating and self-assembly of solution-processed graphene) instead of CVD are also promising for transparent electrodes [17, 107–109]. For example, Howe *et al.* demonstrated a rod-coated graphene film with 900 Ω/□ at 90% [17]. This allows production of flexible transparent graphene conductors with a much lower cost, larger area and lower processing temperature, and it can be deposited directly onto the target substrate as opposed to CVD graphene films. On the other hand, non-transparent printed graphene conductive films find uses in electrical conductors [54, 110–112], as a low-cost, high-performance alternative for conventional carbon and metal based conductors [112, 113]. Figure 2.3(b) is one such demonstration where printed graphene was exploited as conductive circuits [111].

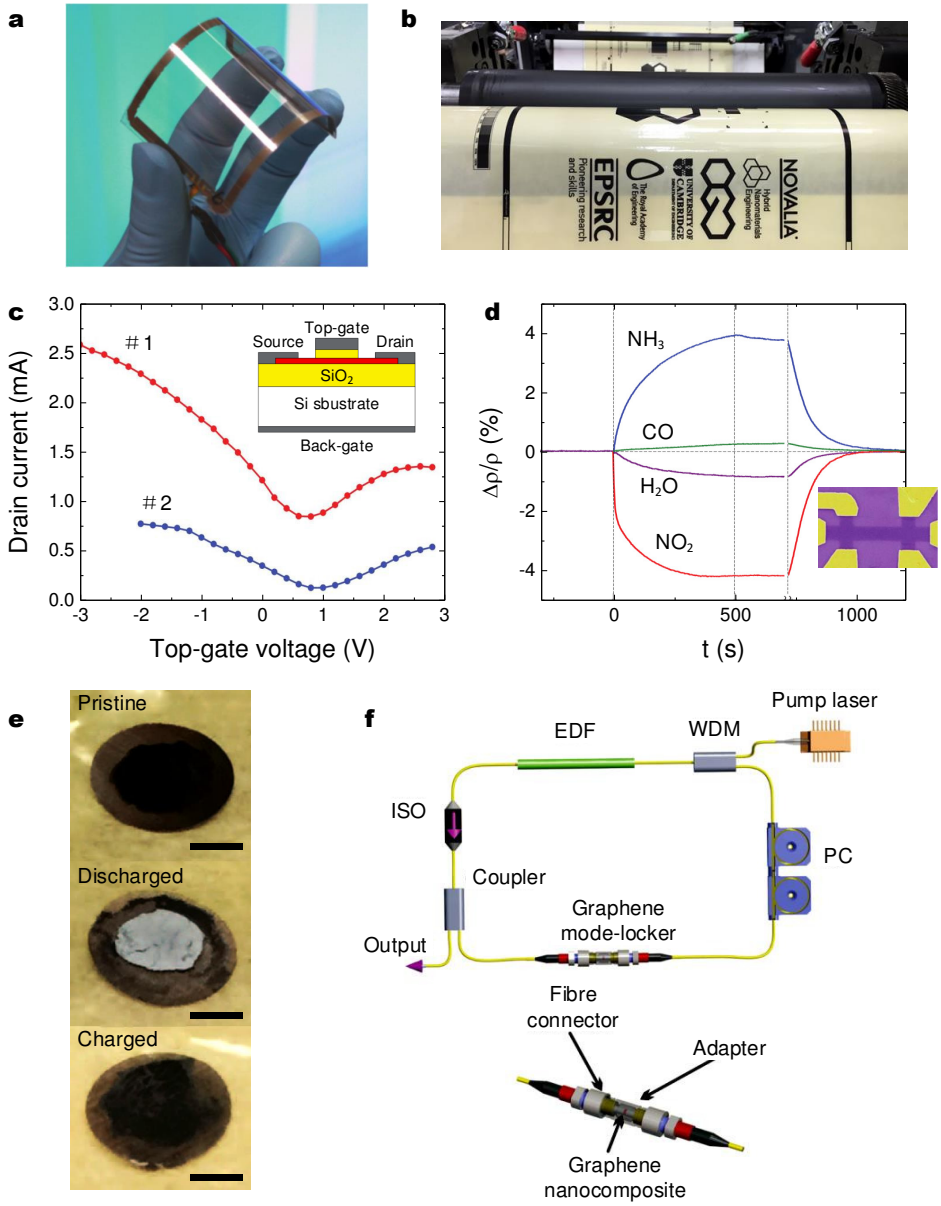

Fig. 2.3 (a) Flexible graphene transparent conductors [105]; (b) Printable conductive graphene circuits; (c) Typical graphene transistor transfer characteristics, inset: schematic figure for top-gated graphene transistor, adapted from Ref. [114]; (d) Individual gas molecule sensor based on graphene transistor structure, adapted from Ref. [115]; (e) Reduced graphene oxide electrodes for lithium-air batteries, scale bar 5 mm [116]; (f) Graphene polymer nanocomposite SAs for ultrafast laser [95].

Such printed graphene conductive circuits can be interfaced with traditional electronics to develop applications such as flexible capacitive touchpads [111].

The high electron mobility and carrier density of graphene hold huge promises for transistors [5, 79, 87, 114]. The inset of Fig. 2.3(c) schematically outlines the structure of

a typical top-gated graphene transistor. Such devices exhibit high carrier mobility (20,000 $cm^2v^{-1}s^{-1}$ [117]) and high intrinsic cut-off frequency (>100 GHz [118]), making them attractive for high frequency applications. However, the zero-bandgap of graphene means that the transistors cannot be effectively switched-off. This seriously limits the I_{ON}/I_{OFF} ratio, typically <100 [37, 79, 114]. For instance, the transfer characteristics in Fig. 2.3(c) show that both the devices have a I_{ON}/I_{OFF} <10. Logic electronic applications, however, typically require a sizeable bandgap (>0.4 eV) and excellent switching capabilities (I_{ON}/I_{OFF} $>10^4$) [114]. Considerable efforts have therefore been devoted to "opening" the graphene bandgap while avoiding diminishing the electronic properties, for instance *via* nanopatterning graphene to create graphene nanoribbons [114]. Unfortunately, for practical applications this goal remains elusive.

The exposed large surface area (theoretical value 2,630 m^2g^{-1}) of graphene allows it to interact strongly with the ambient elements, including moisture, gas, chemicals and biomolecules [77, 119]. The adsorption of such ambient elements can lead to changes of graphene in local carrier concentration and hence, the electrical conductivity [87, 115, 120]. The high carrier mobility of graphene therefore enables a high sensitivity to any changes, even single molecules [87, 115, 121, 122], making graphene a promising material platform for sensing applications [77, 115, 119]. The inset of Fig. 2.3(d) presents a gas sensor based on a transistor architecture. The authors demonstrated that the sensor allowed for detection of individual gas molecules of NO_2, NH_3, H_2O and CO; Fig. 2.3(d) [115]. However, this approach of exploiting the intrinsic properties of pristine graphene cannot give good selective sensitivities, realising which may require covalent or non-covalent functionalisation of graphene [123, 124].

The high specific surface area of graphene is also well-suited for the development of electrode systems for energy storage and conversion (*e.g.* supercapacitors and batteries) [116, 125–129]. The graphene electrode systems can lead to a decrease in film thickness while an increase in electrode-to-electrolyte contact, which when combined with good electrical conductivity offers better performance than current technologies. With regards to manufacturing scalability and miniaturisation, El-Kady *et al.* reported fabrication of supercapacitors using laser scribed graphene-based electrodes [126]. The electrodes exhibited high electrical conductivity and specific surface area for ultrahigh energy density values (up to 1.36 $mWhcm^{-3}$), high power density ($\sim$20 Wcm^{-3}) and excellent cycle stability. More recently, Liu *et al.* reported a lithium-air battery using reduced graphene oxide electrodes; Fig. 2.3(e) [116]. The device exhibited high specific capacities, excellent energy efficiency (93.2%) and impressive rechargeability.

Another key application of graphene is in ultrafast lasers (*i.e.* fs-μs pulse duration). Ultrafast lasers are a technology in high demand in a wide range of applications, *e.g.* materials processing, time-resolved spectroscopy, industrial micromachining and biomedical imaging [94, 130–132]. A most widely used method in such ultrashort pulse output generation is to employ saturable absorbers (SAs). SAs act as fast nonlinear optical switches to convert the output from a low-power continuous-wave signal to a train of high-power ultrashort pulses. Current dominant SA technology is semiconductor saturable absorber mirrors, which however present a narrow tuning range and require a complex fabrication [132–134]. The linear dispersion of Dirac electrons [9] in addition to the nonlinear optical absorption and ultrafast carrier dynamics [135–137] make graphene a promising alternative material for SA operable over a wide spectral range [95, 133]. One dominant, well-developed technology for graphene SA fabrication is through developing graphene flake enriched polymer nanocomposites from solution-processed graphene dispersions [95, 134]. Figure 2.3(f) presents the integration of such graphene nanocomposite SAs into ultrafast laser cavity for the generation of ultrashort ($\sim$460 fs) pulses, pioneered by Sun *et al.* [95].

2.3 Transition metal dichalcogenides (TMDs)

TMDs are a group of $\sim$40 compounds sharing a general formula MX_2, where M represents a transition metal (*e.g.* molybdenum: Mo, tungsten: W, niobium: Nb) and X is a group VI element (*e.g.* sulfide: S, selenide: Se, tellurium: Te) [6–8]. Like graphite, bulk TMDs are crystals formed with stacked layers. Monolayer TMDs consist of a plane of hexagonally bonded M atoms sandwiched between two layers of X atoms *via* chemical bonds [138], as exampled by Fig. 2.4(a). Depending on the coordination and oxidation states of M atoms and the chemical structures between M and X atoms, TMDs are either metallic (*e.g.* $NbSe_2$) or semiconductive (*e.g.* MoS_2, WS_2 and $MoSe_2$) [6–8].

Exfoliation of bulk TMDs can lead to radical changes in the physical properties [6, 7]. A widely studied example is MoS_2 [73]. Monolayer MoS_2 is highly transparent (optical transmittance $>$90% at $\sim$652 nm [139]), with a mechanical strength 30 times that of steel [141]. The larger exposed surface area of exfoliated MoS_2, compared to bulk MoS_2, greatly enhances its chemical reactivities [1]. Bulk MoS_2 is not an efficient electrocatalyst for hydrogen evolution reaction, but exfoliated MoS_2 has been demonstrated as an efficient and viable material, as a result of the significantly increased exposed catalytically active edges [142].

More importantly, for the case of semiconducting TMDs (s-TMDs), quantum confinement due to the decrease in thickness causes changes in the electronic band structure [6, 7]. As shown in Fig. 2.4(b), along with the decrease in the layer numbers of MoS_2, the direct

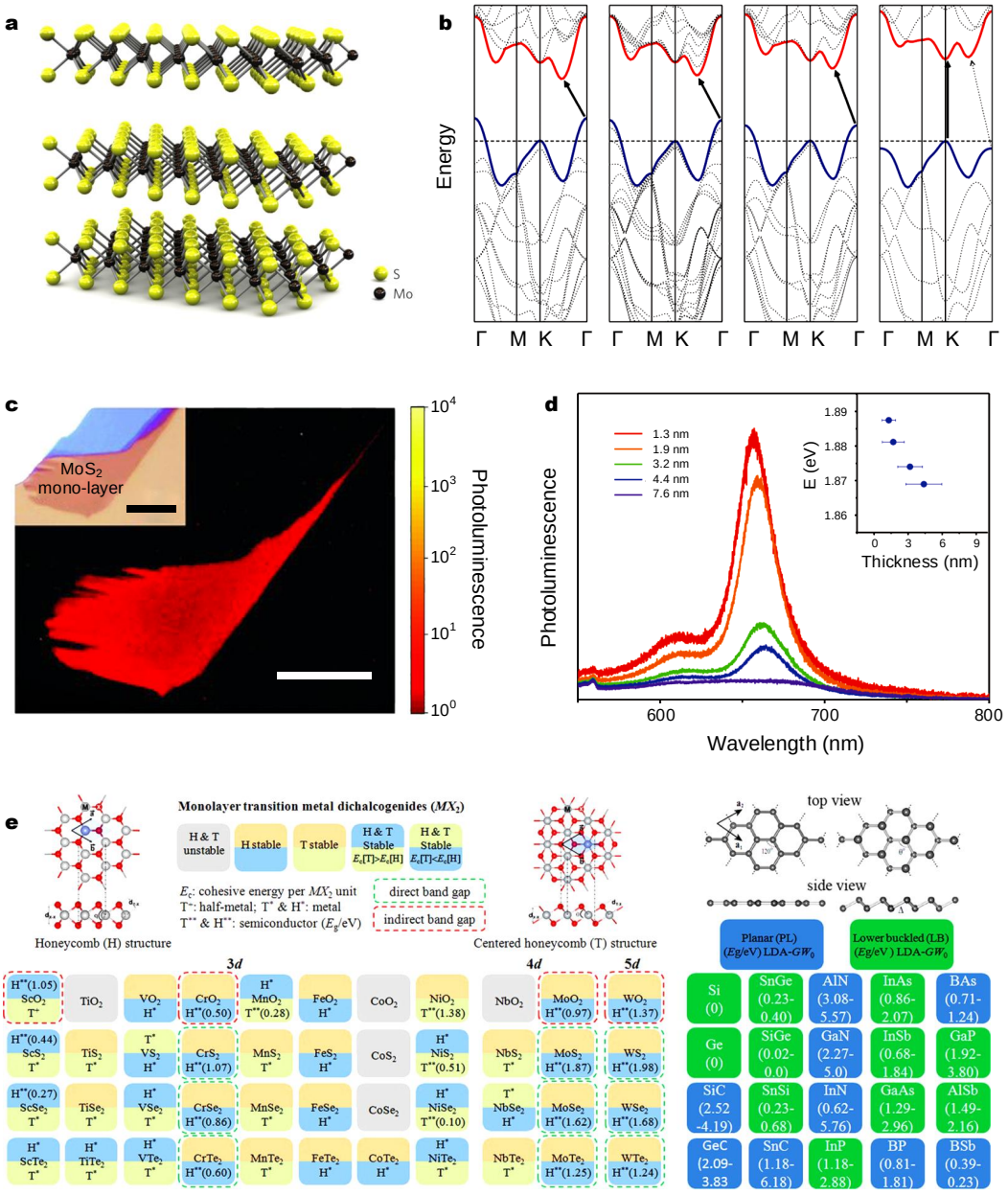

Fig. 2.4 (a) Side-view chemical structure of MoS_2 [73]; (b) Evolution of energy band in bulk, quad-layer, bi-layer and monolayer MoS_2 respectively [81]; (c) Photoluminescence of a monolayer MoS_2 flake produced *via* MC, scale bar 10 µm, adapted from Ref. [139]; (d) Photoluminescence spectra of solution-processed MoS_2 with varied average thickness [140]; (e) Summary of the semiconducting properties of monolayer TMD compound group [6].

excitonic states near the *K* point remains relatively unchanged, whilst those at the Γ point shift significantly such that the indirect bulk bandgap of ∼1.2 eV moves towards a direct monolayer bandgap of ∼1.8 eV [143]. Arising from this bandgap transition, novel and interesting

optoelectronic properties that are not present in bulk MoS_2 are observed. For instance, monolayer MoS_2 exhibits a strong red photoluminescence at ∼660 nm; Fig. 2.4(c) [139]. Eda *et al.* investigated the photoluminescence from solution-processed MoS_2 flakes with respect to the restacking thickness, and demonstrated that both the peak intensity and position of photoluminescence were thickness dependent; Fig. 2.4(d) [140]. Splendiani *et al.* observed a 10^4 times enhancement in photoluminescence from monolayer MoS_2 compared to that from the bulk [81]. Similar to MoS_2, WS_2 also transits from an indirect bulk bandgap of ∼1.3 eV to a direct monolayer bandgap of ∼2.1 eV [144], while $MoSe_2$ changes from 1.1 eV to 1.6 eV [145, 146].

As such, the s-TMDs are of particular interest for optoelectronics and photonics [4, 6, 7] and hence, I focus the remainder of the discussion on s-TMDs. A list of the semiconducting properties of monolayer s-TMDs is summarised in Fig. 2.4(e) [6]. The transition bandgap of some common s-TMDs from bulk to monolayer is summarised in Table 2.1.

The s-TMDs can be exploited in a wide spectrum of optoelectronic and photonic applications. The sizeable bandgap is promising for logic electronics. As discussed, in logic electronics, a bandgap exceeding 0.4 eV [114] and an I_{ON}/I_{OFF} ratio over 10^4 [73] are required. Monolayer s-TMDs with ∼1-2 eV bandgap therefore are well-suited for this purpose, with exceptional high I_{ON}/I_{OFF} reported [73, 152–155]. For instance, the top-gated MoS_2 transistor shown in Fig. 2.5 demonstrated by Radisavljevic *et al.* exhibited an I_{ON}/I_{OFF} exceeding 10^8 [73]. Recently, Wachter *et al.* demonstrated the feasibility of integrating MoS_2 transistors to realise a microprocessor, capable of performing 1-bit logical operation [156]. However, the carrier mobility in such devices is typically 10-50 $cm^2V^{-1}s^{-1}$ [152, 153, 155], significantly lower than that of graphene [114] and silicon based devices [157].

Table 2.1 Bandgap of some common semiconducting TMDs. "-" stands for metallic. Data collected from Ref. [6, 143, 145, 147–151].

Bandgap (eV)		Mo	W	Ti	Zr	Hf	Pd	Pt
S	Monolayer	1.8	2.1	0.65	1.2	1.3	1.2	1.9
	Bulk	1.2	1.3	0.3	1.6	1.6	1.1	1.8
Se	Monolayer	1.6	1.7	0.51	0.7	0.7	1.1	1.5
	Bulk	1.1	1.2	-	0.8	0.6	1.3	1.4
Te	Monolayer	1.1	1.1	0.1	0.4	0.3	0.3	0.8
	Bulk	1.0	0.7	-	-	-	0.2	0.8

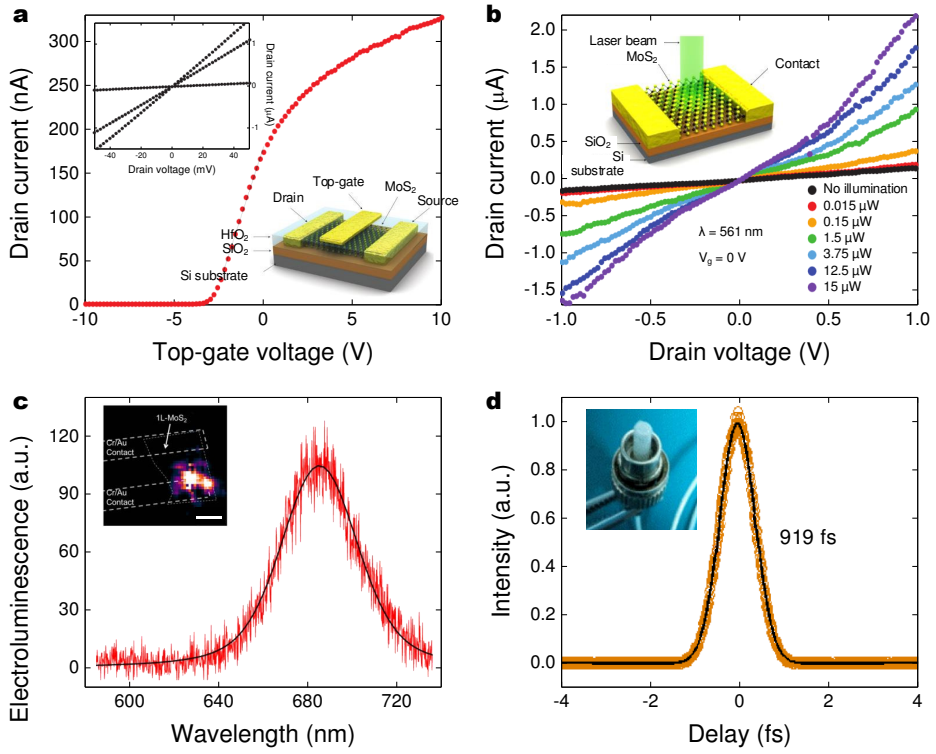

Fig. 2.5 (a) MoS_2 transistor transfer characteristics, inset: schematic figure for top-gated MoS_2 transistor, adapted from Ref. [73]; (b) Ultrasensitive MoS_2 photodetector, adapted from Ref. [158]; (c) Electroluminescence spectrum of a MoS_2 emitter, inset: MoS_2 emission, scale bar 1 μm, adapted from Ref. [80]; (d) WS_2 polymer nanocomposite SAs for ultrafast laser, inset: the laser fibre end with the WS_2 SA integrated, adapted from Ref. [159].

The direct bandgap leads to a high optoelectronic conversion efficiency [143, 144]. As discussed, the photoluminescence from monolayer MoS_2 was increased by a factor of over 10^4 compared to that from the bulk [81]. Such properties can be exploited in a variety of optoelectronic applications, in particular in the development of photodetectors [158, 160–162] and atomically thin monochromatic light emitters [80, 163–165]. Monolayer MoS_2 allowed the fabrication of ultrasensitive photodetectors (Fig. 2.5(b)) operable in the visible spectral range (400-680 nm) with a photoresponsivity of up to 880 AW^{-1} (at 561 nm) [158]. Figure 2.5(c) presents an electroluminescent device based on monolayer MoS_2, where MoS_2 was exploited for the emission for red light [80]. In addition, a smaller bandgap opens up the possibilities for NIR photodetection and emission. Constructing vdW heterostructures (*i.e.* layer by layer stacks of multiple 2d materials) engineers the bandgap, bringing in a broader range of optoelectronic applications [7, 164, 166, 167].

s-TMDs also show potential in photonic applications. The exhibited nonlinear optical absorption properties and ultrafast carrier dynamics allow the application of s-TMDs in

SAs [159, 168, 168, 169]. Figure 2.5(d) shows the integration of a WS_2 flake enriched polymer nanocomposite SA onto the laser fibre end for the generation of ultrashort (595 fs) pulses [159]. The bandgap of s-TMDs of up to $\sim$2 eV suggests the potential for the generation of ultrafast pulses even at the visible wavelengths, a property challenging to achieve with the existing semiconductor materials and technologies [94].

2.4 Black phosphorus

BP is an allotrope of phosphorus. BP does not exist in nature [74, 171, 172], and can only be produced from the other allotropes [69, 74]. Figure 2.6(a) presents typical synthesised bulk BP crystal. Black phosphorus is a puckered hexagonal crystal, where each phosphorus atom bonds to three other neighbouring phosphorus atoms [74, 78, 172, 173], as shown in Fig. 2.6(b) [69].

BP exhibits a high carrier mobility, up to 50,000 $cm^2V^{-1}s^{-1}$ (obtained at 30 K with bulk crystal sample) [4]. One key characteristic of BP is the thickness-dependent electronic structure, similar to what has been observed with s-TMDs (*e.g.* MoS_2). Monolayer BP has a direct bandgap of $\sim$2.0 eV [74, 78, 172, 173]. Angle-resolved photoemission spectroscopy mapping of bulk BP sample shows that it possesses a direct bandgap of 0.3 eV; Fig. 2.6 [69]. This universal direct bandgap is very attractive for optoelectronic applications [4, 7]. On the other hand, the structural anisotropic configuration in lattice leads to in-plane anisotropic optoelectronic properties [78, 172, 173], showing orientation dependent *e.g.* thermal [174] and electrical [175] conductivities, and intrinsic strength [176]. For example, Fig. 2.6(d) shows that the measured photoluminescence peak intensity from monolayer BP is dependent on polarisation [170].

Although graphene and s-TMDs have many superior material properties, they present certain fundamental drawbacks: the zero-bandgap of graphene limits use in logic electronics, whilst the relatively low carrier mobility of s-TMDs also prevents applications [4, 7, 78, 79]. BP, with a sizeable bandgap and a high carrier mobility, is therefore an emerging key 2d material to bridge the gap between graphene and s-TMDs. Indeed, BP has been widely reported in transistor fabrication (*e.g.* Fig. 2.6(e) [69]), with mobility exceeding 1,000 $^2V^{-1}s^{-1}$ and I_{ON}/I_{OFF} over 10^5 reported [56, 78, 177, 178]. This performance is comparable to that of silicon based devices, and sufficient for logic electronics (bandgap $>$0.4 eV, $I_{ON}/I_{OFF} > 10^4$).

The direct bandgap of 0.3-2.0 eV, spanning the visible to IR spectral region, leads to a high efficiency in the optoelectronic processes [81, 143, 144], noting a big difference from s-TMDs. This can be potentially utilised in a variety of visible to IR optoelectronic

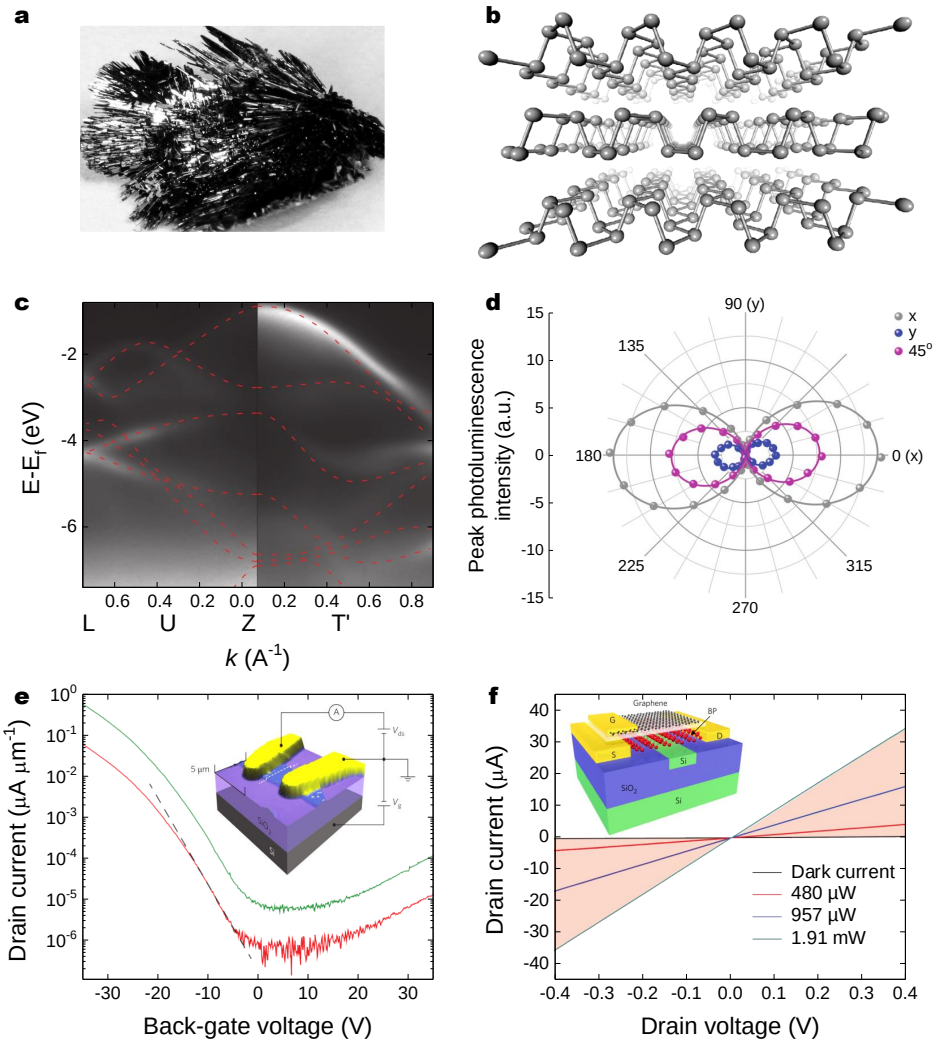

Fig. 2.6 (a) Bulk BP crystal, source Smart Elements; (b) Side-view chemical structure of BP, adapted from Ref. [69]; (c) Band structure of bulk BP mapped by angle-resolved photoemission spectroscopy, adapted from Ref. [69]; (d) Photoluminescence peak intensity as a function of polarisation detection angle [170]; (e) Typical BP transistor transfer characteristics, inset: schematic figure for back-gated BP transistor, adapted from Ref. [69]; (f) Source-drain current versus bias voltage under varied illumination of a waveguide-integrated BP photodetector, inset: schematic figure for the photodetector, adapted from Ref. [82].

applications, for instance atomically thin light emitters [4, 78] (though not yet demonstrated), photodetectors [82, 179], and photovoltaics [180]. The inset of Fig. 2.6(f) is one example of integrating BP into waveguide based silicon photonics for photodetection (graphene as the top-gate) [82]. The authors demonstrated that by integrating BP, the device achieved a low dark current (impractical for graphene based photodetectors) and an intrinsic responsivity up to 657 mAW^{-1} at IR (photodetectors based on monolayer s-TMDs, *e.g.* MoS_2, typically

can only operate at IR limited by the bandgap). Other key applications of BP lie in SAs for ultrafast lasers [181–186], chemical sensors [187], and electrode systems for energy storage [188].

However, a considerable challenge for BP applications is its instability under ambient conditions [78, 181, 189–192]. Favron *et al.* suggested that the oxidation was likely due to a photo-assisted reaction with oxygen dissolved in moisture that was adsorbed on the BP surface [190]. This means that both light and oxygen must be present for the degradation to occur [190]. Hanlon *et al.* demonstrated a solution based exfoliation technique could enhance the stability of BP by forming a solvation shell around the flakes which could prevent interaction with oxygen [181]. Other studies investigated passivation with such as polydimethylsiloxane (PDMS) [191] and parylene [190] to present BP degradation. Island *et al.* showed that sandwiching BP flakes with PDMS could protect them against degradation for over 1 week [191].

2.5 Other 2d materials

Besides these above most commonly studied 2d materials, there are other 2d materials likely to be of interest for applications.

2.5.1 Hexagonal boron nitride

Boron nitride is an inorganic compound typically in cubic, wurtzite or hexagonal lattices [193]. *h*-BN is the hexagonal crystalline form of BN in white colour. Figure 2.7(a) shows a photograph of *h*-BN crystals ($\sim$5 μm particle size). In this hexagonal lattice structure, B and N atoms are alternatively covalently bonded in-plane and are weakly stacked out-of-plane *via* vdW forces [193, 194]; Fig. 2.7(b). With such a layered structure similar to graphite, *h*-BN has been widely used as a lubricant, well known as the "white graphite" [193, 194]. However, unlike graphite, *h*-BN is an electrically insulating and thermally conductive material [194–196]. *h*-BN therefore exhibits better lubricating properties than graphite, especially when under extreme conditions (*e.g.* vacuum, high temperature, oxidising atmosphere) [193, 194]. Figure 2.7(c) presents the energy band structure of *h*-BN, showing that it has a wide bandgap (6 eV [4, 193, 197, 198]). This wide bandgap has been exploited in deep ultraviolet light emission [4, 83]. However, there are debates on the bandgap, with widely dispersed values in 3.6-7.1 eV reported [194]. Also there are arguments on whether *h*-BN is a direct bandgap material [197, 199].

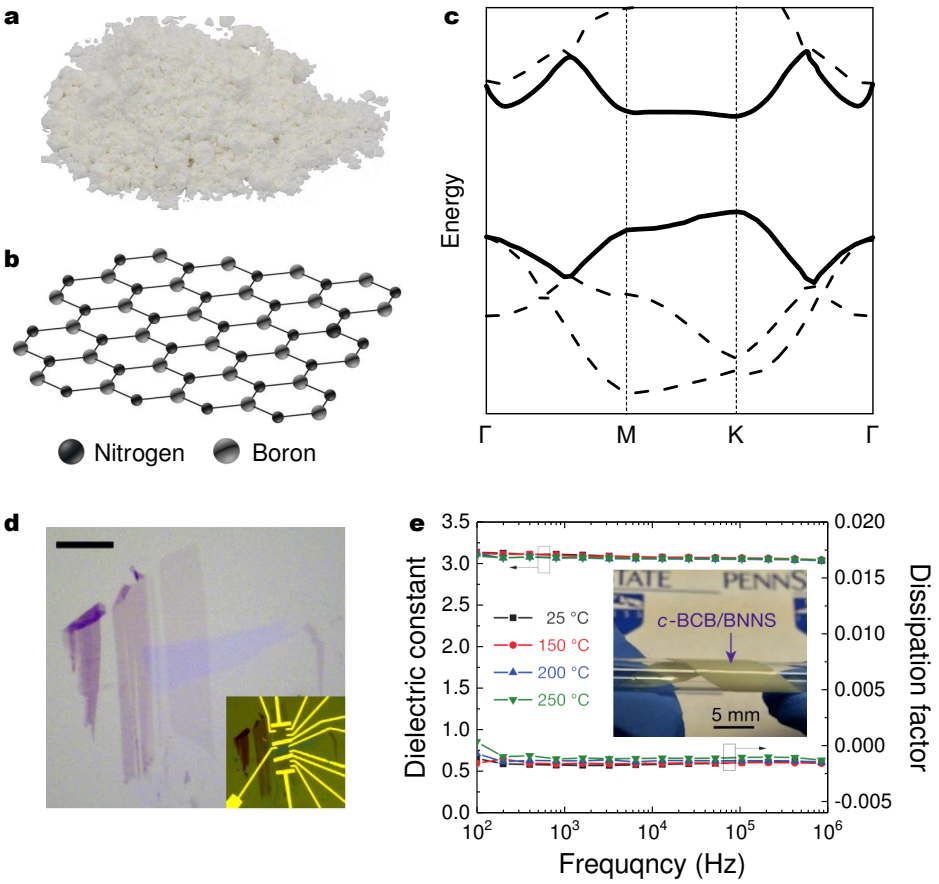

Fig. 2.7 (a) Bulk *h*-BN, source TKB Trading, LLC; (b) Top-view chemical structure of *h*-BN; (c) Energy and structure of *h*-BN, adapted from Ref. [200]; (d) Use of *h*-BN as atomically thin dielectric substrate for graphene transistor, scale bar 10 µm [201]; (e) High dielectric stability of flexible *h*-BN nanocomposite against temperature and frequency, inset: *h*-BN nanocomposite, adapted from Ref. [202].

Few- and monolayer *h*-BN has attracted tremendous attention [4, 193, 198, 203]. In its 2d form, *h*-BN shows many interesting material properties, for instance, colourless appearance, atomically smooth surface, the absence of dangling bonds and charge traps, and significantly enhanced thermal stability [200]. This combination in addition to the lattice structural similarities allows *h*-BN to be used as a dielectric screening substrate for other 2d materials in device fabrication [201, 204–206]. For example, Dean *et al.* used *h*-BN as a substrate for graphene transistor, replacing SiO_2; Fig. 2.7(d). The authors demonstrated that the device carrier mobility was increased by three times [201]. As such, *h*-BN has emerged as a fundamental building block for vdW heterostructures, bringing in myriad novel structures and properties [41, 167]. More recently, *h*-BN was used to passivate BP devices to prevent atmospheric degradation [78].

The combination of the dielectric and thermal properties of *h*-BN allows it to be incorporated into polymer nanocomposites as dielectric and thermally conductive fillers [200, 202, 207]. For example, Li *et al.* introduced solution-processed *h*-BN flakes into cross-linked divinyltetramethyldisi-loxane-bis(benzocyclobutene) (BCB) and developed a flexible *h*-BN nanocomposite with a high dielectric stability against temperature (up to 250°C) and frequency (up to $\sim 10^6$ Hz); Fig. 2.7(e) [202].

2.5.2 MXenes

Transition metal carbides and/or nitrides are a group of 2d materials with a composition of $M_{n+1}X_n$, where M stands for transition metal, X is either carbon or nitrogen, and n is the number of X atoms [76]. They are termed as "MXenes" to emphases the graphene-like layered structure [76, 208]. MXenes can only artificially produced from their counterpart parent compounds, layered ternary transition metal carbides and nitrides, which are commonly termed as MAX phases ($M_{n+1}AX_n$) [75, 76].

In the MAX phases, "A" stands for a group IIIA or IVA element on the periodic table such as aluminium (Al) and silicon [75, 76]. The MAX phases are arranged in a layered hexagonal lattice, where the M planes are closed packed with the X planes in an octahedral prismatic in a composition of $M_{n+1}X_n$, while the A planes are interleaved between. Therefore, the MAX phases are not strictly layered crystals like graphite: the interlayer bonds between A and $M_{n+1}X_n$ are too strong to allow direct exfoliation [1, 75, 76]. However, the force difference between the chemical bonds, M-X and M-A, allows selective etching of the A layers away from the structure [75, 76]; Fig. 2.8. MXenes were first experimentally demonstrated by Naguib *et al.* in 2011 [208]. The authors reported the production of graphene-like Ti_3C_2 thin layers by selectively etching away the Al atoms from its parent compound Ti_3AlC_2 using hydrofluoric acid.

Besides Ti_3C_2, many other types of MXenes, such as Ti_2C, Ti_3CN, Nb_2C and V_2C, were reported in later works [75, 76, 209, 210]. Indeed, the possible combinations for M, A, and X gives $>$60 known MAX phases, well representing the wide spectrum of properties of MXenes [75, 76]. The electronic properties of MXenes are of special interest, with theoretical studies suggesting that MXenes are either metallic or with a very small bandgap [76, 208, 210]. The bandgap of MXenes can be engineered through chemical functionalisation [75, 76].

One major application of MXenes is in electrode systems for electrochemical energy storage [75, 76, 211]. There are indeed many successful demonstrations of MXenes based high-performance proof-of-concept batteries and supercapacitors reported [212–216]. Potential applications of MXenes also include sensors, electronics and conductive reinforcement

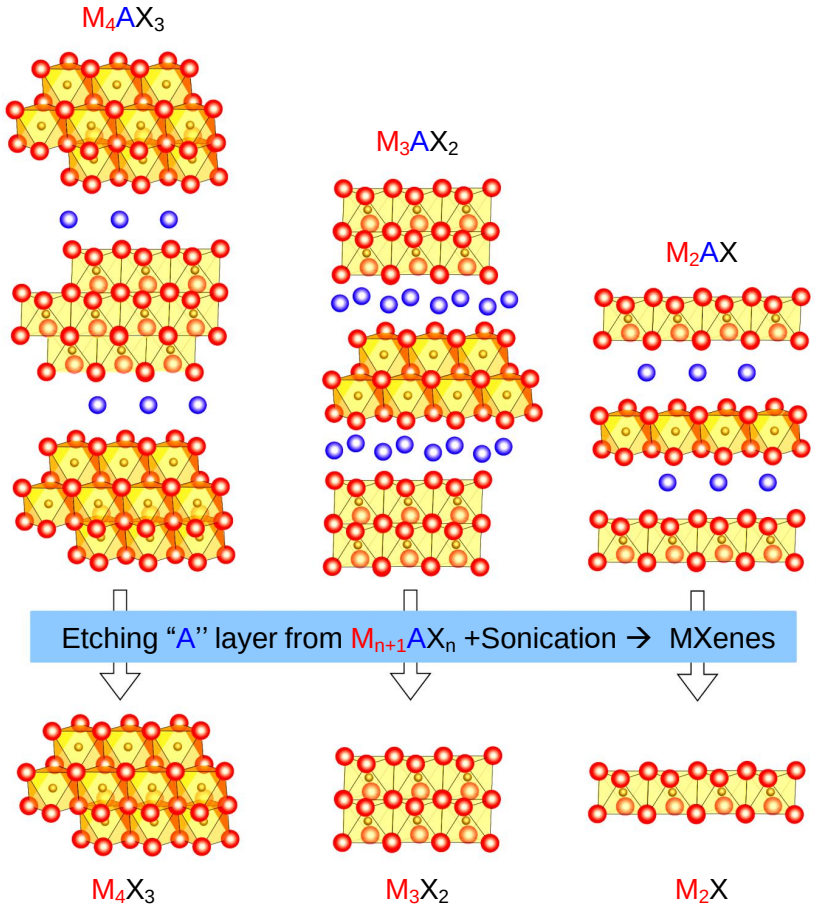

Fig. 2.8 Structure of MAX phases and the corresponding MXenes, adapted from Ref. [76].

additives [75, 76, 209, 210, 217–220]. In addition, MXenes are emerging as potential building blocks for vdW heterostructures (as yet largely unexplored) [75, 76, 221, 222]. In these heterostructures, MXenes may work as the conductive layers whilst simultaneously modifying the electronic properties of other 2d materials that are in vertically contact with the MXenes [220–222]. However, significant reduction in the production cost the MAX phases is required before MXenes can be realistically considered for applications.

2.5.3 Mica

Mica represents a group of layered silicate clays and minerals with nearly perfect basal cleavage [223, 224]. Typical examples of mica include muscovite, phlogopite and biotite [225]. Muscovite is the most commonly occurring form of mica in nature.

The chemical structure of mica (Fig. 2.9) allows intercalation and exfoliation of bulk mica into thin flakes *via* chemical solution processing [1, 224]. As the majority of the mica

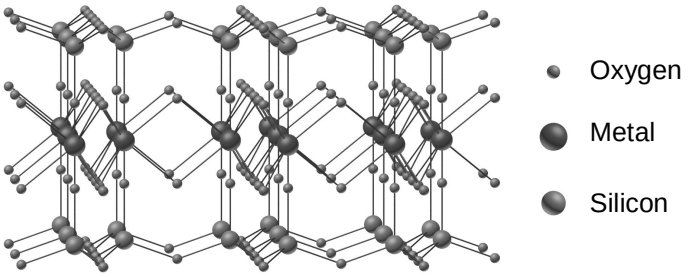

Fig. 2.9 Chemical structure of mica.

members are insulating, mica has been primarily used as inert fillers to enhance the strength of nanocomposites, as barrier materials for packaging, and as pigment for painting [223–225]. The dielectric properties of mica also allow it to be exploited in capacitors [225]. More recently, the large surface area and the possibility of intercalation and exfoliation have indicated potential applications in catalysis, energy storage and sensing [226].

At present, very little work has been done on the 2d form mica. This is largely down to the challenges involved in the exfoliation of mica, due to its charged state in 2d form that requires constant presence of a charge balancing counterion. Only recently, Harvey *et al.* demonstrated successful liquid phase exfoliation of mica sheets from talcum powder as charged layered crystals [227].

2.5.4 Oxides

Layered oxides are a large group of materials with a general formula, A_nMO_2, where A is an alkali metal (*e.g.* lithium, potassium), M is transition metal, O is oxygen, and $0.5 \leq n \leq 1$ [228]. The layered oxides typically occur as *e.g.* metal dioxides and trioxides, perovskites and niobates. The chemical structure of layered oxides typically consists of MO planes separated by the A planes [228]. The ions between the layers can balance the surface charge of the layers and as such retain a stable structure [1, 229]. Solution processing methods *via* ion exchange in acidic solutions can induce agitation to this stable structure to yield layered oxide flakes [1, 229, 230]. 2d layered oxides are wide bandgap semiconductors, exhibiting interesting electronic, electrochemical and photonic properties for transistors and battery electrodes [229, 230].

2.5.5 Metal halides

Metal halides share a general formula MX_n, where M is a transition metal, and X is a Group VII element or halide (*e.g.* chlorine, bromine, iodine), and n can be 2, 3 and 4 depending on

the M [1, 231]. Metal halides structurally resemble TMDs, where the monolayer consists of a plane of transition metal atoms sandwiched by two planes of halide atoms [1]. Metal halides do not naturally exist, and therefore require chemical synthesis [231, 232]. Thus-far, metal halides have been used for light emitting in high-intensity discharge gas discharge lamps [233].

2.6 Summary

In this chapter, I have introduced the structures, properties and applications of 2d materials, with focus on graphene, TMDs and BP. The unique and outstanding properties of 2d materials can potentially enable a range of high-performance, novel applications, in particular in opto-electronics and photonics. However, the examples outlined within this chapter are typically based on 2d material samples produced *via* MC. In practice, MC is an unrealistic process for scaled-up and controllable device fabrication. 2d materials produced *via* other production methods may show compromised properties and device performance, however, exhibit a scalability in device fabrication. For example, solution processing methods are capable of delivering mass-production of 2d materials, and importantly the solution-processed 2d materials are readily adapted to graphics printing for large-scale, low-cost device fabrication. I will discuss the diverse production methods of 2d materials in Chapter 3.

Chapter 3

Solution processing of 2d materials

In the previous chapter, I discussed the properties and potential applications of 2d materials. To make the most of 2d materials, multiple top-down and bottom-up material production methods have been developed. Among them, solution processing achieves scalable and cost-effective production of 2d materials, a big advance towards scalable applications [1, 15, 234–238]. This solution phase approach is also very relevant to the formulation of functional inks for graphics printing technologies, enabling patterning of 2d materials for large-scale, low-cost device fabrication [16, 17, 37]. It is therefore important to briefly summarise the key production methods for 2d materials with the focus given to the methods relevant to ink production – solution processing, providing the context for printing of 2d materials.

In this chapter, I give an overview of the production methods of 2d materials in Section 3.1, followed by the introduction of solution processing methods in Section 3.2. Ultrasonic-assisted liquid phase exfoliation (UALPE) is the main solution processing technique used in my doctoral work as it is a method of producing high-quality, pristine 2d material flakes. In particular, I discuss the fundamentals and processing principles of UALPE in Section 3.3. The characterisation techniques relevant to solution-processed 2d materials are covered in Section 3.4.

3.1 Production method overview

An important part of the research on 2d materials is devoted to the material production methods that are scalable and cost-effective. Figure 3.1 lists some key production methods of graphene. As shown, in general, graphene can be produced *via* either top-down or bottom-up methods: (1) top-down: the bulk is exfoliated directly to yield mono- and few-layer flakes. This includes micro-mechanical cleavage (MC), photoexfoliation and solution processing methods (exampled with UALPE) [1, 3, 15]; (2) bottom-up: individual flakes

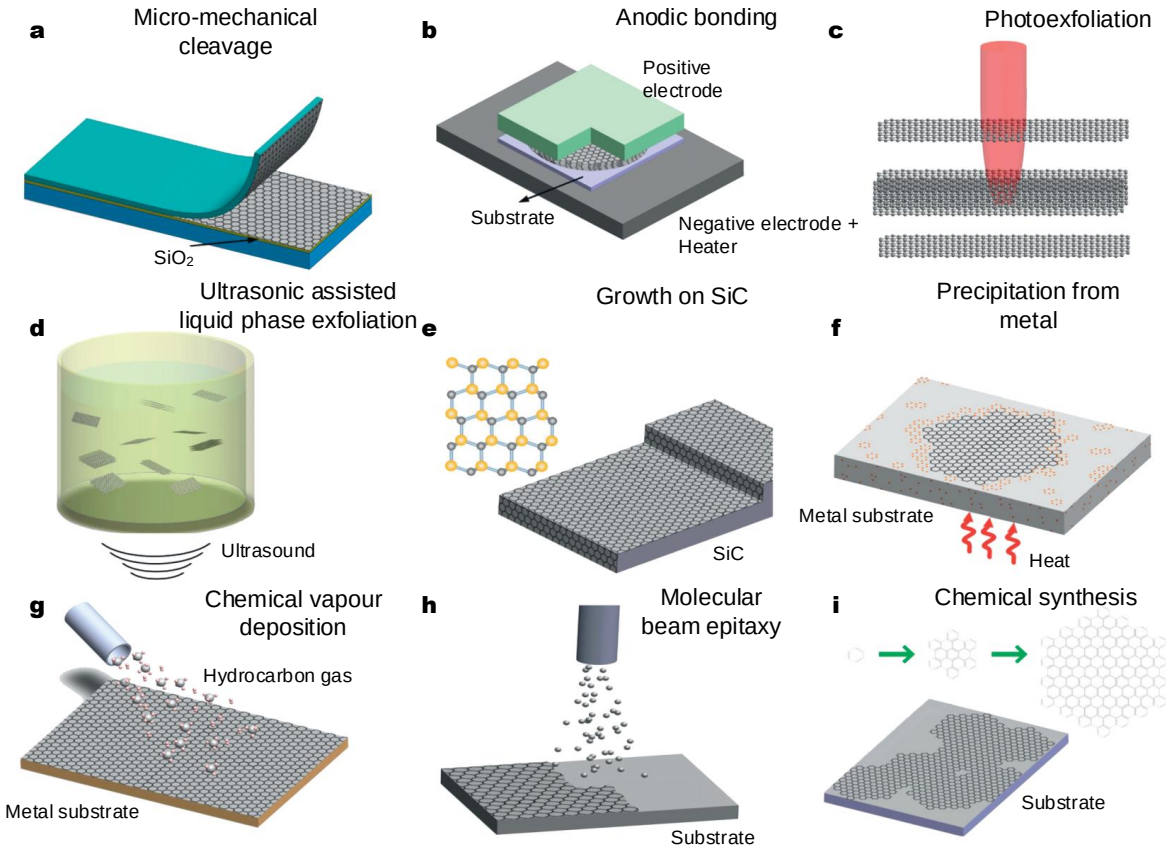

Fig. 3.1 Common production methods of graphene: (a) MC; (b) Anodic bonding; (c) Photoexfoliation; (d) UALPE; (e) Growth on SiC, SiC where gold and grey spheres represent silicon and carbon atoms; (f) Segregation/precipitation from carbon containing metal substrate; (g) CVD; (h) Molecular beam epitaxy; (i) Chemical synthesis using benzene as building block. Adapted from Ref. [15].

are directly grown or synthesised on substrates. This includes anodic bonding, growth on SiC, segregation/precipitation from carbon containing metal substrate, chemical vapour deposition (CVD), molecular beam epitaxy and chemical synthesis using benzene as building block [15]. Some of these methods have been successfully extended to other 2d materials, in particular MC, CVD and UALPE which are now widely exploited in the production of transition metal dichalcogenides (TMDs), black phosphorus (BP) and hexagonal boron nitride (*h*-BN) [1, 3, 6, 15, 73, 170, 181, 234–240].

Micro-mechanical cleavage. MC was first demonstrated in the production of stable graphene flakes in 2004 [2]. This method was later extended to other 2d materials, *e.g.* TMDs and *h*-BN in 2005 [3] and BP in 2014 [69]. In this production process, flakes are exfoliated from bulk crystal by "rubbing" the face of the crystal against a solid surface such as a silicon

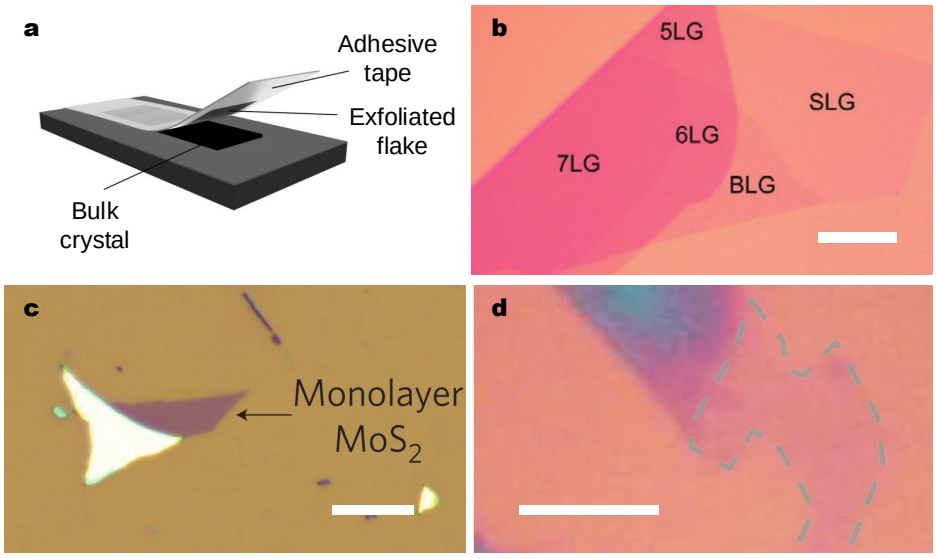

Fig. 3.2 (a) Schematic figure of MC; Representative optical micrographs of MC flakes of (b) graphene with of regions of different thickness, scale bar 20 µm [15], (c) MoS_2, scale bar 10 µm [73], and (c) BP with the monolayer region indicated by the dashed line, scale bar 6 µm [170].

wafer, or by repeatedly cleaving with an adhesive tape, as shown in Fig. 3.2(a). Exfoliation is possible due to the relatively weak interlayer van der Waals (vdW) forces compared to the strong covalent intra-layer bonds. MC overcomes the vdW forces, while the chemical bonds are untouched. As a purely physical process, MC causes no chemical alteration of the exfoliated flakes, producing exceptionally high-quality pristine flakes [2, 3, 15, 79]. Figure 3.2(b-d) are representative optical micrographs of graphene, MoS_2 and BP flakes. As clearly shown, the produced flakes differ in thickness and shapes, while the flake lateral dimension is usually in a scale of micrometres. This means that the production rate of monolayer flakes is extremely low and uncontrollable. Although this process has since been optimised to produce flakes of up to several millimetres in lateral dimension (also limited by the bulk crystal grain size), it is unlikely to be scalable and controllable for mass production, rendering it unsuitable for large-scale device fabrication [9, 15].

Due to these features, MC is thus-far limited to the fundamental studies of 2d materials [15]. For example, the studies of graphene on its transparency [93], carrier mobility [90] and mechanical properties [97] were conducted with suspend graphene flakes prepared by MC; the thickness dependent bandgap transition [143], photoluminescence [81] and electroluminescence [80] of MoS_2 were observed with MC flakes. Extremely high performance devices were also developed from MC flakes, for example graphene transistors with

an intrinsic cut-off frequency of up to 300 GHz [117, 118] and MoS_2 transistors with an I_{ON}/I_{OFF} of up to 10^8 [73].

Chemical vapour deposition. Ever since the discovery of graphene in 2004, CVD that had been widely exploited in the synthesis of carbon materials (*e.g.* carbon nanotubes: CNTs) [242]) was extended to the growth of graphene [15, 241, 243–245]. As shown in Fig. 3.3(a), in a CVD production process of graphene, hydrocarbon gaseous precursor (typically methane) is introduced into a high temperature furnace (typically 1,000 °C); catalysed by the metal substrate (typically polycrystalline copper foil) at this high temperature, the precursor decomposes and forms monolayer graphene on the substrate [15, 241]. CVD gained a huge momentum in 2009 when Li *et al.* first demonstrated uniform graphene films over a scale of 1 cm × 1 cm; Fig. 3.3(b) [241]. Through significant improvements in the past decade, the as-grown graphene film has been scaled-up to >100 m long [244].

However, the as-grown graphene needs to be transferred to target substrate before it can be utilised for applications. Figure 3.3(c) schematically presents a commonly adopted

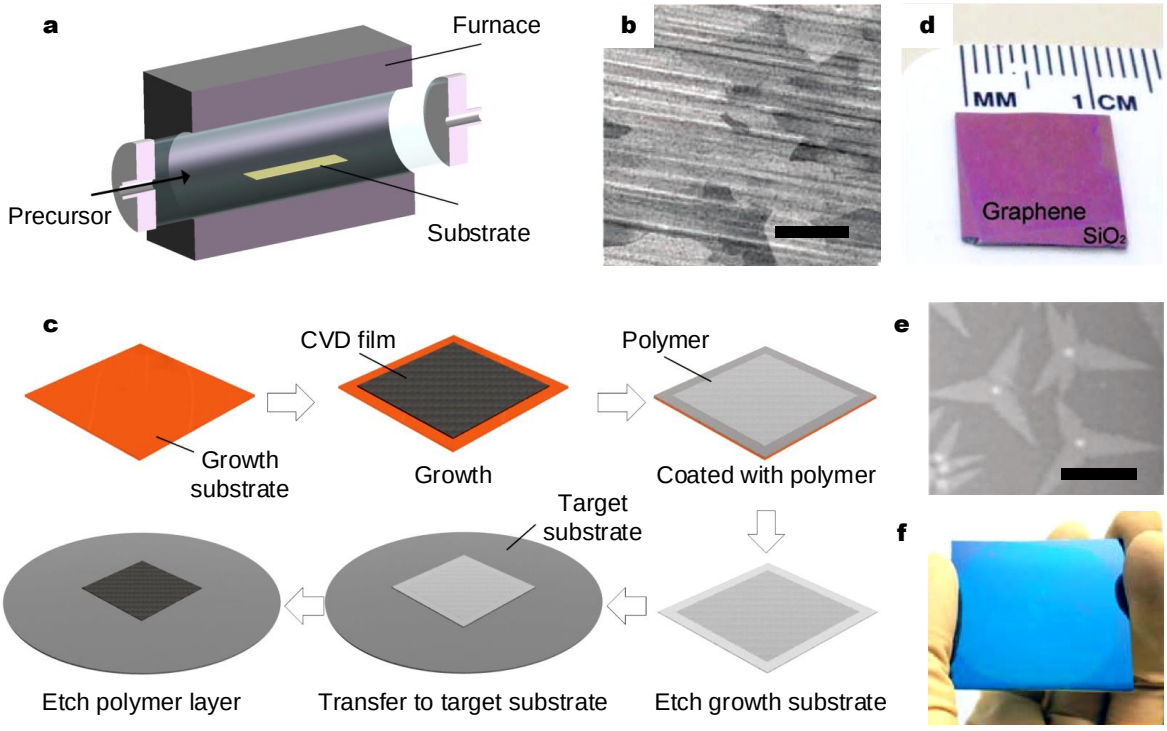

Fig. 3.3 (a) Schematic figure for a typical CVD set-up; (b) SEM image of graphene grown on a copper foil, scale bar 100 µm [241]; (c) Schematic figure for typical wet-transfer process; (d) Graphene film transferred onto SiO_2/Si [241]; (e) Optical micrograph of MoS_2 grown on SiO_2/Si, scale bar 20 µm, adapted from Ref. [240]; (f) 2 inch MoS_2 film transferred onto SiO_2/Si [239].

wet-transfer method. In this process, polymer (*e.g.* polymethyl methacrylate: PMMA) coated graphene is transferred onto a target substrate after the metal substrate is etched away; the coated polymer is removed afterwards. Figure 3.3(d) is an optical micrograph of a wet-transferred graphene film on Si/SiO_2 [241]. However, this process is prone to damaging the graphene films, arising either from physical damages during the transfer process (*e.g.* cracking) or from chemical residues (*e.g.* polymers) [15]. Research efforts now have been directed to growth on dielectric substrates such as glass and quartz so as to eliminate the transfer process [246]. Nevertheless, CVD graphene exhibits high quality. For example, a carrier mobility of $\sim$27,000-45,000 $cm^2V^{-1}s^{-1}$ from large-grain CVD graphene on *h*-BN was reported by Petrone *et al.* [247]. CVD graphene therefore can potentially lead to high performance devices, for instance large-area highly conductive transparent conductors [105], high cut-off frequency transistors [118, 248, 249], and high optical modulation depth saturable absorbers (SAs) [250].

CVD has been successfully extended to other 2d materials. For instance, Ref. [239, 240, 251, 252] present the growth of monolayer MoS_2 film through chemical reactions of Mo/MoO_3 and sulphur on insulating substrates such as SiO_2 or sapphire. Figure 3.3(e) is a representative optical micrograph of as-grown MoS_2 flakes on Si/SiO_2 [240]. There are also demonstrations of other TMDs, for instance WS_2 in Ref. [253] and $MoSe_2$ in Ref. [254, 255]. Making use of these 2d materials may also require transferring onto target substrates through similar wet-transfer processes [15, 239, 240, 251]. Figure 3.3(f) presents a photograph of transferred 2 in MoS_2 film on Si/SiO_2 [239]. Similar to CVD graphene, the properties and performance of these 2d materials are not yet comparable to the ones produced by MC [6, 15].

Although the CVD graphene growth process has been refined to demonstrate large-area films in lab, it is still challenging to transfer this technique to the real-world for mass production of high quality, uniform graphene films [15, 105, 239, 244]. CVD is also not a cost-effective process considering the high requirements on production conditions (*e.g.* high temperature, certain gases and precursors), and the expensive sacrificial growth substrates [15].

3.2 Solution processing methods

Due to the low production rate and the high production cost of MC and CVD (and the other aforementioned production methods), it is necessary to develop cost effective methods that are capable of delivering mass production of 2d materials [1, 15, 236]. Solution processing has emerged as a promising approach. As a top-down exfoliation strategy, it exfoliates directly large quantities of mono- and few-layer flakes from the bulk in a liquid medium mainly *via*

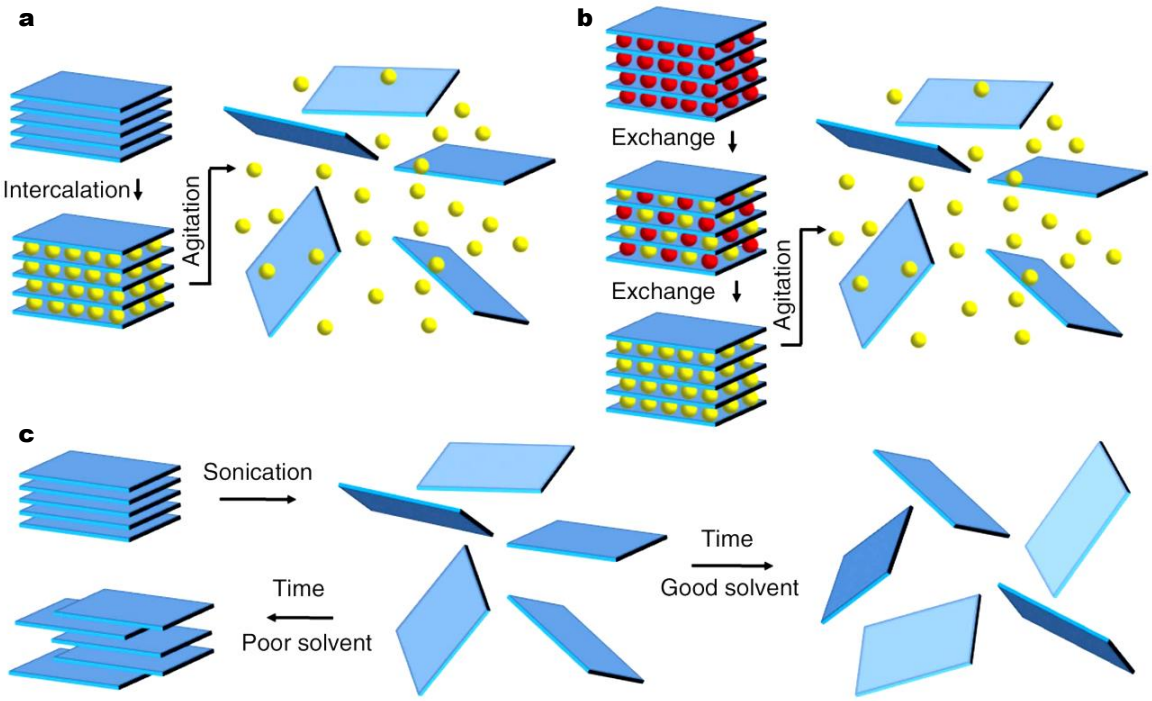

Fig. 3.4 Solution processing *via* (a) ion intercalation, (b) ion exchange, and (c) LPE (exampled with UALPE), showing that in "good solvents" the exfoliated flakes are stabilised against reaggregation, while in "bad solvents" reaggregate and sediment [1].

ion intercalation, ion exchange or liquid phase exfoliation (LPE) [1, 15], as schematically illustrated in Fig. 3.4. It also offers many other advantages, including low-cost processing, equipment and raw materials, and the absence of substrates and subsequently transferring processes. Importantly, the as-produced dispersions are readily adapted to graphics printing technologies, enabling the development of printable optoelectronics and photonics, as well as other applications such as sensors and energy storage and conversion, just like day-to-day printing of paper, magazines and packaging materials [1, 15, 16, 16, 17, 37, 39–42, 48].

3.2.1 Exfoliation based on ion intercalation and exchange

Ion intercalation is one of the earliest approaches of solution processing of 2d materials, dating back to 1841 when Schaffautl *et al.* reported a graphite intercalation compound [256]. Ion intercalation as a method of producing monolayer MoS_2 was reported as early as in 1986 [72]. Later on, it was successfully exploited in obtaining monolayer graphene [107, 257] and other 2d materials [258]. Figure 3.5(a,b) are representative photographs of the as-produced graphene and MoS_2 dispersions [107, 259].

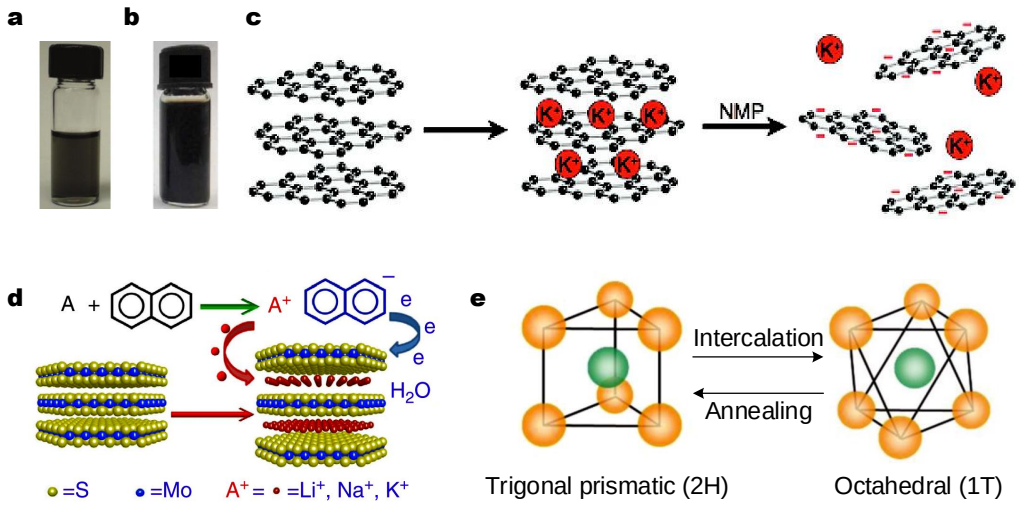

Fig. 3.5 Dispersions of (a) graphene and (b) MoS_2 produced *via* ion intercalation [107] and [259], respectively; (c) Production of graphene flakes using potassium ions as the intercalation agent [257]; (d) Production of MoS_2 flakes using alkali ions as the intercalation agents [259]; (e) Phase change of MoS_2 induced by ion intercalation [140].

The ion intercalation process takes advantage of the layered structure of 2d materials [1, 15]. Small molecules like ionic species or compounds are used to intercalate between the atomic layers. For example, Fig. 3.5(c,d) are schematic figures showing the use of alkali metals (*e.g.* Li^+, Na^+ and K^+) to intercalate graphite and MoS_2 [257, 259]. The intercalated small molecules can effectively increase the interlayer distance, such that the interlayer vdW forces are weakened, leading to the separation of the layers. Mono- and few-layer flakes can then be exfoliated *via* mild sonication (or even stirring in some cases).

Ion intercalation allows production of relatively large flakes with a high yield of monolayer flakes [107, 140, 257–259]. However, this approach may introduce defects, impurities and structural changes to 2d material lattices. This can lead to alteration of the properties of 2d materials. Eda *el al* showed that Li^+ intercalation of MoS_2 caused a lattice change from trigonal prismatic phase (semiconductive) to metastable octahedral phase (metallic). To make use of the optoelectronic properties of MoS_2, the metallic phase would require a high temperature annealing to transform back to the semiconductive phase; Fig. 3.5(e) [140]. Meanwhile, ion intercalation requires strict production conditions (*e.g.* high pressure [140, 259]), which increase the production cost [1, 15].

Solution processing *via* ion exchange is another widely applied solution processing method. It is limited to the layered crystals that contain an interlayer of cations [1, 229]. For example, for the case of layered oxide (Section 2.5.4), MO planes tend to be negatively charged, and the alkali metal cations (*e.g.* K^+, Rb^+, Cs^+) occupy the interlayer space to

ensure charge neutrality. The cations can be ion exchanged with organic ions, leading to swelling and separation of the MO layers. Mono- and few-layer MO layers can then be exfoliated *via* sonication [1, 229]. Similar to ion intercalation, ion exchange can lead to alteration of the properties of 2d materials [1, 229].

3.2.2 Liquid phase exfoliation

In order to avoid alteration of the material properties, an alternative technique, LPE, was adopted. LPE is a solution processing technique that has been widely used in exfoliating and dispersing CNTs [133, 235]. It was first reported in graphene production by Hernandez *et al.* in 2008 [236]. The authors reported exfoliation of mono- and few-layer graphene flakes in organic solvents using ultrasound sonication (*i.e.* UALPE), as illustrated in Fig. 3.6(a,b). UALPE has been since successfully extended to a wide range of 2d materials, including TMDs, BP, *h*-BN and mica [15, 181, 227, 237, 238]. Developing from pure organic solvents, UALPE now utilises a broad range of liquid media including organic solvents, solvent mixtures, aqueous dispersions, and sometimes with the addition of surfactants [15, 48, 234, 260–266].

UALPE can be generalised into two steps: sonication and purification [15, 234, 236, 238]. Sonication starts with immersing a bulk crystal into a liquid medium. Under the effect of ultrasound sonication waves, localised cavitation bubbles are generated between the crystal layers. The bubbles then collapse into high-energy jets and generate high shear forces. The forces overcome the interlayer vdW forces and hence, yield exfoliated flakes. However, after sonication, much of the bulk crystal remains unexfoliated. Purification is applied afterwards to remove these unexfoliated flakes. Centrifugation is a commonly adopted technique for purification, allowing sedimentation of the unexfoliated flakes upon centrifugation. This leaves the supernatant enriched with exfoliated mono- and few-layer flakes. The supernatant is collected as the 2d material dispersion.

Besides ultrasound sonication, other commonly adopted methods for shear force generation include high-shear mixing [267–269], high-pressure mixing [112, 270, 271] and ball-milling [272–274], as illustrated in Fig. 3.6(c-d). Similarly, bulk crystals are exfoliated upon sufficient shear forces that overcome the interlayer vdW forces. Each of these methods differs in the generation of the shear forces. For the case of high-shear/pressure mixing, the forces are generated by rotation of a mixing blade (*e.g.* blenders or blade mixers) [267–269], by forcing the mixture through narrow channels under high pressure (*e.g.* homogenisers) [112, 270, 271], or by flowing the mixture through a meshed screen (*e.g.* impeller mixing) [267]. Differently, ball-milling uses a cylindrical "jar" that contains small balls/beads (typically steel or zirconia). Under correct rotation conditions (*i.e.* fast enough to

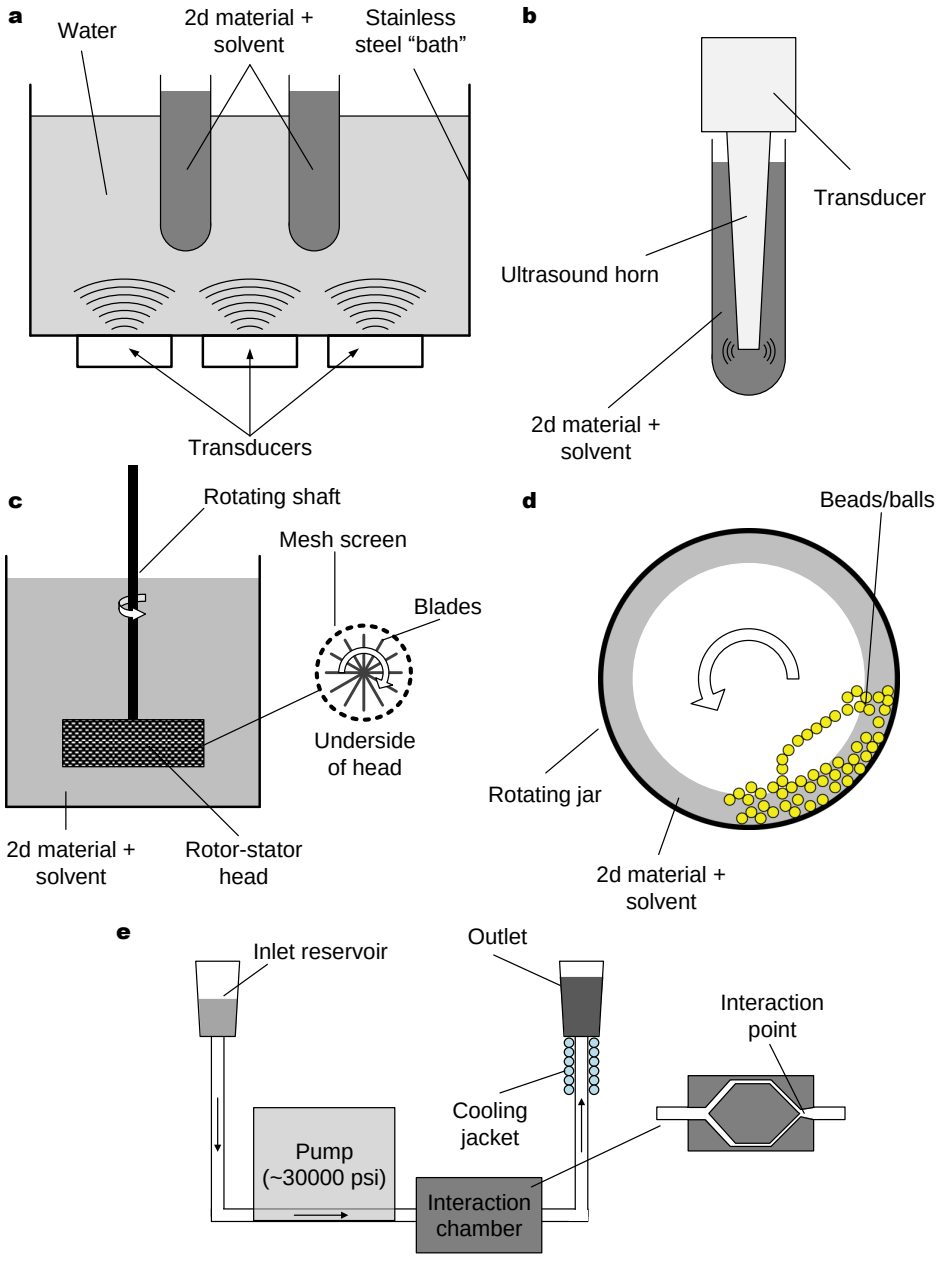

Fig. 3.6 Commonly used LPE techniques: (a) bath sonication, (b) tip sonication, (c) impeller, (d) ball milling and (e) high pressure mixing.

generate movement, but not so fast as to generate tumbling), the balls generate shear forces perpendicular to the walls of the jar for exfoliation [272–274].

Unlike ion intercalation or exchange, as a physical shear force exfoliation approach, LPE does not induce alteration of the properties of the as-produced 2d materials [1, 15, 235, 238]. Indeed, for example, Hernandez *et al.* demonstrated that the as-produced graphene flakes were pristine with minimal defects and chemical functionalisations [236]. LPE therefore is

more relevant to the exploitation of the optoelectronic properties of 2d materials in printable applications. UALPE is the main technique used in my doctoral work. Though a lot of improvements on UALPE have been made in the past decade, there is still much to be done. The production throughput needs to be raised, the exfoliation degree needs to be increased, and the purification processing needs to be controlled (*e.g.* control over flake thickness and size) [1]. Therefore, to successfully practice UALPE and make improvements, a thorough understanding of UALPE is essential, including the exfoliation mechanisms (Section 3.3.1 and 3.3.2) and the centrifugation processing principles (Section 3.3.3).

3.3 Ultrasonic-assisted liquid phase exfoliation (UALPE)

3.3.1 Exfoliation in pure solvents

UALPE exploits ultrasound sonication (either vibrating tip such as tip/horn sonication or ultrasonic bath; Fig. 3.6(a,b)) to generate intralayer shear forces and as such to achieve exfoliation. This exfoliation process and the subsequent dispersal of the exfoliated 2d materials are dependent on the intermolecular interaction between the 2d materials and the liquid medium [15, 234, 236–238]. Typically, the liquid medium is preferably a pure solvent as this does not introduce impurities into the exfoliated 2d materials and hence, the subsequent 2d material based applications. The characteristics that define whether a pure solvent can perform a good intermolecular interaction (*i.e.* "good solvent" as shown in Fig. 3.4(c)) are usually whether the solvent has matched surface tension and Hansen solubility parameters (HSPs) to those derived for the 2d materials [15, 234, 236–238, 275–278].

The understanding and analysis start with the change in Gibbs free energy, ΔG_{mix}. For a typical dispersion, ΔG_{mix} is defined as the free energy difference between the two components in the dispersion (*i.e.* the solute and the solvent) [15, 133, 234, 275, 276]:

$$\Delta G_{mix} = \Delta H_{mix} - \tau \Delta S_{mix} \tag{3.1}$$

where ΔH_{mix} is the change in enthalpy, τ is the temperature and ΔS_{mix} is the change in entropy. A negative or small enough ΔG_{mix} is preferred as this can promote mixing due to small associated energy cost.

In the case of UALPE, ΔG_{mix} is effectively the energy cost of exfoliation between the dispersed 2d material and the solvent. ΔS_{mix} is generally very small due to the large mass of the 2d material flakes, so consequently ΔH_{mix} has to be minimal. ΔH_{mix} is essentially defined by the intermolecular interaction between the two components of the dispersion (*i.e.*

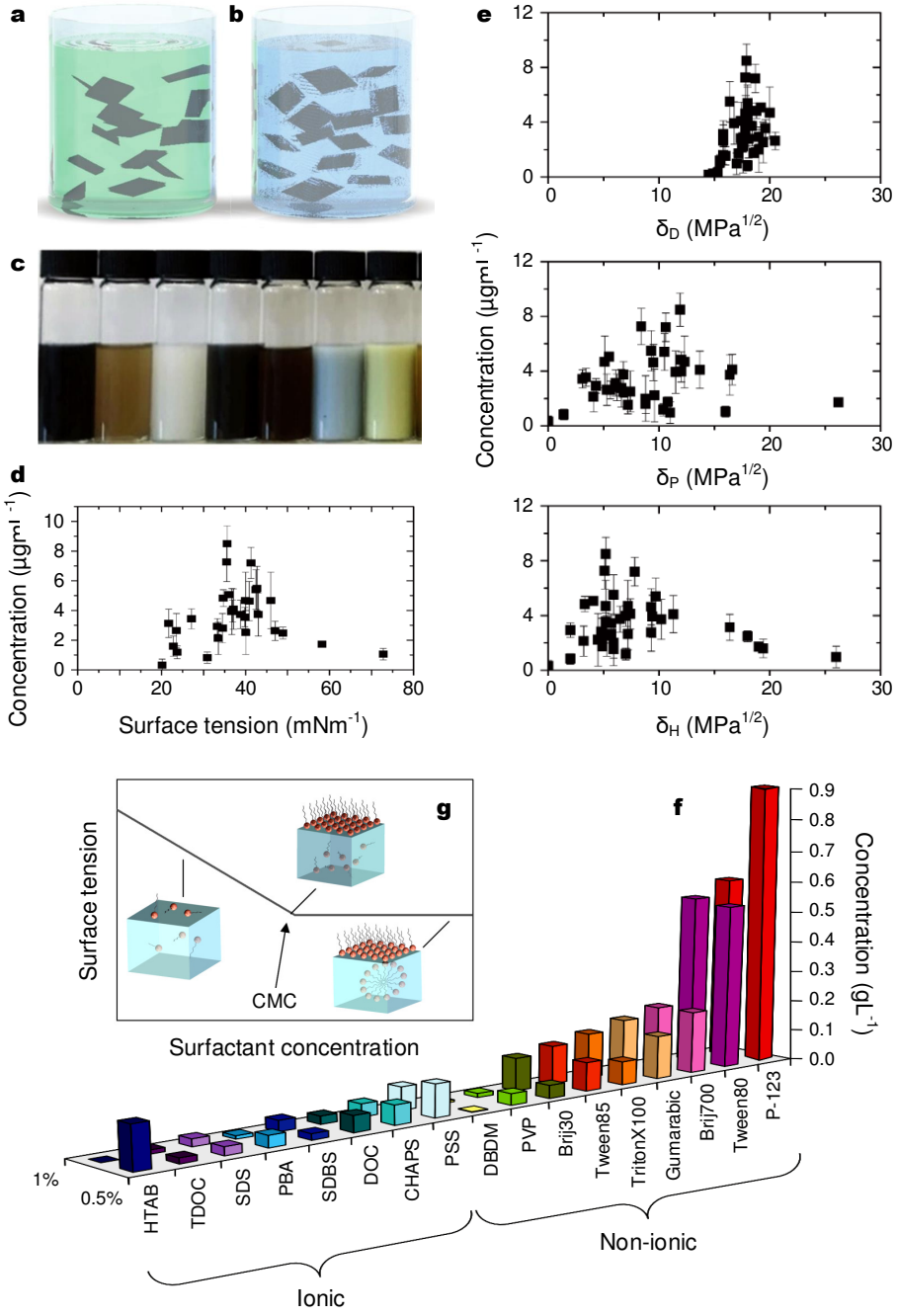

Fig. 3.7 Schematic figures for UALPE dispersions in (a) pure solvents and (b) with surfactants [16]; (c) Photograph of dispersions of different 2d materials, adapted from Ref. [16]; The concentration of graphene dispersions with respect to (d) solvent surface tension and (e) solvent HSPs, adapted from Ref. [275]; (f) The concentration of graphene in aqueous dispersions with different surfactants [264]; (g) The surface tension of a surfactant solution with respect to the surfactant concentration, showing the surface tension is stabilised above CMC.

the 2d material and the solvent) and can be predicated as follows [133, 236]:

$$\Delta H_{mix} \approx \frac{2}{t}(\sqrt{\gamma_s} - \sqrt{\gamma_{2d}})^2 \nu \tag{3.2}$$

where γ_{s} and $\gamma_{2\mathrm{d}}$ stand for the surface energy of the solvent and the 2d material respectively, t represents the flake thickness, and ν is the volume fraction of the 2d material. To ensure ΔH_{mix} is minimal, Eq. 3.2 requires that $\gamma_{\mathrm{s}} \approx \gamma_{2\mathrm{d}}$. This means that the surface energy of the 2d material and the solvent should be matched.

Empirical experiments show that 2d materials (including graphene, TMDs, BP, *h*-BN, *etc*) can be effectively dispersed in a wide range of "good solvents" that have a surface tension of ~40 mNm^{-1}[181, 236, 237, 275, 276]. For instance, as shown in Fig. 3.7(d), the concentration of graphene dispersions is maximised at ~40 mNm^{-1}[275]. The surface tension can be converted to solvent surface energy following the equation:

$$\gamma = \gamma_s - \tau S_s \tag{3.3}$$

where S_{s} = 0.1 mNm^{-1} [133, 278]. At room temperature (*i.e.* τ = 298 K), the surface energy of "good solvents" is estimated as ~ 70 mNm^{-1}. This derives that the surface energy of graphene is ~ 70 mNm^{-1} [275]. Similarly, the surface energies of other 2d materials (*e.g.* TMDs and BP) are also derived as ~70 mNm^{-1} [178, 181, 237, 276]. However, the investigation above is accepted only as a qualitative analysis [275, 276].

A more detailed and accurate analysis looking into this subject was established. In a typical dispersion, the intermolecular interaction between the solute and the solvent can be divided into three HSPs, *i.e.* dispersive(D), polar(P) and hydrogen-bonding(H) [275–277]. The intermolecular interaction is predicated by HSP distance (R_{d}) following:

$$R_d^2 = 4(\delta_{D,s} - \delta_{D,2d})^2 + (\delta_{P,s} - \delta_{P,2d})^2 + (\delta_{H,s} - \delta_{H,2d})^2 \tag{3.4}$$

where $\delta_{\mathrm{i,2d}}$ and $\delta_{\mathrm{i,s}}$ (i: D, P, H) are the HSPs of the 2d material and the solvent, respectively. Equation 3.4 is an important criterion to determine the solubility of the 2d material in the solvent, and a smaller R_{d} means a better solubility. Therefore, to successfully develop a 2d material dispersion, the HSPs δ_{i} (i: D, P, H) of the 2d material and the solvent should be matched [277]. For the case of graphene, Ref. [275] investigated the solubility of graphene in more than 40 solvents and found that the "good solvents" possessed HSPs of δ_{D} ~18 $\mathrm{MP}^{1/2}$, δ_{P} ~9.3 $\mathrm{MP}^{1/2}$ and δ_{H} ~7.7 $\mathrm{MP}^{1/2}$, respectively (Fig. 3.7(e)). These parameters were derived as the HSPs of graphene. For the case of TMDs, similarly, the HSPs were derived as δ_{D} ~18 $\mathrm{MP}^{1/2}$, δ_{P} ~8.5 $\mathrm{MP}^{1/2}$ and δ_{H} ~7 $\mathrm{MP}^{1/2}$, respectively [276]. The above

investigations provide a practical criterion for solvent selection for UALPE: any solvent to develop a stable 2d material dispersion should possess matched HSPs to those empirically derived for the 2d material.

The "good solvents" are typically high boiling point, toxic and expensive organic solvents, for instance N-Methyl-2-pyrrolidone (NMP; 204°C), cyclohexanone (CHO; ∼155°C), N-Cyclohexyl-2-pyrrolidone (CHP; ∼284°C) and dimethylformamide (DMF; ∼153°C) [181, 235, 237, 238, 275, 276]. These solvent characteristics present significant challenges in dispersion processing and material deposition for device fabrication [260, 279–281]. For example, for polymer nanocomposite SA fabrication as in Ref. [95, 133, 282]), if an NMP dispersion is used, long drying times are needed due to the high boiling point, and in particular, careful handling is required due to the toxicity. Their fluidic properties and surface tension are also problematic for printing, as will be discussed in Section 4.4.3.

For many applications, therefore, it would be preferable to use low boiling point, non-toxic solvents such as water and alcohols [260, 279, 281, 283]. However, both water (72 mNm^{-1}; δ_D ∼18.1 $MPa^{1/2}$, δ_P ∼17.1 $MPa^{1/2}$, δ_H ∼16.9 $MPa^{1/2}$ [277]) and alcohols (*e.g.* IPA: 23 mNm^{-1}; δ_D ∼15.8 $MPa^{1/2}$, δ_P ∼6.1 $MPa^{1/2}$, δ_H ∼16.4 $MPa^{1/2}$ [277]) fail to meet the selection criteria above. This suggests that both water and alcohols are "poor solvents" for 2d materials, as widely reported [181, 235, 237, 238, 275, 276].

For the "poor solvents", a strategy of using solvent mixture has emerged [39, 266, 279, 284]. For example, Zhou *et al.* demonstrated that water and alcohol mixture was a viable liquid medium choice [266]. Indeed, the surface tension of alcohol/water mixture can be well-controlled by the amount of alcohol [285] and hence, designed with a matched surface tension to minimise ΔG_{mix}. On the other hand, the HSPs of the mixture can be predicted following [266, 277, 279]:

$$\delta_{mixture} = \Sigma \nu_n \delta_{i,n} \tag{3.5}$$

where ν_{n} is the volume fraction of each solvent, and $\delta_{\mathrm{i,n}}$ stands for the HSPs (*i*: D, P, H) of each solvent. As such, it is possible to design a mixture with minimal HSP distance for metastable dispersion production [39, 266, 279, 284].

3.3.2 Exfoliation using surfactants

For the "poor solvents", an alternative to solvent mixture is to use surfactants to aid UALPE [15, 234, 260, 261, 264, 265, 286, 287], an approach well-developed for CNTs [134, 235]. Surfactant acts by adsorbing onto the surface of 2d materials, promoting the intermolecular interaction with the solvents. Indeed, as shown in Fig. 3.7(f), Guardia *et al.* demonstrated

UALPE production of graphene in water with the presence of a wide range of surfactants, including ionic and non-ionic ones [264].

Previous studies show that some of the most effective ionic surfactants are facial amphiphiles (*i.e.* molecules with a quasi-flat molecular structure with hydrophobic and hydrophilic faces), for instance bile salts such as sodium cholate (SC) and sodium deoxycholate (SDC) [15, 133, 134, 235, 238, 238, 261, 265]. When such ionic surfactant and 2d material interact in water, the surfactant molecule is absorbed onto the surface of the 2d material, generating temporary effective charge. This may balance the intralayer vdW forces and hence, promote exfoliation [235]. The induced charge around the exfoliated 2d material flakes generates a Coulomb repulsion which further prevents reaggregation [133, 260, 286, 287]. The required concentration of an ionic surfactant to stable the dispersion can be estimated by surfactant critical micelle concentration (CMC) [134]. The CMC of a surfactant at a specific temperature can be estimated by measuring the surface tension of its solution against the surfactant concentration [288], as shown in Fig. 3.7(g). Below CMC, addition of the surfactant causes a large change in the surface tension as the surfactant molecules assemble at the solution-air interface [288]. Above CMC, the interface is saturated where the surfactant molecules spontaneously arrange into micelles, such that further addition of surfactant causes minimal changes [288].

Another approach is making use of non-ionic surfactants. Typical examples include oligomers such as Triton X, Tween and Brij series, and polymers such as sodium carboxymethylcellulose (Na-CMC) and polyvinylpyrrolidone (PVP) [264, 289]. The polymers can encapsulate the faces of 2d material flakes and hence, provide a physical separation between the flakes to allow enhanced exfoliation and stabilisation [134, 235, 261, 289, 290]. Indeed, for example, Bourlinos *et al.* showed that the addition of PVP in water could lead to graphene production [291]. The authors suggested that the cellulose made a colloidal dispersion and hence, prevent the graphene flakes from aggregation. Besides, polymers are also of interest for ink formulation, as polymers can allow tuning of the ink properties (*e.g.* rheological properties), as will be discussed in Chapter 4.1.1.

However, unlike solvents, surfactants form an integral part of the deposited films. This can compromise the properties of the 2d materials, such as the electrical conductivity and optoelectronic properties. For certain applications, for example conductive graphene coating that requires a high electrical conductivity and photodetectors that exploit the optoelectronic properties, it is necessary to remove the surfactants following deposition, [46, 48, 51, 53, 56]. Removal of the surfactants is usually done through repeated washing or high temperature (*e.g.* $>400^{\circ}$C) annealing [50, 51, 56]. For some other applications, however, the surfactants may be exploited directly for device fabrication. For instance, polymers such as Na-CMC can

work as the host polymer for 2d material flakes, allowing functional polymer nanocomposites (*e.g.* SAs [134, 282, 292]) to be developed directly from the as-produced UALPE dispersions.

3.3.3 Centrifugation processing principles

Purification is necessary for the separation of the exfoliated flakes from those unexfoliated. This is typically done by using centrifugation. During centrifugation, a dispersed flake is mainly subjected to two forces: the centrifugation force (F_{cen}) towards the bottom of the uplifted rotating centrifuge tube, and the friction force (F_{fric}) opposite to the centrifugation force [15, 236]. The F_{cen} is determined by the centrifugation speed and the mass of the flake, following the equation:

$$F_{cen} = m\omega^2 R_{rad} \tag{3.6}$$

where m is the mass of the flake, ω is the angular velocity of the rotor and R_{rad} is the rotation radius. The F_{fric} is determined as follows:

$$F_{fric} \propto \eta r \upsilon_{cen} \tag{3.7}$$

where η is the viscosity of the dispersion, r is the flake size (*i.e.* flake thickness and lateral dimension), and υ_{cen} is the velocity of the flake. Sedimentation is driven by the imbalance between these two forces.

As such, suitable centrifugation processing allows sedimentation of the unexfoliated flakes, leaving the dispersion supernatant enriched with the exfoliated mono- and few-layer flakes. It may even allow selection of the flake size. Indeed, as shown in Fig. 3.8, there are three major centrifugation processing techniques that are designed for convenient separation on the basis of sedimentation in response to centrifugation (*i.e.* sedimentation

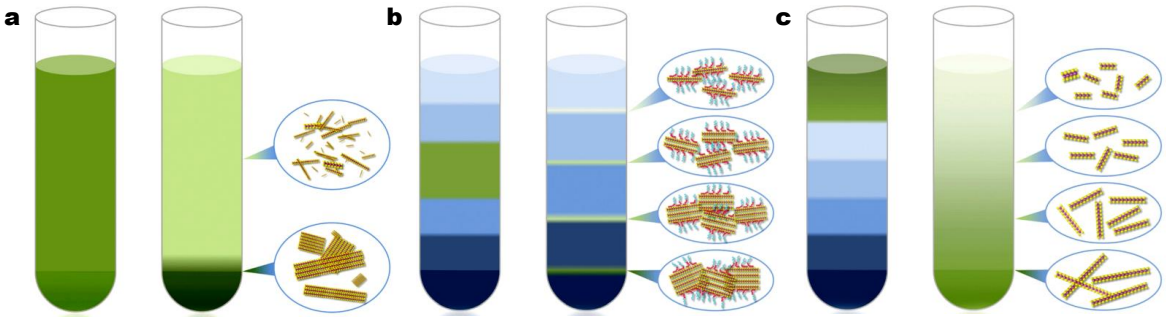

Fig. 3.8 Schematic figures of centrifugation based on (a) SBS to separate exfoliated flakes from the unexfoliated ones, (b) DGU to sort flakes according to thickness, and (c) RZS to sort flakes according to lateral dimension [16].

based separation, SBS), selection of flake thickness *via* density gradient ultracentrifugation (DGU), and selection of flake lateral dimension *via* rate zonal separation (RZS) [15, 16].

SBS is the simplest, most straightforward and most widely exploited technique [15]. It is practised in a uniform liquid medium, for instance pure solvents (*e.g.* NMP) and surfactant solutions (*e.g.* water/SDC). Upon centrifugation, in the case of unexfoliated large and thick flakes, the centrifugation force surpasses the friction force and hence, sediment these flakes due to their large mass. Applying a higher centrifugation speed brings larger centrifugation force to the flakes, leading to the sedimentation of the flakes that would have been able to be stabilised. It is therefore also possible to conveniently control the average flake size through the control of the centrifugation speed [234, 238, 293, 294]. For example, Khan *et al.* reported production of graphene dispersions with a range of flake sizes in conjunction with varied centrifugation speed [294]. On the other hand, dispersion physical properties such as viscosity play an important role on flake sedimentation. A higher viscosity leads to a larger F_{fric}. This can balance a larger F_{cen}, allowing flakes of a large size stabilised in the dispersion upon centrifugation. For example, a water/SDC solution gives a smaller average thickness than NMP [133]. This may be explained by the lower viscosity of water (0.89 mPa·s at 25°C) than NMP (1.67 mPa·s at 25°C).

Since the UALPE dispersions usually have a concentration of <1 gL^{-1} [15, 16, 133, 181, 236–238], it is necessary to significantly increase the concentration for the point of view of material deposition for device fabrication. This is also important for printing of 2d materials. Iterative centrifugation on the basis of SBS has emerged as a practical method to obtain highly concentrated dispersions [15, 16, 294]. This is done by iteratively centrifuging the as-produced UALPE dispersions with (multiple) high centrifuge speeds, and subsequently redispersing the sedimented exfoliated flakes in a smaller amount of solvent. However, a high centrifugation speed may lead to restacking or aggregation of the exfoliated flakes.

Based on SBS, DGU was developed to select flake thickness [15, 16]. A DGU process requires a density gradient medium, which can be designed by the selection of surfactants, for instance SC and sodium dodecylbenzene sulfonate (SDBS) [265, 295, 296]. In a DGU process, the flakes differing in flake thickness move along the ultracentrifuge tube with different velocity until they reach the corresponding isopycnic point, where the F_{cen} matches the F_{fric} experienced in the surrounding density gradient medium. Within the framework of DGU, RZS was developed to achieve selection of flake lateral dimension [15, 16, 297]. RZS exploits the fact that the flakes with larger lateral dimension sediment faster along the centrifugation tube. In a RZS process, the centrifugation is stopped during the transient centrifugal regime before the flakes reach their own isopycnic points, allowing a spatial separation of the flakes differing in lateral dimension along the ultracentrifuge tube.

3.4 Material characterisations

Following solution processing of 2d materials, it is important to characterise the exfoliated 2d materials. Here I introduce optical absorption spectroscopy, microscopic methods and Raman characteristics that are widely used characterisation methods for the solution-processed 2d materials.

3.4.1 Optical absorption spectroscopy

It is important to quantify the concentration of the exfoliated 2d material flakes dispersed in the dispersions. However, this is usually challenging. It is impossible to quantify how much of the starting layered crystals have been exfoliated and dispersed. It is also impractical and inaccurate to directly measure the mass of the 2d materials with a typical micro-balance due to its low concentration (typically <1 gL^{-1} for UALPE dispersions [1, 15, 181, 234–238]). Hence, indirect estimation using optical absorption spectroscopy following Beer-Lambert law is a convenient tool [236, 237]:

$$A = \alpha_\lambda C l \tag{3.8}$$

where A is the absorbance, α_λ is the absorption coefficient at a wavelength λ, C is concentration, and l is optical path of incident light in the dispersion. α_λ relates C to A, and once α_λ is known, C can be calculated from A.

A can be measured using a UV-Vis-NIR spectrophotometer, as schematically illustrated in Fig. 3.9(a). UV-Vis-NIR spectrophotometer is designed to measure the optical absorbance of a compound in solution or as a solid (*e.g.* free standing thin films). It is usually consisted of components including light source (the lamps), a filter, monochromator, sample and reference holders and detectors. As shown, a monochrome beam is split and passed through a sample and a reference, respectively, allowing analysis of the absorbance of the sample at a wavelength at a time. This allows collection of an absorbance spectrum spanning a wide wavelength region. However, I note that in the preceding studies of UALPE production of 2d materials optical extinction (E, *i.e.* the sum of the absorbance and scattering [298]) is usually used to quantify the concentration for the convenience of measurement. For example, Fig. 3.9(b) presents the extinction spectra at 400-1400 nm of graphene dispersions in different solvents [236]. I therefore differentiate these two terminologies in the following discussions of this thesis.

To estimate the concentration from the spectroscopy, an accurate determination of α_λ is crucial. In a commonly adopted method, proposed by Hernandez *et al.* [236, 237], a large volume of dispersion is filtered through a membrane of known mass to extract the flakes. The

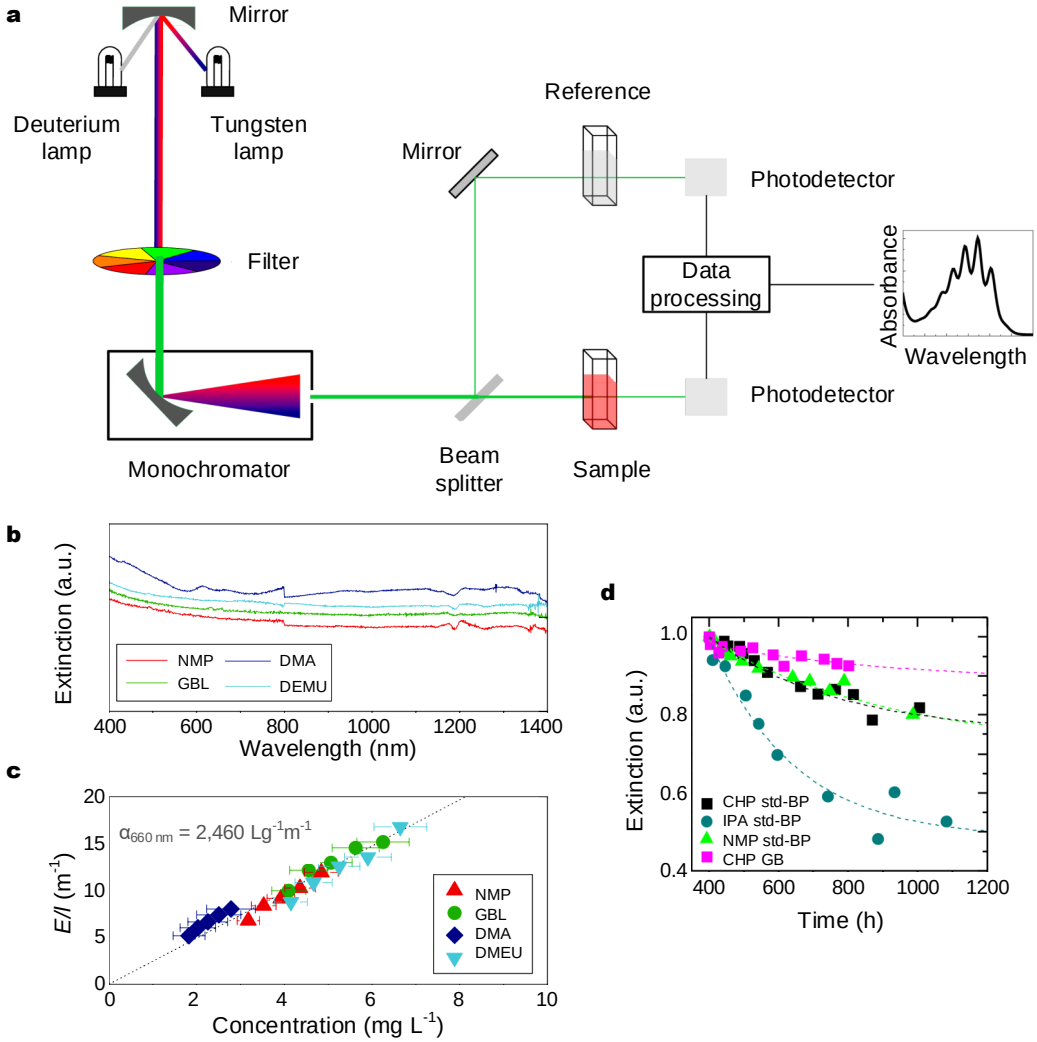

Fig. 3.9 (a) Schematic figure of UV-Vis-NIR spectrophotometer, source - Wikipedia; (b) Optical extinction spectra for UALPE graphene dispersions in different solvents, and (c) the absorbance divided by the cell length with respect to the concentration showing that the absorption coefficient at 660 nm is 2,460 $\mathrm{Lg^{-1}m^{-1}}$, adapted from Ref. [236]; (d) Relative extinction at 465 nm of UALPE BP dispersions in different solvents with respect of time, noted as "std" under ambient conditions and as "GB" under glovebox, adapted from Ref. [181].

residual solvent is then removed by annealing. The mass of the extracted flakes is therefore the mass difference of the membrane before and after filtration. The α_λ is determined by correlating the absorbance of the dispersion with the mass. This α_λ is then used to estimate the concentration. Since α_λ is a study of the optical absorption of the compound, it should be independent on the solvents where the material is dispersed. This is indeed demonstrated in Ref. [236], where the authors Hernandez *et al.* showed that the α_λ of graphene at 660 nm was 2,460 $\mathrm{Lg^{-1}m^{-1}}$ in different solvents; Fig. 3.9(c).

Since extinction is directly related to concentration, optical absorption spectroscopy is also a convenient tool to study the stability of a 2d material dispersion against sedimentation. This is done by collecting the extinction of a stand-by dispersion for a period of time. For stable dispersion, the extinction should remain unchanged. Figure 3.9(d) is the time-dependent extinction at 465 nm of UALPE BP dispersions, showing that CHP produces the most stable dispersion [181]. Meanwhile, it suggests that when under glove box BP is better protected from oxidation than in ambient conditions.

3.4.2 Microscopy characterisations

Atomic force microscopy (AFM). AFM is one type of scanning probe microscopy to study the thickness and the morphology of an object [299]. It consists of a cantilever ended with a sharp tip, usually on the order of nanometres in radius, to scan across the surface the object. The scanning mode of AFM is either static where the tip and the surface contact, or dynamic where the cantilever vibrates. When in operation, the tip is brought into contact with or driven close enough to the surface, the force between the tip and the object is collected to represent the thickness and the surface morphology of the object. AFM offers a resolution on the order of nanometres to micrometres, making it a very effective tool to study 2d materials.

Figure 3.10(a,b) are representative AFM microimages of deposited UALPE MoS_2 flakes [296]. As clearly shown, the flakes are randomly distributed on the substrate, with varied thickness and lateral size. Scanning across individual flakes allows representation of the thickness of the flakes; Fig. 3.10(c). For instance, the flakes labelled with blue and green are consistent in thickness across the investigated positions, with a thickness of $\sim$3 nm and $\sim$4 nm, respectively. This demonstrates that the MoS_2 flakes are successfully exfoliated, and are uniform in terms of layer numbers. However, Fig. 3.10(c) also shows that there are some flakes of larger thickness, up to 10 nm. Statistical analysis of large quantities of flakes allows an estimation of flake size distribution, for instance the flake thickness analysis presented in Fig. 3.10(d). Assuming $\sim$3 nm measured thickness for a monolayer flake and $\sim$1.9 nm increase in thickness for each additional layer, the authors Backes *et al.* obtained an estimation of the layer number distribution with this flake thickness distribution [296]. However, this calculation is different from other studies, for instance in Ref. [300] where $\sim$1 nm is considered as the measured thickness for a monolayer flake and $\sim$0.7 nm is considered as the increase in thickness for each additional layer.

Scanning electron microscopy (SEM). SEM makes use of accelerated electrons as the illumination source to investigate the morphology and the structure of an object [299]. When in operation, the electron beam is fired from an electron gun and subsequently accelerated by

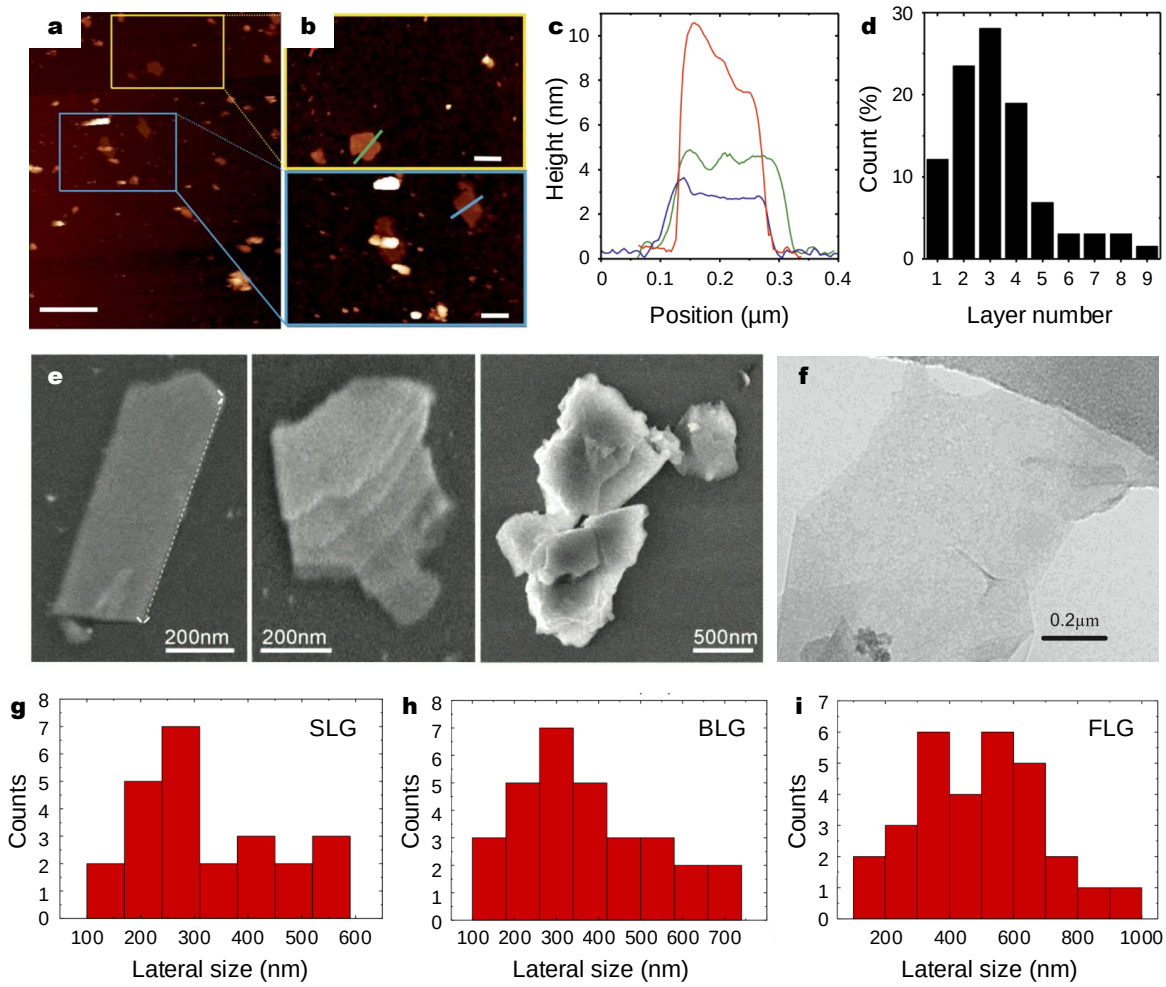

Fig. 3.10 (a, b) Representative AFM microimages of exfoliated UALPE MoS_2 flakes deposited on Si/SiO_2, allowing (c) measurement of thickness of individual flakes and (d) statistical analysis of flake layer number [296]; (e) Representative SEM microimages of a thin flake, a few-layer, and a cluster of aggregated few-layer of UALPE MoS_2 flakes [237]; (f) Representative TEM microimage of UALPE graphene flakes, allowing statistical analysis of lateral size for (g) mono-, (h) bi- and (i) few-layer graphene flakes [37].

a strong electrostatic field. The highly accelerated electron beam is focused by electrostatic and electromagnetic lenses, and finally projected to the surface of the object. The electron beam probes over the surface and is subsequently reflected to produce an image of the surface morphology. The advantage of surface probing is that the resultant scanning images can not only present information of the morphology but also of the cross-section. It offers a higher resolution than AFM, down to 1 nm.

SEM is a useful tool to study the flake morphology and also the cross-sectional stacking of solution-processed 2d materials. Figure 3.10(e) depicts representative SEM microimages

of UALPE MoS_2 flakes, where a very thin flake, a multilayer flake and a cluster of aggregated multilayer flakes are imaged [237]. These microimages clearly present the flake morphologies, allowing the measurement of the lateral size of the investigated flakes. Importantly, the evolution of flake layer numbers is clearly demonstrated. However, unlike AFM, SEM cannot be used to directly represent the thickness of the investigated flakes.

Transmission electron microscopy (TEM). Similar to SEM, TEM investigates an object with accelerated electron beam [299]. However, unlike SEM, the electron beam transmits through the object with some part of the electron beam scattered out, allowing collection of the information of the object. Because the electron beam needs to emerge through the object, the object thickness is required to be extremely thin, typically $<$100 nm. It achieves a resolution at least ten times higher than SEM, down to 50 pm [301]. These above features make TEM particularly suitable for the characterisation of solution-processed 2d material flakes.

Figure 3.10(f) is a TEM microimage of single layer graphene flake produced by UALPE [37]. This image demonstrates that the basal plane of this graphene flake is free from cracks and defects, with sharp, clearly defined flake edges. From the high resolution TEM microimage, it is convenient to distinguish monolayer from multilayer, as clearly shown in Fig. 3.10(f) where the flake exhibits some multilayer regions. As TEM provides the resolution to study individual flakes, it is an effective tool to study the lateral size of the investigated individual flakes and hence, provide statistical analysis. For example, Fig. 3.10(g-i) present lateral size histograms of mono-, bi- and few-layer graphene flakes that were measured by Torrisi *et al.* in determining the size distribution of graphene flakes for a graphene inkjet ink [37]. Further analysis includes electron diffraction pattern, which is to study the lattice structures of the investigated flakes.

3.4.3 Raman spectroscopy

Raman spectroscopy is one of the most widely used non-destructive techniques to study the interatomic vibrations of 2d materials [15, 302, 303]. Interlayer and intralayer bonds in 2d materials have resonant vibrational modes, and these are what Raman spectroscopy probes. When in operation, the sample is illuminated with a monochromatic laser, the photons in the laser beam scatter inelastically from phonons in the sample (*i.e.* they gain or lose energy on interacting with the resonant modes), leading to characteristic energy shifts in the reflected light. The reflected spectrum therefore contains additional characteristic peaks corresponding to the vibrational modes. The position and intensity of the peaks can then be correlated to factors such as number of layers, the density of defects, or the level

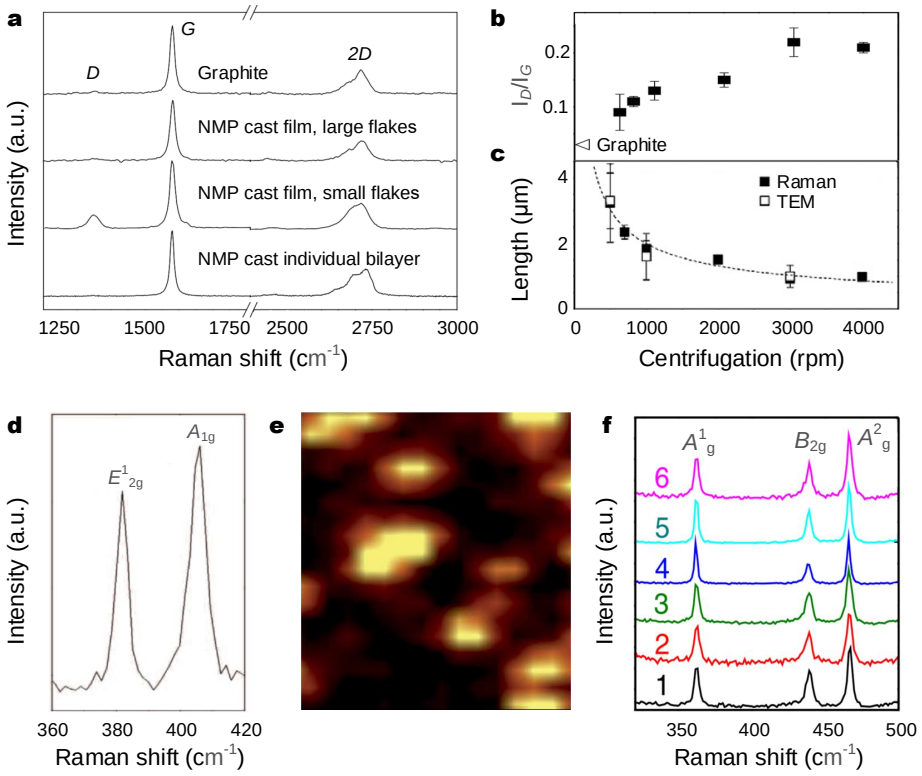

Fig. 3.11 (a) Raman spectra for bulk graphite, vacuum filtered film with the laser spot focused on a large (∼5 μm) flakes and on a small (∼1 μm) flakes, and individual bilayer large flakes [236]; (b) Raman I_D/I_G of graphene flakes after size selection through centrifugation, and (c) correlation between the flake size estimated by Raman I_D/I_G and TEM measurement [294]; (d) Typical Raman spectrum of an individual exfoliated MoS_2 flake [237]; (e) Integrated A_{1g} area mapping of dropcast MoS_2 flakes [296]; (f) Typical Raman spectra for varied spots of dropcast BP flakes [181]. All the Raman spectroscopy characterisations are exampled with UALPE flakes.

of doping or functionalisation [186, 300, 302, 304]. However, when working with solution-processed flakes, one key thing needs to be noted. Due to the relatively small size of flakes, the measured spectrum inevitably includes contributions from multiple flakes with different thickness and size, and hence, gives a qualitative rather than quantitative analysis of the flakes. The measured spectrum is therefore less well defined than with the 2d materials produced *via* other means [15, 236, 275].

Graphene. For pristine graphene, there are usually two major peaks in the Raman spectrum: *G* peak and 2*D* peak, which are located at ∼1580 cm^{-1} and ∼2700 cm^{-1}, respectively [302, 303]. Among them, *G* peak is a primary in-plane vibrational mode, arising from the stretching of the C-C bond; 2*D* is second-order overtone of another in-plane

vibration mode, D peak ($\sim$1350 cm^{-1}). D peak, however, arises from disordered lattice structure of graphene. Therefore, D peak is usually invisible in the Raman spectrum of pristine graphene, and the presence of D peak usually stands for the occurring of defects. As graphene layer number increases, due to the interactions from the stacking of graphene layers, G and $2D$ peaks become wider and shorter (*i.e.* larger full width at half maximum: FWHM), and blue-shift (*i.e.* higher frequency shift). However, the G and $2D$ peaks of graphene over 5 layers are hardly distinguishable from those of graphite.

Figure 3.11(a) presents the Raman spectra of graphite and graphene flakes produced by UALPE in NMP [236]. For graphite, the Raman spectrum does not show D peak, which is expected as there should be minimal defects in graphite. For the large flakes in a cast film, G and $2D$ peaks do not show big variations compared to those of graphite, suggesting the investigated flakes are devoid of defects and are structurally similar to graphite. For the small flakes in the cast film, G peak becomes sharper which confirms exfoliation, and D peak emerges which indicates the occurring of defects. The defects are likely caused by the exfoliation process. For the individual large bilayer flakes, G peak is also sharper, but D peaks is invisible. This for one thing confirms exfoliation, and for another thing indicates that unlike small flakes the bilayer larger flake has minimal defects. In addition, in Ref. [294], Khan *et al.* showed that Raman peak intensity ratio $I_{\mathrm{D}}/I_{\mathrm{G}}$ of UALPE graphene flakes could be well-correlated to the flake size, as presented in Fig. 3.11(b). This suggests that Raman spectrum is useful as a tool to confirm exfoliation.

MoS_2. Figure 3.11(d) is a representative Raman spectrum of exfoliated MoS_2 produced by UALPE [237]. As shown, there are two major peaks in the spectrum, located at $\sim$380 cm^{-1} and $\sim$400 cm^{-1}, respectively. These peaks correspond to in-plane ($E^1_{2\mathrm{g}}$) and out-of-plane ($A_{1\mathrm{g}}$) vibration modes [300, 305, 306]. The vibration modes vary depending on MoS_2 layer numbers and hence, shift in the peak positions. When exfoliated, $E^1_{2\mathrm{g}}$ blue-shifts (bulk to monolayer) as a result of mode stiffening, and $A_{1\mathrm{g}}$ red-shifts (bulk to monolayer) as a result of mode softening [300, 305]. This transition can lead to a progressive decrease in the difference between the peak positions from 25.5 cm^{-1} for bulk to 18.7 cm^{-1} for monolayer MoS_2, observed with MC flakes [300, 305]. Since the solution-processed 2d materials are mixture of mono- and few-layer flakes, it is usually challenging to observe such big shifts in Raman peaks. However, still a relatively small Raman shift is usually considered as an evidence of exfoliation [168]. Figure 3.11(e) is a Raman mapping of integrated $A_{1\mathrm{g}}$ area acquired from dropcast UALPE MoS_2 flakes [296]. The authors Backes *et al.* showed that the bright yellow regions were well-correlated to monolayer MoS_2 flakes. This might suggest that a larger integrated $A_{1\mathrm{g}}$ area indicates thinner flakes.

Black phosphorus. Figure 3.11(f) is a study of Raman spectra of varied spots across dropcast solution-processed BP flakes [181]. The Raman spectrum of BP usually has three major peaks close to 400 cm^{-1}, corresponding to one out-of-plane (A_g^1) and two in-plane (B_{2g}, A_g^2) vibrational modes [189, 190]. The additional in-plane mode compared to MoS_2 arises from the anisotropy of BP that leads to directionality of the vibration [189, 307]. The respective full-width at half maximum (FWHM) of these three Raman peaks is all within ∼2-6.5 cm^{-1}, ∼2-7 cm^{-1} and ∼2-8 cm^{-1} (1-6 layers MC flakes) [189, 190]. These three peaks exhibit small blue-shifts from bulk to monolayer, observed with MC flakes [186, 189, 190].

As discussed in Section 2.4, arising from the puckered hexagonal crystal, BP exhibits anisotropic electron-phonon interactions, making Raman spectrum polarisation-, wavelength- and thickness-dependent [308–310]. Therefore, for exfoliated BP flakes, Raman spectrum should depend on polarisation, *i.e.* the intensities of the Raman peaks are dependent on polarisation. This has been widely observed with MC flakes [170, 190, 309, 310]. However, as shown in Fig. 3.11(f), the collected different Raman spectra do not exhibit any prominent polarisation-dependent properties, suggesting that polarisation had been nullified in this study. This might be due to the fact that during Raman measurement a large quantities of BP flakes that were distributed in a random orientation were investigated.

In addition, Raman spectroscopy has been used as a convenient tool to study the BP oxidation in the preceding studies. Favron *et al.* demonstrated that the integrated intensity ratio of A_g^1 to A_g^2 was well-correlated to the oxidation degree of MC flakes, with a value range of 0.2-0.6 indicating minimal oxidation [190]. However, Hanlon *et al.* argued that a value of $>$0.6 for the intensity of A_g^1 to A_g^2 was an indication for minimal oxidation [181].

3.5 Summary

In this chapter, I have discussed the key production methods of 2d materials, with the focus on solution-based methods and the related characterisation techniques. Among these production methods, MC is a useful laboratorial tool for fundamental studies and device demonstrations, CVD allows controllable synthesis of large-area films but not yet meets the demands for large-scale, low-cost applications, while UALPE has emerged as a mass production method of pristine mono- and few-layer flakes. The UALPE dispersions are readily adapted to a variety of deposition techniques for device fabrication, among which graphics printing technologies (*e.g.* inkjet printing) provide an exciting prospect for low-cost and large-scale device fabrication. In the following Chapter 4, I will discuss the ink systems and the printing technologies, providing a context of formulating 2d materials into functional for the fabrication of printable devices.

Chapter 4

Ink systems and graphics printing technologies

In the previous chapter, I introduced the production methods of 2d materials and highlighted solution processing (in particular, ultrasonic-assisted liquid phase exfoliation: UALPE) for large-scale device fabrication. Adapting solution-processed 2d materials to graphics printing technologies is a promising large-scale, cost-effective device fabrication approach [19, 20, 32, 33]. Inkjet printing, a high-resolution, mask-less, digital patterning technology, is particularly interesting. It is time and cost saving, especially during device prototyping. Inkjet printing is therefore the main printing technology used in my doctoral work. Though much progress has been made in ink formulation and device fabrication of inkjet printing of 2d materials, the fluidic properties, drying dynamics and interaction with substrates of the inks have not been extensively investigated. Indeed, current 2d material ink formulations tend to give unstable ink droplet jetting, poor wetting of the substrates, and formation of coffee rings. This delivers a spatially non-uniform material deposition and hence, a poor reproducibility in device fabrication. Large-scale device printing is therefore not possible, realising which requires a significantly improved ink formulation.

It is therefore necessary to have a thorough understanding of the ink systems (Section 4.1) and the graphics printing technologies (Section 4.2), in particular the inkjet printing principles (Section 4.3) and the current progress and challenges of inkjet printing of 2d materials (Section 4.4).

4.1 Ink systems and formulation

Inks were used as early as in 2,500 BC when ancient Egypt and China developed painting paste that was composed of soot (pigment) bounded together with gums (binder) in water (solvent) [311, 312]. Printing was developed almost 3,000 years later when hand-carved wooden letterpress was invented for letter reproduction. The ink made for this printing was composed of coloured earth, soot or plant (pigment) and gum (binder) dissolved in water (solvent) [311, 312]. This printing process was, however, cumbersome and the printed ink was easily washed out. 1,300 years later, Johannes Guttenberg developed a printing press with metallic moveable type, which is the foundation of modern printing technologies today (*e.g.* inkjet, flexographic, gravure and screen printing). The conventional water-based inks by then were not able to adhere onto the metallic type [313]. Inks based on oil (*e.g.* linseed oil, walnut oil and turpentine; binder) emerged and would therefore go on to dominate printing [311, 312]. Colourful pigments were introduced into the inks in the 18th century, and drying agents (additive) were first used in the 19th century [311, 312]. The more recent developments on printing technologies have promoted the development of inks, with the ink composition and physical properties specifically designed.

4.1.1 Ink composition

As described, an ink is typically composed of pigment, binder, solvent and additives [311, 313, 314]. The ink composition is usually designed with suitable physical (*e.g.* rheological) properties for a specific printing technology. Table 4.1 is a list of ink composition for commonly used printing technologies.

The basic function of pigment is to give a colour to the ink, just like the exploitation of soot, coloured earth and plant in the early days of ink history. More recent inks use colouring pigments such as carbon black (black), lithol (red), phthalocyanine (green) and

Table 4.1 Typical composition and viscosity of inks for graphics printing technologies. The data is collected from Ref. [19, 20, 62, 311, 313–320].

Printing method	Ink composition (wt.%)				Viscosity (mPa·s)
	Pigment	Binder	Solvent	Additive	
Inkjet	5-10	5-20	65-95	1-5	4-30
Flexographic	12-17	40-45	25-45	1-5	1,000-2,000
Gravure	12-17	20-35	60-65	1-2	100-1,000
Screen	12-20	45-65	20-30	1-5	1,000-10,000

indanthrene (blue). Pigments with special colouring functions may also be used. For example, extenders (*e.g.* $CaCO_3$) are pigments that make the colour of other pigments less intense, while opacifiers (*e.g.* TiO_2) are white pigments that make the print opaque such that the pigments underneath cannot be seen. There are also pigments providing gloss, abrasiveness, or even resistance to ambient conditions (*e.g.* light, heat, solvents, chemicals).

In the last twenty years, there has been a growing interest in incorporating functional materials, such as conducting, semiconducting and dielectric materials, into the inks as active pigments. A number of materials have been studied for this purpose, including metallic nanoparticles [26], organic semiconductors [27, 28], carbon materials (*e.g.* carbon black, carbon nanotubes: CNTs) [29–31], and more recently, solution-processed 2d materials [16–18, 37, 39, 40, 42–46, 48–51, 54, 57, 58]. These materials can lend their functionalities to the printed films, allowing functional device fabrication [16, 24, 32].

The binders used in ink systems are typically polymers such as acrylics, alkyds, cellulose and its derivatives, and rubber resins. They form part of the dried film, aiding the adhesion of the ink to the substrate; they also bind the pigment particles to each other. Binders may simply dry to form a stable film, or may require some form of curing such as heating or ultraviolet (UV) illumination to cross-link. Binders may contribute to properties such as gloss and resistance to ambient conditions. For instance, water insoluble polymers (*e.g.* cellulose) can provide resistance to moisture.

Solvent is the diluent to the other ink components (*i.e.* pigments, binders and additives). The primary function of solvent is to keep the ink in a liquid form such that the ink can be applied to printing plate or cylinder until it is transferred to the substrates. Water is one of the most widely used primary solvents. Besides water, there is a broad range of organic solvents to select, depending on the specific printing technology, substrate and printing purpose. For example, processes such as flexographic and gravure printing require rapid ink drying, so the suitable solvents typically have low boiling points, for instance, asethyl acetate (boiling point 77°C) and isopropanol (IPA: boiling point 82.6°C). Other processes such as screen printing need solvents with moderately low evaporative rates, such as cyclohexanone (CHO: boiling point 156°C) and 2-butoxyethanol (boiling point 168.4°C).

Additives are used to alter the properties of the inks and the printed films. For instance, some surfactants are used improve the wetting of either the pigment or the substrate, while defoamers are used to reduce the surface tension of water-based inks to avoid bubble formation. Alkalis can be introduced into water-based inks to develop a mildly basic pH to dissolve polymer binders (*e.g.* cellulose), such that the dried printed films can resist moisture.

4.1.2 Ink formulation processing

For typical ink systems, the mixture of binders, solvents and additives is termed as varnish [311, 314]. The varnish is typically a clear liquid to carry the pigment. Its physical properties define the wetting of the pigment particles. It also directly governs the rheological properties of the final formulated ink and hence, the ink printability [311, 314]. The ink is therefore usually formulated in three steps: the first step is to produce a varnish; the second step is to disperse the pigments into the varnish; the third step is let-down which is the final adjustment process of the ink physical properties by tuning the ink compositions.

A varnish can be classified into two major types: water-based and solvent-based. A water-based varnish uses water as the solvent to dissolve the binders and additives. It is easy to apply as the varnish easily solidifies after water is evaporated. There is a high demand to develop water-based varnish (or inks) as water is not toxic and environmentally friendly. On the contrary, solvent-based varnish uses organic solvents to dissolve the binders and additives. Solidifying of the varnish usually takes places after the solvents are fully evaporated. In some situations, the varnish may require a long drying time or a curing process (*e.g.* annealing, UV) to solidify.

To produce a varnish, the binder and additive particles are dissolved directly into the solvent. This process may require cavitation or rotor mixing. The cavitation mixer generates strong agitation forces by a saw tooth disc. This is suitable to produce highly viscous varnish.

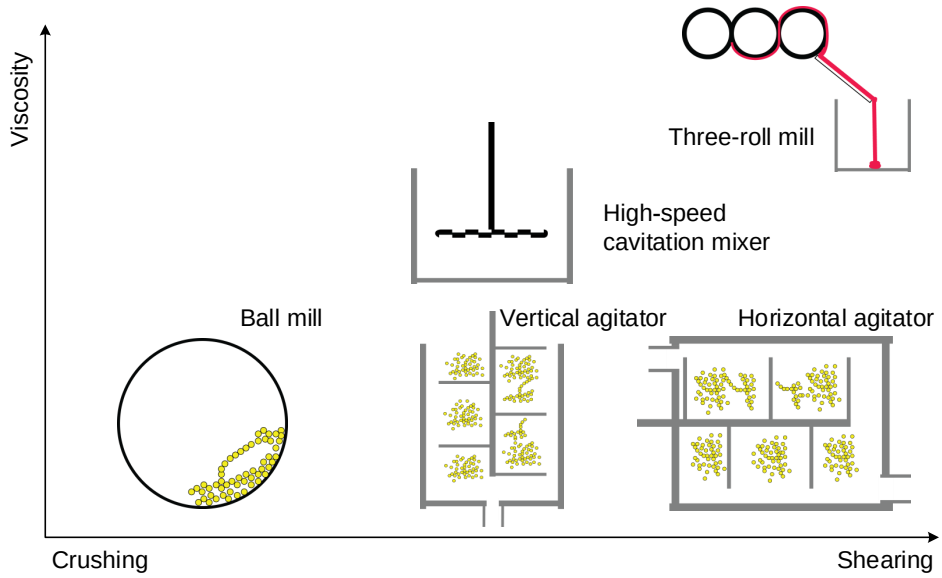

Fig. 4.1 Schematic figure for pigment dispersal, showing that different dispersing equipment is required depending on varnish rheology and the final pigment particle size.

Rotor mixer, oppositely, produces low viscosity varnish. Some binders and additives may require a cooking process (*e.g.* at a temperature over 100°C) to dissolve.

Once the varnish is produced, the pigment is then dispersed into it. The raw pigment is typically in a form of lumps or aggregates. A pigment dispersal process is therefore required to break down such lumps and aggregates into primary acicular, cubic or spherical particles. A range of dispersal technologies can be selected depending on the initial varnish rheology and the desired final pigment particle size, as shown in Fig. 4.1. Ball mill and agitator are suitable for low viscosity systems (*e.g.* inkjet-printable inks), where the ball mill uses grinding media (*e.g.* zirconium, glass and steel balls) to crush the raw pigment, while the agitator exploits impeller blades to shear [311, 313]. High-speed cavitation mixer uses a saw tooth disc that is rotated at high speeds to break up the raw pigment [311, 313]. This technique is suitable for medium viscosity systems (*e.g.* flexographic and gravure printable inks). A modification of this technique is static-rotor mill that has a meshed screen surrounding the saw tooth disc (*e.g.* Silverson shear mixer), which generates additional shear forces. Three-roll mill is suitable for highly viscous systems (*e.g.* screen-printable inks). It consists of a set of cylindrical rolls with precisely controlled gaps to shear the passed through raw pigment [311, 313].

After the pigment is dispersed, a let-down process is implemented to adjust the ink physical properties such that the final ink meets the specifications of the specific printing technology. For example, it may require use of solvents or additives to tune the ink rheological properties.

4.1.3 Ink rheology

For a specific printing technology, the rheological properties are the major consideration of the printability of an ink. Ink rheology is a term that describes how an ink "flows" at different stages of the printing process, more specifically it is a study of the viscosity of a fluid over shear strain and shear time [321, 322]. Therefore, the rheology is directly related to the performance of the ink on the printing press, *i.e.* its ability of transferring from roll to roll and subsequently, onto the substrates [311, 313].

Figure 4.2(a) presents a schematic figure showing the rheological properties of a fluid, *i.e.* the relationship between shear stress and shear rate. *Newtonian* fluid has a linear shear stress/shear rate relationship, meaning that the fluid viscosity (defined as the ratio of shear stress to shear rate) is constant. *Newtonian* fluid is an ideal fluid and in practice, no fluid behaves entirely as *Newtonian* fluid [311, 322, 323]. Indeed, a fluid usually shows some level of deviation from the *Newtonian* behaviour, typically behaving as *pseudoplastic* fluid (shear thinning) or *dilatant* fluid (shear thickening) [311, 322, 323]. *Pseudoplastic*

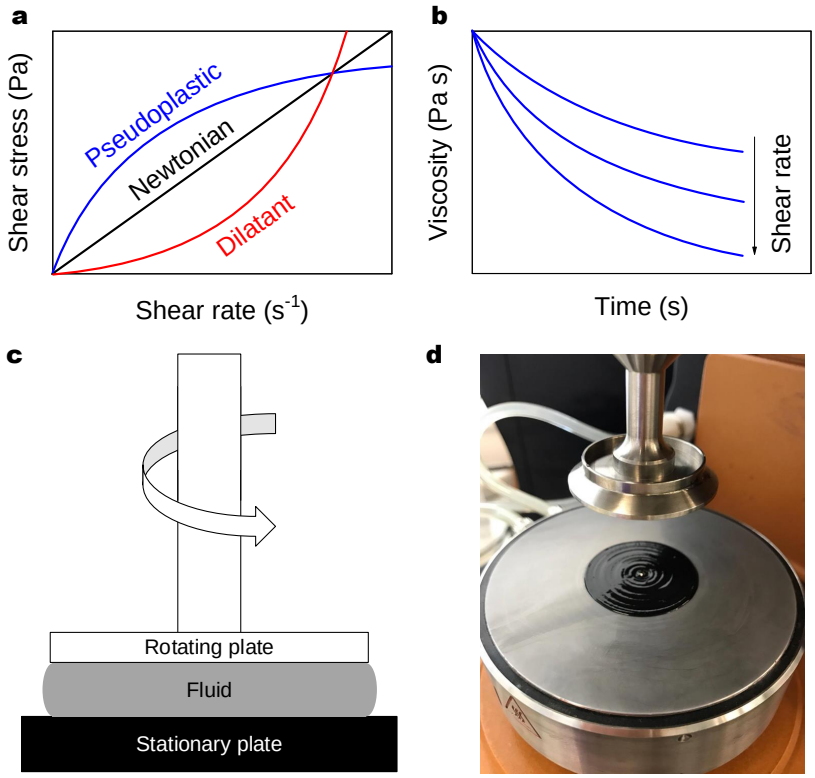

Fig. 4.2 (a) Typical shear stress with respect to shear rate; (b) Time-dependent ink viscosity under shear; (c) Schematic parallel plate viscometer, and (d) photograph of a parallel plate set-up.

fluid shows reduced shear stress under increased shear rate, meaning the ink requires less force to maintain flow at higher shear rates, observed as a drop in viscosity. Typically, *pseudoplastic* behaviour is desired for ink rheology as it allows the ink to flow through the printing press (high shear rate) but prevents the ink to overspread on the substrate (shear rate 0). On the contrary, *dilatant* fluid shows increased viscosity under shear, which is not a preferred ink rheology. *Dilatant* fluid is usually highly concentrated suspensions in a colloidal form [311, 322, 323].

Figure 4.2(b) schematically plots the time-dependent rheological properties of an ink, *i.e. pseudoplastic* fluid. This shows that an ink shear thins over time under a constant shear rate, and the ink viscosity can gradually recover once the shear is removed [311, 322, 323]. Such behaviour is not only desired for ink printing but also ink formulation, as this means that the ink pigment is more readily mixed into the varnish under longer shear.

Typical characterisation methods of ink rheology include capillary viscometer, flow cup, falling sphere viscometer, coaxial rotational viscometer and parallel plate viscometer [311, 313, 322, 323]. Among these methods, parallel plate viscometer is widely used. As shown

in Fig. 4.2(c,d), during measurement, an ink fluid is loaded between two parallel plates, of which one is free to rotate. Upon shear, the shear stress of the ink fluid is measured with respect to shear rate or time.

4.2 Graphics printing technologies

The Johannes Guttenberg metallic moveable printing press have led to various graphics printing technologies, hallmarked by the evolution from rigid to flexible substrates, cm^2 to m^2, and sheet-to-sheet to roll-to-roll (R2R) [25]. The most widely used technologies today include analogue flexographic, gravure and screen printing, and digital inkjet printing. Besides the ink rheological properties (Table 4.1), these technologies differ in printing speed, wet film thickness and printing resolution (*i.e.* printing line width), as listed in Table 4.2.

Table 4.2 Typical printing features of graphics printing technologies. The data is collected from Ref. [19, 20, 62, 313, 316, 317, 319].

Process	Printing speed (m min^{-1})	Wet film thickness (μm)	Resolution (μm)
Inkjet	10	$\ll$1	50
Flexographic	500	3	200
Gravure	1,000	7	100
Screen	30	10-30	100

4.2.1 Flexographic printing

Figure 4.3(a) is a schematic figure of typical flexographic printing process [311, 313, 315]. As shown, a flexographic printing system consists of an ink trough with a "doctor blade", a screened "anilox inking roll", a "printing plate" with soft-relief, and an "impression roll". The soft-relief (*i.e.* printing pattern area) stands out of the printing plate as opposed to being "flat" on the plate. During printing, the anilox roll is rolled through the ink trough and as such the ink fills the engraved cells on the anilox roll. The excessive ink is scraped by the doctor blade. The ink is then transferred to the relief of the printing plate until it is transferred onto the final substrate.

The ink used in the flexographic printing process is usually of a medium viscosity (1,000-2,000 mPa·s; Table 4.1). Due to this R2R feeding system, flexographic printing delivers a printing speed of up to 500 m per minute and hence, low boiling point solvents are used to allow a rapid ink drying. As flexographic printing utilises a relief process, it is incapable of

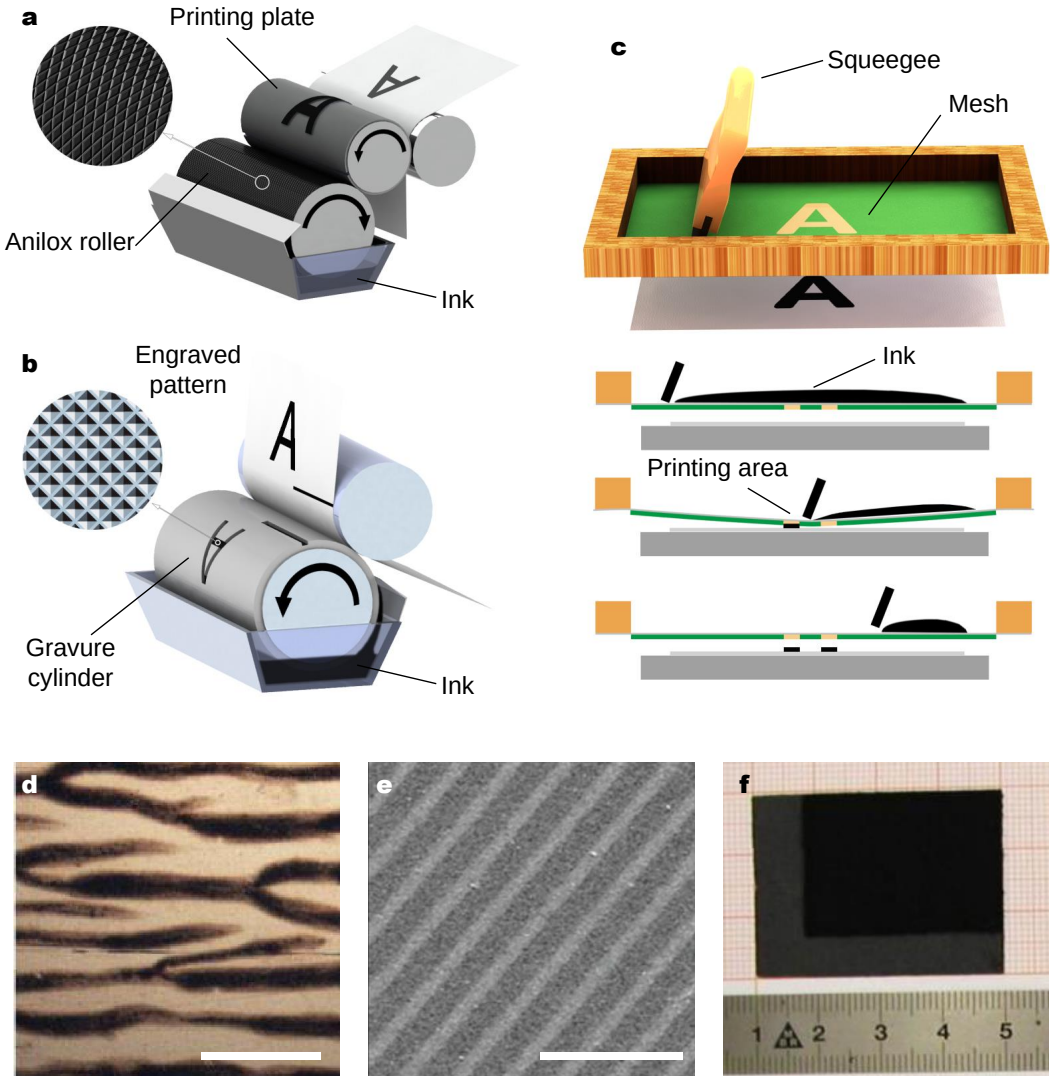

Fig. 4.3 Schematic figures of (a) flexographic printing, (b) gravure printing and (c) screen printing; (d) Optical micrograph of flexographic-printed graphene on ITO, scale bar 100 µm [45]; (e) Large-area scanning electron micrograph of gravure-printed graphene lines on Kapton, scale bar 0.5 mm [46]; (f) Photograph of screen-printed graphene/polyaniline on carbon fabric [324].

depositing a dense layer. It deposits a wet film thickness of ∼3 µm. The printing resolution is typically 200 µm.

By incorporating conductive pigments such as silver nanoparticles into the inks, flexographic printing has been used to print electrodes and contacts [36, 325, 326]. For example, Vena *et al.* demonstrated paper-based chipless radio-frequency identification (RFID) tags using flexographic-printed silver [36]. Flexographic printing of 2d materials was first reported by Baker *et al.* in 2014; Fig. 4.3(d) [45]. The authors developed a graphene/sodium

carboxymethylcellulose (Na-CMC) ink which could be flexographic-printed to fabricate counter-electrodes for photovoltaics, in replacement of expensive platinum with a low loss in efficiency.

4.2.2 Gravure printing

Figure 4.3(b) presents a typical gravure printing process [311, 313, 315–317]. Similar to flexographic printing, a gravure printing system consists of an ink trough with a doctor blade, a metal gravure cylinder and a rubber-covered impression roll. Unlike flexographic printing, the desired pattern is engraved into the metal gravure cylinder. During printing, the gravure cylinder is rolled through the ink trough and as such the ink fills the engraved cells. The excessive ink is scraped by the doctor blade. The ink is then transferred to the target substrate by passing the substrate through the gravure cylinder and the impression roll.

The ink used for gravure printing usually has a medium viscosity (100-1,000 mPa·s; Table 4.1). Also, due to the R2R feeding system, gravure printing delivers a printing speed up to 1,000 m per minute and hence, low boiling point solvents are also required to allow rapid ink drying. As gravure printing use deep-etched engraved cells, it is capable of delivering denser layers, with a wet thickness of $\sim$7 µm. The printing resolution is typically 100 µm.

Similar to flexographic printing, gravure printing of conductive pigments (*e.g.* silver nanoparticles, indium tin oxide (ITO) and semiconducting polymer PEDOT:PSS) have been used to fabricate electrodes and contacts [319, 326–331]. The gravure-printed conductive films can be exploited in areas such as photovoltaic applications. There are also demonstrations of gravure-printed transistors [332–334]. Gravure printing of 2d materials was first reported by Secor *et al.* in 2014; Fig. 4.3(e) [46]. The authors developed a graphene/ethyl cellulose (EC) ink which supported large-area sub-100 µm pattering of graphene on rigid and flexible substrates. The printed graphene exhibited an electrical conductivity of up to 10,000 Sm^{-1} after the binder, EC, was decomposed *via* annealing.

4.2.3 Screen printing

Figure 4.3(c) is a schematic figure of a typical flat-bed screen printing process [19, 311, 313–315, 320]. As shown, screen printing is essentially a stencil process. During printing, the ink is first spread over the screen mesh. A squeegee is then drawn across it, forcing the ink through the open pores of the mesh. At the same time, the substrate is held in contact with the screen to complete the ink transfer.

Unlike the other printing technologies, screen printing requires highly viscous (1-10 Pa·s), non-volatile inks. This high viscosity prevents the ink from flowing through the open pores

prior to printing. The low volatility allows for a long dwell time on the screen (*i.e.* the time between spreading and printing of the ink), avoiding ink drying in the pores and clogging up the mesh. Screen printing is capable of delivering a highly dense printing layer, with a wet film thickness of ∼10-30 µm. Compared to R2R flexographic and gravure, the printing speed of screen printing is much lower, typically ∼30 m per minute. The printing resolution is typically 100 µm. On the basis of the flat-bed screen printing process, R2R screen press was developed to increase the printing speed. It uses a rotary screen mesh roll whereby the ink is loaded inside and forced out to deposit on the substrate in contact with the rotary screen.

A wide range of functional organic and inorganic materials have been adapted to screen printing for device fabrication. One major application is solar cells, where screen-printed films are exploited as the counter-electrode [319, 335–338]. Other common applications include capacitive touchpads [339], organic transistors [340], diabetic glucose strips [341] and financial transaction cards [342]. Screen printing of 2d materials was first demonstrated by Xu *et al.* in 2013; Fig. 4.3(f) [324]. The authors exploited screen-printed graphene/polyaniline as the electrode for supercapacitors, which exhibited an specific capacitance of up to 250 F g^{-1} and an energy density of up to 85.6 Wh kg^{-1}.

4.2.4 Inkjet printing

Inkjet printing is a digital, non-impact printing technique where the ink droplets are propelled from an ink reservoir and deposited in a rapid succession onto the substrate to generate a designed image [23, 24, 28, 37, 62, 311, 343–346]. “Digital” means that the printing pattern is designed electronically, and the deposition of the ink droplets is precisely controlled by computer. Figure 4.4 present the schematic figures of the two droplet jetting mechanisms: continuous inkjet (CIJ) and drop-on-demand inkjet (DOD).

CIJ is a process where a stream of droplets is continuously generated and propelled out of the ink reservoir, as shown in Fig. 4.4(a). The size and frequency of the droplets are controlled by regulating the pressure applied to the ink within the reservoir. Typically, this is done by applying a high-frequency alternating voltage to a piezoelectric material that is in contact with the ink. The droplets then pass through an electrostatic field, such that the individual droplets are either charged or not charged. The droplets are then subjected to an electrostatic field and as such, the charged droplets are selectively deflected to deposit onto substrate while the uncharged ones are collected by the ink receiver.

DOD is a process where the ink droplets are only generated and jetted when demanded. As shown in Fig. 4.4(b,c), the ink droplets are generated either through a piezoelectric inkjet process or a thermal inkjet process. In a piezoelectric inkjet process, a voltage pulse is applied to the piezoelectric material to generate a shape change of the reservoir and hence, a

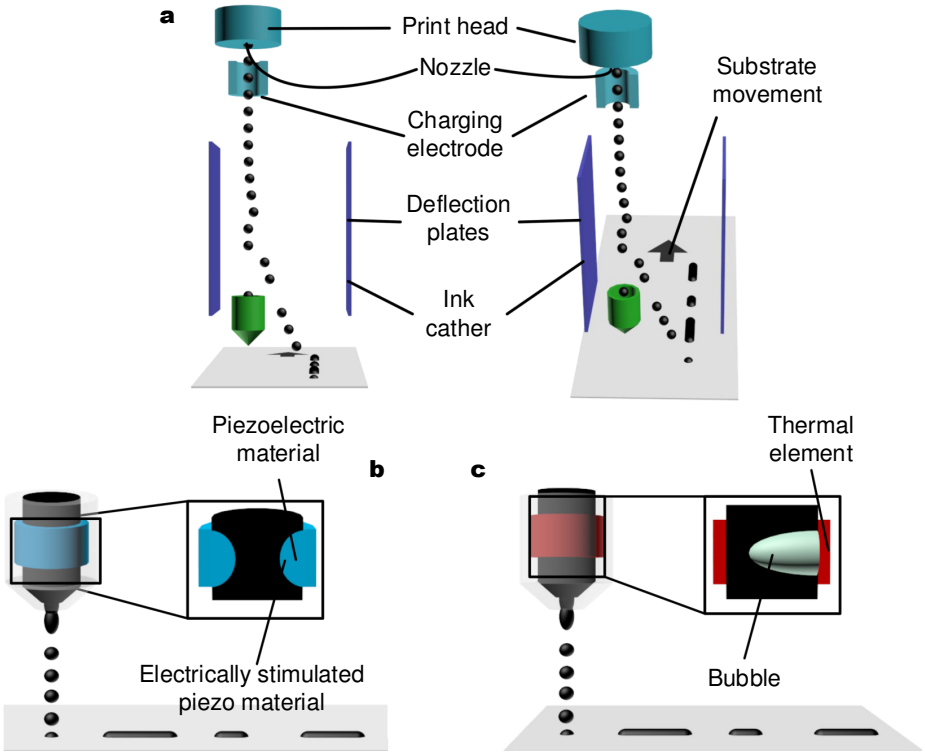

Fig. 4.4 Schematic figures of (a) continuous inkjet printing, (b) drop-on-demand inkjet printing with piezoelectric head and (c) drop-on-demand inkjet printing with thermal head.

pressure pulse on the ink that forces it out of the ink reservoir as ink droplets. In a thermal inkjet process, the ink is rapidly heated up to generate bubbles in the ink. The bubbles propel the ink out of the ink reservoir as ink droplets. The jetted ink droplets then impact, spread, merge and dry on the substrate to form a designed image.

Inkjet printing offers several advantages over analogue flexographic, gravure and screen printing: (1) Because the jetted droplets usually have a low volume of 1-100 pL, inkjet printing achieves a higher resolution, typically ~50 μm [23, 62, 346]; (2) As the printing pattern is digitally defined, there is no need to design physical mask for the inkjet printing image. Inkjet printing is therefore much more flexible, and time and cost saving, particularly during prototyping [24]; (3) Unlike the other printing technologies, inkjet printing is a low loading, low viscosity ink printing process, and it does not require a large amount ink for printing trials. These features make it particularly suitable for prototyping [24], for instance the as-produced UALPE 2d material dispersions are readily adapted to inkjet printing for prototyping [16, 37, 39–42, 48]. However, because the inkjet printing head needs to scan over the substrate to deposit ink droplets, inkjet printing suffers from a low printing speed, typically 10 m per min [320].

Among these two inkjet printing technologies, CIJ offers a number of advantages over its counterpart DOD: it allows a higher jetting speed and hence, a more rapid printing, and the use of volatile inks more readily as there is less risk of nozzle clogging resulting from ink drying. However, the complexity of CIJ (*e.g.* control of droplet jetting, deflecting and recycling) has limited the application of CIJ. Therefore, DOD inkjet printing is the main technology employed in my doctoral work. I then discuss its printing principles in Section 4.3.

4.3 Inkjet printing principles

4.3.1 Stable droplet jetting

A key requirement of inkjet printing is the generation of a stable droplet jetting, *i.e.* a single droplet generation and jetting under each electrical impulse without the formation of satellite droplets (*i.e.* secondary droplets), as shown in Fig. 4.5(a). An unstable jetting may lead to deviation from the droplet jetting trajectory or even deposition onto untargeted areas [23, 24, 37, 62, 346, 347].

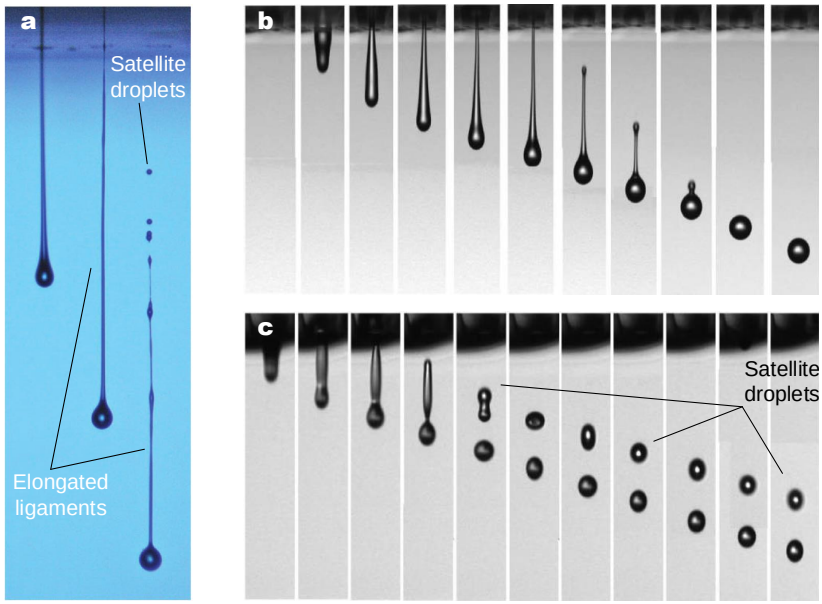

Fig. 4.5 (a) High-speed micrographs of three jetted droplets at different jetting stages, showing elongated ligaments break up into satellite droplets [348]; High-speed micrographs of droplet jetting sequence for (b) stable jetting when Z is 2.2, and (c) jetting with satellite droplets when Z is 17.3 [347]

The droplet jetting behaviour is defined by the ink fluidic properties, which are characterised by the following dimensionless numbers, including Reynolds (*Re*), Weber (*We*) and Ohnesorge (*Oh*) numbers [37, 62, 346]:

$$Re = \frac{\upsilon \rho a}{\eta} \tag{4.1}$$

$$We = \frac{\upsilon^2 \rho a}{\gamma} \tag{4.2}$$

$$Oh = \frac{\sqrt{We}}{Re} = \frac{\eta}{\sqrt{\gamma \rho a}} \tag{4.3}$$

where η, γ and ρ are the viscosity (mPa·s), surface tension (mNm^{-1}) and density (gcm^{-3}) of the ink, respectively, υ is the ejection velocity (ms^{-1}) of the droplet, and a is the diameter (μm) of the jetting nozzle.

Fromm suggested the use of the inverse Ohnesorge number, $Z = 1/Oh$, to determine whether an ink could form a stable jetting [349]. As a rule of thumb, it is commonly accepted that Z should be <14 to avoid formation of satellite droplets [37, 62, 346, 347]. Meanwhile, Z should be >1 to avoid elongated ligaments, which may also break up into satellite droplets [37, 62, 346, 347]. Figure 4.5(b) is a demonstration of stable droplet jetting when Z is within 1-14, while Fig. 4.5(c) shows generation of satellite droplets when Z is over 14. The above investigation allows the generation of a *Re* and *We* map (Fig. 4.6), defining the optimal value region of *Re* and *We* for stable droplet jetting.

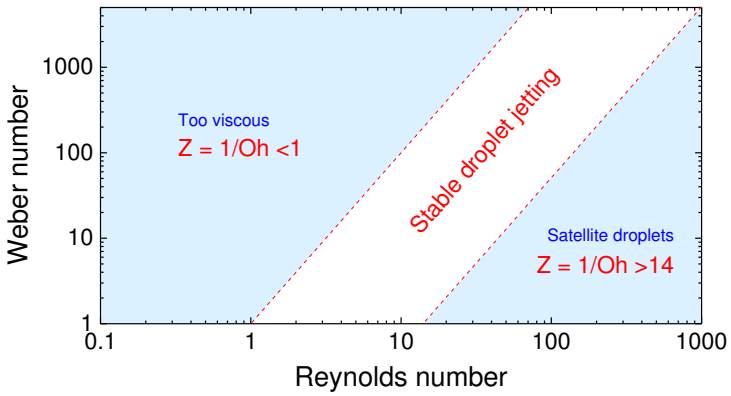

Fig. 4.6 Map of Reynolds and Weber numbers, showing the optimal region of inverse Ohnesorge number (1-14) for stable droplet jetting, adapted from Ref. [346].

4.3.2 Droplet impact and spreading

Following the impact of a droplet on a substrate, subsequent ink spreading and drying define the printed image and morphology. Here I discuss the spreading process, while the drying process is discussed in Section 4.3.3. Figure 4.7 presents the spreading behaviour of a droplet on a substrate. Since the droplet is typically 1-100 pL with low density, the gravitational forces can typically be neglected after the impact [346]. The dominant forces are therefore the inertial and capillary. It was suggested that the spreading after impact can be divided into two stages: the impact driven stage and the capillary driven stage. The impact driven stage is the spreading process immediately after the impact, where the inertial force dominates. This stage leads to a maximum spreading of the droplet until the capillary driven stage, where the capillary force dominates. The capillary driven stage is further divided into two situations depending on the interaction between the droplet and the substrate.

As a rule of thumb, wetting of the substrate requires the surface tension of the ink to be 7-10 mNm^{-1} lower than the substrate surface energy [350]. For the ink that wets, the droplet continues a capillary spreading [350, 351]. For the ink with insufficient wettability, the droplet retracts, leading to discontinuous deposition [350, 351]. Therefore, to ensure a continuous printing feature, the ink surface tension therefore should be sufficiently low.

Provided that the ink can wet the substrate, the impingement of a droplet onto a pre-defined pattern needs to be controlled in a way that it does not cause neither overspreading nor insufficient merging [352]. Figure 4.8(a) schematically illustrates a droplet impinging onto a printed line with different droplet spacing D. When D is excessively small, the droplet impinges on the bead of the line and expands around the bead rather than forms its own

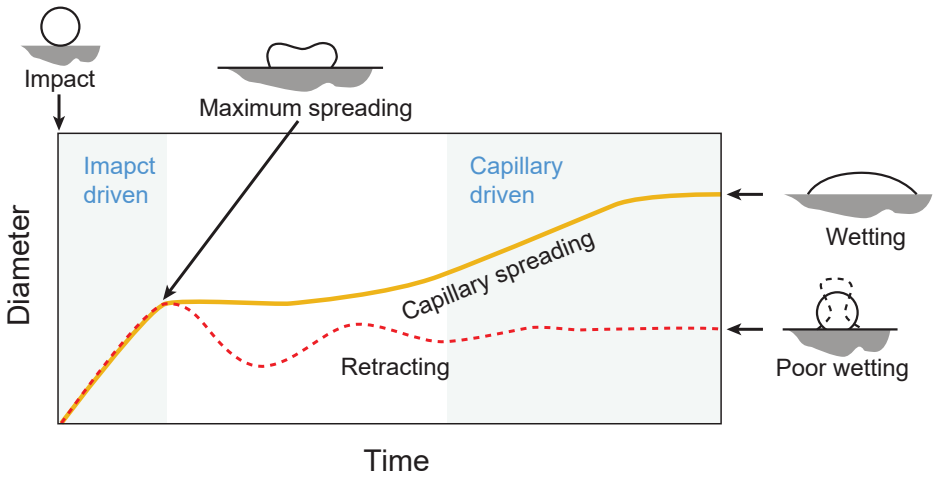

Fig. 4.7 Schematic figure showing the spreading of a droplet after it impacts on a substrate, adapted from Ref. [346].

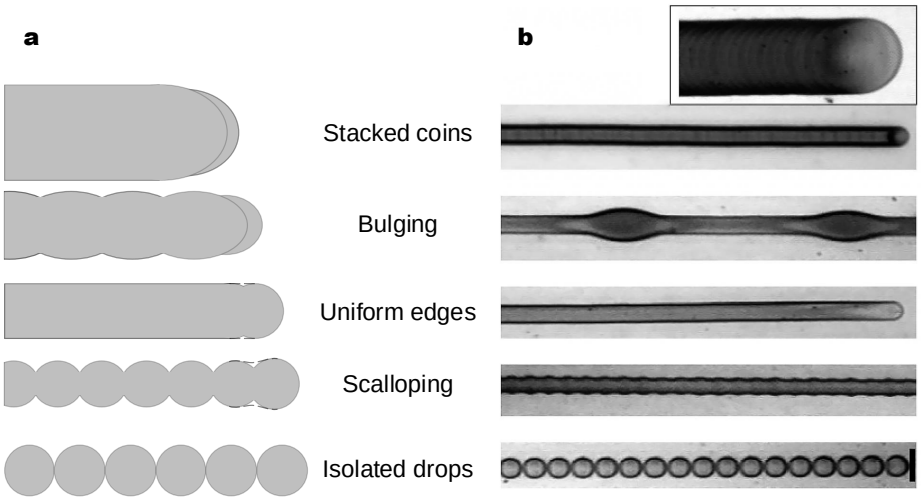

Fig. 4.8 (a) Schematic figure for droplets impinged onto a printed line, showing the formation of different morphologies of printed structures. The dashed lines indicate the contact lines; (b) Photographs showing different printed morphologies [352].

contact line, leading to "stacked coins" or "bulging" [352]. When D is excessively large, the merging of the droplet with the bead is insufficient, forming "scalloping" or even "isolated droplets" [352]. When D is between these two extremes, the droplet merges with the bead and forms contact lines with "uniform edges", the optimal morphology.

Figure 4.9(a) is schematic geometry of a droplet deposited onto a substrate [352]. This geometry is defined by the following relation:

$$\begin{aligned} V_{drop} &= \frac{2}{3}\pi R_0^3 f(\theta) \\ R_0 &= \sqrt[3]{\frac{3V_{drop}}{2\pi f(\theta)}} \end{aligned} \tag{4.4}$$

where V_{drop} and R_{drop} are the volume and radius of a falling droplet, R_0 is the radius of a deposited droplet, and $f(\theta)$ is a contact angle factor to correct the cross-sectional area of the formed half-sphere. Figure 4.9(b) is schematic geometry of a printed line with uniform edges, which is expressed by the following relation [352]:

$$\begin{aligned} \frac{V_{drop}}{D} &= \frac{1}{2}\pi R_1^2 f(\theta') \\ R_1 &= \sqrt{\frac{2V_{drop}}{\pi D f(\theta')}} \end{aligned} \tag{4.5}$$

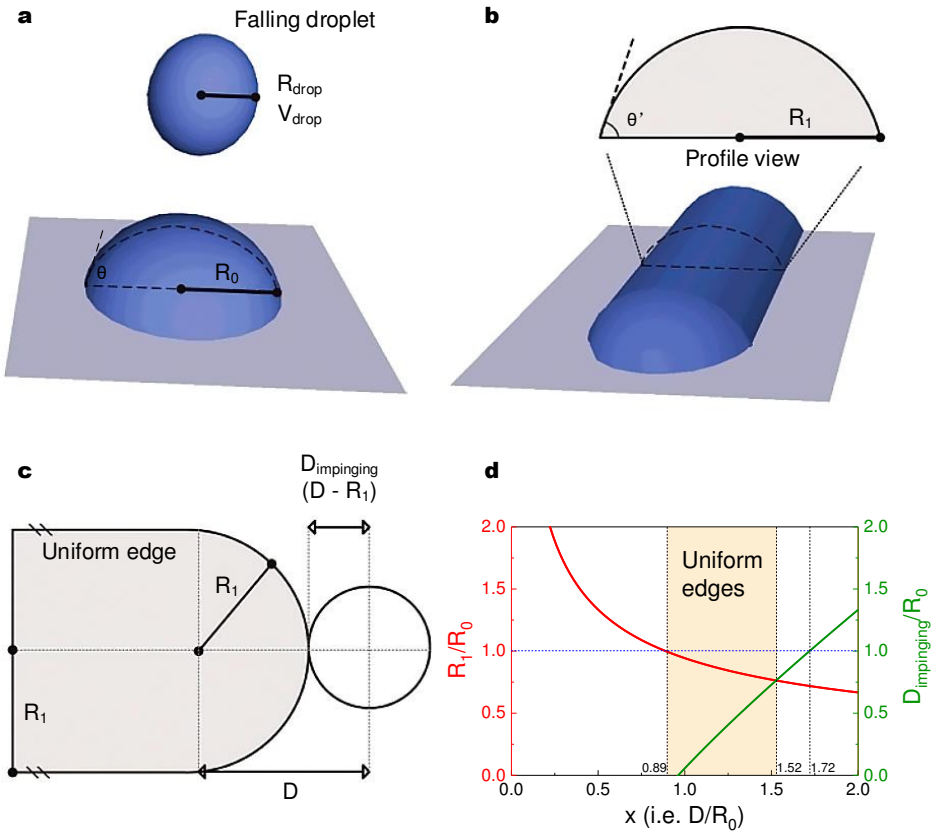

Fig. 4.9 Schematic figures showing (a) geometry of an individual droplet, (b) geometry of a printed line with uniform edges, and (c) impinging droplet contact lines; (d) Plot of Eq. 4.9. Adapted from Ref. [352].

where R_1 is the radius of a printed line with uniform edges, and $f(\theta')$ is a contact angle factor to correct the cross-sectional area of the half-cylinder. Therefore, the relationship between R_0 and R_1 is:

$$\frac{R_1}{R_0} = \sqrt{\frac{4}{3\frac{D}{R_0}}\frac{f(\theta)}{f(\theta')}} = \sqrt{\frac{4}{3x}\frac{f(\theta)}{f(\theta')}} \tag{4.6}$$

where x stands for D/R_0. Figure 4.9(c) schematically depicts a droplet impinging onto the bead of a printed line with a droplet spacing D. Therefore, the impinging distance is defined as [352]:

$$D_{impinging} = D - R_1 \tag{4.7}$$

Therefore, the relationship between D, R_0 and $D_{\text{impinging}}$ is:

$$\frac{D_{impinging}}{R_0} = \frac{D}{R_0} - \frac{R_1}{R_0} = x - \sqrt{\frac{4}{3x}\frac{f(\theta)}{f(\theta')}} \tag{4.8}$$

Soltman *et al.* experimentally estimated $f(\theta)$ and $f(\theta')$ for a PEDOT/PSS aqueous ink, which were 0.568 and 0.852, respectively [352]. Therefore, Eq. 4.6 and Eq. 4.8 are expressed as:

$$\begin{aligned} \frac{R_1}{R_0} &= \sqrt{\frac{0.89}{x}} \\ \frac{D_{impinging}}{R_0} &= x - \sqrt{\frac{0.89}{x}} \end{aligned} \tag{4.9}$$

Equation 4.9 is plotted as Fig. 4.9(d). When $D < R_1$, the droplet impinges directly onto the bead of the printed line rather than expands its own contact lines, leading to an ink overspreading. In this case, $x < 0.89$. When $R_1 = D_{\text{impinging}}$, the impingement reaches a critical point where the droplet exactly lands on the edge of the line bead, and over which the merging of the droplet with the bead will be insufficient. In this case, $x > 1.52$. However, when $D_{\text{impinging}} > D$, the droplet starts to separate from the printed line (x is 1.72). In the end, when $D = 2R_0$, printing forms individual isolated droplets. Therefore, for this PEDOT/PSS aqueous ink the droplet spacing should be 0.89-1.52 of the deposited droplet diameter to ensure a uniform edge morphology of printed patterns. Values for uniform edges have also been found in a similar range for other ink systems [353].

4.3.3 Coffee ring effect

Figure 4.10(a) schematically presents the typical cross-sectional profiles of printed lines. A rectangular shape is desired as this represents a uniform deposition of material and hence, a uniform morphology across the printed structure [20]. However, this usually happens in the case of viscous inks, such as screen-printable inks. For inkjet-printable ink which is of low viscosity, an ideal cross-sectional profile is most likely be represented by a semicircular arc. A common profile, however, is the coffee-ring shape. Depending on the ink viscosity, wetting of the substrate and the solvent vaporisation uniformity, drying an inkjet-printable ink may form a concave central area, as exampled in Fig. 4.10(b).

Indeed, the coffee ring effect is a common phenomenon related to dispersion drying processes [60, 61]. Deegan *et al.* proposed that the coffee ring effect arose from an unbalanced fluid flow caused during the drying process [60, 61]. As presented in Fig. 4.10(b), the deposited droplet first forms contact lines at the droplet-substrate interface upon drying. The higher surface area to volume ratio at the contact edges causes a more rapid solvent evaporation than in the droplet centre. This leads to an outward solvent flow from the droplet centre to the edges to replenish the evaporated solvents [60, 61]. This flow carries the dispersed material to the droplet edges. With no inward flow, the material is deposited at

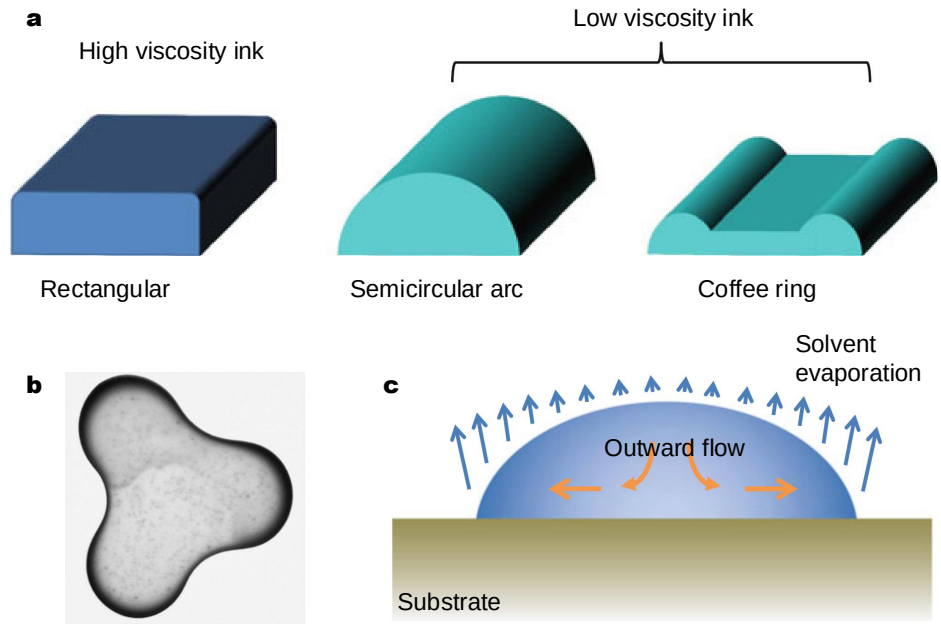

Fig. 4.10 (a) Typical cross-sectional view of printed line [20]; (b) Photograph of a coffee drop [60]; (c) Mechanism of the coffee ring effect, adapted from Ref. [20].

the edges. This not only forms a material ring, but also prevents the droplet from receding further, leaving little to no material deposited at the centre of the dried droplet.

One promising way to overcome this is to induce a secondary inward flow to balance the evaporation-induced outward flow. Preceding studies show that creating a solvent composition variation across the droplet may give rise to a surface tension driven (Marangoni) recirculating flow [24, 354–358]. For example, in an ink composed of a binary solvent mixture, the differing solvent properties can lead to variations in the solvent proportions across the droplet during drying, such that a surface tension gradient is generated to drive a recirculating Marangoni flow. Figure 4.11(a) is a schematic kinetic solvent drying figure of a binary solvent ink of 6,13-bis((triisopropylsilylethynyl) pentacene (TIPS_PEN) [354]. The ink solvents were consisted of chlorobenzene (CB; boiling point 131°C, surface tension 33.6 mNm^{-1}) and dodecane (boiling point 216°C, surface tension 25.3 mNm^{-1}). The authors, Lim *et al.*, proposed that upon drying the droplet centre would be concentrated with CB and the droplet edges would be concentrated with dodecane since CB would evaporate faster from the edges. A combination of the surface tension gradient of these two solvents and the surface tension gradient generated by the latent heat of vapourisation drove the formation of a recirculating Marangoni flow [355–357]. This recirculating Marangoni flow redistributed TIPS_PEN back to the droplet centre, rendering a significantly improved

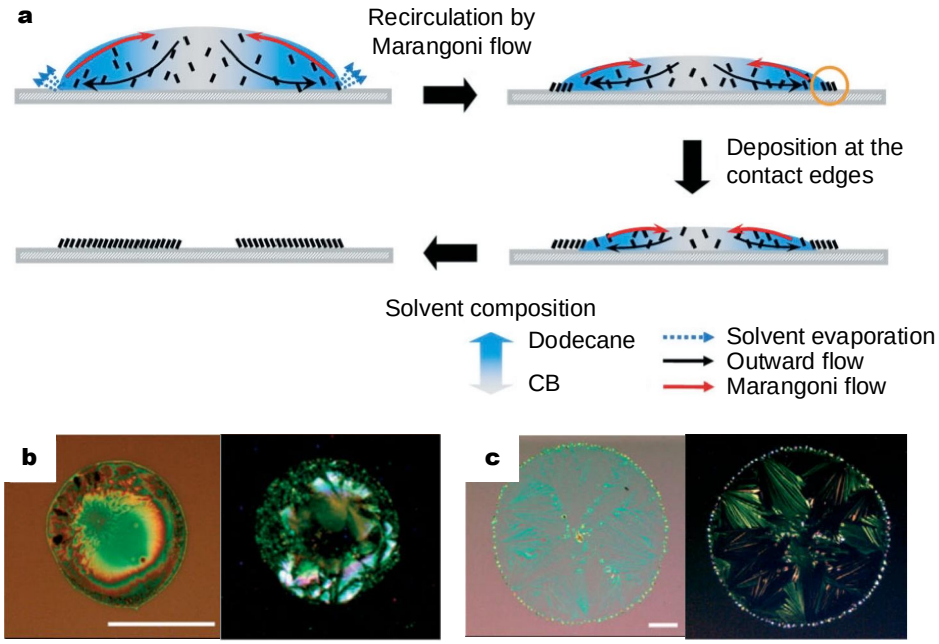

Fig. 4.11 (a) Suppression of the coffee ring effect *via* Marangoni flow, adapted from Ref. [354]; Optical micrographs of inkjet-printed TIPS_PEN droplets in (b) chlorobenzene and (c) mixture of chlorobenzene and dodecane [354].

deposition uniformity, as shown in Fig. 4.11(b,c). In addition, a faster ink drying can also reduce the coffee ring effect [351].

4.4 Inkjet printing of 2d materials

Since the demonstration of inkjet-printed transistors from UALPE graphene [37], there is a great momentum of developing inkjet-printable 2d material inks and applications. Indeed, there has been much progress made in ink formulation and device fabrication. Here I review the current ink formulations, and the challenges presented by these inks for large-scale device printing.

4.4.1 Current 2d material ink formulations

Current 2d material inks for inkjet printing can be generally categorised into three types: pure solvent inks (*i.e.* the as-produced UALPE dispersions in pure solvents), surfactant inks (*i.e.* the as-produced UALPE dispersions with surfactants), and binder inks (*i.e.* exfoliated 2d materials formulated into inks with the addition of polymers). Table 4.3 lists the demonstrated ink formulations and applications enabled by them.

Table 4.3 Current inkjet-printable 2d material inks and their applications.

Inks	Substrates	Treatment	Applications	Ref.
Pure solvent inks				
Graphene NMP	Si/SiO_2; Glass	HMDS; O_2 170°C	Transistor	[37]
Graphene water/ethanol	PET	–	Conductor	[38]
Graphene water/ethanol	Si/SiO_2	–	SA	[39]
Graphene/MoS_2 NMP	Coated PET	200°C	Photodetector	[40]
Graphene/TMDs/*h*-BN NMP	Si/SiO_2	–	Transistor Photodetector	[41]
Graphene/TMDs/*h*-BN NMP	Coated PET	–	Transistor	[42]
Surfactant inks				
Graphene/SDBS/PANI	Carbon	80°C	Electrode	[47]
Graphene/TMDs/PS1	Si/SiO_2	300°C	Photodetector ROM	[48]
Binder inks				
Graphene/EC	Si/SiO_2; Glass	400°C	Transistor	[50]
Graphene/EC	Si/SiO_2; Kapton	up to 450°C	Conductor	[51]
Graphene/Plasdone S-630	Paper	–	Conductor	[52]
Graphene/EC	PET; PEN; PI; Glass	HMDS Pulsed light up to 300°C	Conductor	[53]
Graphene/NC	Glass; Kapton	350°C	Conductor	[54]
Graphene/EC	Si/SiO_2	>400°C	Conductor	[55]
MoS_2/EC	Si/SiO_2	HMDS 450°C	Transistor	[56]

Generally, UALPE dispersions have a viscosity of ∼2 mPa·s with flake dimension of <1 µm, making the dispersions readily deposited with low viscosity printing and coating technologies for device fabrication, in particular inkjet printing [16, 17, 37, 40–42]. This led to the demonstration of inkjet-printed graphene transistors [37]. The authors Torrisi *et al.* used directly the UALPE dispersion of graphene in N-Methyl-2-pyrrolidone (NMP) as a pure solvent ink for inkjet printing [37]. This method was later extended to other 2d materials, including transition metal dichalcogenides (TMDs; *e.g.* MoS_2, WS_2, WSe_2) and hexagonal boron nitride (*h*-BN) [40–42]. However, as discussed in Section 3.3.1, these stable UALPE dispersions are usually produced in high boiling point, toxic organic solvents, such as NMP. This means that printing with the pure solvent inks requires long drying times and excessive careful handling. In addition, these pure solvent inks typically present

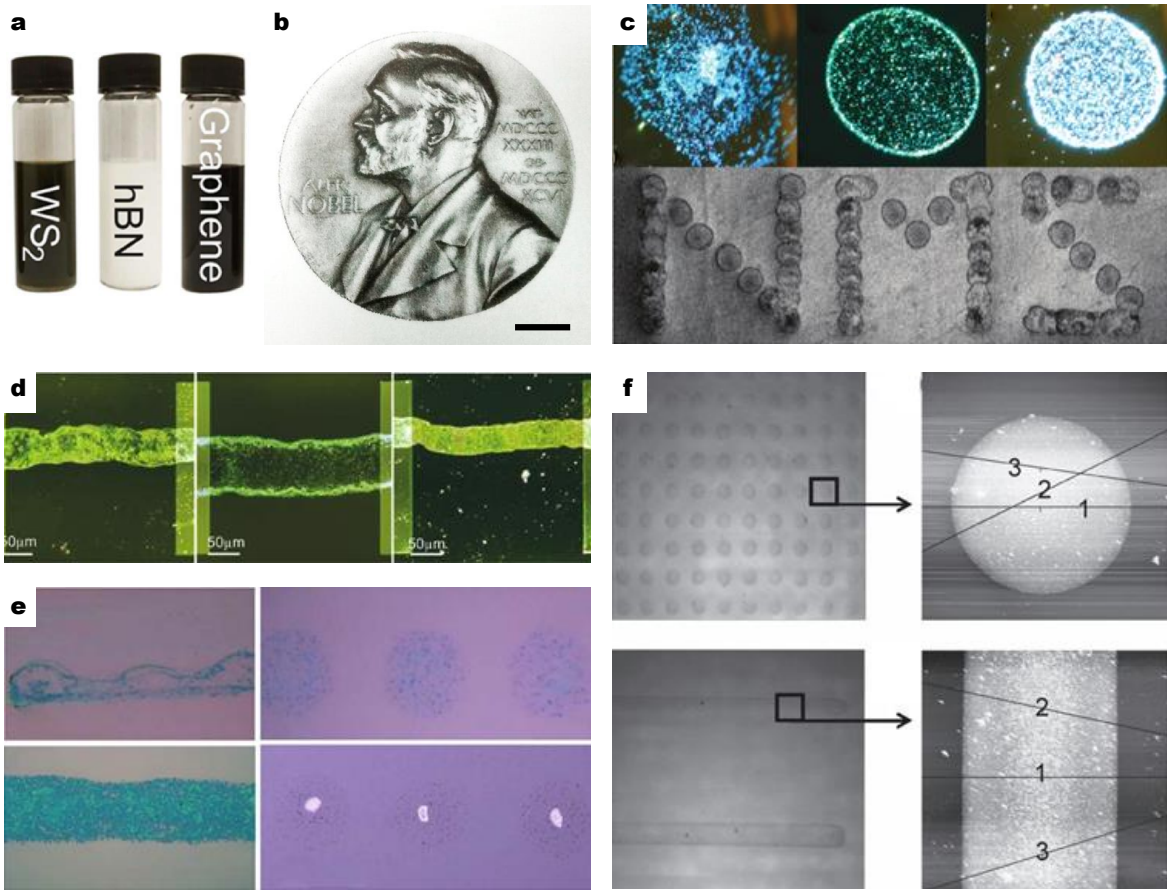

Fig. 4.12 Inkjet printing with current 2d material inks: (a) Photograph of representative NMP inks [41]; (b) Inkjet-printed graphene pattern on paper, scale bar 5 cm [48]; (c) Inkjet-printed droplets of graphene NMP ink on Si/SiO_2 treated with O_2 plasma, untreated Si/SiO_2, Si/SiO_2 treated with HMDS, and paper, respectively [37]; (d) Inkjet-printed lines of graphene NMP ink on Si/SiO_2 treated with O_2 plasma, untreated Si/SiO_2, and Si/SiO_2 treated with HMDS, respectively [37]; (e) Inkjet-printed graphene water/PS1 ink on untreated Si/SiO_2 [48]; (f) Inkjet-printed graphene/EC ink on untreated Si/SiO_2 [50].

challenges for spatially uniform material deposition, as demonstrated in Fig. 4.12(c,d), where the graphene NMP ink delivered uncontrollable depositions with heavy "coffee rings" [37]. Therefore, there is a great interest in developing inks in lower boiling point, non-toxic solvents. One such formulation is adapting directly the UALPE dispersions in water/alcohol to inkjet printing [38, 39]. In particular, the alcohols with a low surface tension are expected to improve the ink wettabilities for improved morphology of the printed films [39].

Though printing with pure solvent inks is preferable as this does not introduce impurities in the dried printed films, there have been attempts in comprising surfactants and polymer binders in ink formulation for improved printed morphologies [16, 17]. For example, Ref. [47, 48] adapted the as-produced UALPE dispersions with surfactants for inkjet printing.

In particular, McManus *et al.* argued that 1-pyrenesulfonic acid sodium salt (PS1) – small molecular surfactant – could lead to improved printed morphologies without compromising the functionalities (*e.g.* electrical conductivity, optoelectronic properties) of the 2d materials [48]. However, Fig. 4.12(e) indicates that the improvements are very limited compared to pure solvent inks (Fig. 4.12(c,d)). Formulating binder inks is a more prevalent and effective approach. This is usually done as follows: (1) extracting the exfoliated 2d materials flakes from UALPE dispersions *via* filtration, sedimentation, solvent exchange, or solvent evaporation; (2) formulating highly concentrated inks by redispersing the extracted flakes in solvents with polymers. The first demonstration of such binder inks was in 2013: graphene produced in dimethylformamide (DMF) was solvent exchanged into ethanol/terpineol and stabilised by ethyl cellulose (EC) [50]. As clearly demonstrated in Fig. 4.12(f), the graphene/EC ink supported highly controllable ink deposition and significantly improved printed morphologies. However, as observed, the ink dried to form a semicircular arc morphology, where the flakes are more concentrated at the central area.

4.4.2 Applications of current 2d material inks

Table 4.3 briefly lists the applications enabled by the current 2d material inks. Here I discuss how the printed 2d materials were exploited in the key applications.

Conductive inks. Printable electronics hold a huge potential to the fields in *e.g.* logic circuits, sensors, photodetectors, flexible displays, RFID, and portable energy storage and conversion [16, 17, 110]. This requires conductive inks to deposit electrical conductors, electrodes and electronic circuits. Currently dominant conductive inks are carbon material inks (which suffer from low conductivity) and metal inks such as silver inks (which require high production cost). Conductive inks are one of the most prevalent applications for solution-processed graphene [110].

Graphene, with good electrical conductivity and high chemical stability, suits this purpose. Indeed, the graphene NMP ink has been exploited for this [37, 40, 42]. However, the measured electrical conductivity of the deposited graphene was poor, for stance Torrisi *et al.* showed a value limited to $\sim$100 Sm^{-1} [37]. This has been significantly improved with other ink formulations. Secor *et al.* demonstrated an electrical conductivity of up to 40,000 Sm^{-1} with a graphene nitrocellulose (NC) ink after NC was decomposed [54]. This conductivity is far greater than that of carbon material inks ($\sim$1,000 Sm^{-1} [359]), however, over 1,000 times smaller than that of metal inks The electrical conductivity of the graphene ink can potentially be further increased by graphene functionalisation [16, 17, 110]. Figure 4.13 is a photograph of representative inkjet-printed graphene circuit pattern on polyimide (PI).

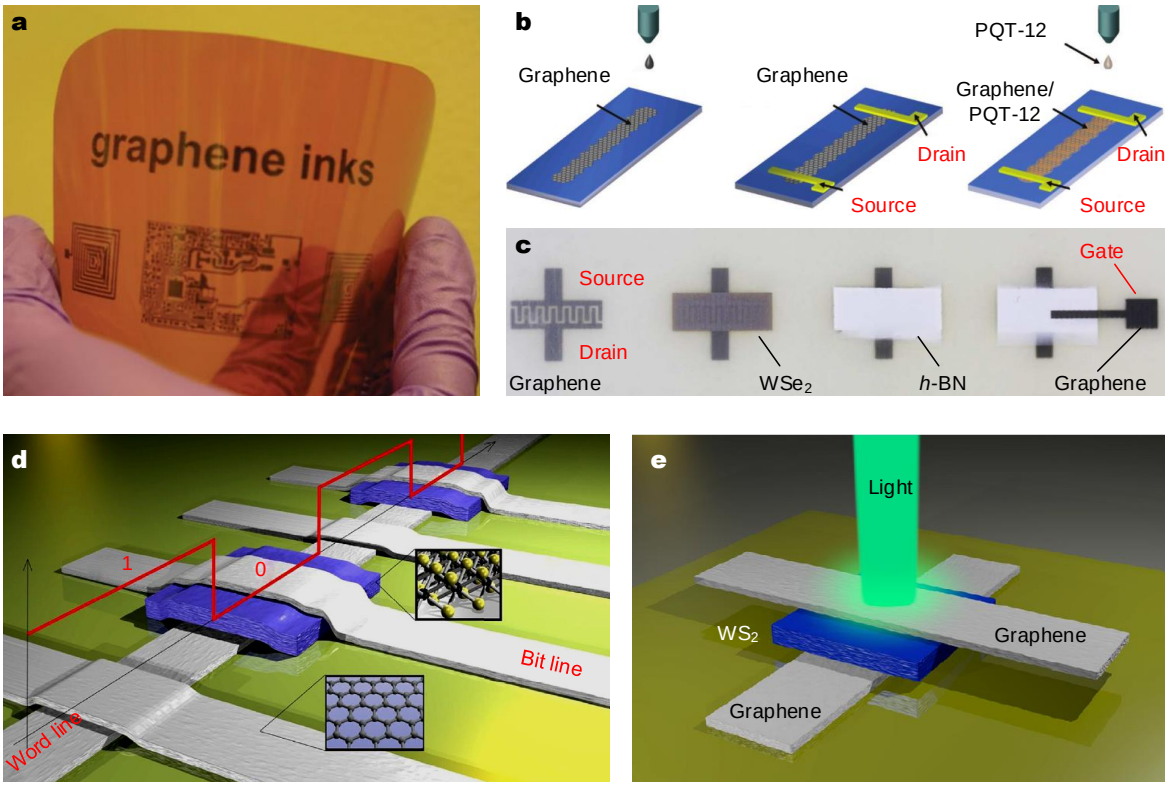

Fig. 4.13 Inkjet-printable applications of current inks: (a) Large-area inkjet-printed graphene circuits on PI [53]; (b) Schematic inkjet-printed graphene transistors on Si/SiO_2 with Cr-Au source/drain contacts [37]; (c) All inkjet-printed transistors on polymer coated PET [42]; (d) Schematic all inkjet-printed read-only memory circuit [48]; (e) Schematic all inkjet-printed photodetector [48].

Electronics. Inkjet-printable electronics from UALPE 2d materials was first demonstrated by Torrisi *et al.* [37]. The authors exploited inkjet-printed graphene as the channel for transistors, as shown in Fig. 4.13(b). The fabricated transistors exhibited a carrier mobility of up to 95 $cm^2V^{-1}s^{-1}$, which is far greater typical than that of printed organic transistors (typically <1 $cm^2V^{-1}s^{-1}$). However, the graphene transistors suffered from a low I_{ON}/I_{OFF}, $\sim$10. The authors then deposited poly[5,50-bis(3-dodecyl-2-thienyl)-2,20-bithiophene] (PQT-12) on top the graphene, and increased the I_{ON}/I_{OFF} to 4×10^5. However, the mobility was decreased to 0.1 $cm^2V^{-1}s^{-1}$. An effective way to increase the I_{ON}/I_{OFF} while retaining the high mobility is still elusive.

Recent advancement focuses on the fabrication of all-inkjet-printed, heterostructure devices through controlled additive pattering of 2d materials differing in materials properties. Figure 4.13(c) is one such demonstration, where inkjet-printed graphene, WSe_2 and *h*-BN were exploited as conductive contacts, channel and insulating separator, respectively [42]. The transistors exhibited a carrier mobility of up to 0.22 $cm^2V^{-1}s^{-1}$ with I_{ON}/I_{OFF} of

up to ∼100. Figure 4.13(d) schematically presents an all-inkjet-printed read-only memory (ROM) based on 2d material junction [48]. As shown, in this device configuration, graphene/WS_2/graphene is interpreted as logic "0", while graphene/graphene is interpreted as logic "1".

Optoelectronics. 2d materials such as semiconducting TMDs exhibit sizeable bandgap that can be exploited in optoelectronics, such as photodetectors [6–8]. Inkjet-printed 2d material photodetector was first demonstrated in 2014 [40]. The device was consisted of inkjet-printed interdigitated graphene electrodes and MoS_2 channel as the active photodetection material. Differently, the photodetector schematically presented in Fig. 4.13(e) exploited graphene/WS_2/graphene junction for photodetection [48]. This device exhibited a photoresponsivity of >1 mAW^{-1}.

4.4.3 Challenges for the current ink formulations

As demonstrated in Fig. 4.12, the pure solvent inks and the surfactant inks (*i.e.* the as-produced UALPE dispersions) present significant challenges for spatially uniform printing. This arises from unstable jetting of ink droplets, poor wetting of the substrates, and the coffee ring effect.

As discussed, inkjet printing requires 1-14 for the inverse Ohnesorge number Z for a stable droplet jetting. I list the Z value of typical UALPE solvents and the current inks, as well the the inks produced by myself, in Table 4.4. As shown, the Z value of the NMP inks and the water/surfactant inks is all >15. This suggests that these inks tend to generate

Table 4.4 Z value of typical UALPE solvents and current 2d material inks.

	Z parameters				Z	Ref.
	η (mPa·s)	γ (mNm^{-1})	ρ (gcm^{-3})	a (μm)		
NMP	1.6	41	1.0	22	19	–
Water	0.9	72	1.0	22	44	–
IPA	2.0	23	0.8	22	10	–
Graphene NMP	1.9	40	1.05	50	24	[37]
NMP inks	–	–	–	–	17	[40]
Water/PS1 inks	–	–	–	–	>20	[48]
Graphene water/IPA	–	–	–	–	12	[39]
NMP inks	2.0	42	1	22	15	This work
Water/SDC inks	0.8	45	1	22	39	This work
Water/IPA inks	2.0	32	0.9	22	13	This work

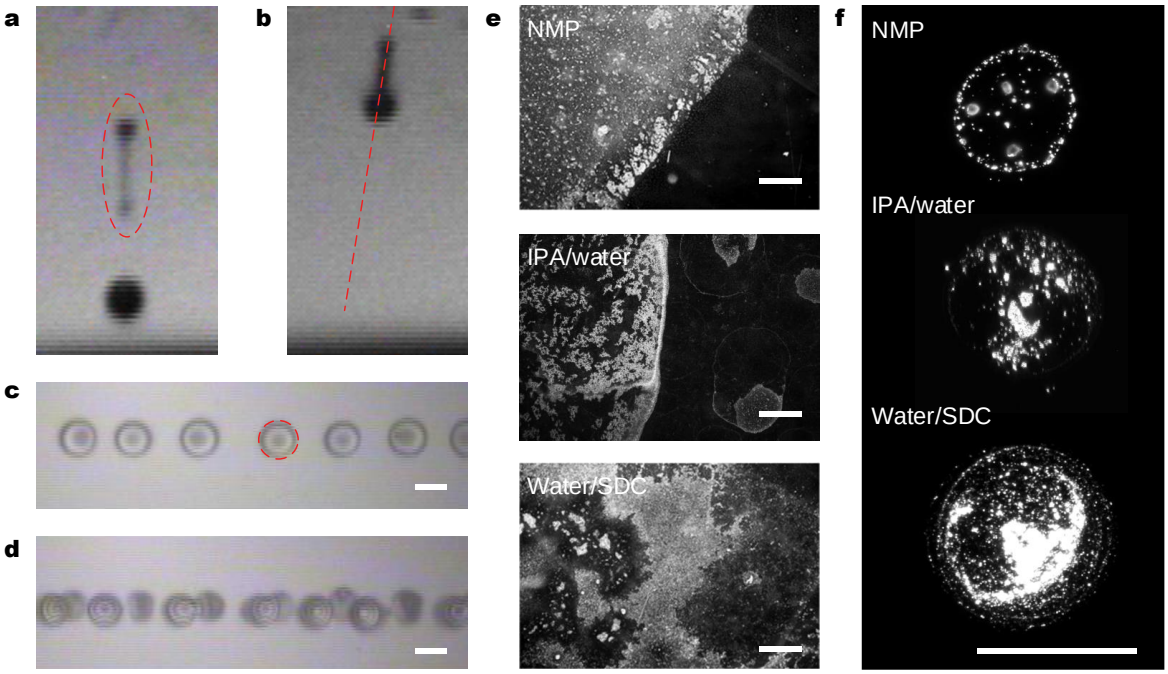

Fig. 4.14 Typical micrographs for the generation of (a) satellite droplet as indicated by the dashed circle, and (b) jetting deviation from the jetting path as indicated by the dashed line, observed through the inkjet printer stroboscopic camera; (c,d) Typical micrographs for printed lines on untreated Si/SiO_2, showing poor wetting and coffee rings indicated by the dashed circle, scale bar 100 µm; (e) Typical dark-field optical micrographs of spray-coated inks on untreated PET (deposition area 3 cm $\times$ 3 cm), scale bar 200 µm; (f) Typical dark-field optical micrographs of inkjet-printed dried droplets ($\sim$10 pL) on untreated Si/SiO_2, scale bar 50 µm. (a-f) are demonstrated with MoS_2 inks.

satellite droplets during printing [37, 62, 346]. Indeed, I observe generation of such satellite droplets with both NMP inks and water/surfactant inks; Fig. 4.14(a). This unstable jetting can even result in jetting deviations from the jetting path, as shown in Fig. 4.14(b), leading to an uncontrollable droplet jetting with the droplets deposited onto untargeted areas. The typical received morphologies from inkjet printing of a straight line (with single and multiple printing repetitions) on untreated Si/SiO_2 as presented in Fig. 4.14(c,d) demonstrate that: (1) the ink can not wet the substrate such that the deposited ink retracts back into individual droplets, forming a discontinuous printing feature; (2) there are heavy coffee rings formed at the edges of each of these retracted droplets. To provide closer examinations of the poor wetting and coffee rings, I present in Fig. 4.14(e,d) the dark-field optical micrographs of deposited films and individual droplets.

A rule of thumb for wetting of the substrate and subsequent continuous printing feature is that the ink surface tension should be 7-10 mNm^{-1} lower than the substrate surface en-

ergy [350]. Therefore, an ink should possess a surface tension of <30 mNm^{-1} to wet the commonly used substrates, including Si/SiO_2 and glass ($\sim$36 mNm^{-1} [360]), and polyethylene terephthalate (PET; $\sim$45 mNm^{-1} [361]). However, as listed in Table 4.4, the inks typically have a surface tension of >40 mNm^{-1}, leading to a poor wetting and hence, a discontinuous printing feature; Fig. 4.14(e). I note that water/alcohol inks cannot wet these substrates properly in spite of having a surface tension of $\sim$30 mNm^{-1}, as clearly demonstrated in Fig. 4.14. During the drying process of a water/alcohol ink, alcohol evaporates rapidly and leaves water to dry on the substrates; water cannot wet these substrates.

On the other hand, the observed coffee ring effect can be attributed to the non-uniformity in solvent evaporation rates across the droplet upon drying [60, 61]. As discussed, the solvent evaporation rates at the droplet edges are higher than those in the centre due to a larger surface area to volume ratio, inducing an outward flow to compensate the solvent evaporative losses at the edges. As a result, the outward flow carries the dispersed 2d material flakes to concentrate and deposit at the edges. These flakes pin the droplet and prevent it from receding until it reaches a critical point where the droplet suddenly recedes and leaves a material ring of flakes. This repeats during the drying process and forms a series of coffee rings; Fig. 4.14(f).

There have been investigations on substrate surface treatment to address the above challenges. For example, Torrisi *et al.* showed that coating Si/SiO_2 with bis(trimethylsilyl)amine (HMDS) could help achieve a more uniform distribution of graphene flakes compared to untreated Si/SiO_2; Fig. 4.3(c) [37]. The authors also demonstrated that etching the Si/SiO_2 with O_2-plasma led to a worse flake distribution due to ink overspreading as a result of increased surface energy. Using substrates with porous coating is an alternative effective approach. For instance, in Ref. [40, 42], the authors used a PET substrate coated with aluminum oxide and poly(vinyl alcohol). This coating creates a porous surface, whereby the 2d material flakes are blocked and evenly deposited on the surface upon printing.

For the binder inks, though spatially uniform printing is ensured, it may be necessary to remove the polymers after printing since unlike solvents the polymers form an integral part of the printed films. For the applications in, for example, conductors, transistors and photodetectors, the polymers compromise the functionalities of the 2d materials and hence, the device performance. Removal of the polymers is usually done using high temperature annealing or intense pulsed light, as presented in Table 4.12. These post-printing treatment can significantly limit the development of printable flexible applications using polymeric substrates.

Therefore, in summary, the current ink formulations and treatment strategies raised above cannot guarantee a spatially uniform inkjet printing of 2d materials. Such an unideal inkjet

printing is impractical to deliver reproducible device fabrication and stable device operation, preventing large-scale printable device fabrication, realising which requires significantly improved ink formulations.

4.5 Summary

In this chapter, I have introduced the ink systems, the formulation processing and the graphics printing technologies. The focus is on inkjet printing, covering its working mechanisms and printing principles, *i.e.* droplet jetting, spreading and drying. In particular, I have discussed the progress of inkjet printing of 2d materials produced by UALPE. The current inks present significant challenges for spatially uniform material deposition and hence, cannot guarantee a reproducible device fabrication. This highlights the necessity of a significantly improved ink formulation. On this basis, I investigate ink formulations of graphene (Chapter 5), TMDs (Chapter 6) and BP (Chapter 7), aiming to overcome the above challenges.

Chapter 5

Formulation of inkjet-printable graphene ink and its applications

There is an ever-growing demand on developing graphene based inkjet-printable applications. Indeed, there are already successful laboratory-scale demonstrations in conductors and electrodes [38, 47, 50, 51], transistors [37, 42], photodetectors [40, 48], supercapacitors [50], and saturable absorbers (SAs) [39]. However, as discussed in Section 4.4.3, ink formulations in these demonstrations are incapable of delivering spatially uniform deposition of graphene on untreated substrates. This arises from suboptimal fluidic properties, poor wetting of the substrates or the formation of coffee rings. Such limitations prevent reproducible, scaled-up device fabrication. A significantly improved ink formulation is key and required to large-scale device printing.

In this chapter, I present the development of a conductive ink formulation of graphene that overcomes the above challenges for a large-scale spatially uniform deposition of graphene. To begin with, I investigate production of graphene *via* ultrasonic-assisted liquid phase exfoliation (UALPE). This leads to a single-step graphene ink formulation in isopropanol (IPA) with polyvinylpyrrolidone (PVP) that supports spatially uniform and high controllable printing of conductive graphene films. These printing features allow me to exploit the inkjet-printed graphene in applications, including the development of CMOS integrated humidity sensor (in collaboration with Dr Sumita Santra at the Indian Institute of Technology and Prof Florin Udrea at the University of Cambridge), and dye-sensitised solar cells (DSSCs; in collaboration with Dr David Dodoo-Arhin at the University of Ghana and Prof Gehan Amaratunga at the University of Cambridge).

5.1 UALPE production of graphene

5.1.1 Exfoliation in pure solvents

Pure solvents are usually preferred for UALPE as the resultant dispersions do not comprise impurities (*e.g.* ionic or non-ionic surfactants). As discussed in Section 3.3.1, the choice of solvent is key to graphene production, and the surface tension and Hansen solubility parameters (HSPs) of the solvents are the major considerations in solvent selection [236, 237, 281]. The "good" solvents should have a surface tension of $\sim$40 mNm^{-1} and HSPs of δ_{D} $\sim$18 MPa$^{1/2}$, δ_{P} $\sim$9.3 MPa$^{1/2}$ and δ_{H} $\sim$7.7 MPa$^{1/2}$, respectively [236, 275]. Under this condition, the good solvents are typically high boiling point, organic solvents, for instance N-Methyl-2-pyrrolidone (NMP; 204°C). Therefore, I investigate NMP as the starting point of my work.

To do this, I mix graphite flakes (Sigma Aldrich, 100 mesh) with NMP at a concentration of 10 gL^{-1}. The mixture then undergoes bath sonication for 12 hours in a 20 kHz bath sonicator at 15°C. Purification is then used to sediment the unexfoliated flakes. This is done by centrifugation at a speed of 4 krpm (*i.e.* 1500g) for 1 hour. The supernatant (top $\sim$70 vol.%) is collected as the graphene dispersion. The dispersion remains visually stable for months.

Figure 5.1(a) presents a photograph of a cuvette containing 5 times diluted graphene NMP dispersion. The extinction spectrum of this diluted dispersion measured using UV-Vis-NIR spectrometer (Fig. 5.1(b)) is featureless within the investigated wavelength region, as expected due to the linear dispersion of Dirac electrons of graphene [95, 133, 236]. By exploiting the Beer-Lambert law ($E = \alpha_{\lambda} Cl$; Section 3.4.1), using α_{660} $\sim$2460 Lg^{-1}m^{-1} [236], the concentration of the as-produced graphene NMP dispersion is estimated as 0.068 gL^{-1} (starting graphite concentration 10 gL^{-1}). This means that the production yield is only 0.68%. Therefore, it is necessary to improve the UALPE process for increased production yield.

However, the high boiling point and toxicity of NMP are problematic for the deposition of graphene flakes as this means long drying times and excessive careful handling [260]. Though inkjet printing with the graphene NMP dispersion is possible [16, 37, 40–42, 48], it is not ideal for long-term stable inkjet printing processes, especially when spatially uniform deposition is required. It is therefore desirable to develop graphene dispersions in lower boiling point, non-toxic solvents.

Cyclohexanone (CHO) is a promising solvent, approaching the above selection criteria with HSPs of δ_{D} $\sim$17.8 MPa$^{1/2}$ and δ_{P} $\sim$6.3 MPa$^{1/2}$, and δ_{H} $\sim$5.1 MPa$^{1/2}$ [277]. Indeed, I show here that graphene is successfully exfoliated and dispersed in CHO with an estimated

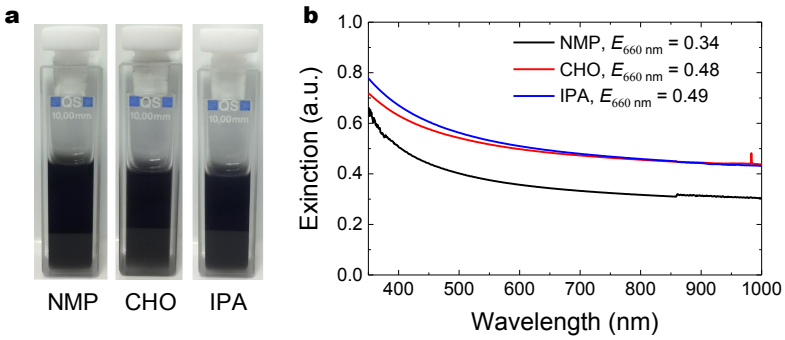

Fig. 5.1 (a) Photograph of the cuvettes containing diluted graphene dispersions in NMP, CHO and IPA, respectively. (b) Optical extinction spectra of diluted graphene dispersions. The dispersions are diluted to 20 vol.% to avoid detector saturation.

concentration of 0.098 gL^{-1}; Fig. 5.1(a,b). CHO is more advantageous than NMP for inkjet printing due to its lower boiling point (155.7°C) and lower surface tension (34.4 mNm^{-1} [362]). Indeed, Secor *et al.* reported an ink formulation of graphene in CHO with cellulose as the stabiliser (through multiple formulation steps; Section 4.4.1) [51, 53]. However, I find the graphene CHO dispersion is very sensitive to external perturbations such that the flakes sediment within 2-3 days.

I then explore other solvents with much lower boiling points and surface tensions such as alcohols. Alcohols are investigated as they are widely used as a primary solvent in graphics and functional inks [311]. Among the different alcohols investigated, I find IPA (boiling point 82.6°C) is able to successfully exfoliate and disperse graphene with an estimated concentration of 0.099 gL^{-1} (Fig. 5.1(a,b)), though its surface tension (23 mNm^{-1}) and HSPs (δ_D ~15.8 $MPa^{1/2}$, δ_P ~6.1 $MPa^{1/2}$, δ_H ~16.4 $MPa^{1/2}$ [277]) fail to meet the selection criteria. Due to the low boiling point and surface tension, the graphene IPA dispersion is expected to present optimal wettabilities and rapid ink drying for a high spatial printing uniformity [50]. However, the dispersion degrades rapidly, with a typical lifetime of up to 1 day. I propose this is due to the mismatched surface tension and HSPs. The lifetime is significantly shorter when the dispersion is loaded into cartridges for inkjet printing. However, I note that this stability is viable for coating techniques such as spray coating, allowing large-area spatially uniform material deposition. Stability of this dispersion therefore needs a significant improvement for inkjet printing.

5.1.2 Exfoliation with surfactants

Compared to organic solvents such as NMP, non-toxic solvents with low boiling point such as water and alcohols offer material processing and deposition advantages for device fabrication.

However, similar to alcohols, the properties of water (72 mNm^{-1}; δ_D ~18.1 $MPa^{1/2}$, δ_P ~17.1 $MPa^{1/2}$, δ_H ~16.9 $MPa^{1/2}$) are greatly deviated from the optimal surface tension and HSPs for UALPE. In this case, I investigate the use of surfactants to assist UALPE.

UALPE in water/sodium deoxycholate. Sodium cholate (SC) and sodium deoxycholate (SDC) are bile salts, one type of ionic surfactants [133, 134]. SC and SDC have very similar structures, consisting of a rigid cyclopentenophenanthrene nucleus with hydrophilic hydroxyl groups (-OH) on one face (commonly termed α), hydrophobic methyl groups (-CH_3) on the other (β) face, and an aliphatic chain terminating in a hydrophilic group [133]; Fig. 5.2(a-c). In particular, SDC has two -OH groups on its α face, while SC has three. This suggests that SDC has a higher hydrophobic index than SC, indicating a stronger adsorption onto the hydrophobic graphene surface [133].

I estimate the required concentration of surfactants for stable dispersion based on their critical micelle concentration (CMC); Section 3.3.2. Figure 5.2(d) presents the surface tension of aqueous dispersions of SC and SDC with respect to concentration measured *via* the pendant droplet method. This shows a critical point at a concentration of 6.9 mM (~3 gL^{-1}) for SC and 4.7 mM (~2 gL^{-1}) for SDC. Therefore, 3 gL^{-1} and 2 gL^{-1} are considered as the CMC for SC and SDC, receptively. Based on the considerations on hydrophobic index and

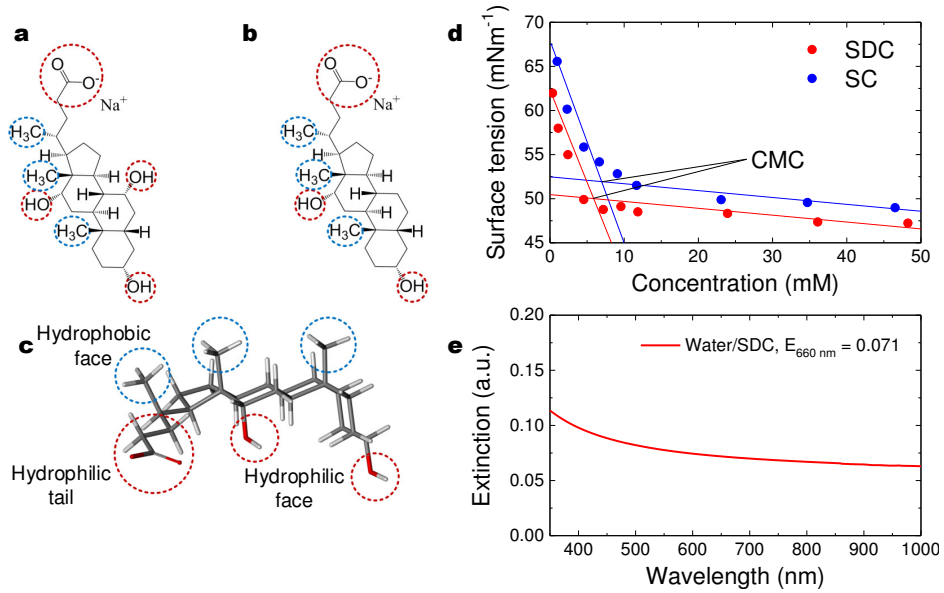

Fig. 5.2 Chemical structures of (a) SC and SDC in (b) 2d and (c) 3d. The hydrophilic (red) and hydrophobic (blue) groups are highlighted; (d) Calculation of the CMC of SC and SDC in water at room temperature; (e) Optical extinction spectra of diluted graphene dispersion. The dispersion is diluted to 20 vol.% to avoid detector saturation.

CMC, I select SDC as the surfactant for graphene production. To do this, I mix 100 mg of graphite with 10 mL, 7 gL^{-1} aqueous solution of SDC for UALPE. Figure 5.2(e) presents the acquired extinction of the dispersion (5 times diluted). Therefore, the estimated concentration of the as-produced dispersion is $\sim$0.014 gL^{-1}.

The graphene water/SDC dispersion remains stable for months, sufficient for inkjet printing. However, this dispersion does not allow spatially uniform deposition (Section 4.4.3). In addition, the presence of SDC can significantly compromise the functionalities (*e.g.* electrical conductivity) of graphene. It is also difficult to be removed from the graphene surface by neither washing nor high temperature annealing. Thus, the water/SDC dispersion is usually limited to the applications where the surfactants does not significantly affect the device performance. One such example is graphene flake enriched polymer nanocomposite SAs for ultrafast lasers [95, 133, 363].

UALPE in isopropanol/polyvinylpyrrolidone. Though the graphene IPA dispersion is readily to achieve spatially uniform deposition, its instability due to sedimentation needs to be addressed before it can proceed with inkjet printing. Making use of non-ionic surfactants such as polymers is a promising strategy [50, 51, 134, 264]. Here, I investigate polyvinylpyrrolidone (PVP) based on the following facts: (1) the N-substituted pyrrolidone ring in PVP is

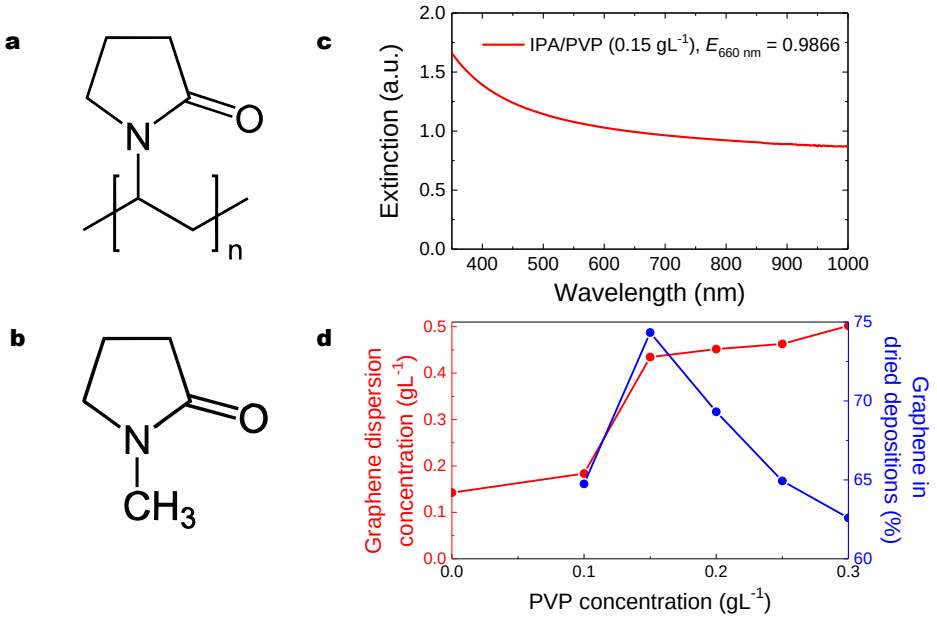

Fig. 5.3 Chemical structures of (a) PVP and (b) NMP; (c) Optical extinction spectrum of graphene dispersion. The dispersion for measurement is diluted to 10 vol.% to avoid detector saturation; (d) Graphene concentration in the dispersions and weight percentage in dried depositions with respect to PVP concentration.

similar to that in NMP (Fig. 5.3(a,b)); (2) PVP adsorbs readily on to the graphite surface, or carbon materials in general, such that it may provide a steric (*i.e.* physical) repulsion between the exfoliated flakes against sedimentation [291, 364]. Indeed, PVP has been successfully used to disperse CNTs [134] and more recently graphene [264]; (3) PVP can be effectively removed by annealing treatment [364].

To do this, I mix 100 mg of graphite with 10 mL, 0.15 gL^{-1} IPA solution of PVP. After bath sonication and centrifugation, this produces a stable dispersion, of which the optical extinction spectrum is shown in Fig. 5.3(c). This gives the concentration of the graphene IPA/PVP dispersion as $\sim$0.4 gL^{-1}, 3 times higher than that obtained using pure IPA (0.099 gL^{-1}) and any other liquids investigated above; Table 5.1. The graphene IPA/PVP dispersion remains stable for months without any visible sedimentations, a lifetime viable for long-term, large-scale printing processes.

Table 5.1 Concentration of the dispersed graphene in different liquids.

	Liquids				
	NMP	CHO	IPA	Water/SDC	IPA/PVP
Concentration (gL^{-1})	0.068	0.098	0.099	0.014	0.4

I then study the effect of the PVP concentration on UALPE production efficiency of graphene; Fig. 5.3(d). As shown, the concentration of graphene increases with the PVP concentration. For inkjet printing, an ink with higher concentration of graphene is more appealing as this means less printing repetition numbers are required to deposit sufficient amount of graphene for the desired application. In this case, a concentration of $\sim$0.5 gL^{-1} of graphene appears more appealing. Meanwhile, Fig. 5.3(d) presents the calculated weight percentage of graphene in the dried graphene-PVP deposition, showing that this weight percentage reaches the maximum value when PVP is 0.15 gL^{-1}. Since PVP forms an integral part of the graphene-PVP deposition, the weight percentage of graphene is a major factor in deciding its electrical conductivity and hence, a crucial consideration in the exploitation of this graphene IPA/PVP dispersion in applications. Therefore, I investigate the graphene IPA/PVP (PVP 0.15 gL^{-1}) dispersion further.

I characterise the thickness and lateral dimension of the exfoliated graphene flakes in the graphene IPA/PVP dispersion using AFM. The sample for AFM is prepared by dip-coating a Si/SiO_2 substrate into a dispersion diluted to 2 vol.% by pure IPA. Since the residual PVP prevents accurate characterisation of the flakes, the sample is annealed at 400°C for 30 min. This temperature is chosen because PVP starts to decompose at this temperature [365] while the exfoliated graphene flakes remain stable [50, 51]. The annealed sample is imaged with a

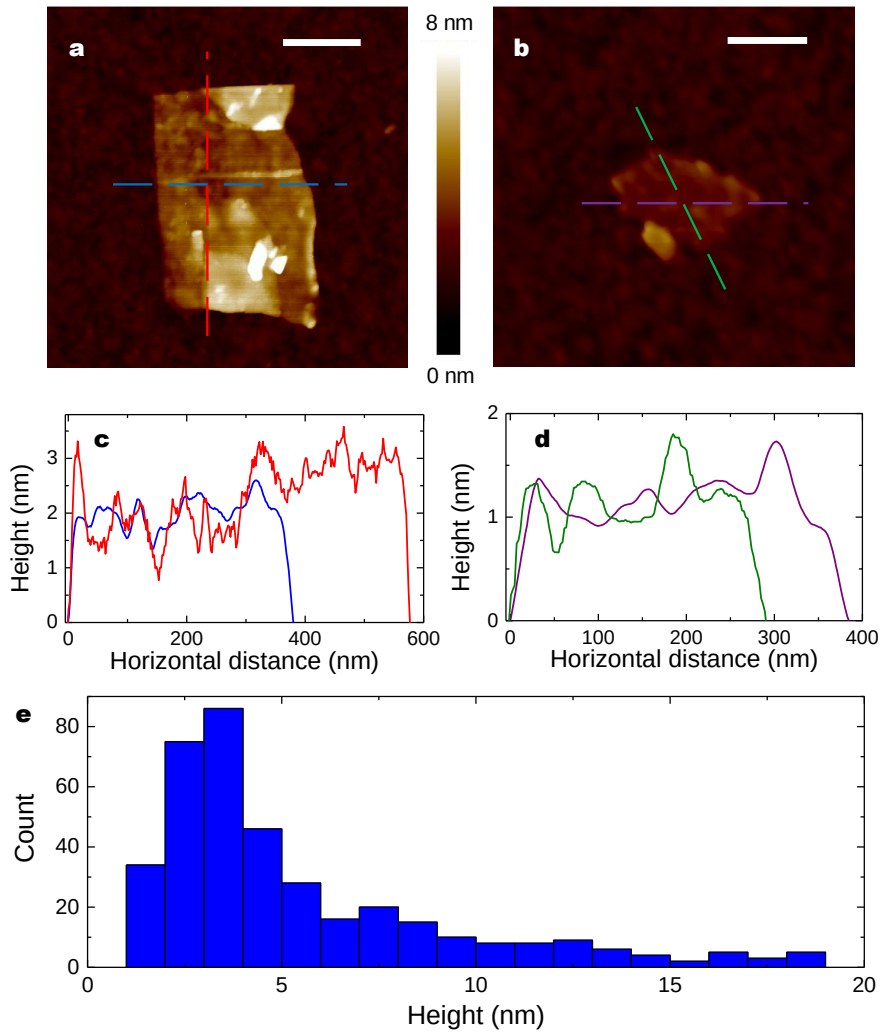

Fig. 5.4 AFM characterization of the exfoliated graphene flakes: (a, b) micrographs of typical flakes, scale bar 200 nm; (c, d) height variations across the dashed lines shown in (a, b), respectively; (e) thickness distribution of the graphene flakes.

Bruker Dimension Icon AFM in ScanAsyst^{TM} mode, using a silicon cantilever with Si_3N_4 tip. AFM micrographs of typical flakes are shown in Fig. 5.4(a,b). The height variations across the investigated flakes are shown in Fig. 5.4(c,d). The thickness distribution of the flakes is presented in Fig. 5.4(e), showing that 63% of the flakes have a thickness $<$5 nm. This corresponds to $<$13 layers, assuming $\sim$0.7 nm measured thickness for the bottom layer and $\sim$ 0.35 nm increase in thickness for each additional layer [366]. The average flake lateral dimension is $\sim$ 204 nm.

To experimentally confirm that the PVP decomposition process does not induce oxidation of the exfoliated graphene flakes, I characterise dropcast samples of graphene/PVP and PVP with Raman spectroscopy before and after annealing; Fig. 5.5. Before annealing,

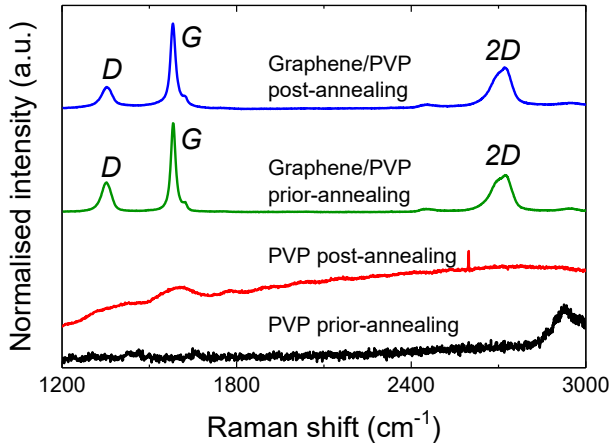

Fig. 5.5 Raman spectra of the exfoliated graphene and PVP before and after annealing (400°C, 30 min).

there are three prominent typical peaks in the Raman shift spectrum of graphene/PVP, *i.e.* 2*D* peak at ∼2700 cm^{-1}, *G* peak at ∼1600 cm^{-1} and *D* peak at ∼1100 cm^{-1}. This is expected, as discussed in Section 3.4.3. Since *D* peak is commonly associated to structural defects [302], this exhibited low intensity of the *D* peak compared to typical UALPE graphene (*e.g.* Ref. [37, 133]) is likely to due to larger average flake thickness. After annealing, there is not any visible shift observed of these three peak positions. This indicates that the graphene flakes do not oxidise by the PVP decomposition process. However, after annealing, the intensity of *D* peak is lower. On the other hand, the Raman shift spectrum of annealed PVP exhibits a featured *G* peak [367], suggesting that the decomposition process leads to carbonisation of PVP. Therefore, I suggest that the lower intensity of the *D* peak is due to the interaction between the graphene flakes and the carbonised PVP.

5.2 Large-scale spatially uniform inkjet printing

5.2.1 Graphene ink properties and printing parameters

After determining that the stability and concentration of the graphene IPA/PVP dispersion are potentially suitable for inkjet printing, I next investigate whether the fluidic properties of the graphene IPA/PVP dispersion are optimal for inkjet printing. I employ pendant drop measurement and parallel plate rheometer to measure its surface tension (γ) and the viscosity (η), respectively. The density (ρ) is estimated by weighing a dispersion with known volume. A Fujifilm Dimatix Materials Printer DMP-2831 is used to conduct inkjet printing. The ink cartridge is Dimatix DMC-11610, with a jetting nozzle diameter (a) of 22 µm. The volume

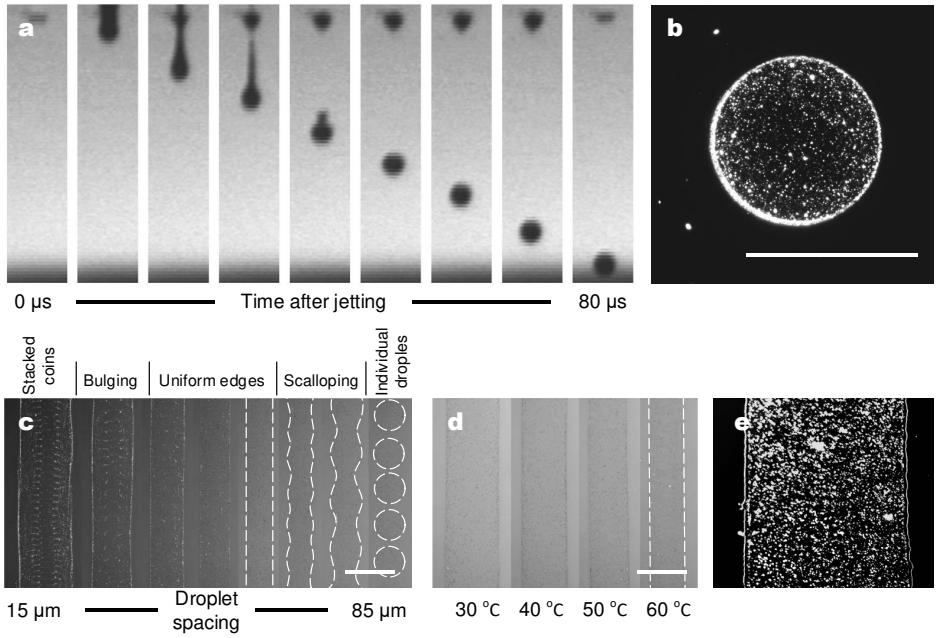

Fig. 5.6 (a) Photographs showing droplet jetting sequence; (b) Optical dark-field micrograph of a dried droplet, substrate temperature 60°C, scale bar 50 µm; (c) Optical bright-field micrographs of printed lines with different droplet spacing, substrate temperature 60°C, scale bar 100 µm; (d) Optical bright-field micrographs of printed lines at different substrate temperature, droplet spacing 35°C, scale bar 100 µm; (e) Optical dark-field micrograph of printed line, showing an even flake distribution, droplet spacing of 35°C, substrate temperature 60°C, scale bar 50 µm. The dashed lines outline the edges of the printed lines/droplets. The substrate is untreated Si/SiO_2 in all cases.

of individual droplets generated by this cartridge is ∼10 pL. This gives an estimation of the inverse Ohnesorge number Z of the dispersion as 10 ($Z = \sqrt{\gamma\rho a}/\eta$: η ∼2.3 mPa·s, γ ∼28 mNm^{-1}, ρ ∼0.8 gcm^{-3}, and a ∼22 µm), well within the optimal Z value range (*i.e.* 1-14), suggesting a stable jetting without formulation of satellite droplets or long filaments. Indeed, this is observed from the printer stroboscopic camera; Fig. 5.6(a).

Figure 5.6(b) presents a typical dried droplet on untreated Si/SiO_2, showing no prominent coffee rings that are typically observed for the case of NMP, water/SDC and water/IPA UALPE dispersions (Section 4.4.3). This is probably due to that the presence of PVP that leads to a colloidal dispersion. Therefore, the dispersed graphene flakes are not that readily transferred to the droplet edges by the evaporation induced outward convection flow upon drying, especially during the final drying stage when the viscosity is increased. Meanwhile, a surface tension of 28 mNm^{-1} ensures wetting of a wide range of substrates, including glass, Si/SiO_2 and PET, without requiring additional surface treatment, as demonstrated in Fig. 5.6(b). Therefore, I conclude that the graphene IPA/PVP dispersion can be used directly

as an ink for inkjet printing with optimal fluidic properties and the capabilities of wetting of substrates and suppressing the coffee ring effect. The graphene IPA/PVP dispersion is therefore termed as the "graphene ink" for the remainder of this chapter.

Before inkjet printing, however, it is necessary to seek the optimal printing parameters for this ink as these define the morphologies of the printed structures (Section 4.3.2). The inkjet printer (Fujifilm Dimatix Materials Printer DMP-2831) allows convenient control over printing parameters such as droplet spacing and substrate temperature. Figure 5.6(c) presents the bright-field optical micrographs of printed lines of one single printing repetition with a droplet spacing of 15-85 μm at 60°C. The variation of droplet spacing produces vastly different morphologies from "isolated droplets" to "stacked coins". In particular, a droplet spacing of 35-55 μm leads to lines with uniform edges. Figure 5.6(d) presents bright-field optical micrographs of printed lines with a droplet spacing of 35 μm at 30-60°C. This droplet spacing ensures uniform edges under all the investigated temperatures. The maximum printing resolution obtained is ∼70 μm. A uniform edge avoids overspreading of the ink and ensures appropriate merging of neighbouring droplets. Therefore, the printing parameters that produce uniform edges are considered as the optimal conditions (35 μm and 30-60 °C for this graphene ink). Under this printing guidance, a line is printed (35 μm, 60 °C), showing an even distribution of the graphene flakes along the entire length without the formation of coffee rings; Fig. 5.6(e).

5.2.2 Printing characteristics

I then assess the characteristics of the patterns printed at 35 μm and 60 °C. Figure 5.7(a) presents a sequence of squares (dimension 6 mm × 6 mm) on untreated glass with 1-30 printing repetitions. As shown, all the presented squares are defined with sharp edges and are spatially uniform. The acquired optical extinction at 550 nm is linearly correlated with the printing repetition, estimating that one printing repetition contributes an extinction of 0.00646 ± 0.000297; Fig. 5.7(b). This demonstrates the capability of the ink to precisely control the deposition densities of printed films, with a 3.5% deviation.

Figure 5.7(c) presents a square (dimension 2 mm × 2 mm) array on untreated glass, showing that all the individual squares are spatially uniform and do not exhibit any noticeable difference. To provide a closer assessment of this spatial uniformity and consistency, I extract the colour intensity of the printed square array in Fig. 5.7(d) and plot in Fig. 5.7(e). Here, the intensity of the background (the maximum intensity) is normalised to 0 (1). The extracted spatial colour intensity also shows high spatial uniformity within the individual squares, and no variation between the individual squares. Indeed, the colour intensity of the first square is 0.953 ± 0.014 (*i.e.* a deviation of 1.5%), and the average intensity of this square array

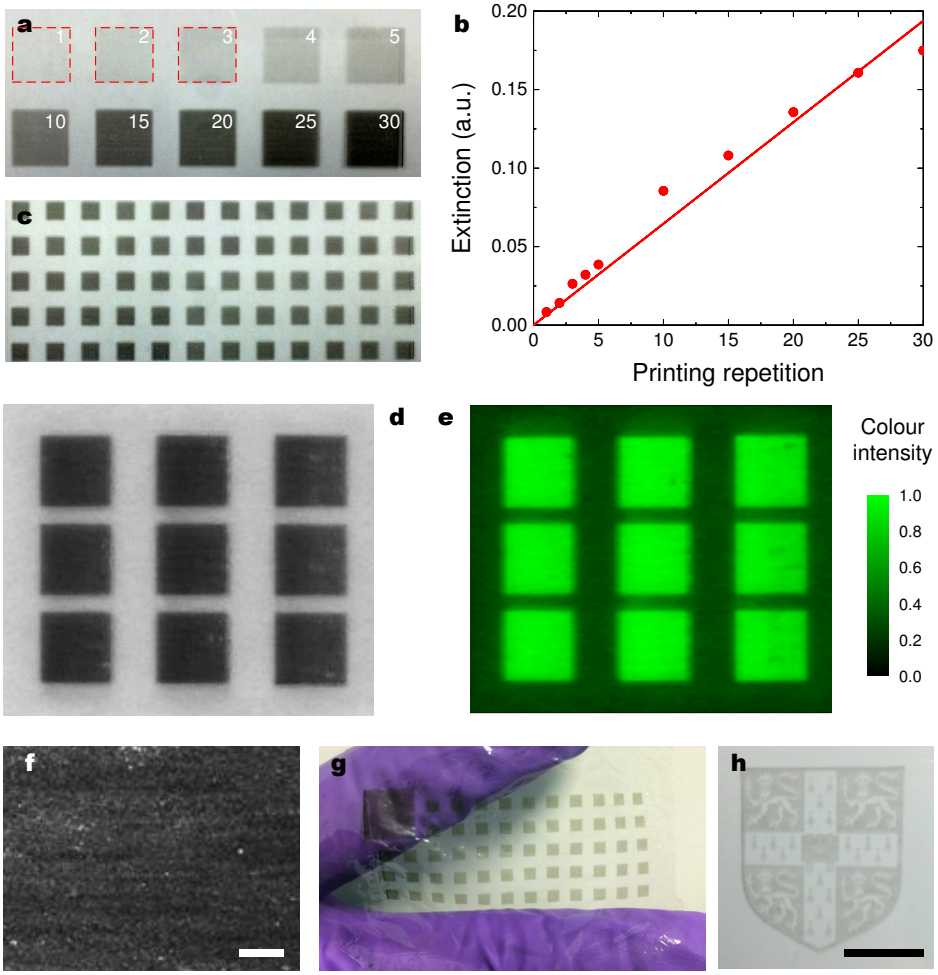

Fig. 5.7 (a) Photograph of a sequence of 6 mm × 6 mm squares with 1-30 printing repetitions on untreated glass, and (b) its optical extinction at 550 nm with respect the printing repetition number; (c) Photograph of a 2 mm × 2 mm square array on untreated glass; (d) Photograph for a sequence of 6 mm × 6 mm squares on untreated glass, and (e) its extracted colour intensity, where the intensity of background is normalised to 0 whereas the maximum intensity of printed graphene is 1; (f) Optical micrograph of the printed graphene on untreated glass, scale bar 200 µm; (g) Photograph for a 2 mm × 2 mm square array printed on LDPE; (h) Printed University of Cambridge crest on ultrathin PET (thickness 1.5 µm, laminated onto photopaper), scale bar 1 cm.

is 0.949 ± 0.026 (*i.e.* a print-to-print deviation of 3%). Figure 5.7(f) is a dark-field optical micrograph of the printed graphene, further confirming the spatially uniform distribution of the graphene flakes.

The spatially uniform inkjet printing of graphene on rigid substrates can be readily transferred to other substrates. For instance, I present in Fig. 5.7(g) a square array printed onto low-density polyethylene (LDPE) substrate, showing that the squares are defined with

sharp edges and are spatially uniform. Figure 5.7(h) is a photograph of printed Cambridge University crest on ultrathin PET (thickness 1.5 μm), demonstrating a high resolution and highly controllable printing. These above investigations confirm that the graphene ink is capable of delivering large-scale, high resolution patterning not only on rigid substrates but also on flexible and comfortable substrates.

I note that the substrates, including Si/SiO_2 (SiO_2 thickness 100 nm), glass and PET (thickness 100 μm) are cleaned with acetone/IPA/DI water before printing. The LDPE (thickness 10 μm) is used directly as purchased without any cleaning. No surface treatment is applied on these substrates before printing.

5.2.3 Electrical properties of inkjet-printed graphene

Within the inkjet-printed graphene-PVP film, the graphene flakes are randomly distributed. The electrical behaviour of randomly arranged conductive objects in an insulating matrix can be described by percolation theory [40]. As shown in Fig. 5.8(a), before continuous pathways of the conductive objects are formed, the conductivity of the matrix is zero; as the conductive pathways start to build up, electrical conductivity becomes non-zero and increases with the increasing number of the conductive pathways. The conductivity follows the relation:

$$\sigma_e \propto (X - X_0)^i \tag{5.1}$$

where σ_e is the electrical conductivity, X_0 is the critical density of the conductive objects above which the density of the objects X results in conductivity, and i is the percolation coefficient.

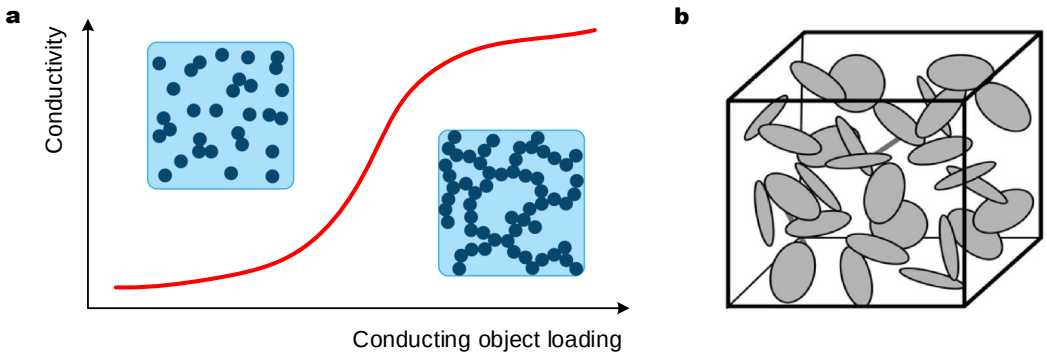

Fig. 5.8 (a) Schematic figure illustrating percolation behaviour in 2d; (b) 3d schematic percolation model of conductive object network [368].

In a 3d bulk model with conductive objects distributed in an insulating matrix (*e.g.* the inkjet-printed graphene-PVP film), the equation can be rewritten in terms of volume fractions:

$$\sigma_e \propto (v - v_0)^i \tag{5.2}$$

where v and v_0 are the volume fraction and the critical volume fraction of the conductive objects, respectively [368]. Since this relation does not take into account of the particle size, shape, orientation or their distribution uniformity inside a matrix, i and v_0 are empirically derived for a given system [368]. Modelling the graphene flakes as thin, circular discs, and considering their random distribution within the graphene-PVP film, v_0 can be derived as:

$$v_0 = \frac{27\pi d^2 t}{4(d + d^*)^3} \tag{5.3}$$

where d and t are the diameter and thickness of the flakes, respectively, and d^* is the interflake distance [368]. If d^* is shorter than the electron hopping distance through the non-conductive matrix, electron hopping takes place, facilitating the formation of conductive pathways. The limit for single-step electron hopping is generally $<$10 nm in insulating polymers [369]. Multi-step electron hopping may also happen for $>$10 nm. A critical value of $\sim$1 μm has been reported for some polymers with embedded conductive objects [369, 370]. With $\sim$4.5 nm average flake thickness and $\sim$204 nm average lateral dimension estimated from AFM measurements, and considering d^* $\sim$10 nm-1 μm, v_0 is estimated as $\sim$0.486-0.003. This therefore requires v $>$0.486 to ensure that the graphene-PVP film is conductive. Bulk density of graphite is $\sim$2.3 gcm^{-3}. However, exfoliated graphene flakes can have a significantly lower density, for instance commercial graphene samples are typically quoted to have a density in the range of 0.03-0.4 gcm^{-3} [371]. Assuming 0.4 gcm^{-3} for the UAPLE graphene, a concentration of $>$0.047 gL^{-1} is required. Therefore, according to this fitting, the inkjet-printed graphene-PVP (ink concentration 0.4 gL^{-1}) is predicted to be conductive.

To experimentally assess the electrical properties of the inkjet-printed graphene-PVP film, the sheet resistance (R_s) of the squares shown in Fig. 5.7(a) is characterised using a standard 4-probe sheet resistance measurement system before annealing. As shown in Fig. 5.9(a), the R_s of the squares with 1-10 printing repetitions is over the maximum measure range of the equipment (100 MΩ/□). The R_s of squares with $\geq$15 printing repetitions is typically $>$1 MΩ/□). This poor electrical performance is primarily due to the presence of PVP. The R_s measured after the decomposition of PVP is decreased significantly, with a value down to $\sim$4.6 kΩ/□. Note that the carbonised PVP may contribute to the electrical conductivity of the annealed graphene film. The R_s can be further decreased by increasing

the printing repetitions. Figure 5.9(b) is the spatial R_s of the square array in Fig. 5.7(d) after annealing. The acquired R_s of this array is 2.99 $\pm$ 0.16 kΩ/□, demonstrating a highly consistent print-to-print electrical performance, with a deviation of ∼5%.

5.3 CMOS integrated graphene humidity sensors

Humidity sensors are widely employed in environmental monitoring, automotive, industrial process, healthcare, agriculture and increasingly, in smart buildings. A range of transduction techniques have been developed for humidity sensors, for instance surface acoustic wave [372–374], resistive [375, 376], capacitive [377], optical fibre [378], field effect transistor [379, 380] and quartz crystal microbalance [381]. The capacitive technique is most widely used due to its linear response to humidity over a wide range [382]. It exploits a thin dielectric layer, typically polymers, to adsorb/desorb water molecules and hence detect changes in the capacitance (*i.e.* electrical permittivity) [382]. However, polymer based capacitive humidity sensors suffer from hysteresis as the cluster of water molecules are adsorbed inside bulk polymers. This may cause deformation and instability of the sensing polymers, reducing the lifetime of the sensor [382]. Meanwhile, the currently dominant sensors rely on semi-automated manufacturing, which increases the overall production cost [383]. In comparison, resistive humidity sensors present advantages as the detection is easier to read out with basic circuitry. However, sensors available in the market are typically bulky or usually have high power consumption [384]. CMOS is a mature, reliable technology and most importantly, it makes integration of sensors with electronics possible for the development of economic, compact and low-power sensors. Therefore, CMOS is an emerging underlying platform for a single chip solution, significantly reducing the production cost [385, 386].

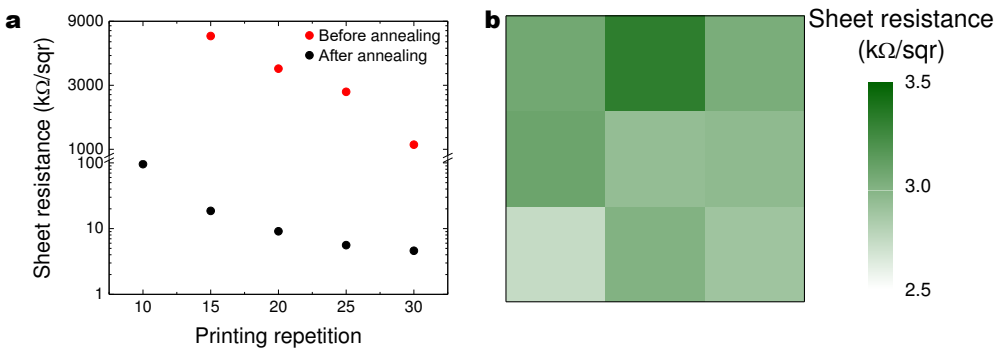

Fig. 5.9 (a) Sheet resistance of the printed graphene squares shown in Fig. 5.7(a); (b) Sheet resistance of the printed graphene square array shown in Fig. 5.7(d) after annealing.

However, to take the advantage of CMOS miniaturisation and single chip solution, the small active sensing area needs to exploit highly sensitive materials. Various functional materials, such as polymers [372, 387], metal oxides [379], carbon nanotubes [388, 389] and graphene oxide based nanocomposites [376, 390], have shown promising results for this. Among these, nanomaterials are of particular interest because of their high surface area to volume ratio, high sensitivity and fast response time. Nanomaterials are therefore ideal candidates for a low-cost CMOS sensing platform. With a high specific surface area and sensitivity to environmental perturbations, graphene holds good potential for various sensing applications including humidity. The lateral size of the graphene flakes produced from UALPE is typically several hundred nanometres, offering high surface area and high concentration of active edges, making them ideal active materials for sensors. Indeed, thus-far there are many demonstrations of graphene based humidity sensors [372, 377, 390–392]. However, mostly of these are based on a non-CMOS platform.

Here, I present exploitation of the inkjet-printed graphene in CMOS integrated humidity sensor fabrication. This work was in collaboration with Dr Sumita Santra at the Indian Institute of Technology and Prof Florin Udrea at the University of Cambridge. The CMOS device was developed by Prof Florin Udrea, and was used as received. My key contributions in this work were fabricating the humidity sensor by integrating the inkjet-printed graphene into the CMOS device, analysing the measurement data, developing the sensing mechanism, and writing the manuscript which was published in *Scientific Reports*: Ref. [393].

5.3.1 CMOS device design

Figure 5.10(a,b) present the schematic figure and optical micrograph of the CMOS device used in my work. The silicon die is 1 mm × 1 mm. It is designed using a 1.0 µm Silicon on

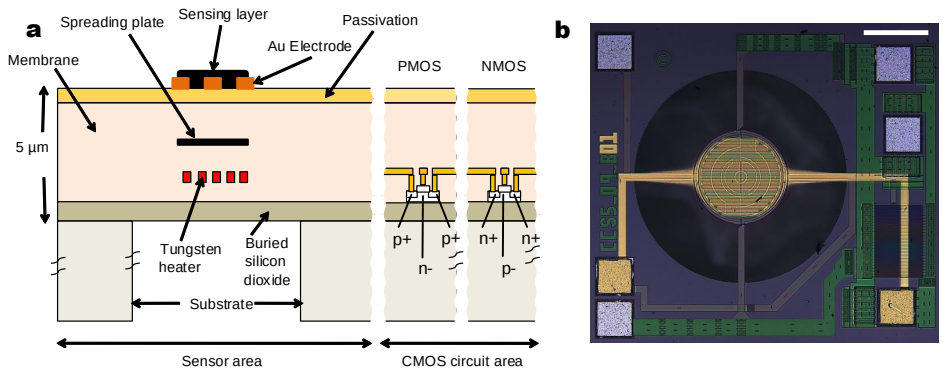

Fig. 5.10 (a) Cross sectional view (not to scale) and (b) optical micrograph of the CMOS device (as received), scale bar 200 µm.

Insulator (SOI) CMOS process technology and fabricated in a commercial foundry, followed by deep reactive ion etching to release the thin membrane. The processing employs SOI wafers with 1 µm buried oxide, 0.25 µm SOI layer and 3 metallisation layers. The key component of the device is the microhotplate (µHP) structure. The µHP consists of an embedded, 0.3 µm thick, resistive tungsten microheater (metal layer 1), 0.3 µm thick heat spreader plate (metal layer 2), and a top gold layer for interdigitated electrodes (IDEs). The diameter of the circular heater and membrane structures is 250 and 600 µm, respectively. The tungsten heater controls the operating temperature of the membrane and sensing layer on top. The IDEs underneath the sensing layer are used to measure the change in resistance due to humidity exposure. Use of tungsten in the heater allows the device to operate at a very high temperature (up to 750°C). Gold is used as the electrode material because of its chemical inertness compared to commonly used aluminium in the SOI process. The silicon underneath the µHP is etched away, with the dioxide layer as the etch stopper, at a wafer level by using deep reactive ion etching technique. This forms a SiO_2/Si_3N_4 (4 µm / 0.5 µm) membrane structure onto which µHP and IDEs are suspended. The membrane structure reduces DC power consumption of the sensing device to $<$5 mW when used for humidity sensing in this work. The heating temperature is uniformly confined over the µHP region, due to the buried heat spreader [394]. The temperature decreases rapidly away from the heater region and is at close to room temperature at the membrane rim, allowing reliable temperature independent on-chip circuit performance [395].

5.3.2 Sensor fabrication with active graphene-PVP sensing layer

The next step is the exploitation of the inkjet-printed graphene-PVP in developing the active sensing layer on the 250 µm diameter µHP. Si_3N_4 has a surface energy of $\sim$40 mNm^{-1} [360]. This means that the graphene ink can wet the µHP membrane without the need for additional surface treatment.

I inkjet print directly the graphene ink (graphene 0.40 gL^{-1}, PVP 0.15 gL^{-1}; Section 5.1.2) onto the µHP of the CMOS device; Fig. 5.11(a). Room temperature evaporation of IPA forms a graphene-PVP sensing layer on µHP. Figure 5.11(b) is a dark-field optical micrograph of the CMOS device with graphene-PVP deposited. The bright spots indicate the graphene flakes in the PVP matrix, demonstrating an even deposition of graphene. The morphology of the deposited graphene-PVP is further characterised using SEM, showing an evenly interspersed graphene-PVP on µHP; Fig. 5.11(c). By annealing the device at 400°C, PVP is decomposed, revealing the even distribution of the graphene flakes; Fig. 5.11(d). Note that the SEM micrograph may show traces of carbonised PVP.

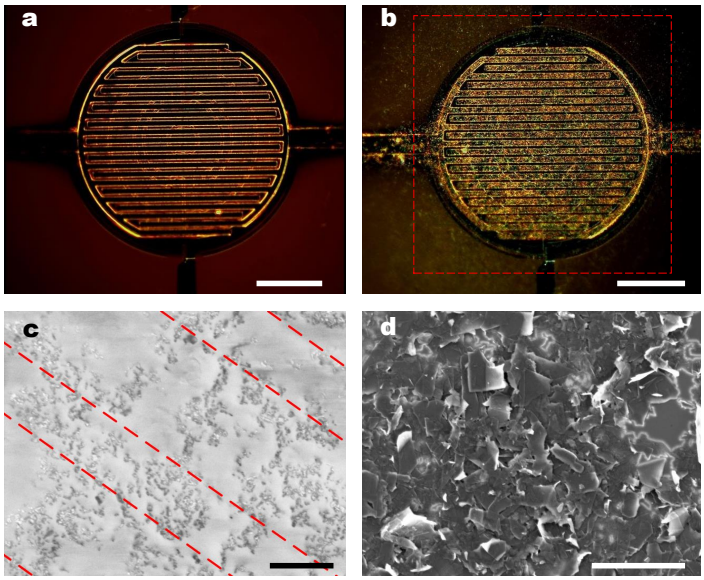

Fig. 5.11 Dark-field optical micrograph of the μHP (a) without and (b) with graphene-PVP deposited, scale bar 100 μm. The targeted printing area is marked by dashed line; (c) SEM micrograph of μHP with graphene-PVP deposited, scale bar 3 μm. The IDEs are marked by dashed lines; (d) SEM micrograph of graphene-PVP after annealing, scale bar 1 μm.

5.3.3 Humidity sensing

The resistance of the graphene-PVP sensing layer between the IDEs at room temperature, 40°C and 70°C is presented Fig. 5.12(a). The linear relationship confirms a good Ohmic contact between the graphene-PVP sensing layer and the IDEs. A control experiment is conducted by inkjet printing a IPA/PVP solution, which shows negligible electrical conductivity as PVP is an insulting polymer. This control sample is then not conducted with further humidity sensing testing.

The sensors are next characterised using different relative humidity (*RH*) levels inside a stainless-steel chamber. Initially the sensors are kept in dry air before they are exposed to 10-80% *RH*. The set-up allows a maximum of 80% *RH* above which condensation of water vapour inside the test chamber starts to appear, making the measurement unreliable. In typical experiments, the sensors are exposed to humid air for 20 minutes followed by dry air purging for 30 minutes. The humidity response is defined as:

$$Response = \frac{\Delta R}{R_{air}} \times 100\% = \frac{R_{humid} - R_{air}}{R_{air}} \times 100\% \tag{5.4}$$

where R_{humid} and R_{air} are the measured resistances when exposed to humid conditions and dry air, respectively. A typical device response at room temperature is plotted in

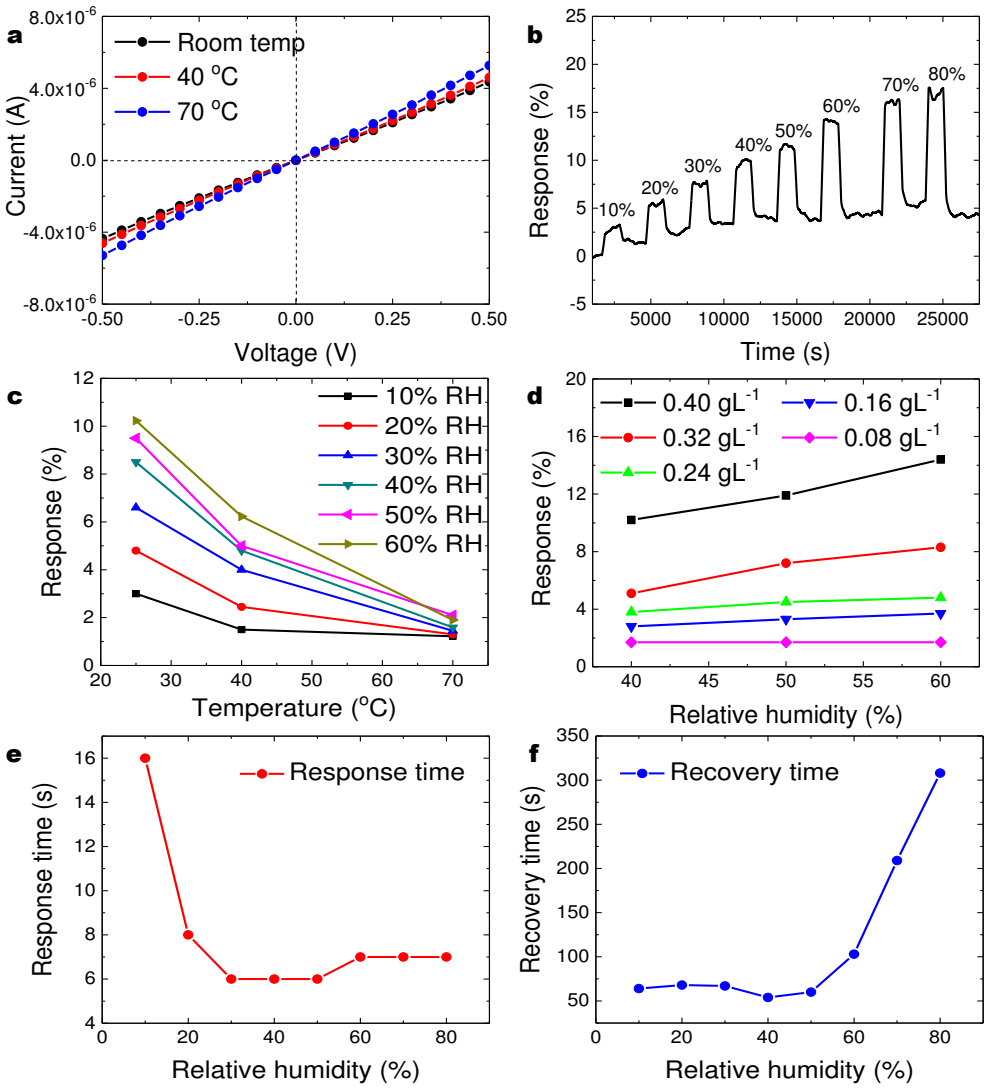

Fig. 5.12 (a) Current versus voltage at room temperature, 40°C and 70°C; (b)Humidity sensing response at room temperature with eight different *RH* levels; (c) Sensing response at room temperature, 40°C and 70°C; (d) Humidity sensing varies with the amount of deposited graphene; (e) Response time and (f) recovery time at different *RH* levels at room temperature.

Fig. 5.12(a), showing an increased *Response* with an increased *RH*. The sensitivity (defined as *Response*/*RH*) achieved from the sensor varies from (0.3%)/(%*RH*) to (0.21%)/(%*RH*) as *RH* increases from 10% to 80%. Note a change in the baseline of response is observed in the lower humidity levels (10-30%). This could be due to trapped water molecules within the sensing layer during the recovery from pre-exposures [396]. The sensor is next characterised at three temperatures (room temperature, 40°C and 70°C) to investigate the effect of temperature on the response; Fig. 5.12(c). The temperature is controlled by the μHP. This shows a reduced response with increasing temperature. Note that the baseline

drift shown in Fig. 5.12(b) reduces with the temperature rise as the trapped water molecules desorb from the sensing layer faster.

To investigate the effect of percolating volume fraction (v), a series of inks with 0.40, 0.32, 0.24, 0.16 and 0.08 gL^{-1} graphene concentration are prepared while keeping the PVP concentration constant. This gives v of 0.889, 0.865, 0.828, 0.762 and 0.615, respectively, all of which are above the critical volume fraction v_0 (0.486). Sensors with these inks deposited are then exposed to 40-60% *RH*, showing an increased response with the increase in graphene concentration under all the *RH* conditions; Fig. 5.12(d). This suggests that more percolating pathways lead to a larger change in resistance, hence a higher response. The larger change is likely due to the fact that more percentage of the percolating pathways are broken due to the polymer swelling effect when the water molecules are absorbed. However, this is yet to be conclusive, requiring further experimental work to understand the electrical conduction and percolation of the graphene-PVP sensing layer.

The sensor with 0.40 gL^{-1} graphene ink exhibits the highest response and is therefore used to investigate typical response and recovery times (defined as the time needed to reach 63% of the maximum response and to recover to the baseline, respectively); Fig. 5.12(e,f). The measured response and recovery times are reasonably fast, varying from ∼6-16 s and ∼60-300 s, respectively. The slower recovery time at higher *RH* could be attributed to the presence of higher partial pressure of water vapour close to the surface of the sensing layer when the sensor recovers through the desorption of water molecules. Note that long humidity on and off times are used to ensure that the device response reaches its saturated limit without any noticeable drift.

Reproducibility of a sensor at different sensing cycles and of sensing over a long period are next investigated. A response reproducibility for over 5 cycles is demonstrated, as shown in Fig. 5.13(a). The long-term operation stability of the sensor is investigated over a 4-week

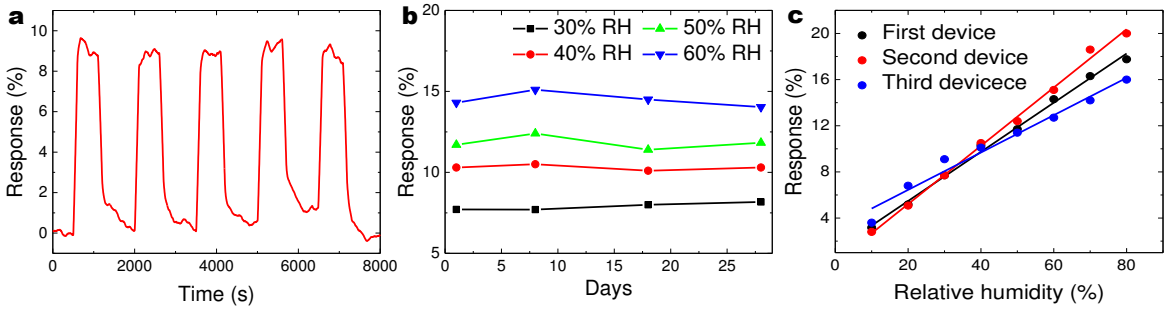

Fig. 5.13 Sensing reproducibilities of (a) one sensor during 5 sensing cycles (at 50% *RH*), (b) long-term stability, and (c) deviation between varied sensors. Characterisations are performed at room temperature.

period. As shown in Fig. 5.13(b), no significant deviation ($\sim$4%) of response at 30, 40, 50 and 60% *RH* during this period can be observed. A characterisation of the response of different sensors with the same design and printing is also performed to investigate the performance deviation between varied sensors, showing a maximum deviation of $\sim$13%; Fig. 5.13(c). Figure 5.13(c) also shows a linear response of the sensors.

5.3.4 Sensing mechanism

Based on the experimental results, the following sensing mechanism is proposed. The adsorbed water molecules on graphene surface may disassociate to H^+ and OH^- ions at the edges of graphene, similar to what has been observed with graphene oxide samples [377]. These H^+ ions may tunnel from one water molecule to another through hydrogen bonding, reducing the overall electrical resistance of the sensing layer [377]. On the other hand, the adsorbed water molecules on graphene surface act as electron donors [376]. As the electron density increases, the normally *p*-type graphene becomes more resistive. This *p*-type semiconducting nature of carbon nanomaterials is in agreement with reported results [122, 397]. Meanwhile, PVP is a hygroscopic, electrically insulating polymer, absorbing up to 25% water molecules at 75% *RH*, swelling the polymer [398]. That moisture absorption and subsequent polymer swelling can increase the distance between the graphene flakes, leading to a reduction of electrically percolating pathways through single-step electron hopping in PVP. However, the change in polymer volume and corresponding increase in distance between the adjacent graphene flakes may also depend on other factors such as chemical composition and graft density of the polymer nanocomposite [399]. Among the two opposing effects on resistance, the effect of the *p*-type semiconductor nature of graphene and the swelling and consequent reduction of percolating pathways seems to be dominant. This results in an increased electrical resistance of the graphene-PVP sensing layer, enabling humidity sensing.

5.4 Graphene based dye-sensitised solar cells

The edge plane sites of solution-processed graphene flakes exhibit fast electron-transfer kinetics and hence may offer high electrocatalytic performance [400–403]. Coupled with this, electrical conductivity and chemical stability potentially make the solution-processed graphene an attractive counter-electrode (CE) material [404, 405]. In this section, I investigate the suitability of the inkjet-printed graphene as CE for dye-sensitised solar cells (DSSCs). This work was in collaboration with Dr David Dodoo-Arhin at the University of Ghana and

Prof Gehan Amaratunga at the University of Cambridge. My key contributions in this work were designing the inkjet-printed graphene CE, analysing the measurement data, and writing the manuscript which was published in *Carbon*: Ref. [406].

DSSCs offer advantages such as cost-effective fabrication and high conversion efficiencies (up to >12%) [408–411]. Figure 5.14(a) is a typical schematic figure for DSSCs, which consists of a CE (*e.g.* platinum), a photoanode consisting of mesoporous networks of nanocrystalline semiconductor oxide (*e.g.* titanium dioxide: TiO_2) that is deposited onto a transparent conductive contact (*e.g.* indium tin oxide: ITO, or fluorine-doped tin oxide: FTO), and electrolyte [408, 411–413]. The porous networks of TiO_2 provide large surface area for the adsorption of sensitising dye molecules (*e.g.* ruthenium(II) bipyridyl dye, organic dyes), allowing light harvesting [408, 411–413].

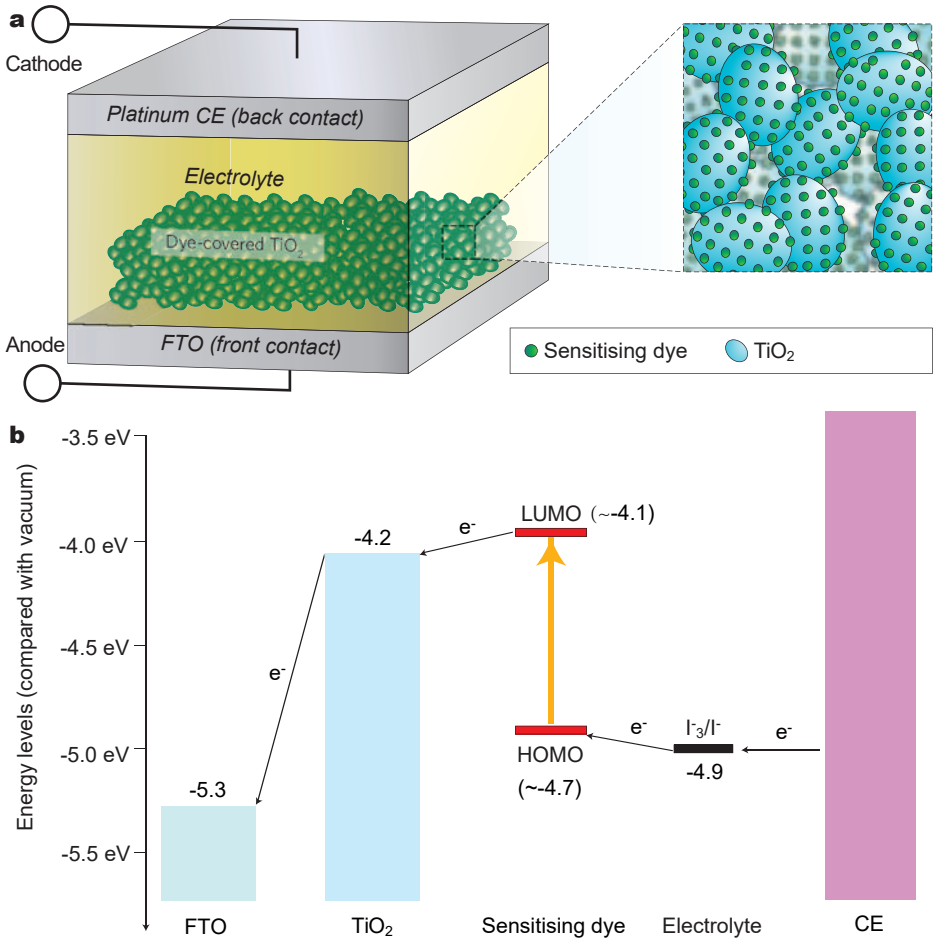

Fig. 5.14 (a) Schematic figure for typical DSSC structure; (b) Energy levels of DSSCs, the work function of platinum is -6.4 eV. Adapted from Ref. [407].

As shown in Fig. 5.14(b), the absorption of photons by the dye molecules creates an excited molecular electronic state. The dye then rapidly returns to its original state *via* electron transfer from iodide ions in the I_3^-/I^- redox electrolyte. The I_3^- ions formed by oxidation of I^- diffuse a short distance (<50 μm) through the electrolyte to the platinum CE coated cathode, where the regenerative cycle is completed by electron transfer to reduce I_3^- to I^- [414]. The dye used as the sensitiser and the CE material are the two most important factors that influence the performance of a DSSC. In this work, these two factors are investigated.

5.4.1 Natural dyes

The key considerations for a dye are the absorption across the solar spectrum and the adsorption/adhesion of the dye molecules to the surface of the semiconductor oxides (*e.g.* TiO_2) [415]. The most widely used sensitisers are those based on heavy transition metal co-ordination compounds (*e.g.* ruthenium (*Ru*)-polypyridyl complexes) due to their efficient metal-to-ligand charge transfer, intense charge-transfer absorption across the visible spectral range, and long excited lifetime [410]. However, *Ru*-polypyridyl based complexes are expensive (∼$1200 per gram), and contain the heavy rare earth metal, *Ru*, that is environmentally undesirable [416]. Therefore, environmentally-friendly, economic and readily available dyes attract a lot of interest [408, 412, 413, 417, 418]. With the advantages such as the wide availability, simple extraction process, usability without further purification, environmental sustainability and low-cost, natural dyes that are extracted from plants are a promising platform this purpose [408, 412, 413, 417, 418]. In particular, anthocyanin molecules extracted from some plant tissues can adsorb onto the surface of porous semiconductor oxides, leading to photoelectron transfer from the anthocyanin molecules to the conduction band of the semiconductor oxides [408].

Here, *P. glaucum*, *H. sabdariffa* and *C. pulcherrima* are investigated. These flowers are native to Ghana, and have HOMO (*i.e.* highest occupied molecular orbital) of ∼-4.7 eV and LUMO (*i.e.* lowest unoccupied molecular orbital) of ∼-4.1 eV [406]. Clean, fresh specimens of *H. sabdariffa*, *C. pulcherrima* and *P. glaucum* are dried under 60°C and crushed into fractionlets. To extract the natural dyes (*i.e.* anthocyanins) from the plants into the solution, 5 g of each of these samples are put in 60 mL of ethanol (96 vol.%) at room temperature without exposure to light. The dye solutions are then filtered to remove the solid residues, giving a concentration of ∼0.4 gL^{-1}. The extracted anthocyanins have a broad absorption band in the visible spectral range [408, 412]. For comparison, an inorganic ruthenizer 535-bisTBA (N719) dye, which is a widely used solar light absorber and charge-transfer sensitiser, is also investigated.

5.4.2 Inkjet-printed graphene counter-electrode based solar cells

The key requirements for the CE are catalytic activity and electrical conductivity. It should also exhibit a low overpotential (*i.e.* the difference between thermodynamic potential and electrical potential) for rapid reduction of the redox couple to carry the generated photocurrent across the width of the solar cell. Platinum is the most widely used material for counter electrode in DSSCs [419]. However, while the required platinum loading for optimum performance of the solar cell is small ($\sim$3.2 gm^{-2}) [420, 421], the dissolution of the platinum film in the corrosive I_3^-/I^- electrolyte and the high-temperature heat treatment ($\sim$300-400°C) [419] required for good platinum adhesion with the substrate limit its use on flexible substrates and in low-cost applications. This drives an interest for chemically stable and cost-effective CE materials for DSSCs such as carbon nanomaterials [401–403].

As briefly discussed, solution-processed (*e.g.* UALPE) graphene is a promising CE material with fast electron-transfer kinetics and high electrocatalytic performance [400–403], as well as a work function of $\sim$-5 eV [422]. In addition, I have presented in Fig. 5.7(b) that the inkjet-printed graphene is highly consistent in print-to-print electrical conductivities. This offers the potential for scalable and reproducible CE fabrication.

The DSSC fabrication process employed here is well documented in Ref. [406]. The photoanode and CE are prepared separately on FTO conductive glass substrates ($\sim$2 cm $\times$ 2 cm, 8 Ω/□, Solaronix). For the case of photoanode, the FTO substrate is immersed in a 40 mM aqueous solution of $TiCl_4$ (Sigma Aldrich) at $\sim$70°C for 30 mins for good adhesion of TiO_2, and is then washed and dried for use. A $\sim$9 μm thick TiO_2 film is deposited by doctor blading, giving an active area of $\sim$0.36 cm^2. Next, the sample is gradually preheated over a period of $\sim$60 mins, and then sintered at 500°C for 30 mins in air. After cooling to $\sim$80°C, the sample is immersed in the dye-ethanol solutions for 12-24 h at 50°C before the excess dyes are washed away with anhydrous ethanol.

For the case of CE, a hole is drilled on the FTO substrate to allow the electrolyte to be injected after device assembly. To prepare graphene CE, I inkjet-print the graphene ink (graphene 0.40 gL^{-1}, PVP 0.15 gL^{-1}) onto the pre-drilled FTO substrate, giving an active area of 2.0 cm $\times$ 1.5 cm. The sample is then annealed at 400°C for 30 mins to decompose the PVP, giving a R_s of $\sim$3 kΩ/□. Figure 5.15(a) presents a SEM micrograph of the after annealing graphene CE, showing a uniform, continuous deposition of graphene flakes. Note that the SEM micrograph may show traces of carbonised PVP. For comparison, a platinum CE is prepared *via* dropcasting $\sim$60 μL of 10 mM chloroplatinic acid (H_2PtCl_6) in IPA followed by 450°C sintering for 30 mins. Note the graphene CE gives a $\sim$97% reduction in production cost (graphene £14 per m^2, platinum £520 per m^2 [406]).

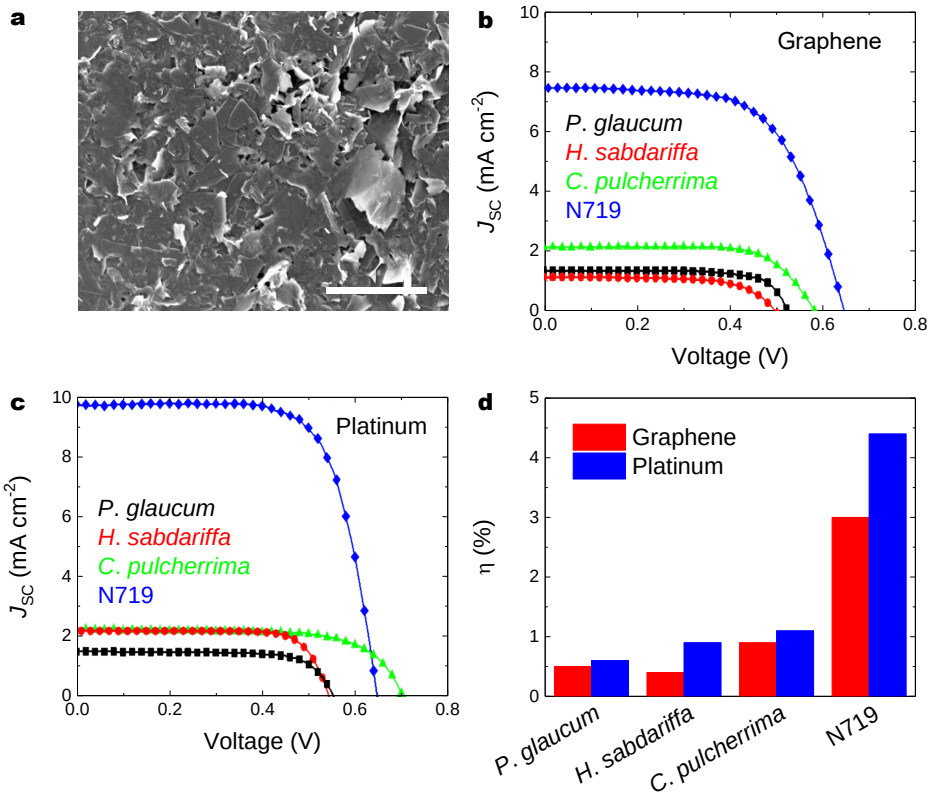

Fig. 5.15 (a) SEM micrograph of inkjet-printable graphene electrodes after annealing, scale bar 1 µm; I-V characteristic curves for (b) graphene based cells and (c) platinum based cells sensitised with *P. glaucum*, *H. sabdariffa*, *C. pulcherrima* and Ruthenizer N719. (d) Comparison of the efficiencies for platinum and graphene based cells.

The photoanode and CE are then assembled into a sandwich-type cell, separated by a 60 µm Surlyn thermoplastic film (Solaronix). An I_3^-/I^- redox electrolyte solution (Iodolyte Z-50, Solaronix) is injected into the cell *via* the pre-drilled hole. The hole is then sealed using a Surlyn film to complete the device assembly.

The assembled DSSCs are characterised using an Oriel solar simulator as the white-light source (100 mWm^{-2}). The measured parameters of the graphene and platinum CE based DSSCs are presented in Fig. 5.15 and Table. 5.2. Note the results here are the average of three devices, with <5% deviation. The short-circuit current density (J_{sc}) is estimated by dividing the measured photocurrent by the actual active area (~0.36 cm^2) of the DSSCs. The fill factor (FF) and the overall light-to-electrical energy efficiency (η_{eff}) are calculated as follows [408]:

$$FF(\%) = \frac{J_{max} \times V_{max}}{J_{sc} \times V_{oc}} \times 100 \tag{5.5}$$

$$\eta_{\text{eff}} = \frac{J_{\max} \times V_{\max}}{P_{\text{in}}} \times 100 = \frac{FF \times J_{\text{sc}} \times V_{\text{oc}}}{P_{\text{in}}} \times 100 \tag{5.6}$$

where V_{oc} is the open circuit voltage, P_{in} is the incident light power, $J_{\max}$ and $V_{\max}$ are the current density and voltage at the point of maximum power output, respectively. The devices show a change $<$10% in η_{eff} over a measurement period of 1-24 h, indicating a good device operation stability.

As shown, DSSCs fabricated with graphene CE and the natural dyes reach a η_{eff} of up to 0.9, $>$80% of that based on platinum and natural dye cells. Meanwhile, the η_{eff} of graphene and N719 based DSSC reaches 3%, $\sim$70% of that of platinum and N719 based DSSC. Meanwhile, the V_{oc} of DSSCs fabricated with graphene CE (up to 580 mV) is smaller than that with platinum (up to 700 mV). This lower V_{oc} may indicate a decrease in the I_3^-/I^- redox energy level, thereby a lower η_{eff}. To conclude, the combination of the significant fabrication cost reduction (97.3%) and the comparable device performance demonstrates the potential of printable DSSCs with graphene CE.

Table 5.2 Parameters of DSSCs fabricated with graphene and platinum (Pt) counter electrodes.

Dyes	V_{oc}		J_{sc}		FF		η_{eff}	
	(mV)	% of Pt	(mAcm^{-2})	% of Pt	(%)	% of Pt	(%)	% of Pt
Graphene CE based DSSCs								
P. glaucum	520	92.9	1.38	87.3	69.5	94.5	0.5	83.3
H. sabdariffa	500	92.6	1.16	52.3	62.6	82.8	0.4	44.4
C. pulcherrima	580	82.9	2.15	96.9	70.9	103.9	0.9	81.8
N719	640	98.5	7.44	76.5	62.0	88.8	3.0	68.2
Platinum CE based DSSCs								
P. glaucum	560	-	1.58	-	73.6	-	0.6	-
H. sabdariffa	540	-	2.22	-	75.6	-	0.9	-
C. pulcherrima	700	-	2.28	-	68.2	-	1.1	-
N719	650	-	9.73	-	69.8	-	4.4	-

5.5 Summary

In this chapter, I have presented the formulation of a graphene ink for inkjet printing and the application of the inkjet-printed graphene in CMOS integrated humidity sensor and solar cells. To begin with, I investigate graphene production *via* UALPE. This leads to the development of an one-step formulation of a graphene IPA/PVP ink that ensures stable jetting, wetting of

untreated substrates, and diminished coffee ring effect. The graphene ink therefore supports large-scale, controllable inkjet printing with a high spatial uniformity ($<$1.5% deviation) and a high print-to-print consistency ($<$3% deviation). By selectively decomposing the PVP through 400°C annealing (which does not induce oxidation of graphene), the inkjet-printed graphene exhibits a print-to-print consistent electrical conductivity ($<$5% deviation).

The above characteristics allow me to explore the inkjet-printed graphene in device fabrication. The first application I demonstrate is investigation of integrating the inkjet-printed graphene/PVP into a CMOS platform to fabricate humidity sensors. Upon humidity exposure, reduction in percolating networks in the sensing layer leads to an increased resistivity for humidity sensing. The response of the humidity sensors is reproducible, with a maximum of $\sim$13% deviation among sensors at different *RH* levels with stable performance ($<$4%) over a period of few weeks. The second application is making use of the inkjet-printed graphene as the CE for DSSCs. By using the graphene electrode, the DSSC devices achieve a significant fabrication cost reduction ($\sim$2.7% of equivalent device based on platinum CE) and a comparable device performance. Both these applications demonstrate the versatility of the inkjet-printable graphene ink.

Chapter 6

TMD ink formulation for large-scale printing of photonics and optoelectronics

Beyond graphene, other 2d materials such as transition metal dichalcogenides (TMDs), in particular the semiconducting members exhibit interesting optoelectronic properties for applications. For instance, as discussed in Section 2.3, the nonlinear optical properties and ultrafast carrier dynamics of TMDs have been extensively exploited in saturable absorbers (SAs) for ultrafast lasers [159, 168, 169]. A well developed method for SA fabrication is through developing TMD flake enriched polymer nanocomposites from ultrasonic-assisted liquid phase exfoliation (UALPE) dispersions. Indeed, through collaborations with Prof Meng Zhang at the Beihang University and Dr Rob Woodward, Dr Edmund Kelleher and Prof Roy Taylor at the Imperial College London, I have demonstrated polymer nanocomposite SAs of TMDs as described in Ref. [423–427]. However, it can be challenging to control the flake distribution and hence, the optical densities of the nanocomposites. The fabrication process is also time consuming due to slow solvent evaporation. This is especially long when high boiling point solvents are used. In this case, inkjet printing of TMDs onto optical components, such as quartz, polymers and optical fibres, can potentially lead to efficient, controlled SA fabrication that enables more flexible laser cavity designs for SA integration. Besides, the sizeable bandgap of TMDs spanning the visible to near-infrared (NIR) spectrum can lead to high performance optoelectronics [6–8]. One such widely reported application is photodetectors [158, 160–162]. Adapting TMDs to inkjet printing can potentially allow large-scale, low-cost photodetector fabrication, avoiding the expensive vacuum deposition and fabrication technologies.

As with graphene, the current ink formulations of TMDs present significant challenges for spatially uniform pattering on untreated substrates. As a result, it is impractical to deliver reproducible and hence, scaled-up device fabrication. In this chapter, using the experimental experience from the graphene ink, I present the design of a binder-free ink formulation of TMDs that overcomes these challenges. To begin with, I investigate production of mono- and few-layer TMD (MoS_2, WS_2 and $MoSe_2$) flakes *via* UALPE. I then extract the TMD flakes through vacuum filtration and redisperse them into a binary alcohol ink carrier for ink formulation. This binary alcohol carrier is carefully designed such that it renders optimal fluidic properties and wetting of untreated substrates, and diminishes the coffee ring effect by an induced Marangoni flow. The inks support large-scale printing with excellent controllability over deposition densities and high print-to-print consistency, as well as additive printing of heterostructures. On this basis, I exploit the inkjet-printed TMDs in large-scale printing of SAs (in collaboration with Prof Meng Zhang at the Beihang University) and photodetectors.

6.1 UALPE production of TMDs

6.1.1 Dispersion production

Similar to graphene, UALPE production of mono- and few-layer TMD flakes has requirements on the solvent properties for the exfoliation and stabilisation of the flakes [237, 276]: the "good" solvents should have a surface tension of $\sim$40 mNm^{-1} and HSPs of δ_D $\sim$18 MPa$^{1/2}$, δ_P $\sim$8.5 MPa$^{1/2}$ and δ_H $\sim$7 MPa$^{1/2}$, respectively [237, 276]. This means that the organic solvents, N-Methyl-2-pyrrolidone (NMP) and cyclohexanone (CHO), previously investigated on graphene are potentially suitable for TMDs. The other solvents (*e.g.* alcohols and water) that do not meet the criteria can exploit ionic and non-ionic surfactants to assist UALPE [286]. Therefore, I investigate UALPE production of TMDs in NMP, CHO, IPA, water/SDC (SDC: 7 gL^{-1}) and IPA/PVP (PVP: 0.15 gL^{-1}). For these experiments, 100 mg of bulk TMDs (MoS_2, WS_2 and $MoSe_2$; Sigma Aldrich) are mixed into 10 mL liquids. The mixtures are sonicated in a 20 kHz bath sonicator for 12 hours at 15°C. The resultant dispersions are then centrifuged at 4 krpm (1500 *g*) for 1 hour. The upper 70% of the resultant dispersions are collected.

Figure 6.1(a) is a photograph of cuvettes containing typical TMD water/SDC dispersions (10 times diluted). Figure 6.1(b) shows the extinction spectra of these diluted dispersions measured using UV-Vis-NIR spectrometer. As shown, the spectra are mostly featureless except for a few extinction peaks as labelled. For MoS_2, there are four major peaks: the

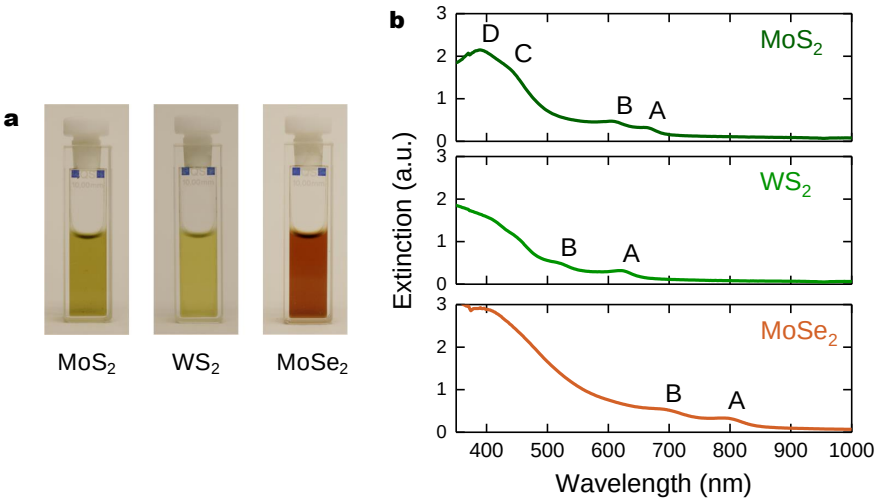

Fig. 6.1 (a) Photographs of the diluted water/SDC dispersions; (b) Optical extinction spectra of the TMD NMP (dashed lines) and water/SDC (solid lines) dispersions, the dispersions are diluted to 10 vol.% to avoid saturation.

peak *A* (∼665 nm) and peak *B* (∼605 nm) are from excitonic transitions, while the peak *C* (∼440 nm) and peak *D* (∼400 nm) are due to the transition between the higher density of state regions of the band structure [428, 429]. For WS_2, there are two major peaks, *i.e.* peak *A* (∼630 nm) and peak *B* (∼520 nm), due to the excitonic transitions [428, 429]. For $MoSe_2$, the peak A and peak B are located at ∼800 nm and ∼710 nm, respectively, also corresponding to the excitonic transitions [428, 429].

Following the Beer-Lambert law ($E = \alpha_\lambda cl$; Section 3.4.1), using α_{672,MoS_2} ∼1268 $Lg^{-1}m^{-1}$, α_{630,WS_2} ∼1324 $Lg^{-1}m^{-1}$ and $\alpha_{710,MoSe_2}$ ∼615 $Lg^{-1}m^{-1}$ (Section 6.1.2), I estimate the concentration of these water/SDC dispersions and the as-produced dispersions in other liquids, as listed in Table 6.1.

As shown, the concentration of the NMP dispersions is typically over 10 times larger than that of the CHO or IPA dispersions, indicating that NMP is the most suitable pure solvent for TMDs. In comparison, water/SDC achieves a concentration >2 times larger

Table 6.1 Concentration of the TMD dispersions

	Concentration (gL^{-1})				
	NMP	CHO	IPA	Water/SDC	IPA/PVP
MoS_2	0.1	0.063	0.013	0.23	0.053
WS_2	0.08	0.066	0.007	0.22	0.032
$MoSe_2$	0.27	0.029	0.037	0.78	0.069

than that of the NMP dispersions, while PVP also significantly improves the concentration of the IPA dispersions. In terms the stability against sedimentation, NMP, water/SDC and IPA/PVP dispersions keep stable for months without visible aggregation, whereas CHO and IPA dispersions typically sediment within several days. The above concentration and the stability, therefore, suggest the feasibility of the NMP, water/SDC and IPA/PVP dispersions for ink formulation.

6.1.2 Determination of optical absorption coefficient

As discussed in Section 3.4.1, optical absorption spectroscopy is widely used as a convenient tool to indirectly estimate the dispersion concentration following the Beer-Lambert law ($E = \alpha_\lambda cl$). To do this, an accurate optical absorption coefficient (α_λ) is crucial. It is commonly determined by correlating the extinction and the estimated concentration of a dispersion [236, 237]. This concentration is acquired by extracting the flakes from a large volume of dispersion through vacuum filtration, and subsequently correlating the mass of the dried flakes with the dispersion volume [236, 237].

However, this method introduces significant errors. Indeed, values of α_λ spread over a wide range have been reported by a same group. Taking MoS_2 as an example, the reported values range from 1020 $Lg^{-1}m^{-1}$ [430] to 3400 $Lg^{-1}m^{-1}$ [237]. The estimated concentration based on these α_λ values therefore is significantly different. The variation may be attributed to the filter membranes of different pore sizes used in these experiments, allowing flakes of different size to pass through the membranes. The flakes may also be insufficiently removed of the residual solvents existing between the flakes and in the membranes. As a result, a significant variation in the estimated mass of the flakes is introduced, leading to the wide spread α_λ.

Here I present an alternative method to improve the accuracy of α_λ. In this method, instead of using filtration, the mass of the dispersed flakes in CHO is measured using a thermogravimetric analysis (TGA) system. TGA is widely used to analyse the changes in the physical and chemical properties of a substance according to the change of mass as a function of increasing temperature. The measurement here is very straightforward. I only take the advantage of the very precise balance of TGA (0.01 μg measurement resolution) and at the same time, ensure all the dispersed flakes, regardless of their size, are measured as the residual mass.

The high decomposition points of these TMDs (*e.g.* MoS_2 1185°C) allow the use of high temperature to decompose the impurities in the TGA systems and that contained in the TMDs and CHO. For the experiment, 100 μL of MoS_2 CHO dispersion is loaded onto the pan of TGA and measured at 800°C. Figure 6.2(a) shows that the residual mass of this MoS_2

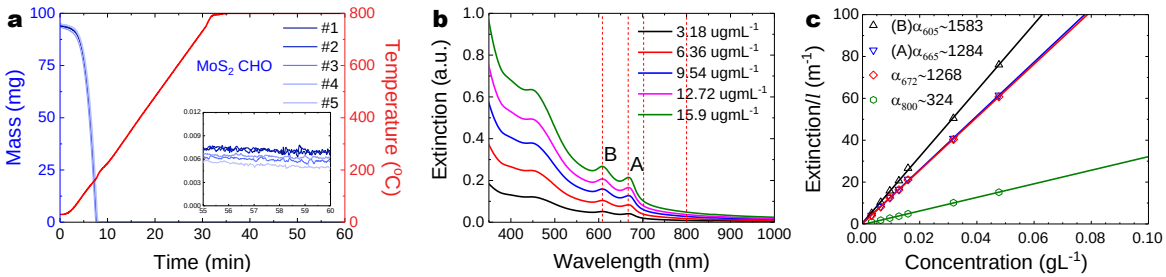

Fig. 6.2 (a) TGA plot of five MoS_2 CHO dispersions with associated temperature profile, inset: stabilized MoS_2 mass at 800°C; (b) Optical extinction spectra for MoS_2 CHO dispersions with different determined concentrations, and associated calculated (c) α at 605, 665, 672 and 800 nm.

CHO dispersion is stabilised at 7.14 µg. Repeating the measurement for five times gives an average residual mass of 6.36 $\pm$ 0.08 µg. Therefore, the concentration of the dispersion is 0.064 gL^{-1}.

Next, I serially dilute the MoS_2 CHO dispersion and measure the optical absorption spectra; Fig. 6.2(b). This gives α_λ of MoS_2 at different wavelengths; Fig. 6.2(c). The wavelengths of 665 nm and 605 nm that correspond to the excitonic absorption peaks are selected to calculate α_λ. In addition, 672 nm is used for comparison with the reported values of α_λ in literature. Indeed, the measured value, $\alpha_{672} \sim 1268$ $Lg^{-1}m^{-1}$, is significantly lower than the reported values (up to 3400 $Lg^{-1}m^{-1}$ [237]). 800 nm is also selected as in a featureless region of the spectrum. Following this strategy, α_λ of WS_2 and $MoSe_2$ are determined and presented in Table 6.2. I note that it is considered that the values should remain largely unaffected by the choice of solvents [236, 237].

Table 6.2 Optical absorption coefficient values for TMDs

	Optical absorption coefficient ($Lg^{-1}m^{-1}$)			
MoS_2	$\alpha_{605} \sim 1583$	$\alpha_{665} \sim 1284$	$\alpha_{672} \sim 1268$	$\alpha_{800} \sim 324$
WS_2	$\alpha_{450} \sim 3738$	$\alpha_{520} \sim 2074$	$\alpha_{630} \sim 1324$	$\alpha_{700} \sim 357$
$MoSe_2$	$\alpha_{410} \sim 3189$	$\alpha_{600} \sim 973$	$\alpha_{710} \sim 615$	$\alpha_{804} \sim 411$

6.1.3 Characterisations of the exfoliated TMD flakes

In this section, I present the AFM and Raman spectroscopy characterisations of the exfoliated TMD flakes in water/SDC dispersions. I mainly exploit the TMD water/SDC dispersions for ink formulation due to their non-toxicity, high concentration and high stability.

AFM characterisation. To prepare the AFM samples, diluted dispersions (5 vol.%) are dropcast onto Si/SiO_2. The samples are then rinsed with water to remove residual SDC to give clean and isolated flakes. Next, the samples are annealed at 120 °C to remove any residual solvent.

Figure 6.3(a) presents AFM scans of typical exfoliated thin TMD flakes. The flakes all have a thickness of ∼3-4 nm and a lateral dimension of ∼90 nm; Fig. 6.3(b). Figure 6.3(c) shows the thickness distribution of the TMD flakes. The acquired average thickness is 4.8 nm for MoS_2, 5.5 nm for WS_2, and 2.6 nm for $MoSe_2$, respectively, demonstrating that the TMDs are successfully exfoliated into thin flakes. For MoS_2, assuming ∼1 nm measured thickness for a monolayer flake and ∼0.7 nm increase in thickness for each additional layer, the estimated average layer number is ∼6 [300]. On the other hand, assuming ∼1 nm measured thickness for a monolayer flake and ∼0.6 nm increase in thickness for each additional layer, the estimated average layer number of WS_2 is ∼8 [431]. And finally for $MoSe_2$, assuming ∼1 nm measured thickness for a monolayer flake and ∼0.7 nm increase in thickness for each additional layer, the estimated average layer number is ∼3 [145, 149]. Meanwhile, the average lateral dimensions for the exfoliated flakes are similar; MoS_2: 50 nm, WS_2: 46 nm, and $MoSe_2$: 61 nm.

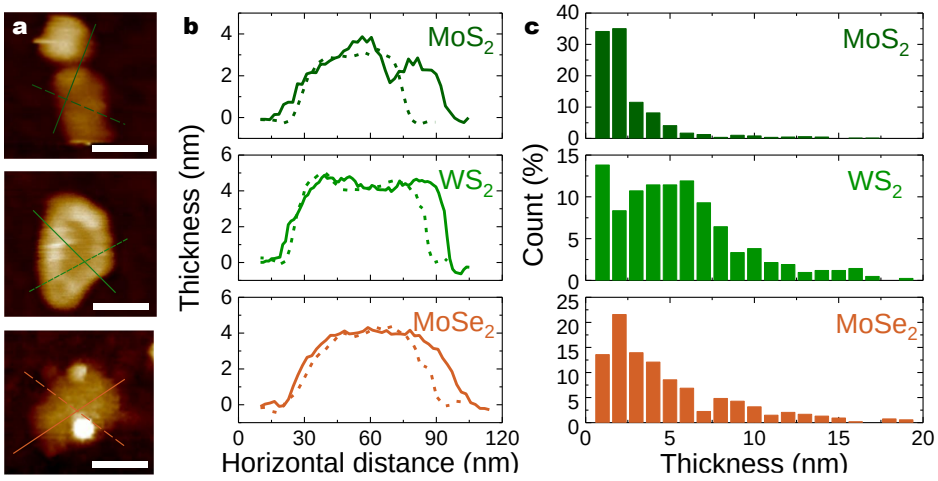

Fig. 6.3 (a) AFM micrographs of typical TMD flakes in water/SDC, and (b) associated thickness profiles, scale bar 50 nm; Distribution of flake (c) thickness and (d) lateral dimension.

Raman spectroscopy. The exfoliated flakes in water/SDC are also characterised by Raman spectroscopy. The dispersions are dropcast onto Si/SiO_2 and dried at 80°C, and subsequently rinsed with water. Raman spectroscopy uses an excitation wavelength of 514 nm with <0.1 mW power and 10 s duration for each measurement. The measurements

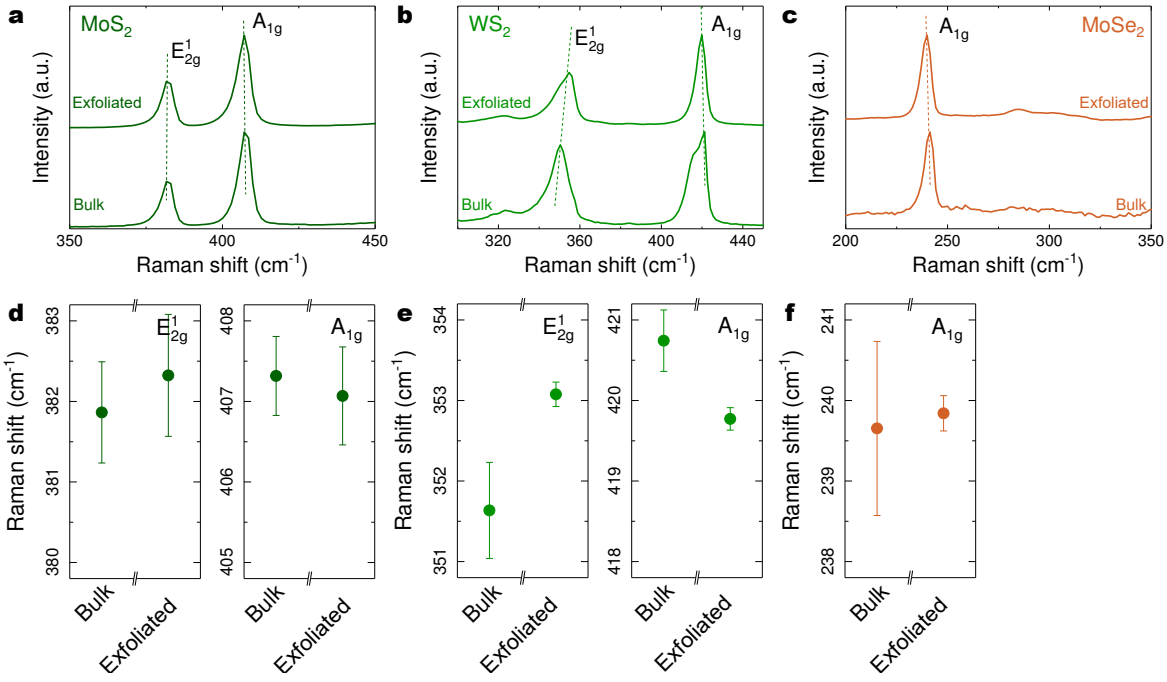

Fig. 6.4 Raman shift spectra for (a) MoS_2, (b) WS_2 and (c) $MoSe_2$: bulk crystals and exfoliated flakes; Raman peak position statistics for (d) MoS_2, (e) WS_2 and (f) $MoSe_2$. Raman excitation wavelength 514 nm.

are also compared with the corresponding bulk crystals (characterised as received from the supplier).

MoS_2 There are two major peaks in the MoS_2 Raman spectrum, located close to 400 cm^{-1} [300, 305, 306]. These peaks correspond to in-plane (E^1_{2g}) and out-of-plane (A_{1g}) vibration modes [300, 305, 306]. The vibration modes vary depending on MoS_2 layer numbers, hence shift in the positions of these two peaks, where E^1_{2g} red-shifts (mono- to bulk) as a result of mode softening, and A_{1g} blue-shifts (mono- to bulk) as a result of mode stiffening [300, 305]. The transition leads to a progressive increase in the difference between the peak positions (Δw) from 18.7 cm^{-1} for mono-layers to 25.5 cm^{-1} for bulk MoS_2.

Figure 6.4(a) presents the typical Raman spectra of the exfoliated MoS_2 flakes and the bulk. The exfoliated spectrum shows a negligible shift in E^1_{2g} and a blue-shift (<1.5 cm^{-1}) in A_{1g}. Figure 6.4(d) presents the Raman peak position statistics of 35 measurement points, showing that E^1_{2g} red-shifts and A_{1g} blue-shifts while Δw decreases from 25.5 cm^{-1} to 25 cm^{-1}. This suggests a successful exfoliation, confirming my AFM characterisation (Fig. 6.3).

WS_2 There are two major peaks in the Raman spectrum for WS_2 at ∼350 cm^{-1} and ∼420 cm^{-1}, corresponding to in-plane (E^1_{2g}) and out-of-plane (A_{1g}) vibration modes, respectively [432]. Similar to what is observed in MoS_2, the shift in peak positions depend on layer numbers, where E^1_{2g} red-shifts and A_{1g} blue-shifts from mono-layer to bulk [432]. Figure 6.4(b) presents the typical Raman spectra of the exfoliated and bulk WS_2. The spectra here exhibit a red-shift (2.8 cm^{-1}) in E^1_{2g} and a blue-shift (2.8 cm^{-1}) in A_{1g}. Figure 6.4(e) shows Raman peak position statistics of 35 measurement points, consistent with the above observation.

$MoSe_2$ There is one major peak in $MoSe_2$ Raman spectrum at ∼240 cm^{-1}, corresponding to out-of-plane (A_{1g}) vibration modes [255]. The peak position of A_{1g} blue-shifts from mono-layer to bulk [255]. Figure 6.4(c) presents the typical Raman spectra of the exfoliated and bulk $MoSe_2$, exhibiting a blue-shift of 1.4 cm^{-1}. The Raman peak position statistics of 35 measurement points (Figure 6.4(f)) also demonstrates a shift in peak position, confirming my AFM observation of exfoliation.

6.2 Large-scale spatially uniform inkjet printing of TMDs

6.2.1 Inkjet printing with IPA/PVP inks

Based on my previous work on inkjet printing of graphene, I investigate the suitability of the TMD IPA/PVP dispersions for inkjet printing. The surface tension (γ), viscosity (η) and density (ρ), giving an inverse Ohnesorge number Z of ∼11.7 ($Z = \sqrt{\gamma\rho a}/\eta$: η ∼1.9 mPa·s, γ ∼28 mNm^{-1}, ρ ∼0.8 gcm^{-3}, and a ∼22 μm). This is within the optimal Z value range (*i.e.* 1-14), indicating that the TMD IPA/PVP dispersions possess suitable fluidic properties for inkjet printing. The dispersions are therefore termed as "TMD IPA/PVP inks" for the following work.

Figure 6.5(a) presents dark-field optical micrographs of printed lines defined under 35 μm and 60 °C on untreated Si/SiO_2, showing no coffee rings. I suggest the mechanism is similar to what I propose for the graphene IPA/PVP ink (Section 5.2.1): The presence of PVP leads to a colloidal dispersion such that the dispersed TMD flakes are not that readily transferred to the droplet edges by the evaporation induced outward convection flow upon drying, especially during the final stage of drying when the viscosity is increased. Therefore, the TMD IPA/PVP dispersions are suitable for inkjet printing with the optimal fluidic properties and uniform flake distribution.

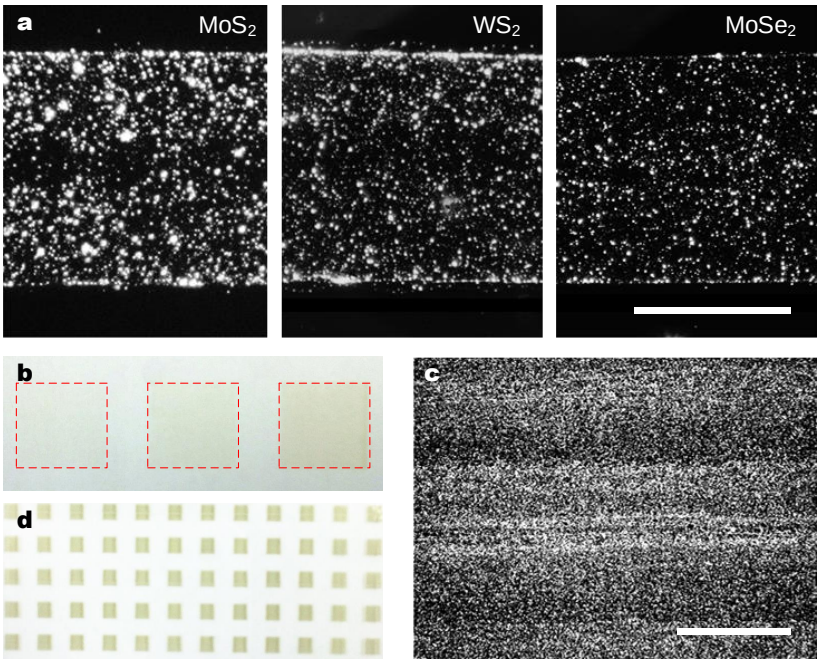

Fig. 6.5 (a) Optical dark-field micrographs of printed MoS_2, WS_2 and $MoSe_2$ lines on untreated Si/SiO_2, showing an even flake distribution, droplet spacing of 35 µm, substrate temperature 60°C, scale bar 50 µm; (b) Photograph of 10 mm × 10 mm MoS_2 squares with 5, 10 and 15 printing repetitions on untreated glass, and (c) corresponding optical micrograph of the printed MoS_2 on untreated glass, scale bar 200 µm; (d) Photograph of a 2 mm × 2 mm MoS_2 square array with 30 printing repetitions on untreated glass.

The printing is then scaled up for glass substrate; Fig. 6.5(b-d). As shown, the printed MoS_2 squares in Fig. 6.5(b) are all well-defined with clear edges and a high spatial uniformity, while the contrast increases along with the printing repetition. Figure 6.5(c) is a corresponding dark-field optical microscopy image, further demonstrating that the MoS_2 flakes are uniformly distributed on glass. Meanwhile, all the individual squares in the array (Fig. 6.5(d)) are visually spatially uniform and identical to the others without noticeable differences.

However, the concentration of the TMD flakes in the IPA/PVP inks is <0.1 gL^{-1}, meaning that many printing repetitions may be required to deposit sufficient TMD flakes. To retain the optoelectronic properties of TMDs, PVP also needs to be removed after printing through >400°C annealing. This limits the choice of substrates for the TMD IPA/PVP inks. Therefore, the TMD IPA/PVP inks are not ideal for the development of devices, in particular flexible applications using polymeric substrates.

6.2.2 Inkjet printing with IPA/2-butanol inks

As discussed in Section 4.4.3, the NMP, water/SDC and water/IPA UALPE dispersions all present significant challenges for spatially uniform inkjet printing on untreated substrates. A significant improvement on ink formulation is therefore required. Prior to my work, the state of art 2d material ink formations incorporated polymer binders (*e.g.* cellulose) to produce highly-concentrated inks for improved printing morphologies [51, 56]. However, similar to the case of the TMD IPA/PVP inks, I intend to avoid this strategy as the polymers would require high temperature decomposition for the majority of optoelectronic applications.

In this section, I design a binder-free highly-concentrated ink formulation of TMDs for inkjet printing that allows spatially uniform printing onto substrates without pre- or post-printing treatments.

Ink formulation. Given the considerations on the toxicity of NMP and the high concentration of water/SDC dispersions, I investigate ink formulation using the water/SDC dispersions. For the convenience of formulation, the TMD flakes are extracted from the UALPE dispersions through vacuum filtration. The flakes are then repeatedly washed with water to remove the residual surfactants and dried in oven at 80°C.

To allow stable droplet jetting for large-scale inkjet printing, the ink has to be designed with 1-14 for the inverse Ohnesorge number Z [37, 62, 346]. Also, since the surface tension of an ink has to be 7-10 mNm^{-1} lower than the substrate surface energy to allow wetting for continuous printing features [350], the ink composition needs to tailored to achieve a surface tension $<$30 mNm^{-1} such that the ink can wet substrates such as Si/SiO_2 and glass ($\sim$36 mNm^{-1} [360]), and polyethylene terephthalate (PET, $\sim$45 mNm^{-1} [361]). In addition, as discussed in Section 4.3.3, studies show that creating a surface-tension-driven flow (Marangoni flow) may help redistribute the dispersed materials for a uniform distribution [355]. Such a flow can be created by inducing a temperature/composition gradient during the ink drying process [354, 358]. This could be achieved by using two solvents of different evaporative rates [354, 358]. I therefore propose a binary solvent ink carrier strategy for the TMD ink formulation that meets the above requirements.

Alcohols are widely used in graphics and functional inks [311] and recent graphene inks [56]. Indeed, alcohols such as IPA exhibit optimal Z values (Table 6.3). Their low surface tensions (typically $<$30 mNm^{-1}) also ensure wetting of untreated substrates. Therefore, alcohols can provide promising solvent choices, and indeed, I have demonstrated IPA based graphene and TMD inks for spatially uniform inkjet printing. IPA is therefore selected as the primary solvent for the TMD ink formulation. To develop the binary solvent carrier, I investigate two other alcohols, methanol and 2-butanol, which have relative evaporative rates

Table 6.3 Z of alcohols and the TMD IPA/2-butanol inks

	Z parameters				Z
	η (mPa·s)	γ (mNm^{-1})	ρ (gcm^{-3})	a (μm)	
Methanol	0.6	23	0.8	22	34
Ethanol	1.1	22	0.8	22	18
IPA	2.0	23	0.8	22	10
2-butanol	4.2	23	0.8	22	5
TMD IPA/2-butanol inks	2.2	28	0.8	22	10

against IPA of 2.7 and 0.2, respectively [433]. Their surface tension is all similar to that of IPA (*i.e.* 23 mNm^{-1}). For ink formulation, the extracted flakes are redispersed simply *via* bath sonication into the binary alcohol mixtures with a concentration of 1 gL^{-1}. The secondary alcohol in the mixtures is varied with 10 or 20 vol.%. Figure 6.6(a) is a photograph showing the formulated dispersions. In comparison, I also prepare an ink in pure IPA.

Figure 6.6(b-d) present dark-field optical micrographs of the dried droplets, showing that IPA forms condensed coffee rings, and IPA/methanol exhibits a heavier flake deposition around the interior ring. However, both IPA/2-butanol show no coffee rings. The coffee ring effect in IPA is attributed to a solo outward flow driven by the higher solvent evaporative rates at the droplet edges [60]. For IPA/methanol, in addition to the outward flow, I propose that a circulating Marangoni flow is induced; Fig. 6.6(f). As methanol evaporates rapidly from the droplet edges upon drying, an evaporation-induced temperature gradient due to latent heat of vapourisation is generated [355]. Driven by this, a surface tension gradient ascending from droplet the centre to the edges is established, which has to be suppressed by a circulating Marangoni flow. In the case of IPA/2-butanol, however, I propose a recirculating Marangoni flow is induced; Fig. 6.6(g). Since IPA evaporates faster from the droplet edges, the edges then have an increased concentration of 2-butanol, hence a reversed temperature gradient due to latent heat of vapourisation [355]. This induces a recirculating Marangoni flow, redistributing the flakes from the droplet edges back to the centre to form an even flake distribution. IPA/2-butanol (20 vol.%), however, exhibits a more condensed deposition at the droplet edges compared to IPA/2-butanol (10 vol.%), suggesting that its induced recirculating Marangoni flow is not strong enough. Also, the dried droplet diameter increases as the volume percentage of 2-butanol increases, with ∼68 μm for 10 vol.% and ∼80 μm for 20 vol.%. An increase in diameter is undesirable as it decreases the printing resolution. This suggests that 10 vol.% is a better ink carrier design.

To confirm that 10 vol.% ink formulation suppresses the coffee ring effect, I measure time-resolved contact angle of the IPA/2-butanol (10 vol.%) dispersion upon drying. As

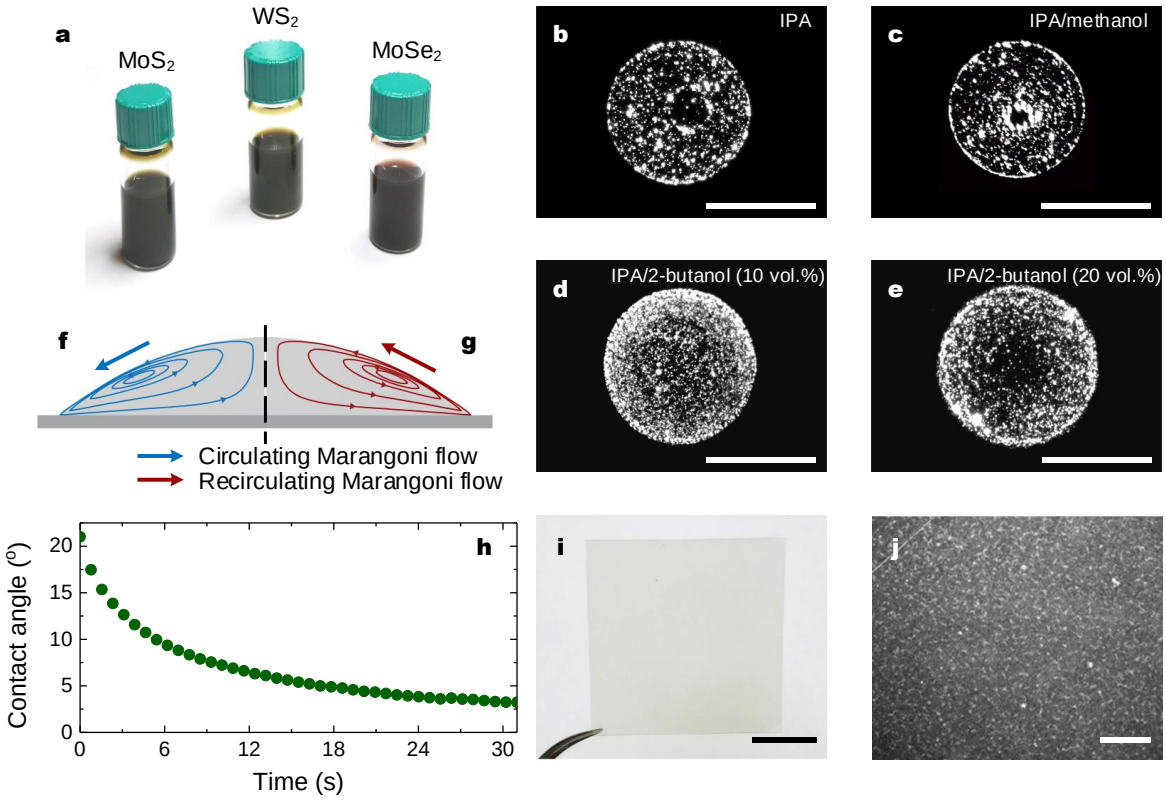

Fig. 6.6 (a) Photograph of the formulated TMD inks; (b-e) Typical optical dark-field micrographs of dried droplets (∼10 pL) in different solvents showing that IPA/2-butanol (10 vol.%) avoids coffee rings, substrate: untreated Si/SiO_2, scale bar 50 µm. IPA/2-butanol (10 vol.%) is therefore chosen as the ink carrier. The contrast has been increased for clarity; Schematic figure showing redistribution of the flakes *via* (f) circulating and (g) recirculating Marangoni flow; (h) Typical time-resolved contact angle of the ink droplet during drying on untreated Si/SiO_2; (i) Spatially uniform, continuous deposition of the ink on untreated PET, scale bar 1 cm, and (j) corresponding optical dark-field micrograph, scale bar 200 µm. The ink is deposited *via* spray coating. (b-e, h-j) are demonstrated with the MoS_2 ink.

shown in Fig. 6.6(h), the acquired contact angle plot is absent from any prominent spikes during the entire drying process. This suggests no sudden, sharp receding of the droplet happened, *i.e.* no coffee rings formed. Given the considerations above, IPA/2-butanol (10 vol.%) is selected for the ink formulation, and the IPA/2-butanol (10 vol.%) dispersions are termed as "IPA/2-butanol inks".

The Z of the IPA/2-butanol inks is ∼10 (Table 6.3), suggesting a stable jetting without formation of satellite droplets. Meanwhile, an ink surface tension of ∼28 mNm^{-1} can wet untreated Si/SiO_2, glass and PET. Indeed, the MoS_2 ink after deposition onto untreated PET *via* spray coating coalesces and forms a continuous film; Fig. 6.6(i,j).

A homemade laser system (Fig. 6.7(a)) is used to assess the ink stability against sedimentation. A 632 nm laser beam is used to transmit through the inks. The inks are diluted to 5 vol.% to avoid absorption saturation during measurement. The laser intensity transmitted through the diluted ink is collected every 100 seconds for 48 hours, while the laser intensity transmitted through the ink carrier (IPA/2-butanol (10 vol.%)) is collected as the baseline. The acquired light intensity absorbed by the TMD flakes, *i.e.* the difference between the base laser intensity and the laser intensity transmitted through the diluted inks, is plotted as normalised absorption in Fig. 6.7(b). For the MoS_2 ink, the absorption shows a drop of $<3\%$, indicating $<3\%$ MoS_2 flakes sediment. Similarly, WS_2 and MoS_2 flakes are stabilised with $<10\%$ and $<10\%$ sedimentation, respectively. This demonstrates a high ink stability that is sufficient for large-scale ink production and printing processes.

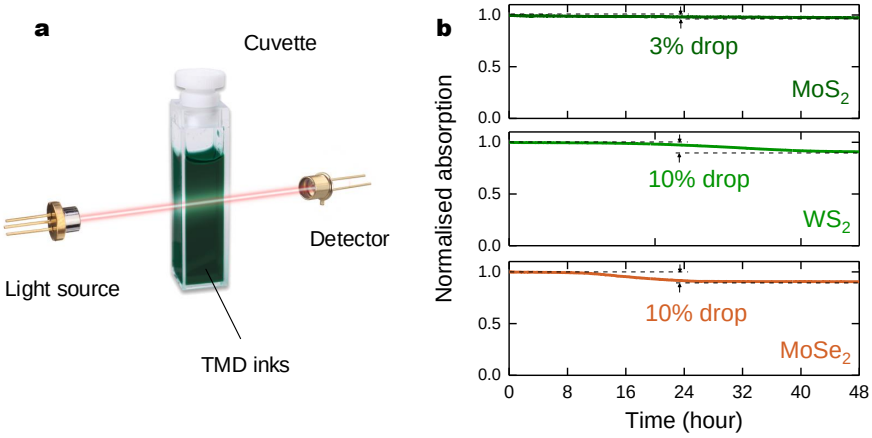

Fig. 6.7 (a) Schematic figure for the homemade ink stability measurement system; (b) Normalised absorption against time, the inks are diluted to 5 vol.%.

Inkjet printing. With optimal fluidic properties, the IPA/2-butanol inks deliver stable jetting of single droplets during printing. This is observed from the printer stroboscopic camera; Fig. 6.8(a). As discussed in Section 4.3.2, the morphologies of inkjet-printed structures are governed by droplet merging behaviour, rendering "stacked coins", "bulging", "uniform edges", "scalloping" and "isolated droplets". This is essentially defined by the droplet spacing (D) and the dried droplet diameter (D_0). Indeed, I demonstrate this with the graphene ink; Section 5.2.1. D_0 is dependent on the substrate temperature; Fig. 6.8(b). Here I show that the variations of D and D_0 produce vastly different morphologies with the inks; Fig. 6.8(c,d). Figure 6.8(c) presents printed lines of MoS_2 on untreated Si/SiO_2 with single printing repetition under varied D, with a fixed D_0 of 68 µm. While D is small (15 µm), printing forms a broad line of stacked coins. A D of 25 µm forms bulges along a thinner line.

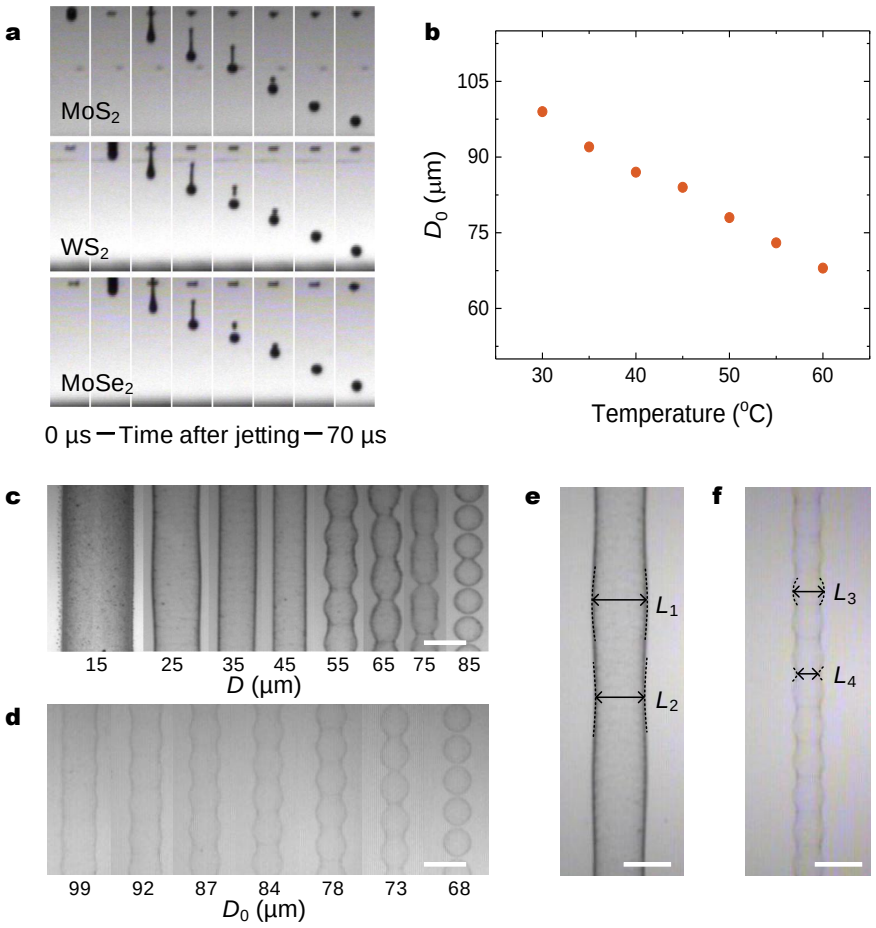

Fig. 6.8 (a) Ink droplet jetting sequence, observed through the printer stroboscopic camera; (b) Dried droplet diameter (D_0) of MoS_2 ink droplets on untreated Si/SiO_2 with respect to the substrate temperature; Photographs of typical printed lines with single printing repetition under (c) varied droplet spacing (D), D_0 68 µm, and (d) varied D_0, D 85 µm; Printed lines on untreated Si/SiO_2 with D (e) 25 µm and (f) 55 µm, D_0 68 µm. (b-f) are demonstrated with the MoS_2 ink. Scale bar 100 µm.

Further increase in D (35 µm) eliminates the bulges, producing line with uniform edges. A larger D (45 µm) gives a uniform edges line of a smaller width. Printing with D >55 µm leads to insufficient merging and as such, scalloping lines and even isolated droplets. Meanwhile, Fig. 6.8(d) show that D_0 presents similar effects, delivering vastly different morphologies.

I propose that a key consideration to distinctly tell the morphology of stacked coins, bulging, uniform, scalloped lines or isolated droplets is the peak-to-peak roughness (ξ) along the line edges. Here, ξ is defined as (L_a - L_b) / 2, where L_a and L_b is the maximum and minimum width of a printed line, respectively. And a ξ <2 µm is considered as the criterion for uniform edges. Figure 6.8(e) replots the bulging line defined at 25 µm in Figure 6.8(c), where the maximal width L_1 is ∼119 µm and the minimal width L_2 is ∼108 µm. The

roughness therefore is calculated as (L_1 - L_2) / 2 = (119 - 108) / 2 µm = 5.5 µm. For the scalloping line defined at 55 µm in Fig. 6.8(f), the maximal width L_3 is ~78 µm and the minimal width L_4 is ~62 µm. So the roughness is calculated as (L_3 - L_4) / 2 = (78 -62) / 2 µm = 8 µm. To clearly distinguish the lines, the roughness of stacked coins and bulging is defined as negative, while scalloping and individual droplets as positive. Therefore, the edge roughness is -5.5 µm for the line in Fig. 6.8(e), and 8 µm for the line in Fig. 6.8(f).

The estimation of ξ allows the generation of colour map of ξ value with respect to D and D_0; Fig. 6.9(a). As shown, the uniform edge region has distinct boundaries for the bulging and scalloping regions. The D/D_0 of this uniform edge region is 0.5-0.8. This provides a general printing guidance: a droplet spacing of 0.5-0.8 of the dried droplet diameter is required for printing with well-defined, uniform edges towards spatially uniform morphology of printed structures.

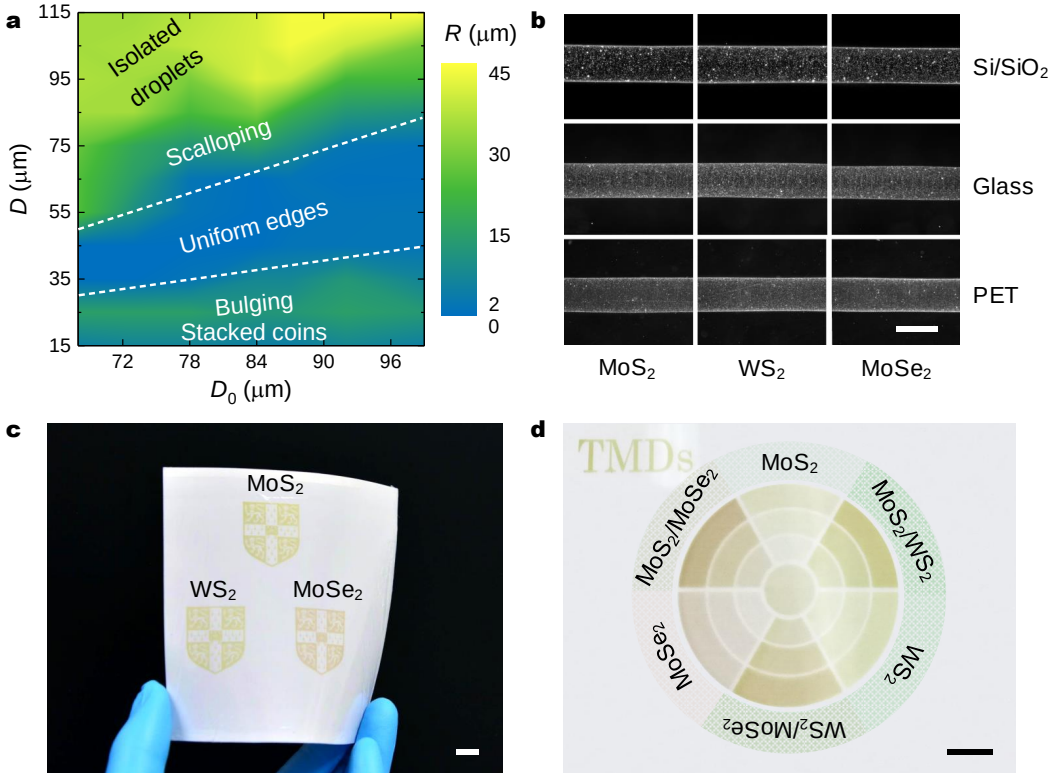

Fig. 6.9 (a) Edge roughness ξ with respect to D and D_0, demonstrated with the MoS_2 ink; (b) Optical dark-field micrographs of printed lines on untreated Si/SiO_2, glass and PET, scale bar 100 µm. The contrast has been increased for clarity; (c) Printed University of Cambridge crest on untreated ultrathin PET (thickness 1.5 µm, laminated onto photopaper), scale bar 1 cm; (d) Three "colour" gradient, overlapped printing of on untreated PET, scale bar 1 cm.

Using this criteria, I achieve high quality printing of MoS_2, WS_2 and $MoSe_2$ on untreated Si/SiO_2, glass and PET; Fig. 6.9(b). As observed, the flakes are evenly distributed in width along the entire length in all the cases, showing no coffee rings. The results obtained indicate that my formulated inks are suitable for scaled-up printing. As a demonstration, Fig. 6.9(c) presents printing of high resolution pattern over 1 inch scale on ultrathin PET (thickness 1.5 μm). Figure 6.9(d) presents gradient, overlapped printing of TMDs over 2 inch scale, where the overlaps of MoS_2/WS_2, $MoS_2/MoSe_2$, $WS_2/MoSe_2$ and $MoS_2/WS_2/MoSe_2$ (the middle circular area) are clearly defined and spatially uniform. This suggests the potential of the inks to form printable heterostructure thin films.

Printing characteristics. Having demonstrated that large-scale spatially uniform printing is possible for the formulated inks, I next investigate the printing characteristics. Figure 6.10(a) presents a photograph of printed MoS_2 square array on untreated PET, showing that the individual squares are spatially uniform and identical. Spatial colour intensity is extracted from this photograph for a detailed investigation; Fig. 6.10(b). This shows that the colour intensity is spatially uniform within each individual square, without showing evident differences across the investigated squares. In addition, the intensity profiles of the first row and the first column are both highly consistent. To provide a closer assessment of the spatial uniformity, the colour intensity profiles of the first square in the array is represented in Fig. 6.10(c). As shown, the acquired horizontal and vertical intensities at different positions are also highly consistent. Due to spreading of ink from 60 printing repetitions, I do not observe sharp square edges. Instead, the colour intensity gradually increases and stabilises. Therefore, only the intensity of the internal region ($\sim$80%) of the square is considered, giving an estimation of the average spatial colour intensity as 0.835 ± 0.007. The small 1% deviation demonstrates a high spatial printing uniformity of the printed squares. In addition, the average intensities are highly consistent across the square array, giving a print-to-print deviation of $<$2.5%.

Next, a sequence of squares (dimension 8 mm $\times$ 8 mm) is printed onto untreated glass with 1-10 printing repetitions. The measured optical absorbance at 550 nm of these squares is linearly correlated with the repetition; Fig. 6.10(d). This gives an absorbance of 0.0167 ± 0.0004 per repetition for MoS_2, of 0.0164 ± 0.0004 per repetition for WS_2, and of 0.0109 ± 0.0001 per repetition for $MoSe_2$. I note that the absorbance deviation of 1-2 printing repetitions observed is likely due to a modification in the air-glass interface after printing. TMD stripes (dimension 1.5 mm $\times$ 1 mm) are printed with 30-80 printing repetitions. The thickness of the stripes measured *via* profilometer establishes a linear function with the repetitions, giving that one printing repetition produces a deposition

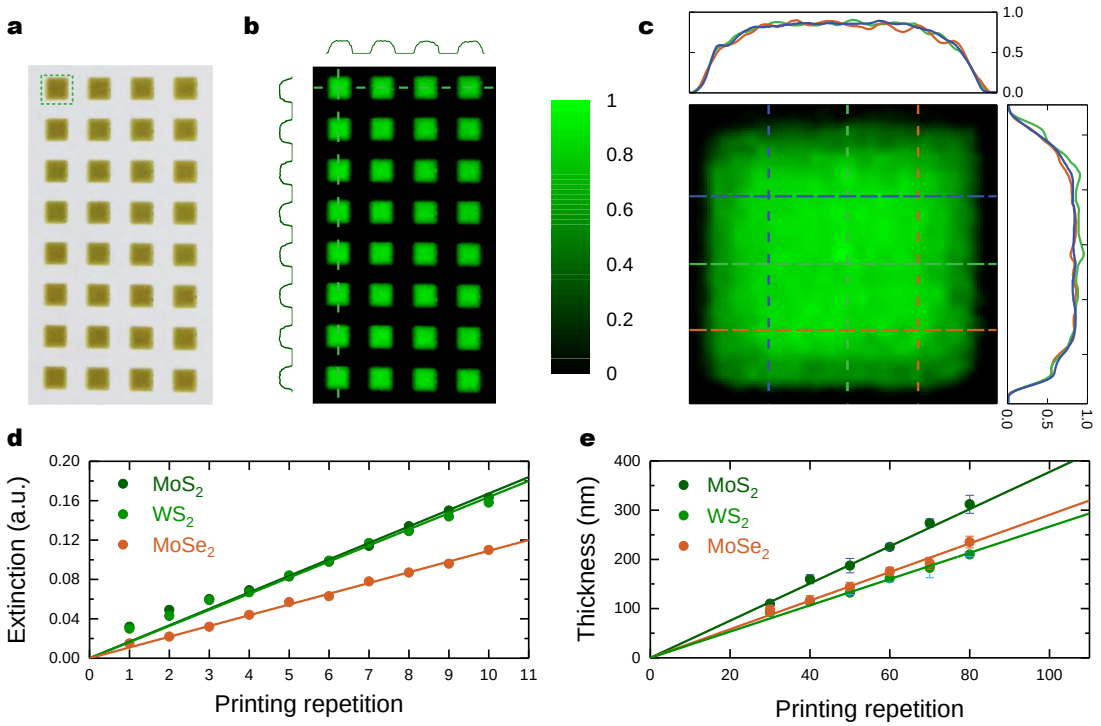

Fig. 6.10 (a) Photograph of printed MoS_2 square (square dimension 2 mm $\times$ 2 mm) array on untreated PET, and its (b) extracted spatial colour intensity with horizontal/vertical intensity profiles across the first row/column. The intensity of the background is normalised to 0, while the intensity of the maximum spike is normalised to 1; (c) Spatial colour intensity of the first square as circled with horizontal/vertical intensity profiles. The dashed lines indicate the investigated positions; (d) Optical extinction at 550 nm and (e) thickness of printed TMDs as a function of printing repetition.

thickness of 3.85 $\pm$ 0.04 nm, 2.68 $\pm$ 0.05 nm and 2.89 $\pm$ 0.05 nm, respectively; 6.10(b). The investigations above demonstrate the capabilities of the inks to precisely control the optical and material densities of printed films, with $<$2.5% deviation.

6.3 Inkjet-printed TMD saturable absorbers

As discussed, the TMD flake enriched polymer nanocomposite SAs present challenges in the control of flake distribution and optical density and requires long preparation process. Alternatively, the SAs can be potentially fabricated by inkjet printing of TMDs onto optical components. This can lead to efficient, controlled device fabrication, and more flexible lasers designs for SA integration. In this section, I investigate the feasibility of inkjet-printed TMDs in the fabrication of SAs, aiming to achieve large-scale printing of SAs with stable device operation for ultrashort pulse generation. This work was in collaboration with Prof Meng

Zhang at the Beihang University. My key contributions in this work were fabricating the SAs, analysing the measurement data, and writing the manuscript which has been submitted for peer-reviewed journal for the consideration of publication.

For SA fabrication, I inkjet print TMD SA array onto the ultrathin PET, which is laminated onto 100 µm thick PET for the ease of handling. The SA pattern is square with a dimension of 2 × 2 mm, and an array typically has over 60 devices. The fabricated TMD SAs can be conveniently peeled off from the 100 µm thick PET to be integrated into laser cavity. The optical properties of the inkjet-printed SAs are next measured using Z-scan technique. Figure 6.11(a) is a schematic Z-scan set-up. As shown, during a typical Z-scan measurement, the mounted sample is moved through the focus of a laser beam along the axis from the position $-Z$ to position $+Z$. This allows the transmitted power to be measured as a function of incident intensity on the sample. Figure 6.11(b) represents a schematic intensity-dependent absorption profile. This absorption can be fitted using a simple two-level saturation model [435, 436]:

$$\alpha(I) = \frac{\alpha_l - \alpha_{ns}}{1 + I/I_{sat}} + \alpha_{ns} \tag{6.1}$$

where α_{l} is the linear absorption at low intensity and α_{ns} is the nonsaturable absorption at high intensity, I is the instantaneous intensity, and I_{sat} is the saturation intensity. The modulation depth (α_{d}) of a device is given by: $\alpha_{\mathrm{d}} = \alpha_{\mathrm{l}} - \alpha_{\mathrm{ns}}$. Consequently, I_{sat} can be defined as the intensity required to reduce the absorption $\alpha(I)$ to $\alpha_{\mathrm{l}} - (\alpha_{\mathrm{d}} / 2)$.

The Z-scan set-up in this measurement utilises an erbium fibre laser operating at 1562 nm, with 150 fs pulse duration at a repetition frequency of 10 MHz. The acquired spatial saturation intensity (I_{sat}), optical linear absorption (α_{l}), optical non-saturable absorption (α_{ns}) and optical modulation depth (α_{d}) are shown in Fig. 6.12 and Table 6.4. This demonstrates that the optical properties of the inkjet-printed SAs all are spatially uniform. This is of vital importance for repeatable operation and performance for ultrashort laser pulse generation.

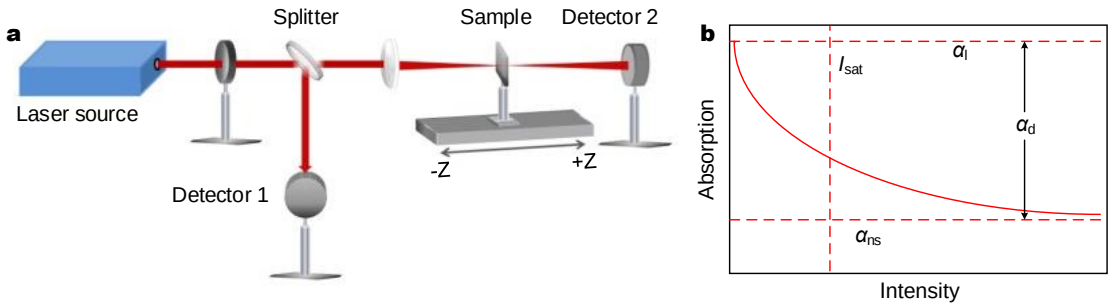

Fig. 6.11 (a) Schematic figure for Z-scan set-up [434]; (b) Schematic SA absorption profile.

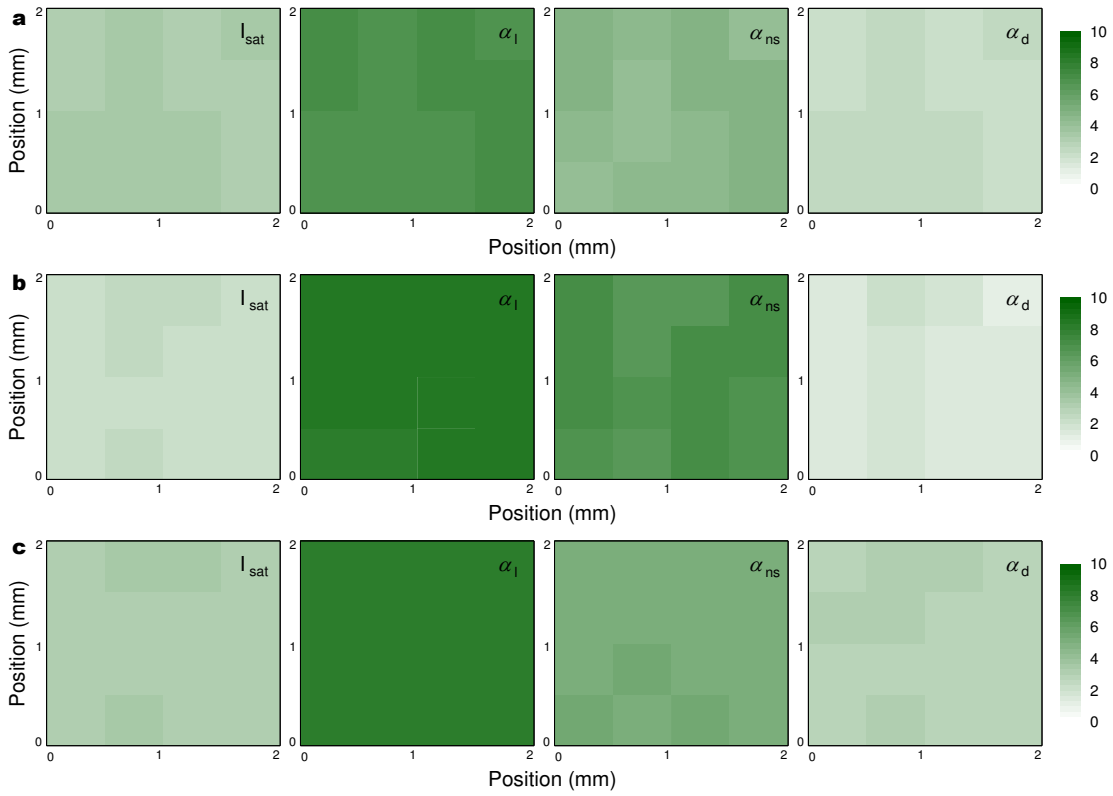

Fig. 6.12 Spatial saturation intensity (I_{sat}, MWcm^{-2}), linear absorption (α_{l}, %), non-saturable absorption (α_{ns}, %), and modulation depth (α_{d}, %) at 1560 nm of the inkjet-printed SAs of (a) MoS_2, (b) WS_2 and (c) $MoS2_2$, spatial step 0.5 mm.

Table 6.4 Average optical absorption of inkjet-printed TMD SAs acquired *via* Z-scan

	α_{l} (%)	α_{ns} (%)	α_{d} (%)	I_{sat} (MWcm^{-2})
MoS_2	6.9 ± 0.13	4.5 ± 0.22	2.38 ± 0.11	3.37 ± 0.11
WS_2	8.4 ± 0.10	6.6 ± 0.22	1.59 ± 0.20	2.26 ± 0.14
$MoSe_2$	8.2 ± 0.10	5.3 ± 0.17	2.9 ± 0.16	3.27 ± 0.13

The printed TMD SAs are then integrated into erbium-doped fibre laser cavity; Fig. 6.13(a). This offers an alignment-free and compact system with single-mode all-fibre integrated components: a single-mode erbium-doped active fibre (LIEKKI Er-8/125, length 0.7 cm) co-pumped by a 980 nm pump laser diode, a polarisation-independent optical isolator to ensure unidirectional propagation, a 10:90 fused fibre output coupler for both spectral and temporal diagnostics, and a polarisation controller to enable a thorough and continuous adjustment of the net cavity birefringence.

This allows generation of a stable self-starting mode-locked train of femtosecond pulses; Fig. 6.13(b). As shown, the pulses are generated at the fundamental cavity repetition

frequency of 31.6 MHz with a central wavelength of ∼1560 nm. The full width at half maximum are ∼4.41 nm for MoS_2, ∼5.87 nm for WS_2 and ∼4.31 nm for $MoSe_2$; Fig. 6.13(b). The corresponding autocorrelation traces of the pulses are well fitted with $sech^2$ pulse shape, indicating pulse duration of 580 fs, 510 fs and 570 fs, respectively; Fig. 6.13(c). The RF spectra at the fundamental frequency show high signal to noise ratios of ∼59 dB, ∼63 dB

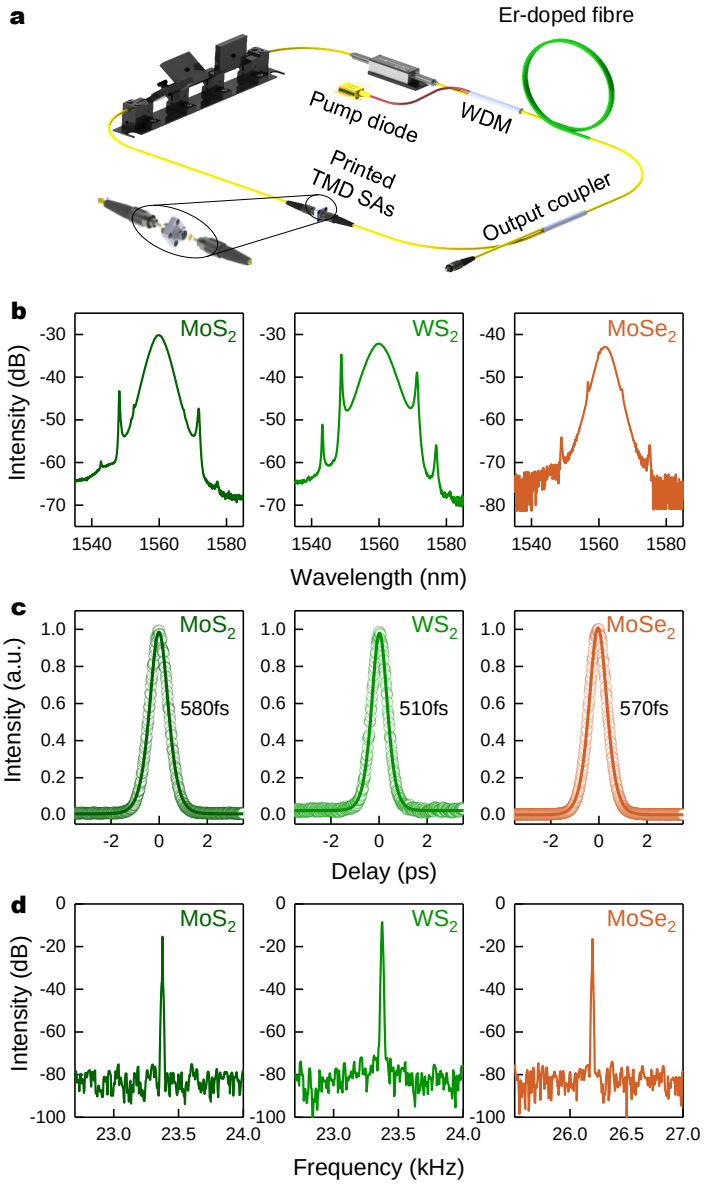

Fig. 6.13 (a) Schematic figure for the erbium-doped ultrafast fibre laser set-up; (b) Output laser pulse spectra; (c) Autocorrelation trace of output pulses, fitted to a $sech^2$ curve; (d) Radio frequency spectra at the cavity fundamental repetition frequency of 31.6 MHz.

and ∼60 dB respectively (Fig. 6.13(d)), indicating a highly stable mode-locking operation capability [437].

I note that 1560 nm corresponds to 0.8 eV, smaller than the bandgaps of these TMDs (>1.0 eV [4]). This sub-bandgap absorption can be attributed to an edge-state effect [438]: edge defects in thin flakes can induce localised edge-states within the bandgap, as a result a non-negligible optical absorption lower than the bandgap.

6.4 Inkjet-printed TMD photodetectors

There is a tremendous interest in developing visible to NIR photodetectors with the TMDs due to their ∼1.0-2.5 eV bandgap and high photoconductivity [4, 158]. Indeed, photodetectors exploiting micro-mechanically cleaved (MC) or chemical vapour deposition (CVD)-grown flakes have been widely reported. For instance, Lopez-Sanchez *et al.* demonstrated a photoresponsivity (R_p) of up to 800 AW^{-1} from micro-mechanical cleaved MoS_2 photodetector [158]. However, such material production methods present low-yield fabrication and require extreme production conditions, limiting large-scale, cost-effective device fabrication [1]. Inkjet printing of TMDs provides a promising solution, with successful laboratory-scale demonstrations to date [40, 41, 48]. A scaled-up device printing with reproducible fabrication, however, is thus-far prevented by the reported ink formulations. I propose that the demonstrated high quality printing of TMDs can potentially lead to large-scale device printing with consistent device-to-device performance.

Figure 6.14(a) presents an array of printed MoS_2 photodetectors, where the ink is inkjet-printed onto the interdigitated gold electrodes (Fig. 6.14(b)) with the MoS_2 flakes uniformly deposited (Fig. 6.14(c)). The photoresponse of the printed photodetectors is characterised using a 635 nm excitation laser with an incident excitation power of 5-40 μW. As shown in Fig. 6.14(d), compared to the dark current, the current under excitation is typically over one order of magnitude larger, with a R_p of up to 150 μAW^{-1}. Figure 6.14(e) presents the time response of the device, showing that the current under excitation remains stable over a period of 60 s (<5% deviation). The photoresponse as a function of the printed MoS_2 thickness (controlled by printing repetitions; Fig. 6.10(e)) is plotted in Fig. 6.14(f). As observed, the current under dark and excitation establishe a linear function with the thickness (log-log scale). This linearity allows conveniently control the device photoresponse. After investigating the device characteristics, the device-to-device consistency is investigated. As presented in Fig. 6.14(g,h), the acquired dark current and R_p of this photodetector array is 0.051 ± 0.0026 nA and 8.77 ± 0.81 μAW^{-1}, respectively, demonstrating a high device-to-device consistency (<10% deviation).

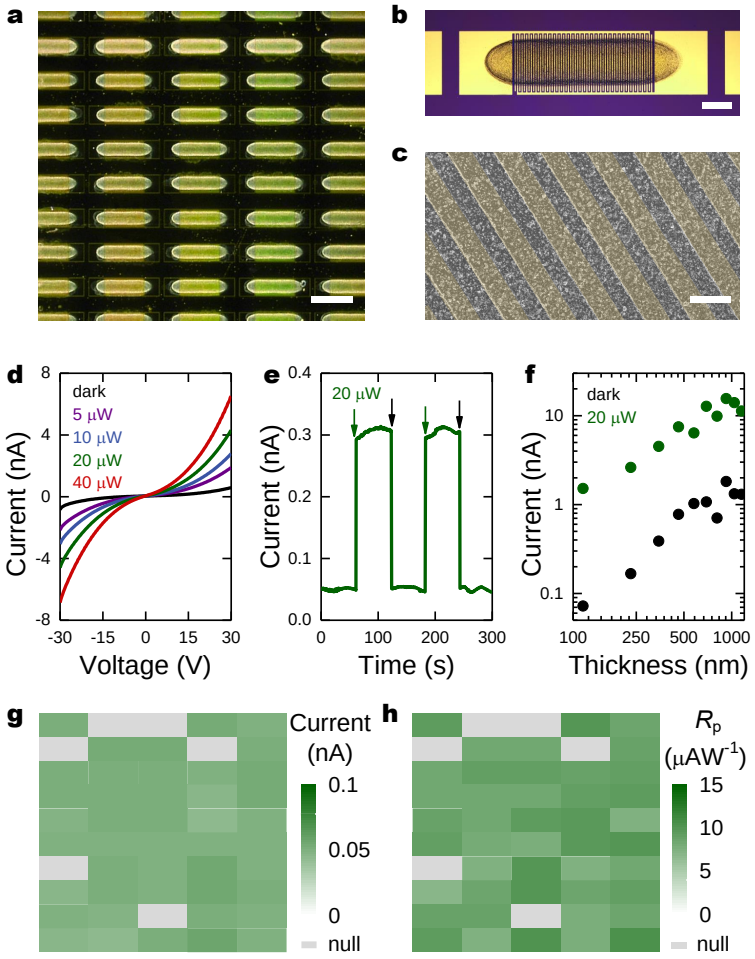

Fig. 6.14 (a) Optical dark-field graph for printed MoS_2 photodetector array, scale bar 500 μm; (b) Micrograph of one single device, scale bar 100 μm; (c) SEM micrograph showing flake distribution over the interdigitated electrodes as coloured, scale bar 100 μm; (d) Typical device current response to varied excitation powers; (e) Typical time response, bias 5 V. The green and black arrows indicate excitation on and off; (f) Device current under dark and excitation as a function of the thickness of printed MoS_2, bias 30 V; Mapping of (g) dark current and (h) photoresponsivity (R_p) under 40 μW of the photodetector array, bias 5 V. The "null" grey spots stand for short-circuited devices. The excitation laser is 635 nm.

Following the same strategy, WS_2 and $MoSe_2$ photodetector arrays are fabricated and characterised. Figure 6.15(a,b) present mapping of R_p under 40 μW excitation at 5 V for the WS_2 and $MoSe_2$ photodetector array with acquired R_p of 2.64 ± 0.25 μAW^{-1} and 16.97 ± 5.58 μAW^{-1}, respectively. Therefore, the device-to-device R_p deviation for the WS_2 and $MoSe_2$ photodetector array is 9.5% and 32.9%, respectively. Figure 6.15(c) presents typical time response of $MoSe_2$ photodetector, showing that the current decreases upon excitation. This suggests that the $MoSe_2$ photodetector devices are not stable upon

the measurements, induced either by the incident light or the applied electrical current. Therefore, I propose that the large deviation of R_p of the $MoSe_2$ photodetector array is due to the instability of $MoSe_2$ but not this device fabrication method. For future experiments, this can likely be addressed by using passivation layer, such as parylene-C. Nevertheless, the R_p of the MoS_2 and WS_2 photodetector arrays exhibit a device-to-device deviation $<10\%$. This demonstrates the capability of the TMD IPA/2-butanol inks for large-scale device fabrications with high device-to-device consistency, promising for large-scale device printing.

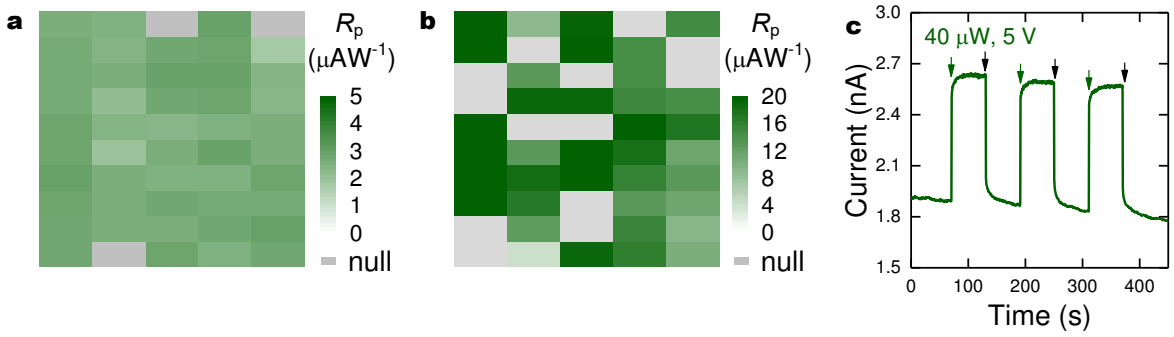

Fig. 6.15 Mapping of photoresponsivity (R_p) under 40 μW at 5 V for (a) WS_2 and (b) $MoSe_2$ photodetector array. The "null" grey spots stand for short-circuited devices. (c) Typical time response of $MoSe_2$ photodetector. The green and black arrows indicate excitation on and off. The excitation laser is 635 nm.

6.5 Summary

In this chapter, I have presented the formulation of binder-free inks of TMDs (MoS_2, WS_2, $MoSe_2$) with large-scale, spatially uniform printing capabilities, and use of which in the fabrication of SAs and photodetector. The TMD flakes are produced *via* UALPE. For ink formulation, I design a binary alcohol ink carrier of IPA and 2-butanol. The formulated inks ensure stable jetting and wetting of untreated substrates including Si/SiO_2, glass and PET. In particular, the designed ink carrier composition induces a recirculating Marangoni flow upon drying to allow even distribution of the flakes on untreated substrates. I also show that the morphologies of the inkjet-printed structures are governed by droplet spacing and dried droplet diameter and hence, present a guidance to seek the optimal printing parameters. Under this guidance, the inks support spatially uniform inkjet printing (1% deviation), with high printing controllability over deposition densities ($<2.5\%$ deviation) and high print-to-print consistency ($<2.5\%$ deviation).

Combining the above printing characteristics with the properties of TMDs, I demonstrate inkjet-printed TMDs based SAs and photodetectors. In particular, the photodetector exhibits

a high device-to-device performance consistency (<10% deviation), demonstrating the potential of the ink for large-scale device printing. Inkjet printing of TMDs with this ink formulation strategy may find use in other optoelectronic and photonic devices [16, 37, 39–42, 48]. Other inks of 2d materials can also be formulated following this strategy, for example the black phosphorus ink in Chapter 7, significantly expanding the potential of inkjet printing of 2d materials for optoelectronics and photonics.

Chapter 7

Inkjet printing of black phosphorus for stable optoelectronics and photonics

In the previous chapters, I presented inkjet printing of graphene and transition metal dichalcogenides (TMDs) and their printable applications. Black phosphorus (BP) is an emerging key 2d material that bridges the gap between graphene and TMDs with unique properties (*e.g.* 0.3-2.0 eV direct bandgap) that could be exploited in optoelectronics and photonics. Ultrasonic-assisted liquid phase exfoliation (UALPE), in protective environment, has been exampled as a mass production method for BP. However, as discussed in Section 2.4, the oxidative degradation of BP under ambient conditions has thus-far prevented controlled deposition of the BP dispersions for device applications.

My previous experimental work on alcohol based ink formulations of graphene and TMDs demonstrates rapid, spatially uniform patterning of these 2d materials at low temperatures. I propose that formulating exfoliated BP flakes into such inks would allow a rapid ink drying and hence, a limited window of time available for BP oxidation during printing. In this chapter, I investigate BP ink formulation following the binary alcohol strategy. I also raise the ink concentration significantly to reduce the number of printing repetitions required to deposit sufficient BP, such that the window of time available for BP oxidation is further decreased. I then investigate passivation of the printed BP with parylene-C (*i.e.* a cross-linked polymer widely used in electronic packaging) to achieve a long-term stability against oxidation. In collaboration with Prof Meng Zhang at the Beihang University and Prof Yang Xu at the Zhejiang University, I explore fabrication of robust photonic and optoelectronic devices with printed BP, including saturable absorbers (SAs) for stable generation of ultrashort pulses under intense irradiation for $>$30 days, and visible to near-infrared (NIR) photodetector devices with operation lifetime $>$7 days.

In this chapter, I present the results published in *Nature Communications*: Ref. [439]. My key contributions were formulating the BP ink, fabricating the SAs and photodetectors, analysing the measurement data, and writing the manuscript.

7.1 UALPE production of black phosphorus

7.1.1 Dispersion production

As discussed in Section 3.3.1, a successful UALPE production of BP without aggregation requires a matched surface tension ($\sim$40 mNm^{-1}) for the solvents. The suitable solvents are typically high boiling point organic solvents, such as N-Methyl-2-pyrrolidone (NMP; 204°C) and N-Cyclohexyl-2-pyrrolidone (CHP; 284°C) [178, 181, 310]. In particular, recent experimental investigations on UALPE of BP in such solvents in protective environment (*e.g.* under nitrogen atmosphere) show the as-produced BP flakes are of minimal oxidation [178, 181, 310]. Therefore, I start BP production with both these solvents. My previous work on inkjet printing of graphene and TMDs demonstrates that alcohol (*e.g.* isopropanol: IPA, 82.6°C) based inks are capable of delivering rapid, spatially uniform patterning. To minimise the drying time of the BP dispersion and hence, BP oxidation, I also investigate UALPE in IPA.

To do this, I mix bulk BP crystals (Smart Elements) into anhydrous NMP, CHP and IPA (Sigma Aldrich) in sonication tubes at an initial concentration of 1 gL^{-1}. I then backfill the tubes with nitrogen and seal them. The mixtures are sonicated for 12 hours in a 20 kHz bath sonicator at 15°C. The resultant dispersions are loaded into tubes, backfilled with nitrogen, and centrifuged for 30 minutes to sediment the unexfoliated flakes. The centrifuge speeds chosen are 1, 2, 3 and 4 krpm (equivalent to 95g, 380g, 850g and 1500g, respectively). The upper 80% of resultant dispersions is collected for analysis and ink formulation.

Figure 7.1(a) shows photographs of the as-produced BP dispersions in NMP, CHP and IPA. At a higher centrifugation speed, the increased sedimentation force leads to a lower concentration, and hence a more colourless dispersion. The distribution of flake size (thickness and lateral dimension) in the dispersion varies with the centrifugation speed, as less exfoliated larger and thicker flakes sediment more readily [294, 296, 430]. The dispersions centrifuged at 4 krpm are therefore selected for following discussions. The optical extinction spectrum (log-log scale) for each dispersion (Fig. 7.1(b)) has a peak at $\sim$465 nm, with an approximately linear decrease at longer wavelengths ($>$500 nm). Using the extinction coefficient, 267 Lg^{-1}m^{-1} at 660 nm [178], the concentrations of the NMP, CHP and IPA dispersions are estimated as 0.54 gL^{-1}, 0.32 gL^{-1} and 0.13 gL^{-1}, respectively.

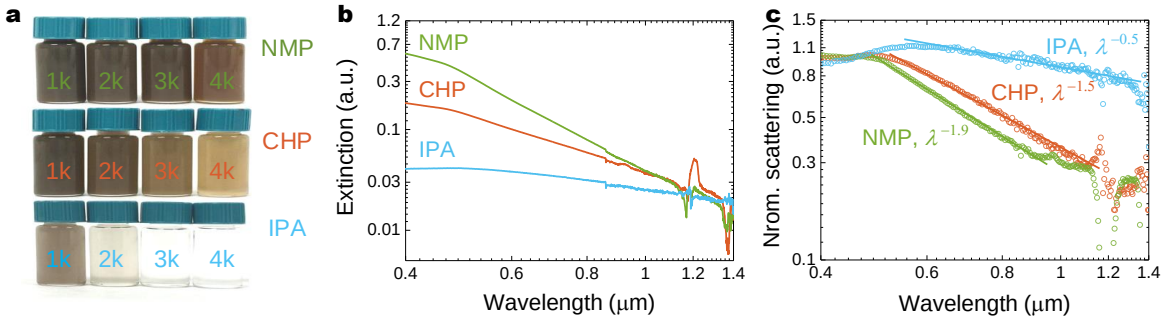

Fig. 7.1 (a) Photographs of the BP dispersions in NMP, CHP and IPA, centrifuged at 1-4 krpm; (b) Optical extinction (log-log scale) of the BP dispersions (centrifuged at 4 krpm) with respect to the wavelength (λ), the dispersions are diluted to 10 vol.% to avoid detector saturation; (c) Optical scattering with associated fitting (log-log scale) of the dispersions, with scattering normalised to the 465 nm extinction peak.

The extinction variations observed at the NIR region can be attributed to the ambient moisture absorbed by the solvents during the exfoliation process [440, 441].

7.1.2 Characterisations on black phosphorus flake size

I then study the flake size of the as-produced BP flakes. As briefly mentioned in Section 3.4.1, the measured optical extinction is subjected to optical scattering from the flakes. This scattering is proportional to the incident wavelength following λ^{-n}, where λ is the wavelength and n is the scattering exponent [296, 430]. Here, the scattering of the BP dispersions is evaluated by subtracting the absorbance obtained using an integrating sphere from the measured extinction; Fig. 7.1(c). The scattering at the longer wavelength region is fitted to $\lambda^{-1.9}$ within ~500-900 nm for NMP, $\lambda^{-1.5}$ within ~550-1100 nm for CHP and $\lambda^{-0.5}$ within ~600-1300 nm for IPA, respectively. A n <4 corresponds to Mie scattering [442, 443], allowing estimation of the characteristic dimensional length of the dispersed flakes.

Treating the BP flakes as non-spherical particles with a characteristic dimensional length L, the relationship between scattering and wavelength can be expressed as a dimensionless size parameter k, where $k = 2\pi L / \lambda$ [442, 443]. For Mie scattering, k ~1 [442, 443]. Therefore, the characteristic dimensional lengths of the BP flakes in the three dispersions are estimated as approximately 80-145 nm, 90-175 nm and 95-210 nm, typical for UALPE 2d material flakes [133, 236, 237, 423, 424, 426, 427]. Meanwhile, the larger n of the NMP dispersion indicates that BP is better exfoliated (producing thinner and smaller flakes) in NMP than in either CHP or IPA [296, 430, 442].

I employ AFM to characterise the BP flake size to confirm the above estimations. Figure 7.2(a) presents representative AFM micrographs of individual thin BP flakes produced

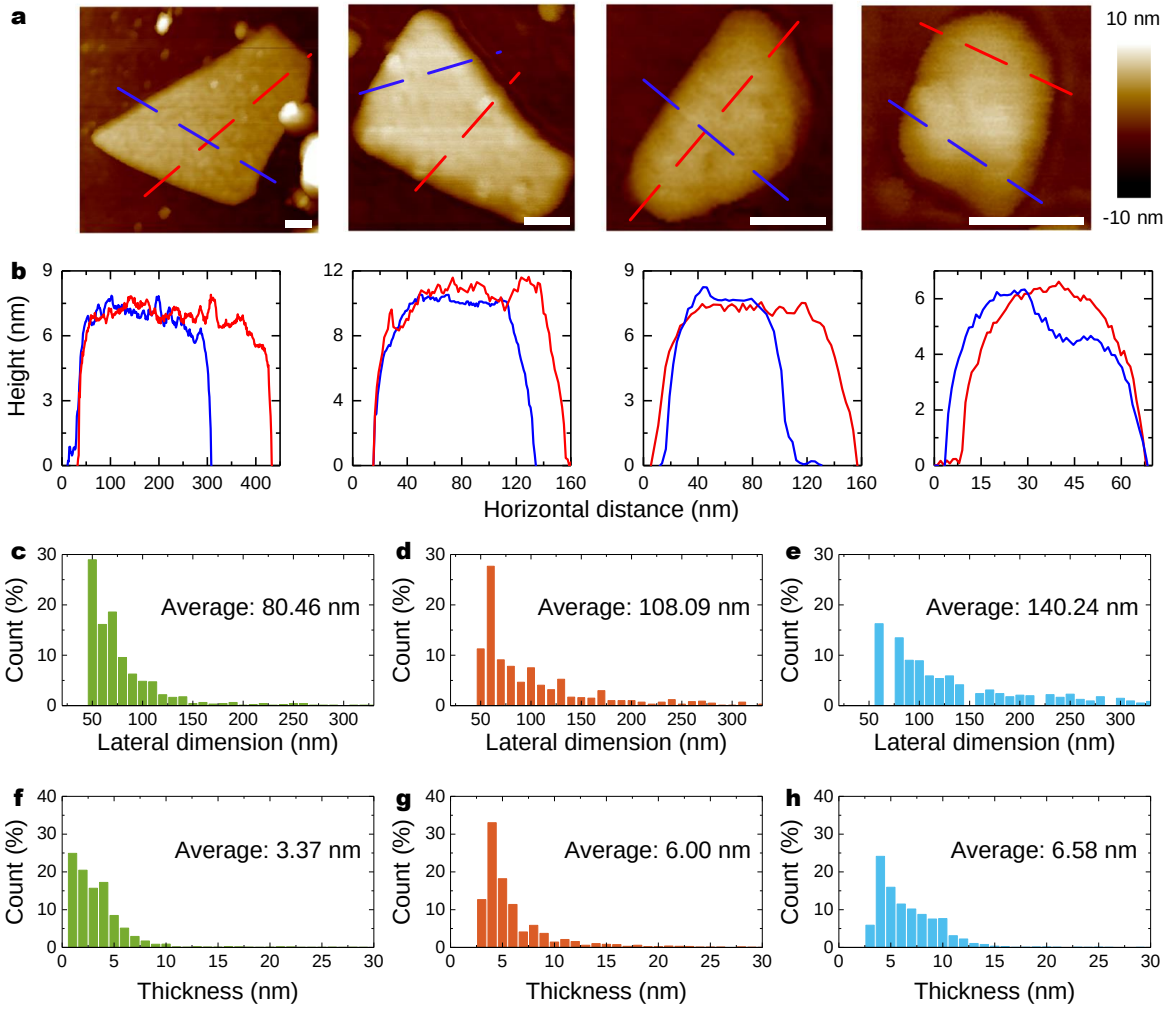

Fig. 7.2 (a) Representative AFM micrographs for individual BP flakes in NMP and (b) the corresponding height profiles, scale bar 50 nm; (b) Distribution in (c-e) lateral dimension and (f-h) thickness of BP flakes measured *via* AFM for the NMP, CHP and IPA dispersions.

in NMP, showing that all the flakes have clean surfaces with clearly defined edges. This suggests that the flakes are not oxidised. The lateral dimension of these BP flakes is varied between 70 nm and 400 nm, while the thickness is typically 4-10 nm; Fig. 7.2(b). I note that the larger, thicker flakes have sharper edges and more distinct morphologies than the smaller flakes, owing to the size and thickness-dependent rate of oxidation over the duration of the scan since the AFM measurements are taken under ambient conditions. Here faster scans of lower but sufficient resolution are used for gathering of size and thickness distributions as presented in Fig. 7.2(d-h). The acquired average lateral dimension correlates well with the estimated characteristic lengths.

Given the consideration on the above investigations, I select the NMP dispersion for ink formulation. The average flake thickness in NMP is 3.37 nm, ∼6 layers (considering 0.9 nm for the first single layer and 0.5 nm for subsequent individual layers [190, 444]).

7.1.3 Raman spectroscopy

As discussed in Section 3.4.3, Raman is a well-suited non-destructive characterisation tool to investigate the quality of the as-produced BP flakes, as well as their oxidation conditions. I then characterise the quality and oxidation of the BP flakes in the NMP dispersion using Raman spectroscopy. The sample is prepared by dropcasting the NMP dispersion onto a Si/SiO_2 and subsequently dried at 70°C under nitrogen. The Raman spectroscopy characterisation uses an excitation wavelength of 514 nm with a power of $<$0.1 mW and a duration of 10 s for each data point.

As discussed in Section 3.4.3, there are debates on whether the Raman spectrum of solution-processed BP is polarisation-dependent. I therefore conduct independent polarisation-dependent Raman measurement to shed light on this. For this case, Raman spectroscopy is measured at one single point for each polarised angle; Fig. 7.3(a). The peak intensities here are normalised to $I(A_g^2)$. As shown, there are three major peaks at around 400 cm^{-1} (out-of-plane A_g^1, and in-plane B_{2g} and A_g^2), of which the intensities show no observable variations under the varied polarisation angles. This demonstrates that the Raman spectrum of my exfoliated BP sample is polarisation-independent. The reasons accounting for this may be that a large number of BP flakes are studied within the area of the laser spot (∼1 μm) during one measurement, and that there is no alignment in the orientation of these flakes. As demonstrated, this nullifies the polarisation dependence.

To study the quality of the exfoliated BP flakes, I compare their Raman spectrum with that of the bulk BP; Fig. 7.3(b). As shown, the respective peaks are all located at ∼363.0 cm^{-1} (∼361.9 cm^{-1}), ∼439.3 cm^{-1} (∼438.3 cm^{-1}) and ∼467.4 cm^{-1} (∼466.4 cm^{-1}) for the exfoliated (bulk) BP sample. This is consistent with previous studies on micro-mechanical cleavage (MC) [189, 190] and UALPE [178, 181, 186, 283, 310] production of BP. Since the peaks are due to BP crystalline lattice vibrations [189], this consistency suggests that my exfoliated BP sample is high crystallinity. Meanwhile, these three peaks show a blue-shift from the bulk to the exfoliated sample, suggesting exfoliation, which has been demonstrated by AFM. On the other hand, the respective full-width at half maximum (FWHM) of these three Raman peaks is 3.9 (3.7) cm^{-1}, 5.3 (5.5) cm^{-1} and 4.9 (3.9) cm^{-1} for the exfoliated (bulk) BP sample. This is also consistent with the preceding studies where the respective FWHM is all within ∼2-6.5 cm^{-1}, ∼2-7 cm^{-1} and ∼2-8 cm^{-1} [190]. Here the acquired FWHM statistical investigation (∼360 measurements) as shown in Fig. 7.3(c) also notes

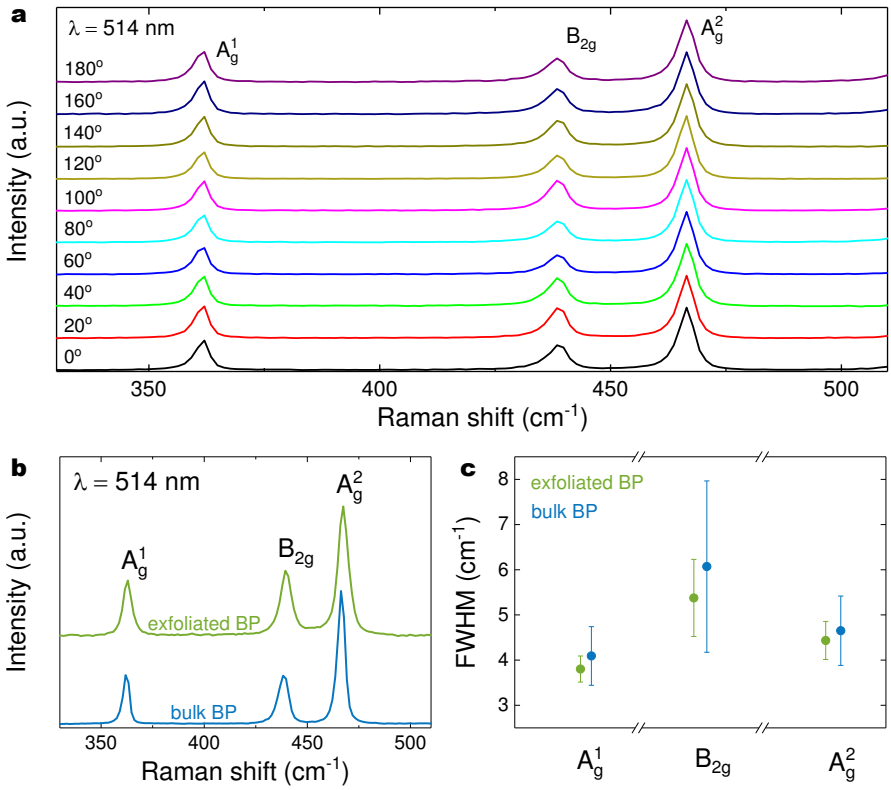

Fig. 7.3 (a) Polarisation-resolved Raman spectra of dropcast dried BP, intensity normalised to $I(A_g^2)$; (b) Raman spectrum for exfoliated and bulk BP, intensity normalised to $I(A_g^2)$; (c) Raman peak FWHM statistics of ∼360 measurement points.

no discrepancy from those above reported in literature. This consistency in FWHM further suggests high crystallinity of the exfoliated BP sample.

7.1.4 Discussion on stability against oxidation

Having shown the BP to be highly crystalline, I then investigate the oxidation conditions of the exfoliated BP flakes through Raman spectroscopy. As discussed in Section 3.4.3, the relationship between the Raman peaks, A_g^1 and A_g^2, has been used as an indication for BP oxidation [181, 190]. However, there are debates on whether the intensity ratio or the integrated intensity ratio of A_g^1 to A_g^2 should be used as the indication. There is also no agreement on the ratio value threshold to determine the oxidation condition (*i.e.* whether the ratio value should be 0.2-0.6 or >0.6). I therefore carry out independent analysis on this ratio.

Figure 7.4(a) represents the intensity ratio, $I(A_g^1)/I(A_g^2)$, acquired from Fig. 7.3(a). This shows that the intensity ratio is constant (0.480 ± 0.04) under the varied polarisation angles,

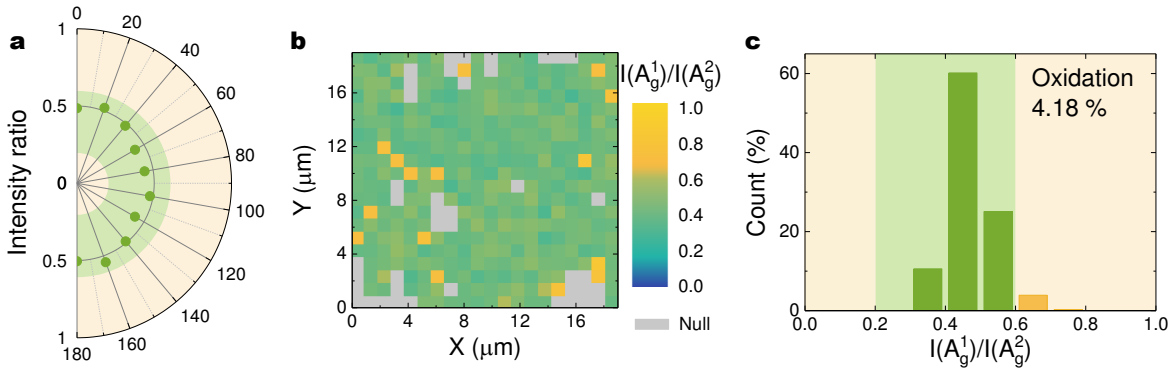

Fig. 7.4 (a) Polarisation-resolved Raman peak intensity ratio, $I(A_g^1)/I(A_g^2)$; (b) Raman map of $I(A_g^1)/I(A_g^2)$ with 1 μm spatial step, and the (c) corresponding histogram. The green region corresponds to low oxidation, and the yellow region high oxidation; the grey squares correspond to regions where the Raman intensity is too low for accurate interpretation.

suggesting that polarisation dependence of $I(A_g^1)/I(A_g^2)$ has also been nullified due to the random distribution of the BP flakes. Figure 7.4(b) shows a Raman map of $I(A_g^1)/I(A_g^2)$ for a typical region of exfoliated BP flakes deposited onto Si/SiO_2, showing no localised clusters with $I(A_g^1)/I(A_g^2)$ >0.6. Figure 7.4(c) is the corresponding histogram, showing that only 4.2% of the measured data points fall outside the 0.2-0.6 range (yellow background). Similar statistical analysis on freshly cleaved bulk BP shows that only 3.1% of the measured data points fall outside the 0.2-0.6 range.

Table 7.1 lists the above intensity ratio and corresponding integrated intensity ratio. This suggests that a ratio value of 0.2-0.6 indicates a low oxidation, otherwise this would mean that 96.9% or 83.9% of the freshly cleaved bulk BP had been oxidised, which is unlikely to happen. On the other hand, the intensity ratio is consistent with BP oxidation process, *i.e.* the high oxidation proportion increases from 3.1% for the bulk BP sample to 4.2% for the exfoliated BP sample. The integrated peak intensity ratio, however, does not prove such consistency. This suggests that the intensity ratio is a reasonable tool to work as the oxidation indication for my exfoliated BP sample.

Table 7.1 Raman integrated intensity ratio and intensity ratio of A_g^1 to A_g^2 outside 0.2-0.6 (%).

	Intensity ratio	Integrated intensity ratio
Bulk BP	3.1	16.1
Exfoliated BP	4.2	1.7

Therefore, I use a peak intensity ratio, $I(A_g^1)/I(A_g^2)$, of 0.2-0.6 as the criterion to determine low oxidation of BP. The proportion 4.2% shows that the UALPE BP flakes are of minimal oxidation.

7.2 Inkjet printing and passivation of black phosphorus

7.2.1 Ink formulation

I then consider inkjet printing of the BP NMP dispersion. In addition to spatially non-uniform deposition arising from suboptimal fluidic properties, poor wetting of the substrates and the formation of coffee rings (Section 4.4.3), the long drying time as a result of the high boiling point of NMP causes heavy oxidation of the deposited BP flakes. It is therefore challenging to deliver inkjet-printable BP based devices so far. In Section 6.2.2, I present a binary alcohol ink formulation of TMDs for spatially uniform material deposition. In particular, the low boiling point of the alcohols enables a rapid ink drying. By adapting this ink formulation to BP, it is therefore possible to give a well-controlled window of time for BP oxidation under ambient conditions during printing. By further increasing the concentration from <1 gL^{-1}, it further reduces the printing repetition numbers and hence, further avoid BP oxidation. Therefore, I formulate BP ink following this binary alcohol ink formulation.

To begin with, I prepare a BP NMP dispersion. I then use a secondary centrifugation step (275,000g for 30 minutes) to sediment the exfoliated BP flakes in the dispersion. Next, I redisperse the sedimented BP flakes in IPA through bath sonication for 10 minutes. The volume of IPA used is 10% of the removed NMP, allowing the concentration of BP increased by 9 times. To finalise the ink formulation, I add 10 vol.% 2-butanol into the redispersed IPA dispersion. The formulated ink is shown in Fig. 7.5(a). For comparison, another ink with 20 vol.% 2-butanol is prepared.

Figure 7.5(b) presents the optical dark-field micrographs of the dried droplets of the above dispersion/inks, while their time-dependent contact angle profiles are presented in Fig. 7.5(b). The droplets are all $\sim$10 pL and inkjet-printed onto untreated Si/SiO_2 and dried at 60°C. As observed, 0 vol.% forms noticeable coffee rings, while both 10 vol.% and 20 vol.% do not, similar to what has been observed with inkjet printing of the TMD inks. The lack of coffee ring suggests that a surface tension gradient is also generated to induce a recirculating Marangoni flow in both the 10 vol.% and 20 vol.% cases. However, the droplet diameter of 20 vol.% ($\sim$85 μm) is also larger that of 10 vol.% ($\sim$75 μm), suggesting a decreased printing resolution for 20 vol.%. Meanwhile, the contact angle for 0 vol.% shows noticeable variations at the end drying process, confirming that the droplet indeed has formed rapidly

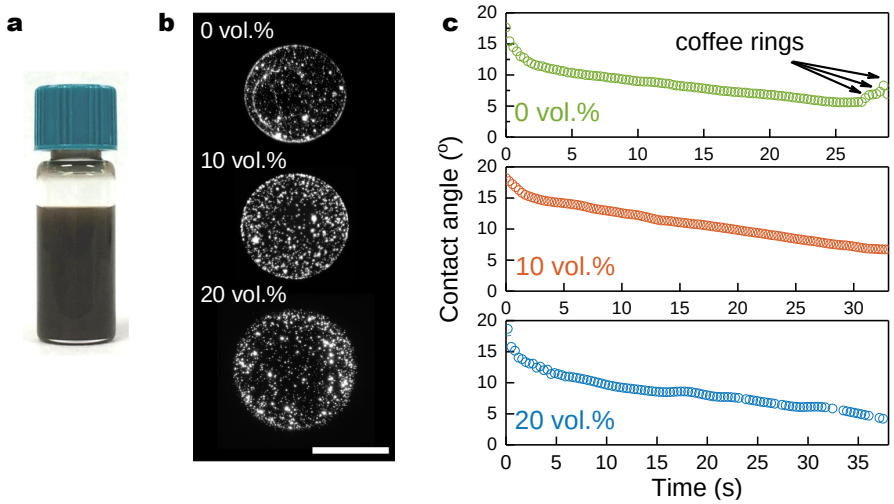

Fig. 7.5 (a) Photograph of formulated BP inkjet ink; (b) Optical micrograph of dried droplets on untreated Si/SiO_2 with 0 vol.%, 10 vol.% and 20 vol.% 2-butanol, scale bar 50 µm; (c) Change in contact angle during droplet (∼2 µL) drying process on untreated Si/SiO_2 at room temperature.

contracts and left a series of material rings. For the case of 10 vol.% and 20 vol.%, the contact angle is absent from any large variations, confirming the lack of coffee ring effect. Based on the above considerations on the coffee-ring effect and the printing resolution, 10 vol.% is confirmed for the ink formulation.

The formulated BP ink has a concentration ∼5 gL^{-1} (compared to 1 gL^{-1} of the TMD inks), verified *via* optical extinction. The optical scattering of the ink can also be fitted to $\lambda^{-1.9}$, consistent with the NMP dispersion, indicating that the ink formulation steps do not induce reaggregation of the BP flakes. The ink possesses an inverse Ohnesorge number Z of ∼10 ($Z = \sqrt{\gamma\rho a}/\eta$: η ∼2.2 mPa·s, γ ∼28 mNm^{-1}, ρ ∼0.8 gcm^{-3}, and a ∼22 µm). This is within the optimal value range for stable jetting, confirmed by the jetting sequence without the formation of secondary droplets (Fig. 7.7(a)). The low ink surface tension gives a contact angle $<30^{\circ}$ on the substrates (Si/SiO_2, glass and PET), ensuring good wetting.

Before conducting inkjet printing with the BP ink, I need to ensure an ink stability against sedimentation. This is done with the homemade stability measurement system (Fig. 6.7(a)). Similarly, a BP ink (diluted to 5 vol.% to avoid absorption saturation) is measured over one week with 5 mins interval. The acquired light intensity absorbed by the BP flakes, *i.e.* the difference between the base laser intensity and the laser intensity transmitted through the diluted ink, is plotted as normalised absorption in Fig. 7.6(a). The absorbed intensity shows only a 1% drop over 180 hours, indicating <1% BP flakes sediment. This demonstrates the

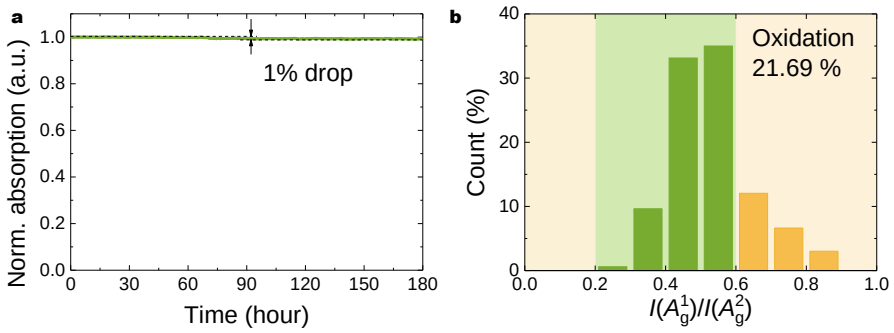

Fig. 7.6 (a) Ink absorption against time, the ink is diluted to 5 *vol.%*; (b) $I(A_g^1)/I(A_g^2)$ histogram for dropcast dried BP ink, the ink has been kept under nitrogen for 2 months.

high stability of the BP ink against sedimentation over a timeframe that would prove viable for large-scale ink production and printing.

I then assess the stability of the ink against oxidation. A Raman mapping of $I(A_g^1)/I(A_g^2)$ is investigated on a dried dropcast ink sample using a formulation prepared two months previously and stored under nitrogen in the interim. The acquired ratio histogram is presented Fig. 7.6(b), showing that the proportion outside 0.2-0.6 is increased to 21.69%. This oxidation of the ink may arise from the moisture and oxygen in the ink carrier. Therefore, whilst this is not an excessive increase given the timescale, it is best to use freshly prepared BP ink for device fabrication.

7.2.2 Large-scale spatially uniform inkjet printing

As with inkjet printing of graphene (Section 5.2.1) and TMDs (Section 6.2.2), the morphologies of inkjet-printed BP are also governed by the droplet merging behaviour, which is essentially defined by the droplet spacing (D) and the dried droplet diameter (D_0) [346, 352]. I then investigate this to seek the optimal printing parameters for the BP ink. Figure 7.7(b) presents printed lines on untreated Si/SiO_2 with varied D while D_0 is 74 µm (defined at a substrate temperature of 60°C), showing stacked coins, bulging, uniform, scalloped lines and isolated droplets. When D is $\leq$25 µm, the line is broad as the droplets significantly overlap and spread further across the substrate, forming stacked coins or bulging. When D is $\geq$75 µm, the droplet merging is insufficient, leading to narrower scalloped lines or even isolated droplets when the droplets are too far apart to merge. When D is between these two extremes, the droplet merges and forms lines with uniform edges, the optimal morphology.

Repeating the above investigations on varied D_0 (by controlling the substrate temperature), I obtain a line-edge peak-to-peak roughness (ξ) map as shown in Fig. 7.7(c). The measurement scheme of ξ follows the method presented in Section 6.2.2. Here, a $\xi <\pm$

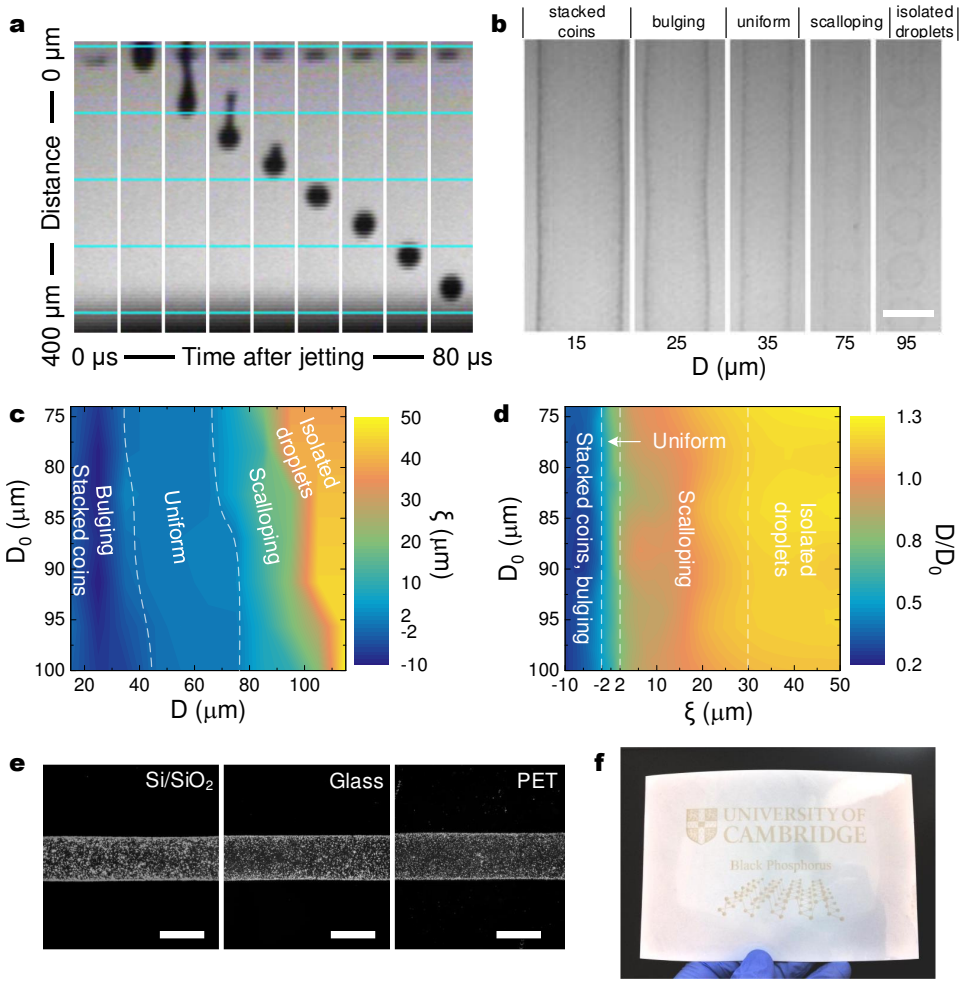

Fig. 7.7 (a) Droplet jetting sequence of the BP ink observed from the printer stroboscopic camera; (b) Photographs of typical printed lines with single printing repetition under varied droplet spacing (D), dried droplet diameter (D_0) 74 µm, scale bar 100 µm; (c) Effect of the spacing and the diameter on the roughness along line edges; (d) The spacing to diameter ratio in each morphology regions with respect to the diameter; (e) Optical dark-field micrographs of printed lines on Si/SiO_2, glass and PET, scale bar 100 µm; (f) Inkjet-printed BP on untreated ultrathin PET (1.5 µm) over an area of 100 mm × 63 mm. The PET is laminated onto photopaper for the ease of handling.

2 µm is also defined as uniform, and the ξ of stacked coins and bulging is also defined as negative to differentiate from that of scalloping and individual droplets. As indicated by the shape and orientation of the highlighted uniform region in the map, D is the dominant factor in defining the morphology. Essentially, the formation of stacked coins, bulging, uniform, scalloped lines and isolated droplets is dependent on the ratio of D to D_0. This ratio value at the different morphology regions with respect to D_0, showing that the uniform region corresponds to a ratio value ~0.5-0.8; Fig. 7.7(d). This again provides a general guidance for

inkjet printing of the BP ink: under different printing conditions, the droplet spacing should be 0.5-0.8 of the dried droplet diameter.

According to this criterion, I select D of 35 µm and a D_0 of 74 µm for inkjet printing of BP since these printing conditions not only allow optimal morphology but also rapid ink drying ($<$10 s observed from the printer fiducial camera), critical for avoiding BP degradation. Optical dark-field microscopy is used to examine the BP flake distribution in lines printed onto Si/SiO_2, glass and PET; Fig. 7.7(e). As shown, the BP flakes are evenly deposited along the length and the width of the lines, without any noticeable coffee rings. This demonstrates that the BP ink is suitable for inkjet printing onto commonly used substrates without requiring any surface treatment. Moving on from individual lines, the ink allows printing on larger areas. Figure 7.7(f) shows a uniform, high resolution inkjet-printed BP pattern on untreated ultrathin PET (1.5 µm) over a 100 mm $\times$ 63 mm area. This demonstrates that the BP ink can potentially fabricate printable devices on a large scale without the loss of printing resolution and material uniformity. I note that the printed BP is free of any surfactants and polymer binders, thus post-printing treatment that may oxidise the BP flakes (*e.g.* high temperature annealing) are avoided.

I then assess the printing characteristics of the inkjet-printed BP. Figure 7.8(a) shows the optical extinction of printed BP squares on untreated glass with 1-10 printing repetitions. The

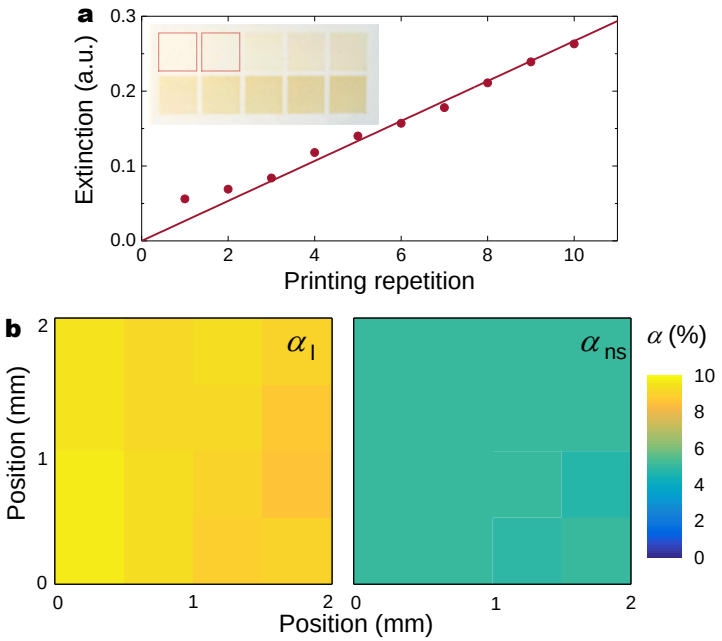

Fig. 7.8 (a) Optical extinction at 550 nm for printed BP with 1-10 printing repetitions, inset: photograph of printed BP squares (8 mm $\times$ 8 mm); (b) Spatial linear (α_l) and nonsaturable (α_{ns}) optical absorption (at 1562 nm) across printed BP, spatial step 0.5 mm.

extinction increases linearly with the printing repetition, with <2% deviation, demonstrating an excellent printing consistency and an ability to control the optical density of the deposited BP through printing repetitions. The deviation of extinction for 1-2 printing repetitions can be attributed to a modification in the air-glass interface after printing. For successive printing repetitions, the trend follows a constant increase with each printing repetition. showing high reproducibility. This demonstrates the excellent printing controllability over deposition densities of the BP ink. The spatial uniformity of printed BP is assessed by its mapping optical absorptions using raster-scanning using a Z-scan set-up. The quantified linear absorption (α_l) under low irradiation intensities, and the nonsaturable absorption (α_{ns}) under high intensities are presented in Fig. 7.8(b). The average α_l and α_{ns} is 9.19 $\pm$ 0.31% and 4.99 $\pm$ 0.09%, respectively, with a deviation of <3.4%, demonstrating a high spatial uniformity. The excellent controllability over deposition densities and the high spatial uniformity across printed patterns, as well as the large-scale printability confirm that the BP ink allows for stable, repeatable and reliable inkjet printing.

The stability of printed BP against oxidation is key to ensuring stable operation of BP based devices. Having shown that the exfoliated BP flakes have a low oxidation proportion (4.2%), here I investigate the oxidation condition of the inkjet-printed BP. Figure 7.9(a) shows the Raman map of $I(A_g^1)/I(A_g^2)$ for a typical printed BP region on Si/SiO_2, with no localised clusters where $I(A_g^1)/I(A_g^2)$ >0.6 or <0.2. The corresponding histogram is in Fig. 7.9(b). As shown, the printed BP still has a low oxidation (10%), indicating that inkjet printing of BP does not adversely affect the BP stability. This small increase may be attributed to oxidation during the solvent exchange and inkjet printing process.

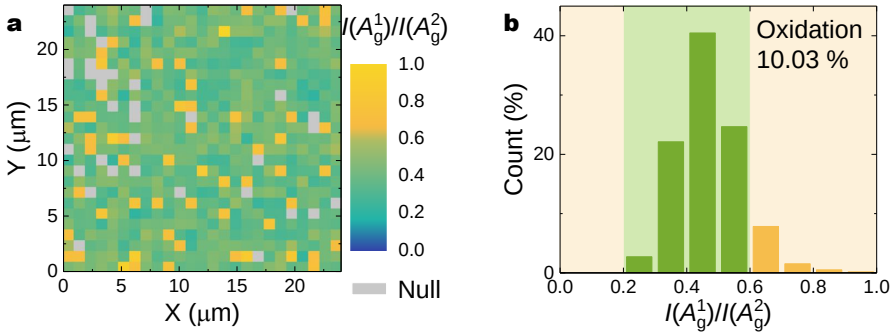

Fig. 7.9 (a) Raman map of the intensity ratio, $I(A_g^1)/I(A_g^2)$, for BP printed onto Si/SiO_2 with 1 μm spatial step. The grey squares correspond to regions where the Raman intensity is too low for accurate interpretation; (b) Corresponding histogram of the map.

7.2.3 Passivation of inkjet-printed black phosphorus

As demonstrated above, the inkjet-printed BP does not show a significant oxidation. However, it is necessary to prevent further degradation of the printed BP for device fabrication. As discussed (Section 2.4), passivation of BP has been demonstrated with polymers such as polydimethylsiloxane (PDMS) [191] and parylene [190]. However, these methods were only demonstrated with individual MC BP flakes, which are atomically smooth. Successful passivation requires a pin-hole free layer, thus printed BP presents a greater challenge due to the relatively small flake size and high roughness, characteristic of deposited films. Indeed, successful passivation for long-term stability has never been reported for solution deposited BP samples.

However, parylene-C, widely used in the microelectronics industry as a chemically inert, pin-hole free and uniform passivation layer [445, 446], is likely to be effective since it forms a conformal coating even on rough surfaces. Therefore, I investigate parylene-C as passivation to protect the inkjet-printed BP against oxidation. Figure 7.10(a) presents the extinction spectra of the as-printed and passivated printed BP samples across the 350-850 nm range over 30 days when exposed to ambient conditions. As shown, the extinction spectrum

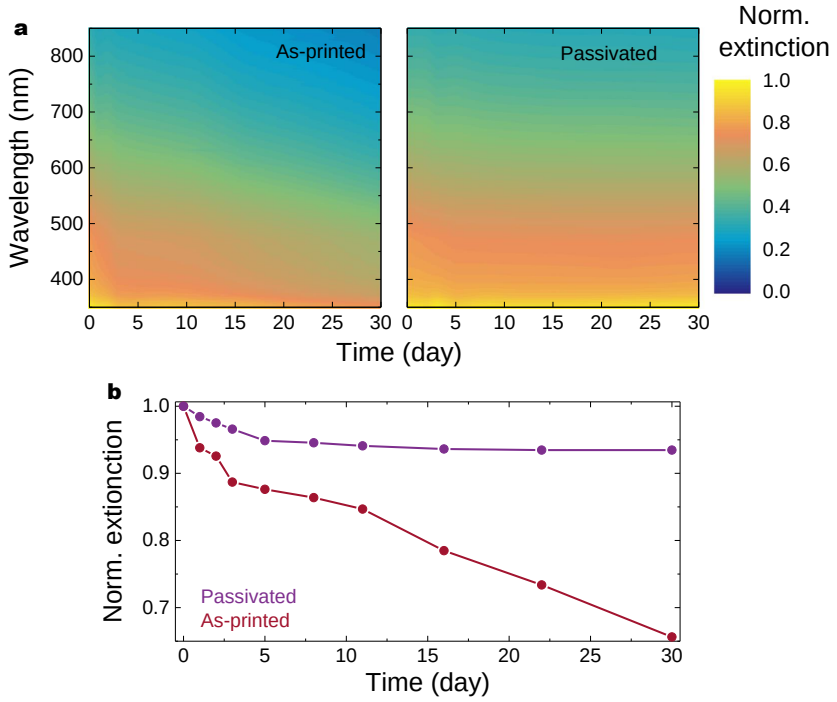

Fig. 7.10 Optical extinction spectra for (a) as-printed and (b) passivated printed BP across 30 days under ambient conditions, the extinction is normalised to the initial extinction value at 350 nm at 0th day; (c) The corresponding change in the normalised optical extinction at 550 nm.

continuously decreases during the measurement period for the as-printed BP sample. For the passivated printed BP sample (100 nm thick parylene-C), the extinction spectrum does not show a significant variation. Figure 7.10(b) is the acquired optical extinction at 550 nm of these two printed BP samples. Indeed, the extinction decreases rapidly for the as-printed sample due to BP oxidation over time and continues its downward trend at the end of this measurement period. For the passivated sample, the extinction shows a slow decrease (5%) during the first 5 days, but it is then stabilised and shows no noticeable changes for the remaining measurement period. Therefore, it is certain that the passivated inkjet-printed BP has long-term stability against oxidation. The initial decrease maybe due to trapped moisture and oxygen in the printed BP sample.

I further study the stability of the passivated inkjet-printed BP sample through the intensity ratio, $I(A_g^1)/I(A_g^2)$; Fig. 7.11(a-d). As discussed, the inkjet-printed BP has a $\sim$10% oxidation proportion. Immediately after passivation with parylene-C, however, the ratio values outside the 0.2-0.6 range is increased to 23.3%. This value is stabilised at 34.3% and 33.9% on the 13th and the 30th day, respectively. Thus, clearly, the $I(A_g^1)/I(A_g^2)$ value shows a large increase immediately after passivation with parylene-C. However, this may not present a high level of oxidation. Indeed, the oxidation threshold of $I(A_g^1)/I(A_g^2)$ for BP passivated with parylene-C is yet to be reported. To investigate the large increase in the $I(A_g^1)/I(A_g^2)$ ratio, a set of freshly cleaved bulk BP sample with and without the parylene-C passivation is characterised. The corresponding ratio values outside the 0.2-0.6 are 3.1% and 5.8%, respectively; Fig. 7.11(e,f). However, this increase is unlikely a result of oxidation of the bulk BP crystal, but the interactions between BP and parylene-C.

Favron *et al.* suggest that $I(A_g^1)$ may be sensitive to perturbations from contacting substances, while $I(A_g^2)$ is not [190]. Indeed, the average value of $I(A_g^1)/I(A_g^2)$ for both the freshly cleaved bulk BP and the printed BP samples increase after passivation; Fig. 7.11. Therefore, this sizeable increase in $I(A_g^1)/I(A_g^2)$ after passivation presented here may be partially as a result of the increase in $I(A_g^1)$ due to close contact with parylene-C. This suggests that the absolute values of $I(A_g^1)/I(A_g^2)$ may not correctly represent the oxidation proportion in BP samples coated with parylene-C. However, the increase from 23.3% to $\sim$33% for the passivated inkjet-printed BP is likely due to limited oxidation of trapped oxygen and moisture. Additionally, the larger increase in $I(A_g^1)/I(A_g^2)$ values for printed BP compared to the bulk BP may arise from the greater surface area of the exfoliated flakes in contact with parylene-C. Therefore, I suggest that the passivated inkjet-printed BP is well protected from degradation under ambient conditions.

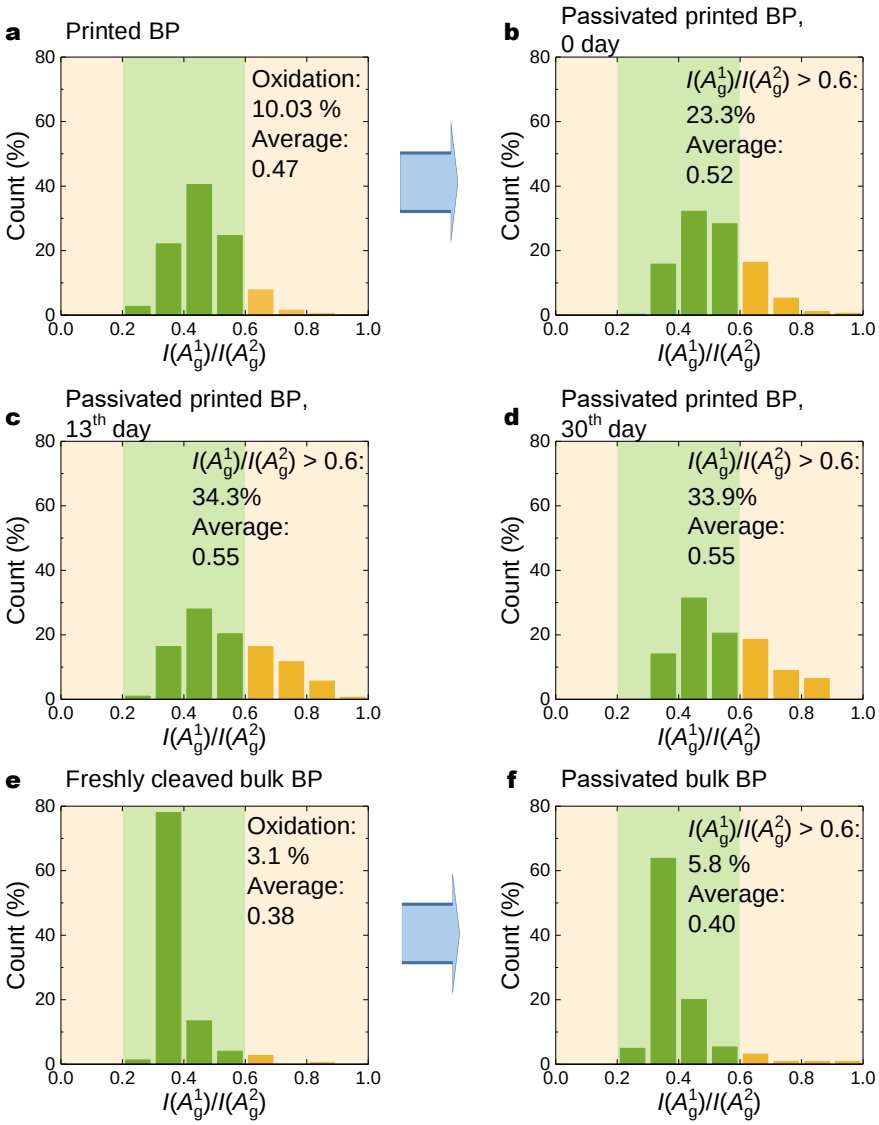

Fig. 7.11 $I(A_g^1)/I(A_g^2)$ histogram for (a) BP after printing, and (b) after passivation with parylene-C, (c) on 13th day and (d) on 30th day; $I(A_g^1)/I(A_g^2)$ histogram for (e) freshly cleaved bulk BP crystal and (f) immediately after parylene-C passivation.

7.3 Inkjet-printed black phosphorus saturable absorbers

The strong saturable optical absorption (Fig. 7.8(b)) suggests the potential of inkjet-printed BP in photonics, *e.g.* as SAs for ultrafast laser [95, 363, 427]. As with inkjet-printed TMD SAs (Section 6.3), inkjet printing of BP directly onto optical components such as quartz, polymers and optical fibres can allow rapid device fabrication with controllable optical absorption and spatial uniformity. Therefore, I explore the application of inkjet-printed BP in SAs. This work is in collaboration with Prof Meng Zhang at the Beihang University.

To fabricate the SA, I inkjet print BP onto the ultrathin PET and subsequently passivate it with 100 nm thick parylene-C. The BP-SA is then introduced into the cavity of an erbium-doped fibre laser for the generation of ultrashort pulses through mode-locking; Fig. 7.12(a). The erbium-doped ultrafast fibre laser set-up consists of single-mode all-fibre integrated components for alignment-free and compact system. The fibre amplifier is composed of a

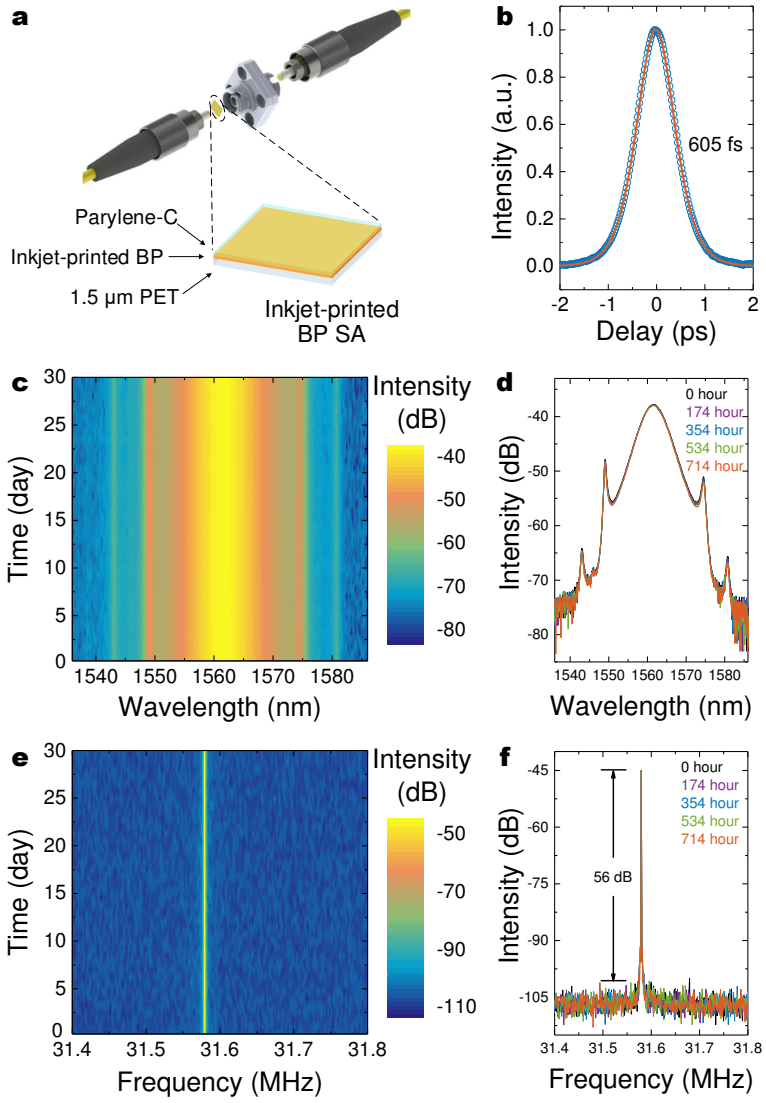

Fig. 7.12 (a) Integration of a inkjet-printed BP SA between fibre patch cords for ultrashort pulse generation with fibre lasers; (b) Autocorrelation trace of output pulses, the blue traces for experimental data and the red curve for sech^2 fit; (c) Output laser spectrum across 30 days, and (d) overlay of the spectrum acquired after 0, 174, 354, 534 and 714 hours of operation; (e) Stable RF spectrum at the cavity fundamental repetition frequency of 31.6 MHz for 30 days, and (f) overlay of radio frequency spectrum after 0, 174, 354, 534 and 714 hours of operation.

0.7 cm long single-mode erbium-doped active fibre (LIEKKI Er-8/125), which is co-pumped by a 980 nm pump laser diode. In addition, this set-up includes a polarisation-independent optical isolator to ensure unidirectional propagation, a 10:90 fused fibre output coupler for both spectral and temporal diagnostics, and a polarisation controller to enable a thorough and continuous adjustment of the net cavity birefringence.

Mode-locking of the ultrafast laser set-up is operated at 1562 nm, with intra-cavity intensities reaching 32.7 $MWcm^{-2}$. Self-starting mode-locking is achieved at the fundamental repetition frequency of 31.6 MHz. The output pulse duration, measured using an intensity autocorrelator, is 605 fs (deconvolved), well fitted with a $sech^2$ pulse shape; Fig. 7.12(b). To evaluate the operation stability of the printed BP-SA and the mode-locking performance of the fibre laser, the parameters of the output pulses are recorded every 6 hours for over 30 days. The output laser pulse spectrum across the 30 days (Fig. 7.12(c)) and the overlay of the laser spectrum acquired after 0, 174, 354, 534 and 714 hours of operation (Fig. 7.12(d)) show no variations, demonstrating an excellent operation stability. The radio frequency (RF) spectrum at the fundamental frequency also shows a high stability across the 30 days (Fig. 7.12(c,d)). The high intensity compared to background ($\sim$53 dB) indicates an excellent mode-locking stability [437]. With regards to BP stability under intense irradiation, the

Table 7.2 Mode-locked fibre lasers using BP SAs. λ – operating wavelength.

Method	Laser type	Laser properties		Lifetime	Ref.
		λ (nm)	Pulse duration	(hours)	
Inkjet printing	Er: fibre	1562	605 fs	>714	This work
MC	Er: fibre	1571	946 fs	28	[182]
MC	Er: fibre	1561	272 fs	-	[183]
MC	Tm: fibre	1910	739 fs	-	[447]
MC	Er: fibre	1559	786 fs	-	[448]
MC	Er: fibre	2783	42 ps	-	[449]
MC	Yb: fibre	1086	7.54 ps	-	[450]
MC	Er fibre	1561	2.66 ps	-	[451]
MC	Er: fibre	1559	805 fs	-	[452]
UALPE	Er: fibre	1560	670 fs	-	[453]
UALPE	Er: fibre	1561	1.44 ps	-	[454]
UALPE	Ho/Pr: fibre	2867	8.6 ps	-	[455]
UALPE	Er: fibre	1532-1570	940 fs	10	[456]
UALPE	Er: fibre	1558	2.18 ps	-	[457]
UALPE	Tm/Ho: fibre	1880-1940	1.58 ps	2	[458]
UALPE	Er: fibre	1568	117.6 ns	-	[459]
UALPE	Er: fibre	1569	280 fs	24	[460]

measurement condition is over three orders of magnitude higher than that reported by Favron *et al.* [190].

Table 7.2 presents the reported results in literature of BP SAs fabricated both through solution processing based techniques and otherwise as a comparison to the work here. The SAs show excellent device operation under intense irradiation for over 714 hours, at least 24 times longer than those previously reported. The generation of stable ultrashort pulses, over a much longer operation period (>24 times longer), demonstrates that inkjet printing of BP can enable scalable fabrication of high performance and long-term stable photonic devices.

7.4 Black phosphorus/graphene/silicon photodetectors

BP is an ideal material for the development of visible to NIR optoelectronic devices such as photodetectors [82, 179, 461, 462]. Recently, graphene/Si Schottky junction photodetectors (Gr/Si) have attracted significant interest due to their advantages, such as ambient condition operation and high photoresponsivity (R_p) [463–466]. Though Gr/Si allows ambient condition operation and high R_p, the operating wavelength range is limited by the bandgap of Si (1.1 eV). Combining this device structure with functional materials, it is possible to tune the Gr/Si Schottky junction barrier and enhance optical absorption for improved detection performance [463]. Inkjet-printed BP therefore may be ideally suited to this role. Therefore, I integrate inkjet-printed BP into Gr/Si for a hybrid BP/graphene/Si Schottky junction photodetectors (BP/Gr/Si). This work is in collaboration with Prof Yang Xu at the Zhejiang University.

The Gr/Si device is received for printing with BP. The fabrication process of the Gr/Si device is as follows, as shown in Fig. 7.13(a): (1) A cleaned Si/SiO_2 wafer (SiO_2 thickness 100 nm) is first patterned through lithography. Subsequently a 50 nm gold (Au) layer is deposited, followed by lift off. This forms the Au electrode pattern, enclosing a Si/SiO_2 window ($\sim$460 µm $\times$ 460 µm). (2) The device is further patterned to give a SiO_2 window of $\sim$450 µm $\times$ 450 µm, followed by etching with hydrofluoric acid. The exposed SiO_2 is etched away to give a Si window $\sim$450 µm $\times$ 450 µm. (4) CVD graphene is then transferred onto the device, covering the Au electrode and the Si window. The transferred CVD graphene is characterised through Raman spectroscopy; Fig. 7.13(c,d). The red dot in Fig. 7.13(c) indicates the position of Raman spectroscopy characterisation. The excitation wavelength is 532 nm, with a power of $\sim$1 mW. In the Raman spectrum, two main peaks at $\sim$1589 cm^{-1} (G peak) and $\sim$2700 cm^{-1} ($2D$ peak) are observed. No noticeable D peak is seen, which is commonly associated with structural defects [302]. The absence of the D peak therefore is a direct indication of high quality for the CVD graphene.

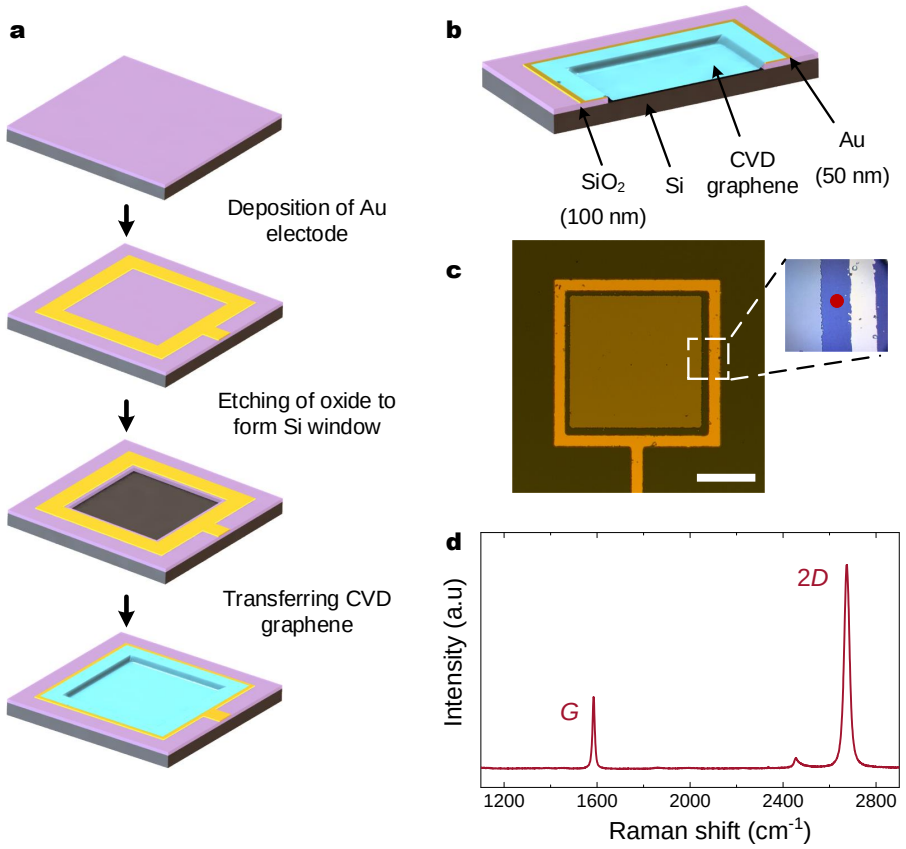

Fig. 7.13 (a) Graphene/silicon Schottky junction photodetector fabrication process; (b) Lateral height profile; (c) Top-view optical micrograph, scale bar 200 μm. The red dot in the zoomed-in view indicates the position where Raman measurement is taken in (d); (d) Raman spectrum of the CVD graphene.

To fabricate the BP/Gr/Si photodetector, I inkjet print BP onto the as-received Gr/Si device and passivate it with Parylene-C. Figure 7.14(a) is a schematic figure showing the architecture of the fabricated BP/Gr/Si photodetector. In Fig. 7.14(b), I show a proposed device band diagram configuration for this hybrid device. As illustrated, there may be a photo-gating effect in this graphene based hybrid devices when in operation [467, 468], *i.e.* charge transfer induced by inkjet-printed BP doping of CVD graphene. Figure 7.14(c) presents the dark currents of Gr/Si and BP/Gr/Si. As shown, the reversed biased dark current of Gr/Si is on the $\sim$1 nA scale, while it is $\sim$100 nA for BP/Gr/Si. This could arise from this above doping effect.

Figure 7.15(a,b) show the photocurrent (after dark current subtraction) of BP/Gr/Si and Gr/Si under 450 nm and 1550 nm excitation, respectively. As shown, Gr/Si shows a reverse R_{p} $\sim$16 mAW^{-1} and no forward response at 450 nm. However, it does not respond to 1550 nm excitation, as expected since 1550 nm (0.8 eV) falls below the bandgap of Si.

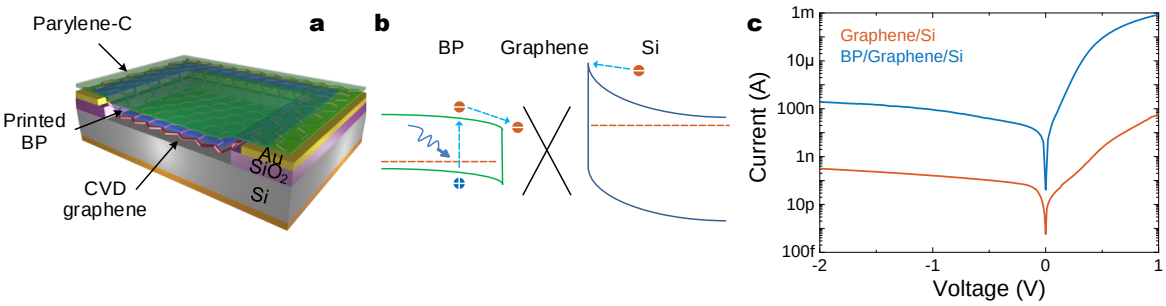

Fig. 7.14 (a) Schematic of the BP/Gr/Si photodetector; (b) Proposed device band diagram configuration; (c) Dark current of Gr/Si and BP/Gr/Si on log-log scale.

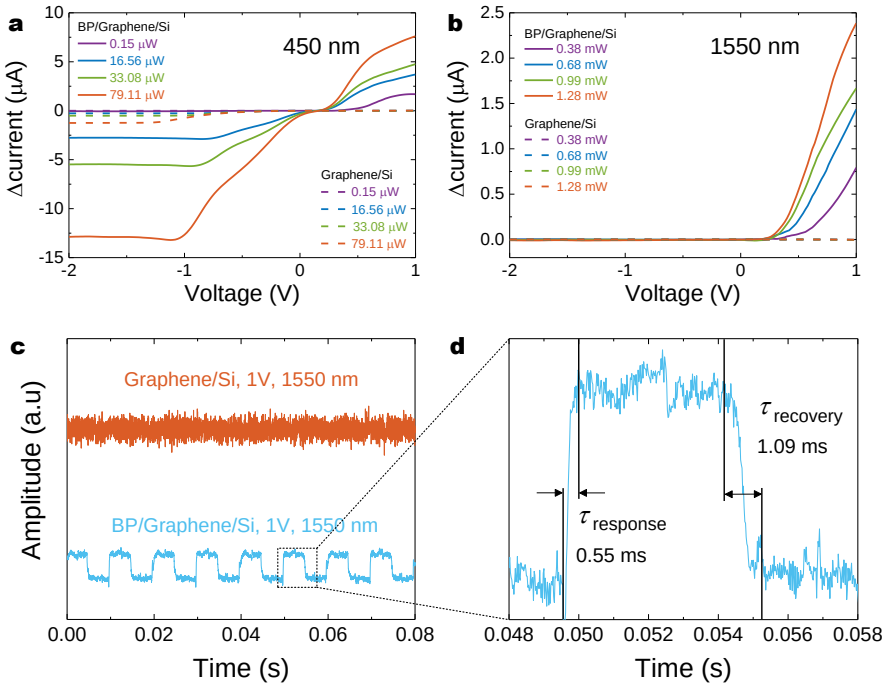

Fig. 7.15 Current response under (a) 450 nm and (b) 1550 nm illumination, with dark current subtracted; (c, d) Time response of Gr/Si and BP/Gr/Si.

However, BP/Gr/Si not only produces a significantly larger reverse R_p ($\sim$164 mAW^{-1}) but also a forward R_p ($\sim$95 mAW^{-1}) under 450 nm excitation. Meanwhile, the device exhibits a forward R_p $\sim$1.8 mAW^{-1} under 1550 nm excitation, demonstrating that printed BP enables the Gr/Si device to work in the near-infrared region. The performance enhancement indicates that BP improves optical absorption of the hybrid structure. In addition to the thermal effect for Schottky based devices [466] that possibly exists in BP/Gr/Si as a result of the increased optical absorption due to printed BP, the forward photo detection ability may be attributed to BP induced charge transfer, a photo-gating effect previously observed in graphene based hybrid devices [467, 468]. This may alter the Fermi energy of graphene and consequently

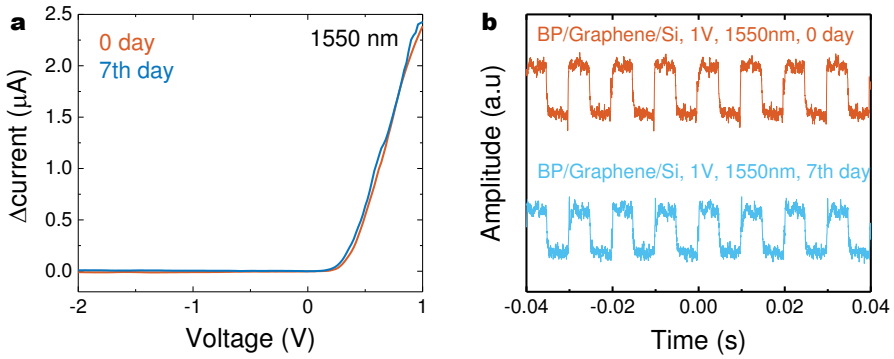

Fig. 7.16 BP/Gr/Si photodetection performance after 7 days exposed in open air: (a) photocurrent change; (b) time response.

lead to variations in the Gr/Si Schottky barrier height that controls the charge transport, as shown in inset of Fig. 7.14(b). Figure 7.15(c) presents the time response of Gr/Si and BP/Gr/Si at 1550 nm. Gr/Si shows no response, whereas BP/Gr/Si exhibits a stable and reproducible response. The response time of the cycle shown in Fig. 7.15(d) is ∼0.55 ms, and the recovery time is ∼1.09 ms.

Figure 7.16(a) presents the photocurrent changes and the time response of BP/Gr/Si at 1550nm after 7 days (168 hours) exposure to ambient conditions. As shown, the device shows negligible changes in both the photocurrent changes and the time response. This demonstrates a high operation stability of the device.

Table 7.3 presents the comparison between the BP/Gr/Si and the current BP photodetectors with different device structures reported thus-far. The visible to NIR BP/Gr/Si operating

Table 7.3 Photodetector based on BP. FET – field effect transistor

Fabrication	Structure	Properties		Lifetime	Ref.
		Responsivity (mAW^{-1})	Response time	(hours)	
Inkjet printing	Schottky junction	164	0.55 ms	>168	This work
MC	FET	20	-	-	[179]
MC	FET	4.8	1 ms	-	[469]
MC	FET	82	-	-	[461]
MC	FET	-	-	-	[470]
MC	Waveguide	657	-	-	[82]
MC	p-n junction	1.5	40 μs	-	[462]
MC	Heterojunction	418	-	-	[471]
MC	Heterojunction	22.3	15 μs	-	[472]

in both forward and reverse configurations demonstrates the potential of inkjet-printed BP in high performance broadband optoelectronic applications. By exploiting inkjet-printed BP, there is huge potential to integrate with alternative device structures including CMOS compatible and waveguide based photodetectors for silicon photonics [82].

7.5 Summary

In this chapter, I have presented the formulation of a BP ink for inkjet printing and the application of the inkjet-printed BP in SAs and photodetectors. Among the three organic solvents investigated for UALPE, through AFM, optical absorption and light scattering, I show that NMP is the most effective solvent for BP exfoliation. Since the NMP dispersion is poorly suited to inkjet printing, I extract the exfoliated BP flakes and formulate them into a BP ink in a binary solvent carrier. The ink ensures stable jetting, appropriate wetting, diminished coffee ring effect, and rapid ink drying ($<$10 s) at low temperatures ($\leq$60°C). By examining the droplet spacing and substrate temperature, I determine the optimal printing parameters for the ink to allow high printing consistency ($<$2% diversion) and spatial uniformity ($<$3.4% deviation). By passivation the inkjet-printed BP with parylene-C, I keep the inkjet-printed BP stable against oxidation for $>$30 days. Owning to the above printing characteristics and the long-term stability, I explore the inkjet-printed BP in the development of highly stable SAs for ultrafast laser and broadband Schottky junction photodetectors with enhanced photoresponsivity. With the BP SAs, an ultrashort pulses is generated and remains stable under an intense irradiation of 32.7 MWcm^{-2} for over 30 days. The photodetectors not only show $>$10 times enhancement in photoresponsivity at 450 nm, but also extend the detection range to include 1550 nm.

In addition to the SAs and photodetectors demonstrated here, inkjet printing of BP may also hold huge potential in other applications, such as printable electronics and energy storage. Though there are no reports of such BP based printable devices yet, there are many successful demonstrations using other functional materials including the 2d materials, for instance inkjet-printed graphene transistors [37], all inkjet-printed 2d material based read-only memories [48], and all inkjet-printed carbon nanotubes based flexible supercapacitors [473]. The BP ink can potentially be used for the fabrication of such devices.

Chapter 8

Functional inks of commercial graphene nanoplatelets for high-speed printing

Carbon materials, including carbon black, graphite and carbon nanotubes (CNTs) are widely used as the conductive pigments in functional inks for printable electronics with the graphics printing technologies such as inkjet, flexographic, gravure and screen printing [474]. However, each of these carbon materials has specific drawbacks. Carbon black is not conductive enough, and thus requires additional printing of overlay grids or boundaries of other conductive materials, for instance metal inks (*e.g.* sintered silver nanoparticles) [475]. Graphite platelets, on the other hand, are typically too large to be useful for certain printing technologies [475]. Meanwhile, both carbon black and graphite typically require a high loading in the inks (*i.e.* weight percentage per unit volume ink), typically $>$20 wt.% which is $>$200 gL^{-1}, to achieve a reasonable electrical conductivity. Such a high loading can degrade mechanical properties (*e.g.* strength and stiffness) of dried printed films. Though CNTs can be used to develop functional inks with good electrical property, they are still expensive in production and challenging to disperse [475].

Graphene has emerged as a promising alternative to carbon black, graphite and CNTs for printable electronics [16, 37, 77, 476, 477], for instance, the inkjet-printed graphene based humidity sensors and solar cells as demonstrated in Chapter 5. However, for industrial-scale manufacture, inkjet printing is limited by the printing speed (typically 10 m min^{-1}). Compared to inkjet printing, the other technologies including flexographic, gravure and screen printing are more appealing, potentially offering a much higher volume patterning of graphene with a much higher speed (Table 4.2). This can lead to high-speed industrial-scale device manufacture. These printing technologies require a loading of $>$10 wt.% (Table 4.1). This is problematic for UALPE graphene as this means that formulating 1 L of such inks would require over 100 L of the UALPE dispersions ($<$0.1 wt.%).

Along with UALPE, there are other methods developed to deliver much higher production throughput (*e.g.* plasma cracking of hydrocarbons), scaled up for commercial use [475, 478]. Indeed, there are already graphene nanoplatelets (GNPs) available in the market. Using such GNPs in ink formulation allows the convenience of tuning the ink composition and hence, ink properties for different printing technologies. In this chapter, I present my work on ink formulation of commercial GNPs. On this basis, in collaboration with Novalia Ltd., I demonstrate high-speed printing (100 m min^{-1}) of graphene-based conductive electronic circuits for capacitive touchpad applications with commercial roll-to-roll (R2R) flexographic press. This method has been used to file a UK/US patent application (WO2017013263 A1), currently at the PCT stage [479].

8.1 Formulating commercial graphene nanoplatelet inks

I investigate four types of commercial GNP products, which are designated as G1, G2, G3 and G4. The product datasheet of G1 and G2 lists the average flake thickness as $<$1 nm, with a lateral dimension of 0.25-1 μm (average 0.5 μm). Figure 8.1 is a representative SEM micrograph of G3, showing that this product consists of graphene flakes with $>$1 μm lateral dimension. The specific surface area of the four GNPs are measured using a Nova Quantachrome 2200e, with nitrogen as an adsorbate; Table 8.1.

Table 8.1 Measured specific surface area for the four types of GNPs.

GNPs	Specific surface area ($m^2\,g^{-1}$)
G1	210
G2	76
G3	10
G4	103

I start formulating inks of the GNPs with solvent selection. As discussed in Section 3.3.1, the solvents suitable for solution processing of graphene are usually high boiling, toxic solvents with a surface tension of $\sim$40 mNm^{-1} and Hansen solubility parameters (HSPs) of $\delta_D \sim$18 $MPa^{1/2}$, $\delta_P \sim$9.3 $MPa^{1/2}$ and $\delta_H \sim$7.7 $MPa^{1/2}$, for instance N-Methyl-2-pyrrolidone (NMP; boiling point 204°C) and dimethylformamide (DMF; boiling point 153°C). This surface tension may raise challenges for wetting of the substrates including Si/SiO_2, glass and many polymeric substrates. In addition, the high boiling point leads to long drying times and may require high temperature annealing. The organic solvents may also be incompatible with many polymeric substrates. Therefore, I avoid use of such solvents and propose a ternary

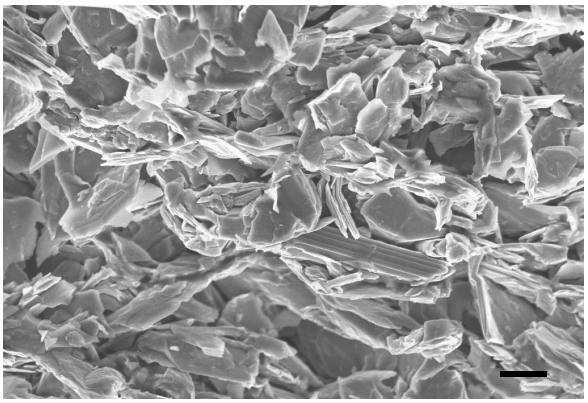

Fig. 8.1 SEM micrograph of G3 GNP, scale bar 1 μm.

solvent carrier consisting of two base solvents and a viscosity modifying solvent, aiming to develop a binder-free graphene ink system *via* bath sonication and high shear mixing (using a Silverson L5M high-shear mixer).

As discussed in Section 3.3.1, the water/alcohol mixture is viable for solution processing of graphene and other 2d materials [266]. Typically, a mass fraction of alcohol of $\geq$20% ensures a surface tension of $<$40 mNm^{-1} to allow wetting of the GNPs [285]. On this basis, stabilising the dispersed GNPs relies on a balance between gravity (whether negative or positive buoyancy) and the frictional force experienced by the GNPs during sedimentation. The frictional force is proportional to the viscosity of the ink carrier (Eq. 3.7). In this case, I select ethylene glycol (EG) as the viscosity modifier, which has a viscosity of $\sim$16 mPa·s. This is much higher than both water ($\sim$0.9 mPa·s) and alcohols (*e.g.* ethanol $\sim$2 mPa·s) [433]. In addition, EG is miscible with water and alcohols. Therefore, I investigate a ternary solvent ink carrier of alcohol/water/EG.

In a typical dispersion, the intermolecular interaction between the solute and the solvent is governed by the HSP distance (R_{d}), and a small HSP distance indicates a better stability. However, the "stability" for high-loading inks is different from the "stability" described on the UALPE dispersions or the inkjet-printable inks. The stability for these inks is similar to commercial inks and paints: as long as the inks/paints maintain stable for 24 hours and be readily agitated to return to a fully functional form, the inks/paints are considered as stable. According to Eq. 3.4 and Eq. 3.5, the R_{d} of the ternary solvent ink carrier is calculated and presented in Fig. 8.2.

As shown, R_{d} is smallest for this ternary solvent composition when ethanol is 20-65 wt.%, water is $<$50 wt.% and EG is $<$30 wt.% Therefore, I use 5 : 65 : 30 wt.% for water : ethanol : EG as a typical carrier for ink formulation. The four GNPs are added into this carrier and sonicated in a bath at 15°C for about 30 minutes to disassociate any large GNP

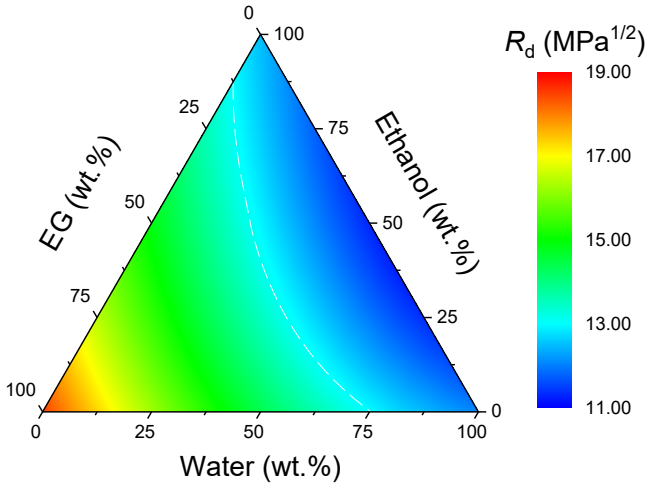

Fig. 8.2 HSP distance (R_d) of ink carrier, *i.e.* a ternary solvent mixture of water, ethanol and EG.

aggregates. The as-produced dispersions are then stirred for about 12 hours to achieve inks with a homogeneous and stable state. Up to 25 wt.% (G1: 2 wt.%, G2: 3 wt.%, G3: 25 wt.%, G4: 25 wt.%) is achieved by this mild mixing, limited only by the resultant viscosity. Figure 8.3(a,b) present the formulation of a 25 wt.% G3 ink. The other inks with the above maximum loading are termed as G1, G2 and G4 ink. The formulated inks all remain visually stable for at least one month when stored undisturbed at room temperature. Note that other alcohols (*e.g.* isopropanol: IPA) and compositions (*e.g.* 30 : 50 : 20 wt.%) are also viable, and that a higher loading of up to 75 wt.% is possible, achieved *via* high shear mixing.

Figure 8.3(c) presents the viscosity of the formulated G1, G2, G3 and G4 inks, measured using a parallel plate rheometer (TA Instruments Discovery HR-1) within a shear rate range of 5 s^{-1} to 1000 s^{-1}. The viscosity plots show that the inks behave as a pseudoplastic liquid, desired for ink formulations (Section 4.1.3). In addition, the presented rheological properties suggest that the inks are suitable without further modifications for printing technologies such as flexographic and gravure printing (Table 4.1). Note that screen printing is possible with inks of a higher loading (*e.g.* 50 wt.%).

I then use dropcasting and blade coating of the inks onto paper or glass substrate (Fig. 8.4(a,b)) to run quick test of electrical properties of the inks. After deposition, the samples are baked at 50°C for 10 mins. The typical sheet resistance (R_s) is ∼4 kΩ/□, ∼4.5 kΩ/□, ∼40 Ω/□ and ∼300 Ω/□ for the G1, G2, G3 and G4 inks, respectively. G3 forms the most conductive conducting ink among these four GNPs, therefore I select G3 for the following investigations.

To allow a good adhesion to the substrates, polymer binders are required for the ink. Here, I investigate PVA as the binder at varied ratio. The "ratio" here is the weight ratio of PVA to

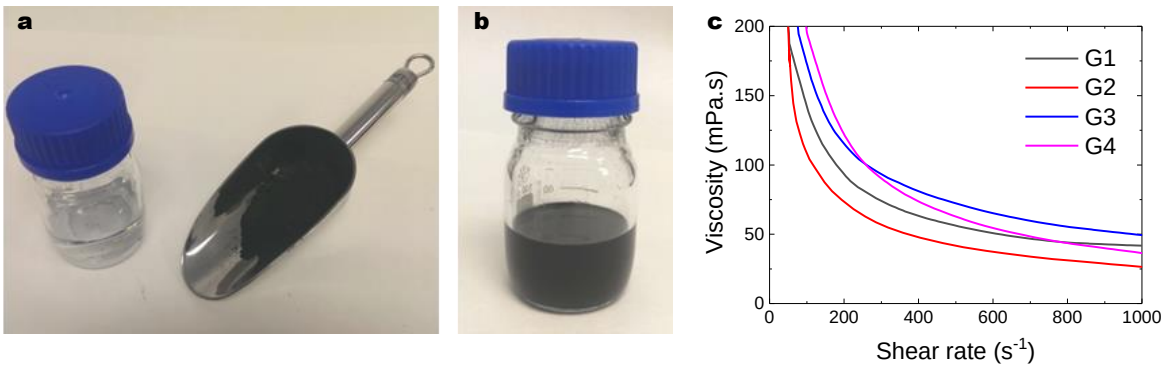

Fig. 8.3 (a) G3 GNPs and the ink carrier; (b) The formulated G3 ink; (c) The rheological properties of the formulated G1, G2, G3 and G4 ink.

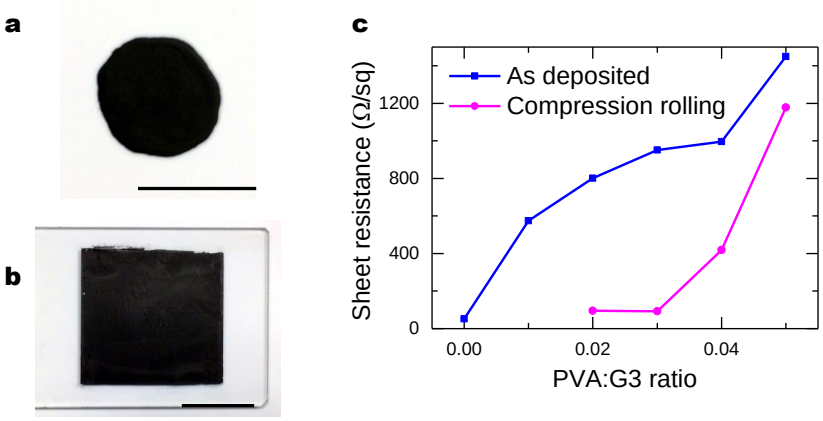

Fig. 8.4 (a) Dropcasting onto photopaper, and (b) doctor blading onto glass, scale bar 10 mm. Exampled with G3 ink. (3) The sheet resistance of dropcast G3/PVA ink.

G3. The change in R_s of the dropcast G3/PVA films with respect to PVA ratio is presented as the "as deposited" curve in Fig. 8.4(c). This shows an increase in R_s with the increasing PVA ratio. Since the dried G3/PVA films are of a porous structure, a compression roll is used to press the films and such that the inter distance of the GNPs is decreased. The electrical behaviour after compression is shown in the "compression roll" curve in Fig. 8.4(c). The compression damages the ratio 0 and 0.01 films such that their R_s cannot be measured, while the other samples remain robust, giving a measured R_s down to ~90 Ω/□. The G3/PVA (PVA weight ratio 0.03) ink is also deposited on glass by blade coating, also giving a R_s of ~90 Ω/□ after compression. Other polymers such as sodium carboxymethyl cellulose (Na-CMC) show similar effects.

The investigation above demonstrates that: (1) Binders can be used to fabricate robust printed GNP films. However, the electrical conductivity of the printed films are compromised;

(2) When a well-developed binder is used, the formulated ink can retain the high conductivity of GNPs.

8.2 Use of GNP inks as additive for conductive inks

As discussed, carbon based inks (typically £50 per kg) are widely used in printable conductive electronic circuits, but their applications are limited due to poor electrical conductivity (*e.g.* $>$20 kΩ/□ with flexographic-printed films). The overlay printing of metal nanoparticles inks, such as silver nanoparticle ink ($>$£1500 per kg, $<$1 Ω/□ with flexographic-printed films), however, significantly increases the device manufacturing complexity and cost. Meanwhile, unlike carbon, the metal nanoparticles are not biodegradable and therefore present challenges for recycling. The performance of the G3 ink suggests that its incorporation into commercial carbon inks might offer significant cost-performance advantages.

For this, I investigate a commercial carbon ink. This carbon ink is water based and contains a binder that requires a mildly basic pH to dissolve, therefore the ink is water resistant once printed and dried. The physical properties of the ink are designed for high-speed commercial R2R flexographic press. The G3 ink is introduced into the carbon ink by mild stirring, with the weight content of the G3 ink in the resultant G3/carbon ink varied within 1-15 wt.%. The mixing does not induce visible aggregation or sedimentation of the carbon ink.

To quantitatively investigate the effect of the addition of the G3 ink on the carbon ink, the viscosity of the mixed inks is characterised; Fig. 8.5(a). As shown, the inks with varied G3 ink content undergo similar shear thinning behaviour, with the viscosity showing no prominent differences within the investigated shear rate region. Overall, this demonstrates that the effect of the additive on the ink viscosity is negligible, suggesting that the printability of the G3/carbon inks is not substantially affected. On the other hand, Fig. 8.5(b) presents the contact angle of the G3/carbon inks on glass at room temperature. As shown, the contact angle is highly consistent, with deviation <3% for all levels of additive, suggesting that the wettability of the G3/carbon inks is also not substantially affected. The above investigations indicate that the G3/carbon inks are readily used with commercial R2R flexographic press.

To quickly test the printability and the electrical properties of the G3/carbon inks, I run Mayer bar coating of the G3/carbon inks onto paper and PET. Mayer bar coating uses a rod wrapped with a coiled wire to deposit films with controlled and uniform thickness. This technique requires an ink viscosity of $<$500 mPa·s and delivers a printing speed of up to 600 m min^{-1}, similar to flexographic printing. Here I use a K2 Mayer bar, which gives a $\sim$12 μm wet thickness. Figure 8.6(a) is a photograph of Mayer bar coated G3/carbon films

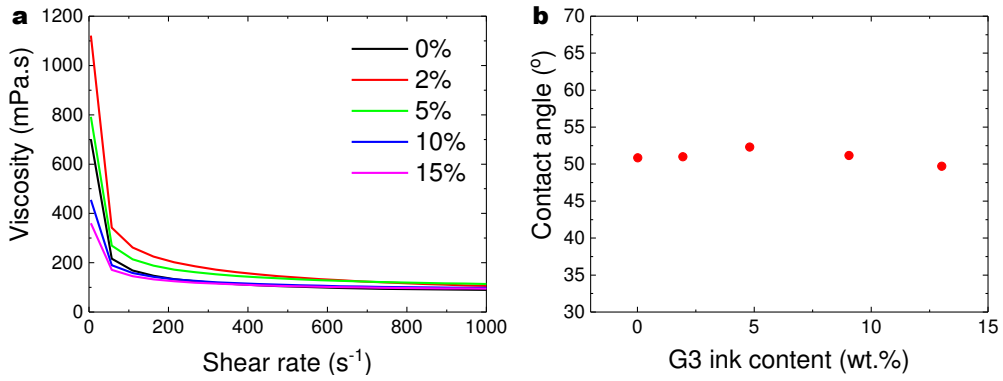

Fig. 8.5 (a) The viscosity of the G3/carbon inks with respect of the G3 ink content; (b) The contact angle of the G3/carbon inks on glass with respect of the G3 ink content.

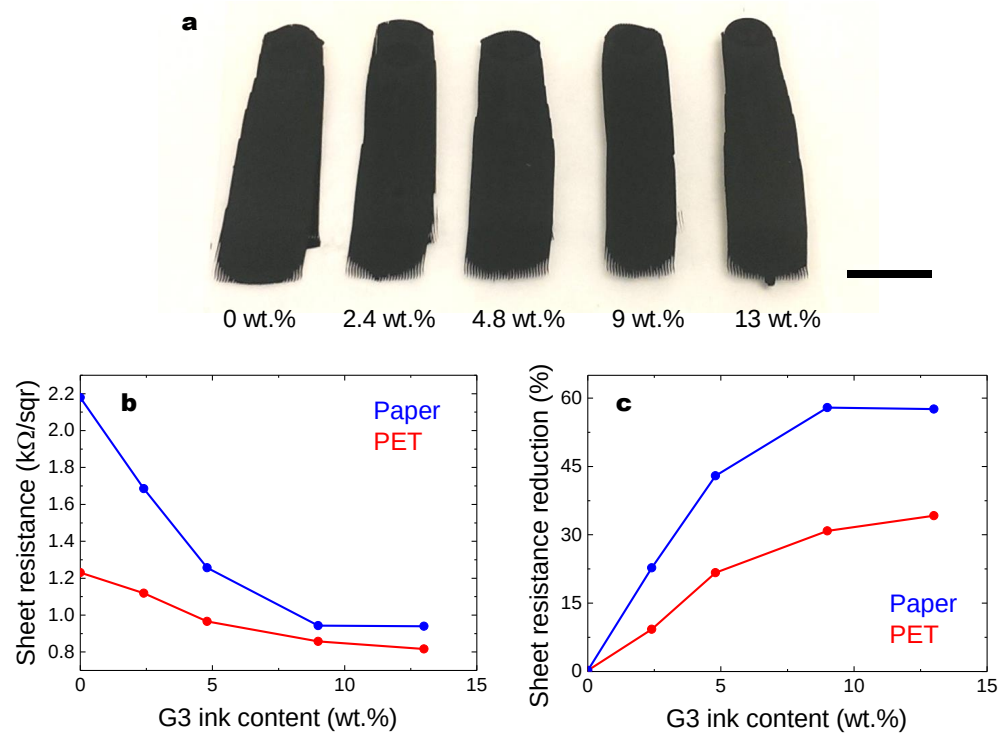

Fig. 8.6 (a) Photograph for Mayer bar coated G3/carbon films on PET with different G3 ink content, scale bar 3 cm; (b) Measured sheet resistance and the associated (c) reduction of Mayer bar coated G3/carbon films with respect to G3 ink content.

on PET. As clearly shown, the G3/carbon inks are very well patterned without any visible spatially non-uniformities. Its measured R_s and the reduction compared to Mayer bar coated carbon film are presented in Figure 8.6(b,c). As shown, when the G3 ink is introduced, the electrical performance of the carbon ink is significantly improved, with the R_s reduced from $\sim$1.2 k$\Omega/\square$ to $\sim$0.8 k$\Omega/\square$, *i.e.* a reduction of 34%. However, the R_s is stabilised when the G3

ink content is over ∼10 wt.%. Similarly, when deposited onto paper, similar improvements are observed, with a minimum R_s down to ∼1.0 kΩ/□ and a maximum reduction of up to ∼58%.

The investigation above demonstrates that an addition of ∼10 wt.% G3 ink allows a maximum enhancement in electrical conductivity while keeping physical properties minimally affected. Therefore, the G3/carbon (10 wt.% : 90 wt.%) ink is adapted to a commercial R2R flexographic press to print the circuits for capacitive touchpads, where the carbon ink is originally patterned. Using the G3/carbon ink in replacement of the carbon ink may bring in lower manufacturing complexity and cost by avoiding overlay printing of metal inks. The press used is a Nilpeter FA4, a R2R flexographic press that is widely used in graphic printing and packaging industry. I note that no modifications are made to the press prior to printing, and the G3/carbon ink is handled in the same way as the carbon ink.

Figure 8.7 is the layout designed for this circuit, consisting of a "touchpad" area which detects the capacitive change in the printed electronic in response to touch, and a "PCB connection point" which transfers the detected information to an affixed PCB board that processes the information and practices certain functions. The G3/carbon ink (Fig. 8.8(a))

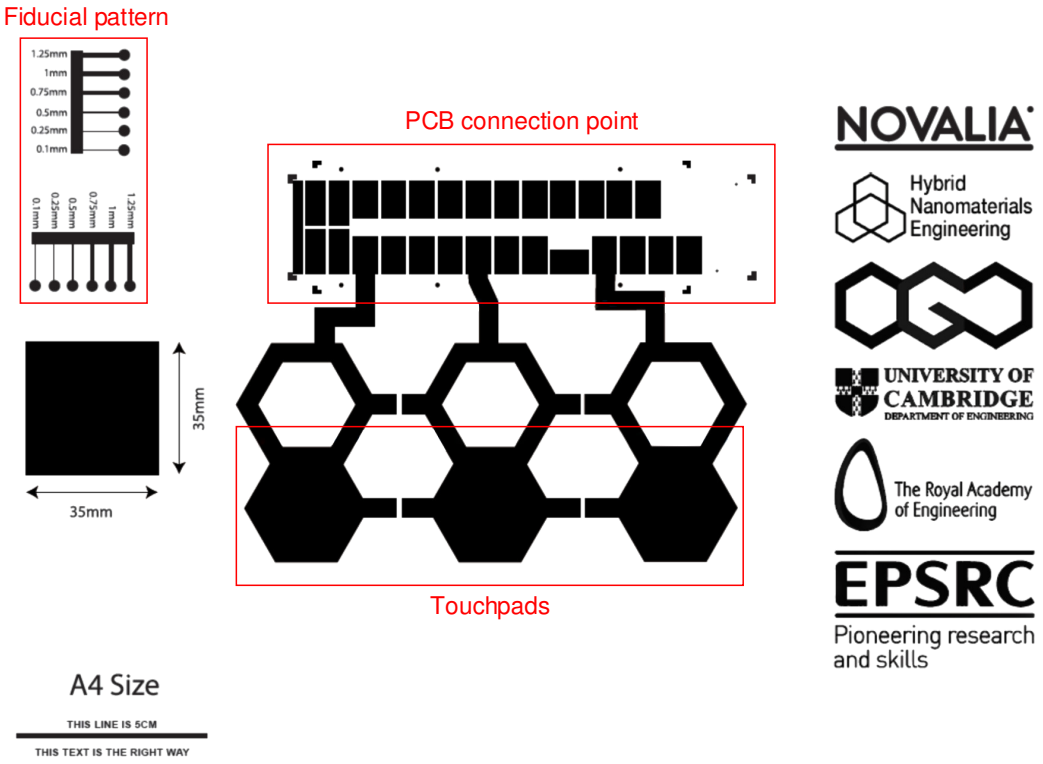

Fig. 8.7 The printing pattern for the trial run on the commercial press, showing the touchpads, PCB connection area and fiducial pattern sections.

is printed onto both paper (Fig. 8.8(b)) and PET (Fig. 8.8(c)) at ∼100 m min^{-1}, allowing printing of hundreds of circuits in one minute. As shown, the printed patterns are very well defined and visibly uniform. The measured R_s from this printing trial is ∼16.5 kΩ/□ and ∼11.5 kΩ/□ for paper and PET, respectively. The R_s above is higher than that from the K2 Mayer bar, as a result of a smaller wet printed film thickness from this press (∼1 μm). The corresponding R_s reduction is ∼30% and ∼45%, respectively.

Figure 8.8(f) presents affixing a PCB board to a cut printed electronic circuit using adhesive tape, which is sandwiched between the PCB connection point and the PCB board. The PCB board (powered with batteries) is programmed to process the received capacitive changes and trigger a sound output through a speaker. While in operation, when the printed G3/carbon touchpad area is touched, a sound output is triggered. This demonstrates that the improvement in electrical conductivity of the carbon ink caused by G3 ink addition is sufficient for this touchpad application without requiring a second-step silver overlay printing.

Fig. 8.8 Photographs of (a) GNP/carbon ink; printing trial on (b) PET and (c) paper using the commercial press; (d) Close-up view of the printing plate; (e) printed PET and paper rolls; (f) printed conductive electronic circuits with PCB board, battery and speaker integrated.

8.3 Use of GNP inks as additive for nanocomposites

Besides functional inks, graphene is also widely exploited as fillers in polymer nanocomposite and adhesives to enhance their electrical, thermal or mechanical properties [480–482]. Typically, GNP nanocomposites are produced from well-mixed GNPs and polymers [483–486]. GNPs can be directly dispersed into molten polymers (*e.g.* thermoplastics). However, melting typically requires high temperature, and achieving a fine mixture (to provide a suitably homogenous distribution of GNPs in the resultant nanocomposites) in this case can be challenging, especially when the loading of GNPs is high. It is therefore preferable to prepare the mixture by blending a dispersion of GNPs with a polymer solution or precursor.

Here, I investigate the feasibility of developing G3/polymer nanocomposites. The G3 ink dispersion is homogeneously mixed into aqueous solution of PVA (5 wt.%) with the content varied within 2.5-10 w/w%. Here the content (w/w%) is the weight content of G3 in the dried G3/PVA films. The high solid content of the G3 ink (25 wt.%) means that only a small ink volume is required to achieve the requisite fill factor, presenting minimal effect on the stability of the polymer dispersions. The measured resistivity of as-produced G3/PVA nanocomposites is presented in Fig. 8.9, showing that the addition of the G3 ink can significantly introduce an electrical conductivity into the nanocomposites. The above investigation demonstrates the potential of this strategy to develop property enhanced nanocomposite systems.

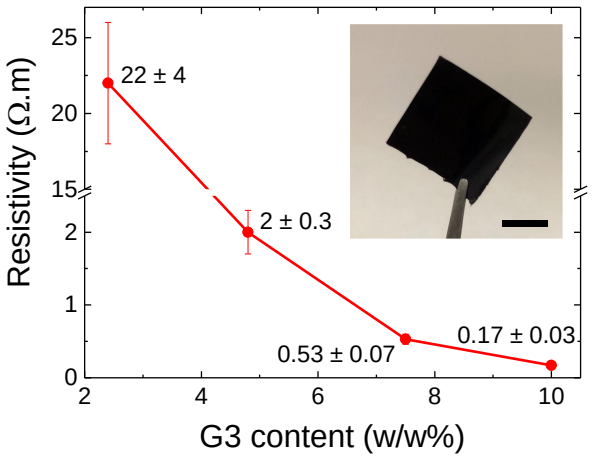

Fig. 8.9 Electrical resistivity of G3/PVA nanocomposite films with respect to G3 content, inset: photograph of a 10 w/w% nanocomposite, scale bar 1 cm.

8.4 High-loading ink formulation of other 2d materials

In the above discussions, I present ink formulation of commercial GNPs and its application as conductive inks and as additives to other ink and composite systems. 2d materials host a wide range of materials with a wide spectrum of properties than can be exploited for applications [4–6, 75, 77]. If the above ink formulation strategy on the commercial GNPs can be adapted to other 2d materials, its potential will be significantly increased. However, thus-far, there is no commercial nanoplatelets of other 2d materials available in the market. Therefore, instead, I use 2d materials produced *via* UALPE as the material sources to investigate the feasibility of this ink formulation strategy.

Here, bulk MoS_2 (Sigma, average particle size 6 μm) and *h*-BN (Sigma, average particle size 1 μm) are mixed into an ink carrier consisting of water : IPA : EG (30 : 50 : 20) at a loading of 3 wt.%. Note that a loading of up to 80 wt.% and 30 wt.% is possible for these two materials. The mixtures are then sonicated for 60 hours to achieve homogeneous and stable dispersions. However, unlike typical UALPE process, the resultant dispersions are not centrifuged to remove the thick or unexfoliated flakes. Therefore, the materials here for ink formulation are actually a mixture of mono- and few-layer thin flakes, thick flakes and unexfoliated bulk crystals. By comparison, the same processes are repeated in the single solvent component of the ink carrier, *i.e.* water, IPA and EG.

Figure 8.10 presents the photographs of the corresponding dispersions and inks taken at 0, 1, 5 and 24 hours after exfoliation. As shown, after 24 hours, obvious sedimentation is observed for the dispersions in water, IPA and EG. In water, turbid suspensions are observed with obvious flocculants floating to the meniscus of the liquid. A high degree of layered separation could be observed in IPA and EG. However, the ink samples show no signs of separation. Time-dependent optical extinction is used to quantitively characterise the stability, finding that the extinction of the inks is decreased by less than 15% after 24 hours. This indicates that less than 15% of the dispersed MoS_2 and *h*-BN sediment. The significant improvement in the stability against sedimentation demonstrates the viability of this ink formulation for MoS_2 and *h*-BN, or other 2d materials in general. Provided there are commercially available nanoplatelets of these 2d materials, results similar to those of GNPs can be achieved.

Fig. 8.10 Photographs for (a) MoS_2 and (b) *h*-BN in water, IPA, EG and the ink carrier at 0, 1, 5 and 24 hours after exfoliation. The dashed lines indicate the sedimentation of *h*-BN.

8.5 Summary

In this chapter, I have presented the development of graphene inks using commercial GNPs, and the application of the inks as additives to ink and polymer composite systems. By considering the surface tension, stability and HSP distance, I design a ternary solvent ink carrier consisting of water, alcohol and a viscosity modifying solvent to disperse commercial GNPs from different sources for binder-free ink formulation. A loading of up to 25 wt.% is achieved *via* mild mixing processes (stirring and bath sonication), while 75 wt.% is possible *via* high shear mixing. The formulated GNP inks show a long-term (over one month) stability against sedimentation. Rheological characterisation shows that the inks are well-suited for such as flexographic and gravure printing.

The inks can be used as conductive inks (with/without polymer binders comprised) with a R_s down to <100 Ω/□, as additives to other functional ink systems showing significant performance improvements (*e.g.* a GNP/carbon ink achieves a R_s reduction of up to 58%), and as additives to polymer composite systems for property enhancements. In particular, based on the results above, the GNP/carbon ink shows minimal changes in the physical properties and hence, can be adapted to commercial R2R flexographic press for printing of conductive electronic circuits that can be used in capacitive touchpad applications. This delivers hundreds of circuits printed within one minute.

Beyond graphene, the feasibility of this ink formulation strategy to the other 2d materials is demonstrated using the 2d materials exfoliated *via* UALPE.

Chapter 9

Conclusions and outlook

In this thesis, I presented the formulation of 2d material inks for different printing technologies, and the application of these inks in device fabrication. I have developed two types of inks: inkjet-printable inks of solution-processed 2d materials (including of graphene, transition metal dichalcogenides: TMDs, and black phosphorus: BP), and high-loading inks of commercial graphene nanoplatelets (GNPs) for high-speed roll-to-roll (R2R) flexographic printing. Based on these ink formulations, I have explored a range of printable applications through research and industry collaborations. The printed graphene was employed as the active sensing layer in CMOS integrated humidity sensors, as counter-electrodes (CEs) in natural dye based dye-sensitised solar cells (DSSCs), and as conductive electronic circuits for capacitive touchpads; while the printed TMDs and BP were exploited to develop saturable absorbers (SAs) for femtosecond pulsed laser generation, and photodetectors operable at the visible to near-infrared (NIR) wavelength region.

In this final chapter, I summarise the ink formulation in Section 9.1, and the demonstrated printable applications in Section 9.2. I then discuss the potential for the technologies demonstrated in this thesis in Section 9.3.

9.1 2d material inks

Inkjet-printable inks. I began the formulation of inkjet-printable inks with the production of mono- and few-layer 2d material flakes *via* ultrasonic-assisted liquid phase exfoliation (UALPE). I investigated UALPE in pure organic solvents including N-Methyl-2-pyrrolidone (NMP), cyclohexanone (CHO), N-Cyclohexyl-2-pyrrolidone (CHP) and isopropanol (IPA), as well as in surfactant solutions including water/sodium deoxycholate (SDC) and IPA/polyvinylpyrrolidone (PVP). For the organic solvents, I showed that the concentration of 2d materials in NMP was typically higher (even being over an order of magnitude)

than in the others. In terms of the stability against sedimentation, NMP dispersions remained stable for months without visible aggregation, while the other solvents could only offered metastable dispersions (*i.e.* sedimentation within several days). NMP is therefore the most suitable solvent for the 2d materials among the solvents investigated. This is due to the matching of its surface tension ($\sim$40 mNm^{-1}) and Hansen solubility parameters (HSPs) to those derived for the 2d materials. In particular, I demonstrated with Raman spectroscopy that UALPE production of BP in NMP under inert atmosphere induced minimal oxidation to the BP flakes. In comparison, both water/SDC and IPA/PVP produced stable dispersions; the addition of PVP significantly increased the concentration of the IPA dispersions by up to $\sim$4 times.

Given the consideration to concentration and stability, the NMP, water/SDC and IPA/PVP dispersions could be potentially adapted to inkjet printing or exploited for ink formulation. Indeed, I demonstrated that the IPA/PVP dispersions of graphene and TMDs were well-suited for inkjet printing on a range of untreated substrates, allowing large-scale spatially uniform printing (1.5% deviation) as a result of the low surface tension ($\sim$23 mNm^{-1}), low boiling point (82.6°C) of IPA and the presence of PVP. The printed graphene was electrically conductive through percolating pathways of graphene flakes in the deposited graphene-PVP composite, allowing use in printable applications. Neither the NMP nor the water/SDC dispersions, however, were able to deliver spatially uniform printing.

Further to this, I developed a binder-free binary alcohol ink formulation of TMDs and BP. To do this, the exfoliated TMD and BP flakes in NMP or water/SDC were extracted and redispersed in an IPA/2-butanol ink carrier. This binary alcohol carrier was designed to achieve optimal ink fluidic properties, wetting of a range of substrates without surface treatment, and suppression of the coffee ring effect by induced recirculating Marangoni flow. This enabled spatially uniform ($<$3.4% deviation) and high print-to-print consistent ($<$2.5% deviation) large-scale printing. In particular, I demonstrated that the rapid drying ($<$10 s) at low temperatures ($\leq$60°C) of the BP ink ensured minimal oxidation; the printed BP could retain a long-term (over one month) stability with passivation of parylene-C.

I also showed that printing parameters such as the droplet jetting spacing and the substrate temperature could greatly govern the morphologies of the printed patterns. I therefore developed a methodology to seek the optimal inkjet printing parameters for a spatially uniform morphology. I found that for the 2d materials inks a droplet spacing of 0.5-0.8 of the dried droplet diameter was required.

High-speed printable graphene inks. Printing technologies such as R2R flexographic and gravure deliver a much higher printing speed (*e.g.* 500 m min^{-1} for flexographic) than inkjet

printing (10 m min^{-1}), which, correspondingly, far greater appeal for industrial-scale device manufacture. This requires an ink with a loading of >10 wt.% (compared to <0.05 wt.% for the IPA/PVP inks, and <0.5 wt.% for the binary alcohol inks). As opposed to the 2d materials produced *via* UALPE, I selected commercial graphene GNPs for ink formulation, given that otherwise, formulating 1 L of such inks would require over 100 L of UALPE dispersions (typically <0.1 wt.%). I developed a ternary solvent ink carrier of water, alcohol and a viscosity modifying solvent to disperse commercial GNPs from different sources for binder-free ink formulation. This ternary solvent carrier was designed with suitable Hansen solubility parameter distance to allow dispersion and stabilisation of the GNPs. The formulated GNP inks could be used as conductive inks, and as additives to other functional ink and polymer composite systems for enhanced properties. For example, a GNP/carbon hybrid ink was developed that led to a reduction in sheet resistance of up to 58%.

The GNP/carbon hybrid ink showed only minimal alteration in its physical properties (including the ink rheology and wettability) with respect to the original commercial water-based carbon ink, designed for use in a commercial R2R flexographic press. Therefore, this GNP/carbon ink was effortlessly adapted to a commercial R2R flexographic press, allowing printing of conductive electronic circuits for capacitive touchpads of a printing speed of ∼100 m min^{-1}.

9.2 Printable applications

CMOS integrated humidity sensors. In collaboration with Dr Sumita Santra at Indian Institute of Technology and Prof Florin Udrea at the University of Cambridge, I integrated inkjet-printed graphene-PVP as the effective sensing layer in CMOS device for resistive humidity sensor fabrication. These devices exploited the percolating electrical conductivity of graphene-PVP, whereby upon exposure to humidity the resistance of graphene-PVP increased as a result of a decrease in the number of electrically percolating pathways of graphene flakes due to PVP swell. These graphene based CMOS integrated humidity sensors are small (1 mm^2) and have low power consumption, ideal for further integration into products such as cell phones and smart watches. This technology therefore represents a promising solution for the high-level integration, flexible manufacturing and miniaturisation for sensors.

Printable graphene DSSCs. In collaboration with Dr David Dodoo-Arhin at the University of Ghana and Prof Gehan Amaratunga at the University of Cambridge, I exploited the inkjet-printed graphene (after PVP decomposition) as CEs for the fabrication of natural dye based DSSCs. The good electrical conductivity, high electrocatalytic performance, and

excellent chemical stability, as well as the suitable work function of the UALPE graphene made it a suitable candidate for this application. The natural dyes, *i.e.* the "chloroplast" of solar cells, were extracted from flowers. The DSSCs with graphene CEs exhibited a light-to-electrical energy efficiency of $>80\%$ of those based on expensive platinum CEs. The production cost, however, was reduced by 97.3%, demonstrating the potential of printable graphene CEs for energy storage and conversion. Indeed, there is a high chance that this method could be used for printable flexible batteries and supercapacitors in the near future.

High-speed printable graphene electronics. In collaboration with Novalia Ltd., I developed the GNP/carbon hybrid ink. As mentioned, the GNP/carbon ink was used to run a commercial R2R flexographic press rial to deliver high-speed patterning of graphene. This allowed hundreds of electronic conductive circuits to be printed within one minute for capacitive touchpad application. The graphene circuit alone exhibited sufficient electrical conductivity and hence, required no second overprint of expensive silver ink, significantly reducing the manufacturing complexity and cost.

Large-scale printable photodetectors. 2d materials such as semiconducting TMDs and BP are of great interest for optoelectronics with a sizeable bandgap that spans the visible to NIR wavelength region. One such widely reported application are photodetectors. Thusfar, one key challenge in exploiting TMDs and BP in photodetectors is the scalability. The spatially uniform, highly consistent pattering capabilities of the binary alcohol ink formulation made scalable device printing possible. Indeed, I demonstrated large-scale printing of TMDs and BP which were used for the fabrication of photodetectors. In particular, inkjet-printed BP integrated graphene/silicon Schottky junction photodetectors not only exhibited improved performance, but also extended the operable wavelength region outside that of silicon (in collaboration with Prof Yang Xu at the Zhejiang University).

Printable saturable absorbers for ultrafast lasers. Ultrafast lasers employing SAs for ultrashort pulsed laser generation have tremendous opportunities in industrial, medical and sensing applications. 2d materials are promising in this area with nonlinear optical properties and ultrafast carrier dynamics. A well developed fabrication method for 2d material based SAs is through developing flake-enriched polymer nanocomposites form UALPE dispersions. Inkjet-printable SAs, however, are more appealing due to higher fabrication efficiency and better control of the distribution and optical density of the 2d material flakes. In collaboration with Prof Meng Zhang at the Beihang University, I demonstrated 500-600 fs pulsed laser generation with inkjet-printed SAs of TMDs and BP.

9.3 Outlook

Through my doctoral work, I have made several key accomplishments in the field of 2d material printing that can potentially open up real opportunities in the exploitation of these materials for real-world applications. Though only inks of graphene, TMDs and BP were demonstrated, the ink formulation strategies demonstrated could potentially be extended to other 2d materials such as boron nitride, MXenes and mica. Furthermore, beyond the applications demonstrated in this thesis, printing of 2d materials is a promising material deposition route in other fields such as transistors, light emitters, energy storage and conversion, and biosensors. Together, there is evidently significant scope for expanding upon the technologies presented in this thesis.

The complementary properties of 2d materials, coupled with the highly controllable patterning capabilities of the ink formulation strategies, offer the possibility of fabricating all-printed, heterostructure devices through additive pattering of different 2d materials. Crucially, this process could be seamlessly integrated with existing CMOS technologies (as demonstrated) and integrated circuits, affording a highly flexible and versatile route for manufacturing miniaturised sensing and interactive devices. The thin-form factors and flexibility offered by printing technologies, along with the capability for direct integration with functional 3d printing, offer unprecedented advantages in the fabrication of emerging technological systems, such as in conformable interactive touch surfaces, wearable sensors, RFID tags and even artificial electronic skins.

References

[1] Nicolosi, V., Chhowalla, M., Kanatzidis, M. G., Strano, M. S. & Coleman, J. N. Liquid exfoliation of layered materials. *Science* **340**, 1226419–1226419 (2013).

[2] Novoselov, K. S. *et al.* Electric field effect in atomically thin carbon films. *Science* **306**, 666–669 (2004).

[3] Novoselov, K. S. *et al.* Two-dimensional atomic crystals. *Proc. Natl. Acad. Sci.* **102**, 10451–10453 (2005).

[4] Xia, F., Wang, H., Xiao, D., Dubey, M. & Ramasubramaniam, A. Two-dimensional material nanophotonics. *Nat. Photonics* **8**, 899–907 (2014).

[5] Bonaccorso, F., Sun, Z., Hasan, T. & Ferrari, A. C. Graphene photonics and optoelectronics. *Nat. Photonics* **4**, 611–622 (2010).

[6] Xu, M., Liang, T., Shi, M. & Chen, H. Graphene-like two-dimensional materials. *Chem. Rev.* **113**, 3766–3798 (2013).

[7] Wang, Q. H., Kalantar-Zadeh, K., Kis, A., Coleman, J. N. & Strano, M. S. Electronics and optoelectronics of two-dimensional transition metal dichalcogenides. *Nat. Nanotechnol.* **7**, 699–712 (2012).

[8] Chhowalla, M. *et al.* The chemistry of two-dimensional layered transition metal dichalcogenide nanosheets. *Nat. Chem.* **5**, 263–275 (2013).

[9] Geim, A. K. & Novoselov, K. S. The rise of graphene. *Nat. Mater.* **6**, 183–191 (2007).

[10] Garcia de Abajo, F. J. Graphene Nanophotonics. *Science* **339**, 917–918 (2013).

[11] Sun, Y. & Shi, G. Graphene/polymer composites for energy applications. *J. Polym. Sci. Part B Polym. Phys.* **51**, 231–253 (2013).

[12] Choi, H.-J. *et al.* Graphene for energy conversion and storage in fuel cells and supercapacitors. *Nano Energy* **1**, 534–551 (2012).

[13] Li, Y.-Q., Yu, T., Yang, T.-Y., Zheng, L.-X. & Liao, K. Bio-inspired nacre-like composite films based on graphene with superior mechanical, electrical, and biocompatible properties. *Adv. Mater.* **24**, 3426–3431 (2012).

[14] Lu, Y., Goldsmith, B. R., Kybert, N. J. & Johnson, A. T. C. DNA-decorated graphene chemical sensors. *Appl. Phys. Lett.* **97**, 083107 (2010).

[15] Bonaccorso, F. *et al.* Production and processing of graphene and 2d crystals. *Mater. Today* **15**, 564–589 (2012).

[16] Bonaccorso, F., Bartolotta, A., Coleman, J. N. & Backes, C. 2D-crystal-based functional inks. *Adv. Mater.* **28**, 6136–6166 (2016).

[17] Howe, R. C. T., Hu, G., Yang, Z. & Hasan, T. Functional inks of graphene, metal dichalcogenides and black phosphorus for photonics and (opto)electronics. In *SPIE Nanosci. + Eng.*, 95530R (2015).

[18] Torrisi, F. & Coleman, J. N. Electrifying inks with 2D materials. *Nat. Nanotechnol.* **9**, 738–9 (2014).

[19] Tracton, A. A. *Coatings technology handbook* (CRC Press, 2005), 3rd edn.

[20] Suganuma, K. Printing Technology. 23–48 (2014).

[21] Fukuda, K. & Someya, T. Recent progress in the development of printed thin-film transistors and circuits with high-resolution printing technology. *Adv. Mater.* (2016).

[22] Leenen, M. a. M., Arning, V., Thiem, H., Steiger, J. & Anselmann, R. Printable electronics: flexibility for the future. *Phys. Status Solidi A* **206**, 588–597 (2009).

[23] Calvert, P. Inkjet printing for materials and devices. *Chem. Mater.* **13**, 3299–3305 (2001).

[24] Singh, M., Haverinen, H. M., Dhagat, P. & Jabbour, G. E. Inkjet printing-process and its applications. *Adv. Mater.* **22**, 673–685 (2010).

[25] Nisato, G., Lupo, D. & Ganz, S. *Organic and printed electronics : Fundamentals and applications* (CRC Press, 2016).

[26] Lee, H.-h., Chou, K.-s. & Huang, K.-c. Inkjet printing of nanosized silver colloids. *Nanotechnology* **16**, 2436–2441 (2005).

[27] Sirringhaus, H. *et al.* High-resolution inkjet printing of all-polymer transistor circuits. *Science* **290**, 2123–2126 (2000).

[28] de Gans, B.-J., Duineveld, P. C. & Schubert, U. S. Inkjet printing of polymers: State of the art and future developments. *Adv. Mater.* **16**, 203–213 (2004).

[29] Beecher, P. *et al.* Ink-jet printing of carbon nanotube thin film transistors. *J. Appl. Phys.* **102**, 043710 (2007).

[30] Liu, Z., Zhang, Z.-B., Chen, Q., Zheng, L.-r. & Zhang, S.-l. Solution-processable nanotube/polymer composite for high-performance TFTs. *IEEE Electron Device Lett.* **32**, 1299–1301 (2011).

[31] Liu, Z., Li, H., Qiu, Z., Zhang, S.-L. & Zhang, Z.-b. Small-hysteresis thin-film transistors achieved by facile dip-Coating of nanotube/polymer composite. *Adv. Mater.* **24**, 3633–3638 (2012).

[32] Cui, Z. *Printed electronics: Materials, technologies and applications* (John Wiley & Sons Singapore Pte. Ltd, Singapore, 2016), 1st edn.

[33] Chabinyc, M. *et al.* Printing methods and materials for large-area electronic devices. *Proc. IEEE* **93**, 1491–1499 (2005).

[34] Miettinen, J. *et al.* Inkjet printed System-in-Package design and manufacturing. *Microelectronics J.* **39**, 1740–1750 (2008).

[35] Park, H. *et al.* Fully roll-to-roll gravure printed rectenna on plastic foils for wireless power transmission at 13.56 MHz. *Nanotechnology* **23**, 344006 (2012).

[36] Vena, A. *et al.* Design of chipless RFID tags printed on paper by flexography. *IEEE Trans. Antennas Propag.* **61**, 5868–5877 (2013).

[37] Torrisi, F. *et al.* Inkjet-printed graphene electronics. *ACS Nano* **6**, 2992–3006 (2012).

[38] Capasso, A. *et al.* Ink-jet printing of graphene for flexible electronics: An environmentally-friendly approach. *Solid State Commun.* **224**, 53–63 (2015).

[39] Bianchi, V. *et al.* Terahertz saturable absorbers from liquid phase exfoliation of graphite. *Nat. Commun.* **8**, 15763 (2017).

[40] Finn, D. J. *et al.* Inkjet deposition of liquid-exfoliated graphene and MoS_2 nanosheets for printed device applications. *J. Mater. Chem. C* **2**, 925–932 (2014).

[41] Withers, F. *et al.* Heterostructures produced from nanosheet-based inks. *Nano Lett.* **14**, 3987–3992 (2014).

[42] Kelly, A. G. *et al.* All-printed thin-film transistors from networks of liquid-exfoliated nanosheets. *Science* **356**, 69–73 (2017).

[43] Hyun, W. J., Secor, E. B., Hersam, M. C., Frisbie, C. D. & Francis, L. F. High-resolution patterning of graphene by screen printing with a silicon stencil for highly flexible printed electronics. *Adv. Mater.* **27**, 109–115 (2015).

[44] Chang, T.-L., Chen, Z.-C. & Tseng, S.-F. Laser micromachining of screen-printed graphene for forming electrode structures. *Appl. Surf. Sci.* **374**, 305–311 (2016).

[45] Baker, J., Deganello, D., Gethin, D. T. & Watson, T. M. Flexographic printing of graphene nanoplatelet ink to replace platinum as counter electrode catalyst in flexible dye sensitised solar cell. *Mater. Res. Innov.* **18**, 86–90 (2014).

[46] Secor, E. B. *et al.* Gravure printing of graphene for large-area flexible electronics. *Adv. Mater.* **26**, 4533–4538 (2014).

[47] Xu, Y. *et al.* Inkjet-printed energy storage device using graphene/polyaniline inks. *J. Power Sources* **248**, 483–488 (2014).

[48] McManus, D. *et al.* Water-based and biocompatible 2D crystal inks for all-inkjet-printed heterostructures. *Nat. Nanotechnol.* **12**, 343–350 (2017).

[49] Sriprachuabwong, C. *et al.* Inkjet-printed graphene-PEDOT:PSS modified screen printed carbon electrode for biochemical sensing. *J. Mater. Chem.* **22**, 5478 (2012).

[50] Li, J. *et al.* Efficient inkjet printing of graphene. *Adv. Mater.* **25**, 3985–3992 (2013).

[51] Secor, E. B., Prabhumirashi, P. L., Puntambekar, K., Geier, M. L. & Hersam, M. C. Inkjet printing of high conductivity, flexible graphene patterns. *J. Phys. Chem. Lett.* **4**, 1347–1351 (2013).

[52] Arapov, K., Abbel, R., de With, G. & Friedrich, H. Inkjet printing of graphene. *Faraday Discuss.* **173**, 323–336 (2014).

[53] Secor, E. B., Ahn, B. Y., Gao, T. Z., Lewis, J. A. & Hersam, M. C. Rapid and versatile photonic annealing of graphene inks for flexible printed electronics. *Adv. Mater.* **27**, 6683–6688 (2015).

[54] Secor, E. B. *et al.* Enhanced conductivity, adhesion, and environmental stability of printed graphene inks with nitrocellulose. *Chem. Mater.* acs.chemmater.7b00029 (2017).

[55] Wang, F., Zhu, H. & He, H. Low temperature sintering of Ag nanoparticles/graphene composites for paper based writing electronics. *J. Phys. D. Appl. Phys.* **49**, 415501 (2016).

[56] Li, J., Naiini, M. M., Vaziri, S., Lemme, M. C. & Ostling, M. Inkjet printing of MoS_2. *Adv. Funct. Mater.* **24**, 6524–6531 (2014).

[57] Huang, L., Huang, Y., Liang, J., Wan, X. & Chen, Y. Graphene-based conducting inks for direct inkjet printing of flexible conductive patterns and their applications in electric circuits and chemical sensors. *Nano Res.* **4**, 675–684 (2011).

[58] Vuorinen, T., Niittynen, J., Kankkunen, T., Kraft, T. M. & Mäntysalo, M. Inkjet-printed graphene/PEDOT:PSS temperature sensors on a skin-conformable polyurethane substrate. *Sci. Rep.* **6**, 35289 (2016).

[59] Cao, L. *et al.* Direct laser-patterned micro-supercapacitors from paintable MoS_2 Films. *Small* **9**, 2905–2910 (2013).

[60] Deegan, R. D. *et al.* Capillary flow as the cause of ring stains from dried liquid drops. *Nature* **389**, 827–829 (1997).

[61] Deegan, R. D. *et al.* Contact line deposits in an evaporating drop. *Phys. Rev. E* **62**, 756–765 (2000).

[62] Hutchings, I. M. & Martin, G. D. (eds.) *Inkjet technology for digital fabrication* (John Wiley & Sons, Ltd, Chichester, UK, 2012).

[63] Garašanin, M. The Eneolithic period in the Central Balkan Area. In Boardman, J., Edwards, I. E. S., Hammond, N. G. L. & Sollberger, E. (eds.) *Cambridge Anc. Hist.*, 136–162 (Cambridge University Press, Cambridge, 1982).

[64] Mas-Ballesté, R., Gómez-Navarro, C., Gómez-Herrero, J. & Zamora, F. 2D materials: To graphene and beyond. *Nanoscale* **3**, 20–30 (2011).

[65] Brodie, B. C. On the atomic weight of graphite. *Philos. Trans. R. Soc. London* **149**, 249–259 (1859).

[66] Ruess, G. & Vogt, F. Hochstlamellarer kohlenstoff aus graphitoxyhydroxyd. *Monatshefte Chem.* **78**, 222–242 (1948).

[67] Mouras, S., Hamm, A., Djurado, D. & Cousseing, J.-C. Synthesis of first stage graphite intercalation compounds with fluorides. *Rev. Chim. minérale* **24**, 572–582 (1987).

[68] Bodenmann, A. K. & MacDonald, A. H. Graphene: Exploring carbon flatland. *Phys. Today* **60**, 35–41 (2007).

[69] Li, L. *et al.* Black phosphorus field-effect transistors. *Nat. Nanotechnol.* **9**, 372–377 (2014).

[70] Lipp, A., Schwetz, K. & Hunold, K. Hexagonal boron nitride: Fabrication, properties and applications. *J. Eur. Ceram. Soc.* **5**, 3–9 (1989).

[71] Frindt, R. F. & Yoffe, A. D. Physical properties of layer structures: Optical properties and photoconductivity of thin crystals of molybdenum disulphide. *Proc. R. Soc. A Math. Phys. Eng. Sci.* **273**, 69–83 (1963).

[72] Joensen, P., Frindt, R. & Morrison, S. Single-layer MoS_2. *Mater. Res. Bull.* **21**, 457–461 (1986).

[73] Radisavljevic, B., Radenovic, A., Brivio, J., Giacometti, V. & Kis, A. Single-layer MoS_2 transistors. *Nat. Nanotechnol.* **6**, 147–150 (2011).

[74] Bridgman, P. W. Two new modifications of phosphorus. *J. Am. Chem. Soc.* **36**, 1344–1363 (1914).

[75] Anasori, B. *et al.* Two-dimensional, ordered, double transition metals carbides (MXenes). *ACS Nano* **9**, 9507–9516 (2015).

[76] Naguib, M., Mochalin, V. N., Barsoum, M. W. & Gogotsi, Y. MXenes: A new family of two-dimensional materials. *Adv. Mater.* **26**, 992–1005 (2014).

[77] Ferrari, A. C. *et al.* Science and technology roadmap for graphene, related two-dimensional crystals, and hybrid systems. *Nanoscale* **7**, 4598–4810 (2015).

[78] Castellanos-Gomez, A. Black phosphorus: Narrow gap, wide applications. *J. Phys. Chem. Lett.* **6**, 4280–4291 (2015).

[79] Geim, A. K. Graphene: Status and prospects. *Science* **324**, 1530–1534 (2009).

[80] Sundaram, R. S. *et al.* Electroluminescence in single layer MoS_2. *Nano Lett.* **13**, 1416–1421 (2013).

[81] Splendiani, A. *et al.* Emerging photoluminescence in monolayer MoS_2. *Nano Lett.* **10**, 1271–1275 (2010).

[82] Youngblood, N., Chen, C., Koester, S. J. & Li, M. Waveguide-integrated black phosphorus photodetector with high responsivity and low dark current. *Nat. Photonics* **9**, 247 (2015).

[83] Kubota, Y., Watanabe, K., Tsuda, O. & Taniguchi, T. Deep dltraviolet light-emitting hexagonal boron nitride synthesized at atmospheric pressure. *Science* **317**, 932–934 (2007).

[84] Hui, F. *et al.* On the use of two dimensional hexagonal boron nitride as dielectric. *Microelectron. Eng.* **163**, 119–133 (2016).

[85] Castellanos-Gomez, A. *et al.* Atomically thin Mica flakes and their application as ultrathin insulating substrates for graphene. *Small* **7**, 2491–2497 (2011).

[86] Alateyah, A. I., Dhakal, H. N. & Zhang, Z. Y. Processing, properties, and applications of polymer nanocomposites based on layer silicates: A review. *Adv. Polym. Technol.* (2013).

[87] Castro Neto, A. H., Guinea, F., Peres, N. M. R., Novoselov, K. S. & Geim, A. K. The electronic properties of graphene. *Rev. Mod. Phys.* **81**, 109–162 (2009).

[88] Ye, J. *et al.* Accessing the transport properties of graphene and its multilayers at high carrier density. *Proc. Natl. Acad. Sci.* **108**, 13002–13006 (2011).

[89] Baringhaus, J. *et al.* Exceptional ballistic transport in epitaxial graphene nanoribbons. *Nature* **506**, 349–354 (2014).

[90] Bolotin, K. *et al.* Ultrahigh electron mobility in suspended graphene. *Solid State Commun.* **146**, 351–355 (2008).

[91] Kim, Y.-J., Kim, Y., Novoselov, K. & Hong, B. H. Engineering electrical properties of graphene: chemical approaches. *2D Mater.* **2**, 042001 (2015).

[92] Das, A. *et al.* Monitoring dopants by Raman scattering in an electrochemically top-gated graphene transistor. *Nat. Nanotechnol.* **3**, 210–215 (2008).

[93] Nair, R. R. *et al.* Fine structure constant defines visual transparency of graphene. *Science* **320**, 1308–1308 (2008).

[94] Keller, U. Recent developments in compact ultrafast lasers. *Nature* **424**, 831–838 (2003).

[95] Sun, Z. *et al.* Graphene mode-locked ultrafast laser. *ACS Nano* **4**, 803–810 (2010).

[96] Peigney, A., Laurent, C., Flahaut, E., Bacsa, R. & Rousset, A. Specific surface area of carbon nanotubes and bundles of carbon nanotubes. *Carbon* **39**, 507–514 (2001).

[97] Lee, C., Wei, X., Kysar, J. W. & Hone, J. Measurement of the elastic properties and intrinsic strength of monolayer graphene. *Science* **321**, 385–388 (2008).

[98] Ramanathan, T. *et al.* Functionalized graphene sheets for polymer nanocomposites. *Nat. Nanotechnol.* **3**, 327–331 (2008).

[99] Briggs, B. D. *et al.* Electromechanical robustness of monolayer graphene with extreme bending. *Appl. Phys. Lett.* **97**, 223102 (2010).

[100] Blees, M. K. *et al.* Graphene kirigami. *Nature* **524**, 204–207 (2015).

[101] Balandin, A. A. *et al.* Superior thermal conductivity of single-layer graphene. *Nano Lett.* **8**, 902–907 (2008).

[102] De, S. & Coleman, J. N. Are there fundamental limitations on the sheet resistance and transmittance of thin graphene films?. *ACS Nano* **4**, 2713–2720 (2010).

[103] Huang, X., Zeng, Z., Fan, Z., Liu, J. & Zhang, H. Graphene-based electrodes. *Adv. Mater.* **24**, 5979–6004 (2012).

[104] Craciun, M. F., Bointon, T. H. & Russo, S. Is graphene a good transparent electrode for photovoltaics and display applications? *IET Circuits, Devices Syst.* **9**, 403–412 (2015).

[105] Bae, S. *et al.* Roll-to-roll production of 30-inch graphene films for transparent electrodes. *Nat. Nanotechnol.* **5**, 574–578 (2010).

[106] De, S. *et al.* Flexible, transparent, conducting films of randomly stacked graphene from surfactant-stabilized, oxide-free graphene dispersions. *Small* **6**, 458–464 (2010).

[107] Li, X. *et al.* Highly conducting graphene sheets and Langmuir-Blodgett films. *Nat. Nanotechnol.* **3**, 538–542 (2008).

[108] Shim, J. *et al.* Two-minute assembly of pristine large-area graphene based films. *Nano Lett.* **14**, 1388–1393 (2014).

[109] Hempel, M., Nezich, D., Kong, J. & Hofmann, M. A novel class of strain gauges based on layered percolative films of 2D materials. *Nano Lett.* **12**, 5714–5718 (2012).

[110] Secor, E. B. & Hersam, M. C. Graphene inks for printed electronics. Available at: http://www.sigmaaldrich.com/technical-documents/articles/technology-spotlights/graphene-inks-for-printed-electronics.html (Accessed: 24/05/2015).

[111] New graphene based inks for high-speed manufacturing of printed electronics | University of Cambridge. Available at: http://www.cam.ac.uk/research/news/new-graphene-based-inks-for-high-speed-manufacturing-of-printed-electronics.

[112] Karagiannidis, P. G. *et al.* Microfluidization of graphite and formulation of graphene-based conductive inks. *ACS Nano* **11**, 2742–2755 (2017).

[113] Liu, Y., Xu, Z., Zhan, J., Li, P. & Gao, C. Superb electrically conductive graphene fibers *via* doping strategy. *Adv. Mater.* **28**, 7941–7947 (2016).

[114] Schwierz, F. Graphene transistors. *Nat. Nanotechnol.* **5**, 487–496 (2010).

[115] Schedin, F. *et al.* Detection of individual gas molecules adsorbed on graphene. *Nat. Mater.* **6**, 652–655 (2007).

[116] Liu, T. *et al.* Cycling Li-O_2 batteries via LiOH formation and decomposition. *Science* **350**, 530–533 (2015).

[117] Liao, L. *et al.* Top-gated graphene nanoribbon transistors with ultrathin high-*k* dielectrics. *Nano Lett.* **10**, 1917–1921 (2010).

[118] Liao, L. *et al.* High-speed graphene transistors with a self-aligned nanowire gate. *Nature* **467**, 305–308 (2010).

[119] Yavari, F. & Koratkar, N. Graphene-based chemical sensors. *J. Phys. Chem. Lett.* **3**, 1746–1753 (2012).

[120] Martin, P. Electrochemistry of gaphene: New horizons for sensing and energy storage. *Chem. Rec.* **9**, 211–223 (2009).

[121] Rumyantsev, S., Liu, G., Shur, M. S., Potyrailo, R. A. & Balandin, A. A. Selective gas sensing with a aingle pristine graphene transistor. *Nano Lett.* **12**, 2294–2298 (2012).

[122] Yuan, W. & Shi, G. Graphene-based gas sensors. *J. Mater. Chem. A* **1**, 10078 (2013).

[123] Shao, Y. *et al.* Graphene based electrochemical sensors and biosensors: A Review. *Electroanalysis* **22**, 1027–1036 (2010).

[124] Georgakilas, V. *et al.* Functionalization of graphene: Covalent and non-covalent approaches, derivatives and applications. *Chem. Rev.* **112**, 6156–6214 (2012).

[125] Shao, Y. *et al.* Graphene-based materials for flexible supercapacitors. *Chem. Soc. Rev.* **44**, 3639–3665 (2015).

[126] El-Kady, M. F., Strong, V., Dubin, S. & Kaner, R. B. Laser scribing of high-performance and flexible graphene-based electrochemical capacitors. *Science* **335**, 1326–1330 (2012).

[127] Xie, Y. *et al.* Stretchable all-solid-state supercapacitor with wavy shaped polyaniline/graphene electrode. *J. Mater. Chem. A* **2**, 9142–9149 (2014).

[128] Cao, J. *et al.* High voltage asymmetric supercapacitor based on MnO_2 and graphene electrodes. *J. Electroanal. Chem.* **689**, 201–206 (2013).

[129] Le, L. T., Ervin, M. H., Qiu, H., Fuchs, B. E. & Lee, W. Y. Graphene supercapacitor electrodes fabricated by inkjet printing and thermal reduction of graphene oxide. *Electrochem. commun.* **13**, 355–358 (2011).

[130] Yu, S., Wu, X., Wang, Y., Guo, X. & Tong, L. 2D materials for optical modulation: Challenges and opportunities. *Adv. Mater.* **29**, 1606128 (2017).

[131] Martinez, A. & Sun, Z. Nanotube and graphene saturable absorbers for fibre lasers. *Nat. Photonics* **7**, 842–845 (2013).

[132] Wang, F. *et al.* Wideband-tuneable, nanotube mode-locked, fibre laser. *Nat. Nanotechnol.* **3**, 738–742 (2008).

[133] Hasan, T. *et al.* Solution-phase exfoliation of graphite for ultrafast photonics. *Phys. Status Solidi B* **247**, 2953–2957 (2010).

[134] Hasan, T. *et al.* Nanotube-polymer composites for ultrafast photonics. *Adv. Mater.* **21**, 3874–3899 (2009).

[135] Breusing, M., Ropers, C. & Elsaesser, T. Ultrafast carrier dynamics in graphite. *Phys. Rev. Lett.* **102**, 086809 (2009).

[136] Sun, D. *et al.* Ultrafast relaxation of excited dirac fermions in epitaxial graphene using optical differential transmission spectroscopy. *Phys. Rev. Lett.* **101**, 157402 (2008).

[137] Seibert, K. *et al.* Femtosecond carrier dynamics in graphite. *Phys. Rev. B* **42**, 2842–2851 (1990).

[138] Marseglia, E. A. Transition metal dichalcogenides and their intercalates. *Int. Rev. Phys. Chem.* **3**, 177–216 (1983).

[139] Amani, M. *et al.* Near-unity photoluminescence quantum yield in MoS_2. *Science* **350**, 1065–1068 (2015).

[140] Eda, G. *et al.* Photoluminescence from Chemically Exfoliated MoS_2. *Nano Lett.* **11**, 5111–5116 (2011).

[141] Bertolazzi, S., Brivio, J. & Kis, A. Stretching and breaking of ultrathin MoS_2. *ACS Nano* **5**, 9703–9709 (2011).

[142] Laursen, A. B., Kegnæs, S., Dahl, S. & Chorkendorff, I. Molybdenum sulfides - efficient and viable materials for electro - and photoelectrocatalytic hydrogen evolution. *Energy Environ. Sci.* **5**, 5577 (2012).

[143] Mak, K. F., Lee, C., Hone, J., Shan, J. & Heinz, T. F. Atomically thin MoS_2: A new direct-gap semiconductor. *Phys. Rev. Lett.* **105**, 136805 (2010).

[144] Kuc, A., Zibouche, N. & Heine, T. Influence of quantum confinement on the electronic structure of the transition metal sulfide TS_2. *Phys. Rev. B* **83**, 245213 (2011).

[145] Zhang, Y. *et al.* Direct observation of the transition from indirect to direct bandgap in atomically thin epitaxial $MoSe_2$. *Nat. Nanotechnol.* **9**, 111–115 (2013).

[146] Yun, W. S., Han, S. W., Hong, S. C., Kim, I. G. & Lee, J. D. Thickness and strain effects on electronic structures of transition metal dichalcogenides: 2H-MX_2 semiconductors (M = Mo, W; X = S, Se, Te). *Phys. Rev. B* **85**, 033305 (2012).

[147] Duan, X., Wang, C., Pan, A., Yu, R. & Duan, X. Two-dimensional transition metal dichalcogenides as atomically thin semiconductors: opportunities and challenges. *Chem. Soc. Rev.* **44**, 8859–8876 (2015).

[148] Kam, K. K. & Parkinson, B. A. Detailed photocurrent spectroscopy of the semiconducting group VIB transition metal dichalcogenides. *J. Phys. Chem.* **86**, 463–467 (1982).

[149] Tongay, S. *et al.* Thermally driven crossover from indirect toward direct bandgap in 2D semiconductors: $MoSe_2$ versus MoS_2. *Nano Lett.* **12**, 5576–5580 (2012).

[150] Ruppert, C., Aslan, O. B. & Heinz, T. F. Optical properties and band gap of single- and few-layer $MoTe_2$ crystals. *Nano Lett.* **14**, 6231–6236 (2014).

[151] Zhao, W. *et al.* Evolution of electronic structure in atomically thin sheets of WS_2 and WSe_2. *ACS Nano* **7**, 791–797 (2013).

[152] Fuhrer, M. S. & Hone, J. Measurement of mobility in dual-gated MoS_2 transistors. *Nat. Nanotechnol.* **8**, 146–147 (2013).

[153] Kang, K. *et al.* High-mobility three-atom-thick semiconducting films with wafer-scale homogeneity. *Nature* **520**, 656–660 (2015).

[154] Georgiou, T. *et al.* Vertical field-effect transistor based on graphene-WS_2 heterostructures for flexible and transparent electronics. *Nat. Nanotechnol.* **8**, 100–103 (2012).

[155] Radisavljevic, B. & Kis, A. Mobility engineering and a metal-insulator transition in monolayer MoS_2. *Nat. Mater.* **12**, 815–820 (2013). 1301.4947.

[156] Wachter, S., Polyushkin, D. K., Bethge, O. & Mueller, T. A microprocessor based on a two-dimensional semiconductor. *Nat. Commun.* **8**, 14948 (2017).

[157] Electrical properties of silicon. Available at: http://www.ioffe.ru/SVA/NSM/Semicond/Si/electric.html (Accessed: 30/07/2017).

[158] Lopez-Sanchez, O., Lembke, D., Kayci, M., Radenovic, A. & Kis, A. Ultrasensitive photodetectors based on monolayer MoS_2. *Nat. Nanotechnol.* **8**, 497–501 (2013).

[159] Wu, K., Zhang, X., Wang, J., Li, X. & Chen, J. WS_2 as a saturable absorber for ultrafast photonic applications of mode-locked and Q-switched lasers. *Opt. Express* **23**, 11453 (2015).

[160] Kufer, D. & Konstantatos, G. Highly sensitive, encapsulated MoS_2 photodetector with gate controllable gain and speed. *Nano Lett.* **15**, 7307–7313 (2015).

[161] Perea-Lopez, N. *et al.* Photosensor device based on few-layered WS_2 films. *Adv. Funct. Mater.* **23**, 5511–5517 (2013).

[162] Xue, Y. *et al.* Scalable production of a few-layer MoS_2 /WS_2 vertical heterojunction array and its application for photodetectors. *ACS Nano* **10**, 573–580 (2016).

[163] Palacios-Berraquero, C. *et al.* Atomically thin quantum light-emitting diodes. *Nat. Commun.* **7**, 12978 (2016).

[164] Withers, F. *et al.* Light-emitting diodes by band-structure engineering in van der Waals heterostructures. *Nat. Mater.* **14**, 301–306 (2015).

[165] Jo, S., Ubrig, N., Berger, H., Kuzmenko, A. B. & Morpurgo, A. F. Mono- and bilayer WS_2 light-emitting transistors. *Nano Lett.* **14**, 2019–2025 (2014).

[166] Shanmugam, M., Bansal, T., Durcan, C. a. & Yu, B. Molybdenum disulphide/titanium dioxide nanocomposite-poly 3-hexylthiophene bulk heterojunction solar cell. *Appl. Phys. Lett.* **100**, 153901 (2012).

[167] Geim, A. K. & Grigorieva, I. V. Van der Waals heterostructures. *Nature* **499**, 419–425 (2013).

[168] Wang, K. *et al.* Ultrafast saturable absorption of two-dimensional MoS_2 nanosheets. *ACS Nano* **7**, 9260–9267 (2013).

[169] Sun, Z., Martinez, A. & Wang, F. Optical modulators with 2D layered materials. *Nat. Photonics* **10**, 227–238 (2016).

[170] Wang, X. *et al.* Highly anisotropic and robust excitons in monolayer black phosphorus. *Nat. Nanotechnol.* **10**, 517–521 (2015).

[171] Liu, S. *et al.* Thickness-dependent Raman spectra, transport properties and infrared photoresponse of few-layer black phosphorus. *J. Mater. Chem. C* **3**, 10974–10980 (2015).

[172] Kou, L., Chen, C. & Smith, S. C. Phosphorene: Fabrication, properties, and applications. *J. Phys. Chem. Lett.* **6**, 2794–2805 (2015).

[173] Ling, X., Wang, H., Huang, S., Xia, F. & Dresselhaus, M. S. The renaissance of black phosphorus. *Proc. Natl. Acad. Sci.* **112**, 4523–4530 (2015).

[174] Jain, A. & McGaughey, A. J. H. Strongly anisotropic in-plane thermal transport in single-layer black phosphorene. *Sci. Rep.* **5**, 8501 (2015).

[175] Fei, R. & Yang, L. Strain-engineering the anisotropic electrical conductance of few-layer black phosphorus. *Nano Lett.* **14**, 2884–2889 (2014).

[176] Wei, Q. & Peng, X. Superior mechanical flexibility of phosphorene and few-layer black phosphorus. *Appl. Phys. Lett.* **104**, 251915 (2014).

[177] Liu, H. *et al.* Phosphorene: An unexplored 2D semiconductor with a high hole mobility. *ACS Nano* **8**, 4033–41 (2014).

[178] Kang, J. *et al.* Solvent exfoliation of electronic-grade, two-dimensional black phosphorus. *ACS Nano* **9**, 3596–3604 (2015).

[179] Engel, M., Steiner, M. & Avouris, P. Black phosphorus photodetector for multispectral, high-resolution imaging. *Nano Lett.* **14**, 6414–6417 (2014).

[180] Buscema, M., Groenendijk, D. J., Steele, G. A., van der Zant, H. S. J. & Castellanos-Gomez, A. Photovoltaic effect in few-layer black phosphorus PN junctions defined by local electrostatic gating. *Nat. Commun.* **5**, 4651 (2014).

[181] Hanlon, D. *et al.* Liquid exfoliation of solvent-stabilized few-layer black phosphorus for applications beyond electronics. *Nat. Commun.* **6**, 8563 (2015).

[182] Chen, Y. *et al.* Mechanically exfoliated black phosphorus as a new saturable absorber for both Q-switching and Mode-locking laser operation. *Opt. Express* **23**, 12823 (2015).

[183] Sotor, J., Sobon, G., Macherzynski, W., Paletko, P. & Abramski, K. M. Black phosphorus saturable absorber for ultrashort pulse generation. *Appl. Phys. Lett.* **107**, 051108 (2015).

[184] Mu, H. *et al.* Black phosphorus-polymer composites for pulsed lasers. *Adv. Opt. Mater.* n/a–n/a (2015).

[185] Li, D. *et al.* Electric-field-induced strong enhancement of electroluminescence in multilayer molybdenum disulfide. *Nat. Commun.* **6**, 7509 (2015).

[186] Guo, Z. *et al.* From black phosphorus to phosphorene: Basic solvent exfoliation, evolution of Raman scattering, and applications to ultrafast photonics. *Adv. Funct. Mater.* **25**, 6996–7002 (2015).

[187] Cho, S.-Y. *et al.* Superior chemical sensing performance of black phosphorus: Comparison with MoS_2 and graphene. *Adv. Mater.* **28**, 7020–7028 (2016).

[188] Sun, J. *et al.* Formation of stable phosphorus-carbon bond for enhanced performance in black phosphorus nanoparticle-graphite composite battery anodes. *Nano Lett.* **14**, 4573–4580 (2014).

[189] Castellanos-Gomez, A. *et al.* Isolation and characterization of few-layer black phosphorus. *2D Mater.* **1**, 025001 (2014).

[190] Favron, A. *et al.* Photooxidation and quantum confinement effects in exfoliated black phosphorus. *Nat. Mater.* **14**, 826–832 (2015).

[191] Island, J. O., Steele, G. A., van der Zant, H. S. J. & Castellanos-Gomez, A. Environmental instability of few-layer black phosphorus. *2D Mater.* **2**, 011002 (2015).

[192] Huang, S.-Z. *et al.* Three-dimensional (3D) bicontinuous hierarchically porous Mn_2O_3 single crystals for high performance lithium-ion batteries. *Sci. Rep.* **5**, 14686 (2015).

[193] Jiang, X.-F. *et al.* Recent progress on fabrications and applications of boron nitride nanomaterials: A review. *J. Mater. Sci. Technol.* **31**, 589–598 (2015).

[194] Liu, L., Feng, Y. P. & Shen, Z. X. Structural and electronic properties of *h*-BN. *Phys. Rev. B* **68**, 104102 (2003).

[195] Jo, I. *et al.* Thermal conductivity and phonon transport in suspended few-layer hexagonal boron nitride. *Nano Lett.* **13**, 550–554 (2013).

[196] Liem, H. & Choy, H. Superior thermal conductivity of polymer nanocomposites by using graphene and boron nitride as fillers. *Solid State Commun.* **163**, 41–45 (2013).

[197] Watanabe, K., Taniguchi, T. & Kanda, H. Direct-bandgap properties and evidence for ultraviolet lasing of hexagonal boron nitride single crystal. *Nat. Mater.* **3**, 404–409 (2004).

[198] Pakdel, A., Bando, Y. & Golberg, D. Nano boron nitride flatland. *Chem. Soc. Rev.* **43**, 934–959 (2014).

[199] Cassabois, G., Valvin, P. & Gil, B. Hexagonal boron nitride is an indirect bandgap semiconductor. *Nat. Photonics* **10**, 262–266 (2016).

[200] Miró, P., Audiffred, M. & Heine, T. An atlas of two-dimensional materials. *Chem. Soc. Rev.* **43**, 6537 (2014).

[201] Dean, C. R. *et al.* Boron nitride substrates for high-quality graphene electronics. *Nat. Nanotechnol.* **5**, 722–726 (2010).

[202] Li, Q. *et al.* Flexible high-temperature dielectric materials from polymer nanocomposites. *Nature* **523**, 576–579 (2015).

[203] Golberg, D. *et al.* Boron nitride nanotubes and nanosheets. *ACS Nano* **4**, 2979–2993 (2010).

[204] Meric, I. *et al.* Graphene field-effect transistors based on boron nitride gate dielectrics. In *2010 Int. Electron Devices Meet.*, 23.2.1–23.2.4 (IEEE, 2010).

[205] Meric, I. *et al.* Graphene field-effect transistors based on boron-nitride dielectrics. *Proc. IEEE* **101**, 1609–1619 (2013).

[206] Li, L. H. *et al.* Dielectric screening in atomically thin boron bitride nanosheets. *Nano Lett.* **15**, 218–223 (2015).

[207] Wang, X. *et al.* Large-surface-area BN nanosheets and their utilization in polymeric composites with improved thermal and dielectric properties. *Nanoscale Res. Lett.* **7**, 662 (2012).

[208] Naguib, M. *et al.* Two-dimensional nanocrystals produced by exfoliation of Ti_3AlC_2. *Adv. Mater.* **23**, 4248–4253 (2011).

[209] Ling, Z. *et al.* Flexible and conductive MXene films and nanocomposites with high capacitance. *Proc. Natl. Acad. Sci.* **111**, 16676–16681 (2014).

[210] Khazaei, M. *et al.* Novel electronic and magnetic properties of two-dimensional transition metal carbides and nitrides. *Adv. Funct. Mater.* **23**, 2185–2192 (2013).

[211] Tang, Q., Zhou, Z. & Shen, P. Are MXenes promising anode materials for Li ion batteries? Computational studies on electronic properties and Li storage capability of Ti_3C_2 and Ti_3C_2 X_2 (X = F, OH) monolayer. *J. Am. Chem. Soc.* **134**, 16909–16916 (2012).

[212] Xie, Y. *et al.* Prediction and characterization of MXene nanosheet anodes for non-lithium-ion batteries. *ACS Nano* **8**, 9606–9615 (2014).

[213] Sun, D. *et al.* Two-dimensional Ti_3C_2 as anode material for Li-ion batteries. *Electrochem. commun.* **47**, 80–83 (2014).

[214] Er, D., Li, J., Naguib, M., Gogotsi, Y. & Shenoy, V. B. Ti_3C_2 MXene as a high capacity electrode material for metal (Li, Na, K, Ca) ion batteries. *ACS Appl. Mater. Interfaces* **6**, 11173–11179 (2014).

[215] Wang, X. *et al.* Pseudocapacitance of MXene nanosheets for high-power sodium-ion hybrid capacitors. *Nat. Commun.* **6**, 6544 (2015).

[216] Dall'Agnese, Y., Taberna, P.-L., Gogotsi, Y. & Simon, P. Two-dimensional vanadium carbide (MXene) as positive electrode for sodium-ion capacitors. *J. Phys. Chem. Lett.* **6**, 2305–2309 (2015).

[217] Rakhi, R. B., Ahmed, B., Hedhili, M. N., Anjum, D. H. & Alshareef, H. N. Effect of postetch annealing gas composition on the structural and electrochemical properties of Ti_2CT_x MXene electrodes for supercapacitor applications. *Chem. Mater.* **27**, 5314–5323 (2015).

[218] Xu, B. *et al.* Ultrathin MXene-micropattern-based field-effect transistor for probing neural activity. *Adv. Mater.* **28**, 3333–3339 (2016).

[219] Wang, F. *et al.* An organ-like titanium carbide material (MXene) with multilayer structure encapsulating hemoglobin for a mediator-free biosensor. *J. Electrochem. Soc.* **162**, B16–B21 (2014).

[220] Xu, J., Shim, J., Park, J.-H. & Lee, S. MXene electrode for the integration of WSe_2 and MoS_2 field effect transistors. *Adv. Funct. Mater.* **26**, 5328–5334 (2016).

[221] Ma, Z. *et al.* Tunable band structures of heterostructured bilayers with transition-metal dichalcogenide and MXene monolayer. *J. Phys. Chem. C* **118**, 5593–5599 (2014).

[222] Guo, Z., Miao, N., Zhou, J., Sa, B. & Sun, Z. Strain-mediated type-I/type-II transition in MXene/blue phosphorene van der Waals heterostructures for flexible optical/electronic devices. *J. Mater. Chem. C* **5**, 978–984 (2017).

[223] Annabi-Bergaya, F. Layered clay minerals. Basic research and innovative composite applications. *Microporous Mesoporous Mater.* **107**, 141–148 (2008).

[224] Chen, B. *et al.* A critical appraisal of polymer–clay nanocomposites. *Chem. Soc. Rev.* **37**, 568–594 (2008).

[225] Dolley, T. P. *2008 minerals yearbook: Mica* (National Minerals Information Center, 2008).

[226] Kim, W.-g. & Nair, S. Membranes from nanoporous 1D and 2D materials: A review of opportunities, developments, and challenges. *Chem. Eng. Sci.* **104**, 908–924 (2013).

[227] Harvey, A. *et al.* Exploring the versatility of liquid phase exfoliation: producing 2D nanosheets from talcum powder, cat litter and beach sand. *2D Mater.* **4**, 025054 (2017).

[228] Delmas, C., Fouassier, C. & Hagenmuller, P. Structural classification and properties of the layered oxides. *Phys. B+C* **99**, 81–85 (1980).

[229] Ma, R. & Sasaki, T. Nanosheets of oxides and hydroxides: Ultimate 2D charge-bearing functional crystallites. *Adv. Mater.* **22**, 5082–5104 (2010).

[230] Osada, M. & Sasaki, T. Exfoliated oxide nanosheets: New solution to nanoelectronics. *J. Mater. Chem.* **19**, 2503 (2009).

[231] Pray, A. R. *et al.* Anhydrous metal chlorides,. In Angelici, R. J. (ed.) *Inorg. Synth. Reagents Transit. Met. complex Organomet. Synth.*, 321–323 (John Wiley & Sons, Inc., 1990).

[232] Greenwood, N. N. & Earnshaw, A. *Chemistry of the elements* (Butterworth-Heinemann, 1997).

[233] Hordeski, M. F. *Dictionary of energy efficiency technologies* (Fairmont Press, 2004).

[234] Ciesielski, A. & Samor, P. Graphene via sonication assisted liquid-phase exfoliation. *Chem. Soc. Rev.* **43**, 381–398 (2014).

[235] Coleman, J. N. Liquid-phase exfoliation of nanotubes and graphene. *Adv. Funct. Mater.* **19**, 3680–3695 (2009).

[236] Hernandez, Y. *et al.* High-yield production of graphene by liquid-phase exfoliation of graphite. *Nat. Nanotechnol.* **3**, 563–568 (2008).

[237] Coleman, J. N. *et al.* Two-dimensional nanosheets produced by liquid exfoliation of layered materials. *Science* **331**, 568–571 (2011).

[238] Coleman, J. N. Liquid exfoliation of defect-free graphene. *Acc. Chem. Res.* **46**, 14–22 (2013).

[239] Lin, Y.-C. *et al.* Wafer-scale MoS_2 thin layers prepared by MoO_3 sulfurization. *Nanoscale* **4**, 6637 (2012).

[240] Lee, Y.-h. *et al.* Synthesis of large-area MoS_2 atomic layers with chemical vapor deposition. *Adv. Mater.* **24**, 2320–2325 (2012).

[241] Li, X. *et al.* Large-area synthesis of high-quality and uniform graphene films on copper foils. *Science* **324**, 1312–1314 (2009).

[242] Cassell, A. M., Raymakers, J. A., Kong, J. & Dai, H. Large scale CVD synthesis of single-walled carbon nanotubes. *J. Phys. Chem. B* **103**, 6484–6492 (1999).

[243] Zhu, Y. *et al.* Graphene and graphene oxide: Synthesis, properties, and applications. *Adv. Mater.* **22**, 3906–3924 (2010).

[244] Kobayashi, T. *et al.* Production of a 100-m-long high-quality graphene transparent conductive film by roll-to-roll chemical vapor deposition and transfer process. *Appl. Phys. Lett.* **102**, 023112 (2013).

[245] Dreyer, D. R., Ruoff, R. S. & Bielawski, C. W. From conception to realization: An historial account of graphene and some perspectives for its future. *Angew. Chemie Int. Ed.* **49**, 9336–9344 (2010).

[246] Chen, Y. *et al.* Growing uniform graphene disks and films on molten glass for heating devices and cell culture. *Adv. Mater.* **27**, 7839–7846 (2015).

[247] Petrone, N. *et al.* Chemical vapor deposition-derived graphene with electrical performance of exfoliated graphene. *Nano Lett.* **12**, 2751–2756 (2012).

[248] Wu, Y. *et al.* High-frequency, scaled graphene transistors on diamond-like carbon. *Nature* **472**, 74–78 (2011).

[249] Liao, L. & Duan, X. Graphene for radio frequency electronics. *Mater. Today* **15**, 328–338 (2012).

[250] Bao, Q. *et al.* Atomic-layer graphene as a saturable absorber for ultrafast pulsed lasers. *Adv. Funct. Mater.* **19**, 3077–3083 (2009).

[251] Zhan, Y., Liu, Z., Najmaei, S., Ajayan, P. M. & Lou, J. Large-area vapor-phase growth and characterization of MoS_2 atomic layers on a SiO_2 substrate. *Small* **8**, 966–971 (2012).

[252] Liu, K.-K. *et al.* Growth of large-area and highly crystalline MoS_2 thin layers on insulating substrates. *Nano Lett.* **12**, 1538–1544 (2012).

[253] Zhang, Y. *et al.* Controlled growth of high-quality monolayer WS_2 layers on sapphire and imaging its grain boundary. *ACS Nano* **7**, 8963–8971 (2013).

[254] Wang, X. *et al.* Chemical vapor deposition growth of crystalline monolayer $MoSe_2$. *ACS Nano* **8**, 5125–5131 (2014).

[255] Lu, X. *et al.* Large-area synthesis of monolayer and few-layer $MoSe_2$ films on SiO_2 substrates. *Nano Lett.* **14**, 2419–2425 (2014).

[256] Dresselhaus, M. & Dresselhaus, G. Intercalation compounds of graphite. *Adv. Phys.* **30**, 139–326 (1981).

[257] Valles, C. *et al.* Solutions of negatively charged graphene sheets and ribbons. *J. Am. Chem. Soc.* **130**, 15802–15804 (2008).

[258] Zeng, Z. *et al.* An effective method for the fabrication of few-layer-thick inorganic nanosheets. *Angew. Chemie Int. Ed.* **51**, 9052–9056 (2012).

[259] Zheng, J. *et al.* High yield exfoliation of two-dimensional chalcogenides using sodium naphthalenide. *Nat. Commun.* **5** (2014).

[260] Lotya, M. *et al.* Liquid phase production of graphene by exfoliation of graphite in surfactant/water solutions. *J. Am. Chem. Soc.* **131**, 3611–3620 (2009).

[261] Ciesielski, A. *et al.* Harnessing the liquid-phase exfoliation of graphene using aliphatic compounds: A supramolecular approach. *Angew. Chemie Int. Ed.* **53**, 10355–10361 (2014).

[262] Nuvoli, D. *et al.* High concentration few-layer graphene sheets obtained by liquid phase exfoliation of graphite in ionic liquid. *J. Mater. Chem.* **21**, 3428–3431 (2011).

[263] Park, J. S., Yu, L., Lee, C. S., Shin, K. & Han, J. H. Liquid-phase exfoliation of expanded graphites into graphene nanoplatelets using amphiphilic organic molecules. *J. Colloid Interface Sci.* **417**, 379–384 (2014).

[264] Guardia, L. *et al.* High-throughput production of pristine graphene in an aqueous dispersion assisted by non-ionic surfactants. *Carbon* **49**, 1653–1662 (2011).

[265] Green, A. A. & Hersam, M. C. Solution phase production of graphene with controlled thickness via density differentiation. *Nano Lett.* **9**, 4031–4036 (2009).

[266] Zhou, K.-G., Mao, N.-N., Wang, H.-X., Peng, Y. & Zhang, H.-L. A mixed-solvent strategy for efficient exfoliation of inorganic graphene analogues. *Angew. Chemie Int. Ed.* **50**, 10839–10842 (2011).

[267] Paton, K. R. *et al.* Scalable production of large quantities of defect-free few-layer graphene by shear exfoliation in liquids. *Nat. Mater.* **13**, 624–630 (2014).

[268] Varrla, E. *et al.* Large-scale production of size-controlled MoS_2 nanosheets by shear exfoliation. *Chem. Mater.* **27**, 1129–1139 (2015).

[269] Varrla, E. *et al.* Turbulence-assisted shear exfoliation of graphene using household detergent and a kitchen blender. *Nanoscale* **6**, 11810–11819 (2014).

[270] Shang, J., Xue, F. & Ding, E. The facile fabrication of few-layer graphene and graphite nanosheets by high pressure homogenization. *Chem. Commun.* **51**, 15811–15814 (2015).

[271] Xue, F., Ding, E. & Shang, J. Efficient exfoliation of molybdenum disulphide nanosheets by a high-pressure homogeniser. *Micro Nano Lett.* **10**, 589–591 (2015).

[272] Ibrahem, M. A. *et al.* High quantity and quality few-layers transition metal disulfide nanosheets from wet-milling exfoliation. *RSC Adv.* **3**, 13193 (2013).

[273] Zhao, W. *et al.* Preparation of graphene by exfoliation of graphite using wet ball milling. *J. Mater. Chem.* **20**, 5817 (2010).

[274] Yao, Y. *et al.* Large-scale production of two-dimensional nanosheets. *J. Mater. Chem.* **22**, 13494 (2012).

[275] Hernandez, Y., Lotya, M., Rickard, D., Bergin, S. D. & Coleman, J. N. Measurement of multicomponent solubility parameters for graphene facilitates solvent discovery. *Langmuir* **26**, 3208–3213 (2010).

[276] Cunningham, G. *et al.* Solvent exfoliation of transition metal dichalcogenides: Dispersibility of exfoliated nanosheets varies only weakly between compounds. *ACS Nano* **6**, 3468–3480 (2012).

[277] Hansen, C. M. *Hansen solubility parameters: A user's handbook* (CRC Press, 2007), 2 edn.

[278] Lyklema, J. The surface tension of pure liquids. *Colloids Surfaces A Physicochem. Eng. Asp.* **156**, 413–421 (1999).

[279] Yi, M., Shen, Z., Ma, S. & Zhang, X. A mixed-solvent strategy for facile and green preparation of graphene by liquid-phase exfoliation of graphite. *J. Nanoparticle Res.* **14**, 1003 (2012).

[280] Xu, L. *et al.* Production of high-concentration graphene dispersions in low-boiling-point organic solvents by liquid-phase noncovalent exfoliation of graphite with a hyperbranched polyethylene and formation of graphene/ethylene copolymer composites. *J. Phys. Chem. C* **117**, 10730–10742 (2013).

[281] O'Neill, A., Khan, U., Nirmalraj, P. N., Boland, J. & Coleman, J. N. Graphene dispersion and exfoliation in low boiling point solvents. *J. Phys. Chem. C* **115**, 5422–5428 (2011).

[282] Torrisi, F. *et al.* Stable, surfactant-free graphene-styrene methylmethacrylate composite for ultrafast lasers. *Adv. Opt. Mater.* **4**, 1088–1097 (2016).

[283] Kang, J. *et al.* Stable aqueous dispersions of optically and electronically active phosphorene. *Proc. Natl. Acad. Sci.* 201602215 (2016).

[284] Tasis, D., Papagelis, K., Spiliopoulos, P. & Galiotis, C. Efficient exfoliation of graphene sheets in binary solvents. *Mater. Lett.* **94**, 47–50 (2013).

[285] Vazquez, G., Alvarez, E. & Navaza, J. M. Surface tension of alcohol water + water from 20 to 50 ^{o}C. *J. Chem. Eng. Data* **40**, 611–614 (1995).

[286] Smith, R. J. *et al.* Large-scale exfoliation of inorganic layered compounds in aqueous surfactant solutions. *Adv. Mater.* **23**, 3944–3948 (2011).

[287] May, P., Khan, U., Hughes, J. M. & Coleman, J. N. Role of solubility parameters in understanding the steric stabilization of exfoliated two-dimensional nanosheets by adsorbed polymers. *J. Phys. Chem. C* **116**, 11393–11400 (2012).

[288] Butt, H.-J., Graf, K. & Kappl, M. *Physics and chemistry of interfaces* (Wiley-VCH Verlag GmbH & Co. KGaA, Weinheim, FRG, 2003).

[289] Hasan, T. *et al.* Stabilization and 'debundling' of single-wall carbon nanotube dispersions in N-Methyl-2-pyrrolidone (NMP) by polyvinylpyrrolidone (PVP). *J. Phys. Chem. C* **111**, 12594–12602 (2007).

[290] Liang, Y. T. & Hersam, M. C. Highly concentrated graphene solutions via polymer enhanced solvent exfoliation and iterative solvent exchange. *J. Am. Chem. Soc.* **132**, 17661–17663 (2010).

[291] Bourlinos, A. B. *et al.* Aqueous-phase exfoliation of graphite in the presence of polyvinylpyrrolidone for the production of water-soluble graphenes. *Solid State Commun.* **149**, 2172–2176 (2009).

[292] Bonaccorso, F., Zerbetto, M., Ferrari, A. C. & Amendola, V. Sorting nanoparticles by centrifugal fields in clean media. *J. Phys. Chem. C* **117**, 13217–13229 (2013).

[293] Zhang, X. *et al.* Dispersion of graphene in ethanol using a simple solvent exchange method. *Chem. Commun.* **46**, 7539 (2010).

[294] Khan, U. *et al.* Size selection of dispersed, exfoliated graphene flakes by controlled centrifugation. *Carbon* **50**, 470–475 (2012).

[295] Bonaccorso, F. *et al.* Density gradient ultracentrifugation of nanotubes: Interplay of bundling and surfactants encapsulation. *J. Phys. Chem. C* **114**, 17267–17285 (2010).

[296] Backes, C. *et al.* Edge and confinement effects allow in situ measurement of size and thickness of liquid-exfoliated nanosheets. *Nat. Commun.* **5**, 4576 (2014).

[297] Sun, X., Luo, D., Liu, J. & Evans, D. G. Monodisperse chemically modified graphene obtained by density gradient ultracentrifugal rate separation. *ACS Nano* **4**, 3381–3389 (2010).

[298] Marchesini, R., Bertoni, A., Andreola, S., Melloni, E. & Sichirollo, A. E. Extinction and absorption coefficients and scattering phase functions of human tissues in vitro. *Appl. Opt.* **28**, 2318 (1989).

[299] Yang, L. *Materials Characterization: Introduction to Microscopic and Spectroscopic Methods* (Wiley, 2009), 2 edn.

[300] Lee, C. *et al.* Anomalous lattice vibrations of single- and few-layer MoS_2. *ACS Nano* **4**, 2695–2700 (2010).

[301] Erni, R., Rossell, M. D., Kisielowski, C. & Dahmen, U. Atomic-resolution imaging with a Sub-50-pm electron probe. *Phys. Rev. Lett.* **102**, 096101 (2009).

[302] Ferrari, A. C. *et al.* Raman spectrum of graphene and graphene layers. *Phys. Rev. Lett.* **97**, 187401 (2006).

[303] Jorio, A., Saito, R., Dresselhaus, G. & Dresselhaus, M. S. *Raman spectroscopy in graphene related systems* (Wiley-VCH Verlag GmbH & Co. KGaA, Weinheim, Germany, 2011).

[304] Li, J. *et al.* A simple route towards high-concentration surfactant-free graphene dispersions. *Carbon* **50**, 3113–3116 (2012).

[305] Li, H. *et al.* From bulk to monolayer MoS_2: Evolution of Raman scattering. *Adv. Funct. Mater.* **22**, 1385–1390 (2012).

[306] Zhang, X. *et al.* Raman spectroscopy of shear and layer breathing modes in multilayer MoS_2. *Phys. Rev. B* **87**, 115413 (2013).

[307] Li, Z. *et al.* Indirect band gap emission by hot electron injection in metal/MoS_2 and Metal/WSe_2 heterojunctions. *Nano Lett.* **15**, 3977–3982 (2015).

[308] Xia, F., Wang, H. & Jia, Y. Rediscovering black phosphorus as an anisotropic layered material for optoelectronics and electronics. *Nat. Commun.* **5** (2014).

[309] Ling, X. *et al.* Anisotropic electron-photon and electron-phonon interactions in black phosphorus. *Nano Lett.* **16**, 2260–2267 (2016).

[310] Yasaei, P. *et al.* High-quality black phosphorus atomic layers by liquid-phase exfoliation. *Adv. Mater.* **27**, 1887–1892 (2015).

[311] Leach, R. H., Pierce, R. J., Hickman, E. P., Mackenzie, M. J. & Smith, H. G. (eds.) *The printing ink manual* (Springer Netherlands, Dordrecht, 1993), 5th edn.

[312] Carvalho, D. N. *Forty centuries of ink* (Echo Library, 2007).

[313] Goldschmidt, A., Streitberger, H.-J. & Goldschmidt, A. *BASF handbook on basics of coating technology* (Vincentz Network, 2007).

[314] Flick, E. W. *Printing ink and overprint varnish formulations* (Noyes Publications, 1999).

[315] Lievens, H. Wide web coating of complex materials. *Surf. Coatings Technol.* **76-77**, 744–753 (1995).

[316] Lahti, M., Leppävuori, S. & Lantto, V. Gravure-offset-printing technique for the fabrication of solid films. *Appl. Surf. Sci.* **142**, 367–370 (1999).

[317] Nguyen, H. A. D., Lee, C., Shin, K.-H. & Lee, D. An investigation of the ink-transfer mechanism during the printing phase of high-resolution roll-to-roll gravure printing. *IEEE Trans. Components, Packag. Manuf. Technol.* **5**, 1516–1524 (2015).

[318] Smith, T. Flexographic inks. *Pigment Resin Technol.* **15**, 11–12 (1986).

[319] Krebs, F. C. Fabrication and processing of polymer solar cells: A review of printing and coating techniques. *Sol. Energy Mater. Sol. Cells* **93**, 394–412 (2009).

[320] Kipphan, H. E. *Handbook of Print Media* (Springer, 2001).

[321] Doraiswamy, D. The origins of rheology: A short historical excursion. *Rheol. Bull.* **71**, 1—-9 (2002).

[322] Barnes, H. A., Hutton, J. F. J. F. & Walters, K. *An introduction to rheology* (Elsevier, 1989).

[323] Coquel, F., Godlewski, E. & Seguin, N. Relaxation of fluid systems. *Math. Model. Methods Appl. Sci.* **22**, 1250014 (2012).

[324] Xu, Y. *et al.* Screen-Printable Thin Film Supercapacitor Device Utilizing Graphene/Polyaniline Inks. *Adv. Energy Mater.* **3**, 1035–1040 (2013).

[325] Yu, J.-S. *et al.* Silver front electrode grids for ITO-free all printed polymer solar cells with embedded and raised topographies, prepared by thermal imprint, flexographic and inkjet roll-to-roll processes. *Nanoscale* **4**, 6032 (2012).

[326] Krebs, F. C., Fyenbo, J. & Jørgensen, M. Product integration of compact roll-to-roll processed polymer solar cell modules: methods and manufacture using flexographic printing, slot-die coating and rotary screen printing. *J. Mater. Chem.* **20**, 8994 (2010).

[327] Voigt, M. M. *et al.* Gravure printing inverted organic solar cells: The influence of ink properties on film quality and device performance. *Sol. Energy Mater. Sol. Cells* **105**, 77–85 (2012).

[328] Voigt, M. M. *et al.* Gravure printing for three subsequent solar cell layers of inverted structures on flexible substrates. *Sol. Energy Mater. Sol. Cells* **95**, 731–734 (2011).

[329] Kopola, P. *et al.* High efficient plastic solar cells fabricated with a high-throughput gravure printing method. *Sol. Energy Mater. Sol. Cells* **94**, 1673–1680 (2010).

[330] Puetz, J. & Aegerter, M. A. Direct gravure printing of indium tin oxide nanoparticle patterns on polymer foils. *Thin Solid Films* **516**, 4495–4501 (2008).

[331] Cho, C.-K. *et al.* Mechanical flexibility of transparent PEDOT:PSS electrodes prepared by gravure printing for flexible organic solar cells. *Sol. Energy Mater. Sol. Cells* **95**, 3269–3275 (2011).

[332] Noh, J. *et al.* Fully gravure-printed D flip-flop on plastic foils using single-walled carbon-nanotube-based TFTs. *IEEE Electron Device Lett.* **32**, 638–640 (2011).

[333] Choi, Y. *et al.* Characteristics of gravure printed InGaZnO thin films as an active channel layer in thin film transistors. *Thin Solid Films* **518**, 6249–6252 (2010).

[334] Kempa, H. *et al.* Complementary ring oscillator exclusively prepared by means of gravure and flexographic printing. *IEEE Trans. Electron Devices* **58**, 2765–2769 (2011).

[335] Winther-Jensen, B. & Krebs, F. C. High-conductivity large-area semi-transparent electrodes for polymer photovoltaics by silk screen printing and vapour-phase deposition. *Sol. Energy Mater. Sol. Cells* **90**, 123–132 (2006).

[336] Krebs, F. C., Alstrup, J., Spanggaard, H., Larsen, K. & Kold, E. Production of large-area polymer solar cells by industrial silk screen printing, lifetime considerations and lamination with polyethyleneterephthalate. *Sol. Energy Mater. Sol. Cells* **83**, 293–300 (2004).

[337] Ito, S. *et al.* Fabrication of screen-printing pastes from TiO_2 powders for dye-sensitised solar cells. *Prog. Photovoltaics Res. Appl.* **15**, 603–612 (2007).

[338] Shaheen, S. E., Radspinner, R., Peyghambarian, N. & Jabbour, G. E. Fabrication of bulk heterojunction plastic solar cells by screen printing. *Appl. Phys. Lett.* **79**, 2996–2998 (2001).

[339] Hyun, W. J. *et al.* All-printed, foldable organic thin-film transistors on glassine paper. *Adv. Mater.* **27**, 7058–7064 (2015).

[340] Kang, B., Lee, W. H. & Cho, K. Recent advances in organic transistor printing processes. *ACS Appl. Mater. Interfaces* **5**, 2302–2315 (2013).

[341] McAleer, J. F., Scott, D., Hall, G., Alvarez-Icaza, M. & Plotkin, E. V. Disposable glucose test strip and method and compositions for making same (1999).

[342] Kiekhaefer, J. H. Transparent/translucent financial transaction card (2004).

[343] Magdassi, S. *The Chemistry of inkjet inks* (WORLD SCIENTIFIC, 2009).

[344] Korvink, J. G., Smith, P. J. & Shin, D.-Y. (eds.) *Inkjet-based micromanufacturing* (Wiley-VCH Verlag GmbH & Co. KGaA, Weinheim, Germany, 2012).

[345] Tekin, E., Smith, P. J. & Schubert, U. S. Inkjet printing as a deposition and patterning tool for polymers and inorganic particles. *Soft Matter* **4**, 703 (2008).

[346] Derby, B. Inkjet printing of functional and structural materials: Fluid property requirements, feature stability, and resolution. *Annu. Rev. Mater. Res.* **40**, 395–414 (2010).

[347] Jang, D., Kim, D. & Moon, J. Influence of fluid physical properties on ink-jet printability. *Langmuir* **25**, 2629–2635 (2009).

[348] Martin, G. D., Hoath, S. D. & Hutchings, I. M. Inkjet printing - the physics of manipulating liquid jets and drops. *J. Phys. Conf. Ser.* **105**, 012001 (2008).

[349] Fromm, J. E. Numerical calculation of the fluid dynamics of drop-on-demand jets. *IBM J. Res. Dev.* **28**, 322–333 (1984).

[350] Robertson, G. L. *Food packaging: Principles and practice* (CRC Press, 2012), 3rd edn.

[351] Aleeva, Y. & Pignataro, B. Recent advances in upscalable wet methods and ink formulations for printed electronics. *J. Mater. Chem. C* **2**, 6436 (2014).

[352] Soltman, D. & Subramanian, V. Inkjet-printed line morphologies and temperature control of the coffee ring effect. *Langmuir* **24**, 2224–2231 (2008).

[353] Moon, Y. J. *et al.* Effect of contact angle and drop spacing on the bulging frequency of inkjet-printed silver lines on FC-coated glass. *J. Mech. Sci. Technol.* **28**, 1441–1448 (2014).

[354] Lim, J. A. *et al.* Self-organization of ink-jet-printed triisopropylsilylethynyl pentacene via evaporation-induced flows in a drying droplet. *Adv. Funct. Mater.* **18**, 229–234 (2008).

[355] Hu, H. & Larson, R. G. Marangoni effect reverses coffee-ring depositions. *J. Phys. Chem. B* **110**, 7090–7094 (2006).

[356] Hu, H. & Larson, R. G. Analysis of the effects of Marangoni stresses on the microflow in an evaporating sessile droplet. *Langmuir* **21**, 3972–3980 (2005).

[357] Wang, H., Wang, Z., Huang, L., Mitra, A. & Yan, Y. Surface patterned porous films by convection-assisted dynamic self-assembly of zeolite nanoparticles. *Langmuir* **17**, 2572–2574 (2001).

[358] Liu, H. *et al.* Line printing solution-processable small molecules with uniform surface profile via ink-jet printer. *J. Colloid Interface Sci.* **465**, 106–111 (2016).

[359] Phillips, C., Al-Ahmadi, A., Potts, S.-J., Claypole, T. & Deganello, D. The effect of graphite and carbon black ratios on conductive ink performance. *J. Mater. Sci.* **52**, 9520–9530 (2017).

[360] Luo, S., Harris, T. & Wong, C. Study on surface tension and adhesion for flip chip packaging. In *Proc. Int. Symp. Adv. Packag. Mater. Process. Prop. Interfaces (IEEE Cat. No.01TH8562)*, 299–304 (2001).

[361] Solid surface energy data (SFE) for common polymers. Available at: http://www.surface-tension.de/solid-surface-energy.htm (Accessed: 21/07/2015).

[362] Yaws, C. L. *Thermophysical Properties of Chemicals and Hydrocarbons* (William Andrew, 2008).

[363] Woodward, R. I. *et al.* Few-layer MoS_2 saturable absorbers for short-pulse laser technology: Current status and future perspectives. *Photonics Res.* **3**, A30 (2015).

[364] Wajid, A. S. *et al.* Polymer-stabilized graphene dispersions at high concentrations in organic solvents for composite production. *Carbon* **50**, 526–534 (2012).

[365] Chou, K.-S. & Chen, C.-C. Fabrication and characterization of silver core and porous silica shell nanocomposite particles. *Microporous Mesoporous Mater.* **98**, 208–213 (2007).

[366] Gupta, A., Chen, G., Joshi, P., Tadigadapa, S. & Eklund. Raman scattering from high-frequency phonons in supported n-graphene layer films. *Nano Lett.* **6**, 2667–2673 (2006). 0606593.

[367] Schwan, J., Ulrich, S., Batori, V., Ehrhardt, H. & Silva, S. R. P. Raman spectroscopy on amorphous carbon films. *J. Appl. Phys.* **80**, 440–447 (1996).

[368] Li, J. & Kim, J.-K. Percolation threshold of conducting polymer composites containing 3D randomly distributed graphite nanoplatelets. *Compos. Sci. Technol.* **67**, 2114–2120 (2007).

[369] Dani, A. Electrical percolation behavior of short-fiber composites: Experimental characterization and modeling. *Compos. Sci. Technol.* **56**, 911–920 (1996).

[370] Wang, S. & Ogale, A. Continuum space simulation and experimental characterization of electrical percolation behavior of particulate composites. *Compos. Sci. Technol.* **46**, 93–103 (1993).

[371] Strem-Company. Graphene nanoplatelets (2015).

[372] Li, Y., Deng, C. & Yang, M. A novel surface acoustic wave-impedance humidity sensor based on the composite of polyaniline and poly(vinyl alcohol) with a capability of detecting low humidity. *Sensors Actuators, B Chem.* **165**, 7–12 (2012).

[373] Xuan, W. *et al.* Fast response and high sensitivity ZnO/glass surface acoustic wave humidity sensors using graphene oxide sensing layer. *Sci. Rep.* **4**, 7206 (2014).

[374] Guo, Y. *et al.* Graphene/$LiNbO_3$ surface acoustic wave device based relative humidity sensor. *Opt. - Int. J. Light Electron Opt.* **125**, 5800–5802 (2014).

[375] Mogera, U., Sagade, A. A., George, S. J. & Kulkarni, G. U. Ultrafast response humidity sensor using supramolecular nanofibre and its application in monitoring breath humidity and flow. *Sci. Rep.* **4**, 4103 (2015).

[376] Zhang, D., Tong, J. & Xia, B. Humidity-sensing properties of chemically reduced graphene oxide/polymer nanocomposite film sensor based on layer-by-layer nano self-assembly. *Sensors Actuators B Chem.* **197**, 66–72 (2014).

[377] Bi, H. *et al.* Ultrahigh humidity sensitivity of graphene oxide. *Sci. Rep.* **3**, 2714 (2013).

[378] Wong, W. C. *et al.* Polyvinyl alcohol coated photonic crystal optical fiber sensor for humidity measurement. *Sensors Actuators B Chem.* **174**, 563–569 (2012).

[379] Kuang, Q., Lao, C., Wang, Z. L., Xie, Z. & Zheng, L. High-sensitivity humidity sensor based on a single SnO_2 nanowire. *J. Am. Chem. Soc.* **129**, 6070–6071 (2007).

[380] Hu, P. *et al.* Carbon nanostructure-based field-effect transistors for label-free chemical/biological sensors. *Sensors* **10**, 5133–5159 (2010).

[381] Wang, X., Ding, B., Yu, J., Wang, M. & Pan, F. A highly sensitive humidity sensor based on a nanofibrous membrane coated quartz crystal microbalance. *Nanotechnology* **21**, 055502 (2010).

[382] Farahani, H., Wagiran, R. & Hamidon, M. Humidity sensors principle, mechanism, and fabrication technologies: A comprehensive review. *Sensors* **14**, 7881–7939 (2014).

[383] Simon, I., Bârsan, N., Bauer, M. & Weimar, U. Micromachined metal oxide gas sensors: Opportunities to improve sensor performance. *Sensors Actuators B Chem.* **73**, 1–26 (2001).

[384] HUMICAP® humidity and temperature transmitter series HMT310 (2015).

[385] Gardner, J., Cole, M. & Udrea, F. CMOS gas sensors and smart devices. In *Proc. IEEE Sensors*, vol. 1, 721–726 (IEEE).

[386] Guha, P. *et al.* Novel design and characterisation of SOI CMOS micro-hotplates for high temperature gas sensors. *Sensors Actuators B Chem.* **127**, 260–266 (2007).

[387] Fei, T., Zhao, H., Jiang, K., Zhou, X. & Zhang, T. Polymeric humidity sensors with nonlinear response: Properties and mechanism investigation. *J. Appl. Polym. Sci.* **130**, 2056–2061 (2013).

[388] Chen, W.-P., Zhao, Z.-G., Liu, X.-W., Zhang, Z.-X. & Suo, C.-G. A capacitive humidity sensor based on multi-wall carbon nanotubes (MWCNTs). *Sensors* **9**, 7431–7444 (2009).

[389] Han, J.-W., Kim, B., Li, J. & Meyyappan, M. A carbon nanotube based ammonia sensor on cellulose paper. *RSC Adv.* **4**, 549–553 (2014).

[390] Zhang, D., Tong, J., Xia, B. & Xue, Q. Ultrahigh performance humidity sensor based on layer-by-layer self-assembly of graphene oxide/polyelectrolyte nanocomposite film. *Sensors Actuators B Chem.* **203**, 263–270 (2014).

[391] Ghosh, R., Midya, A., Santra, S., Ray, S. K. & Guha, P. K. Chemically reduced graphene oxide for ammonia detection at room temperature. *ACS Appl. Mater. Interfaces* **5**, 7599–7603 (2013).

[392] Borini, S. *et al.* Ultrafast graphene oxide humidity sensors. *ACS Nano* **7**, 11166–11173 (2013).

[393] Santra, S. *et al.* CMOS integration of inkjet-printed graphene for humidity sensing. *Sci. Rep.* **5**, 17374 (2015).

[394] Ali, S., Udrea, F., Milne, W. & Gardner, J. Tungsten-based SOI microhotplates for smart gas sensors. *J. Microelectromechanical Syst.* **17**, 1408–1417 (2008).

[395] Santra, S., Guha, P. K., Ali, S. Z., Haneef, I. & Udrea, F. Silicon on insulator diode temperature sensor - A detailed analysis for ultra-high temperature operation. *IEEE Sens. J.* **10**, 997–1003 (2010).

[396] Tai, H., Li, X., Jiang, Y., Xie, G. & Du, X. The enhanced formaldehyde-sensing properties of P3HT-ZnO hybrid thin film OTFT sensor and further insight into its stability. *Sensors* **15**, 2086–2103 (2015).

[397] Lu, G., Ocola, L. E. & Chen, J. Gas detection using low-temperature reduced graphene oxide sheets. *Appl. Phys. Lett.* **94**, 083111 (2009).

[398] Bhattacharya, S. *et al.* Plasticization of poly(vinylpyrrolidone) thin films under ambient humidity: Insight from single-molecule tracer diffusion dynamics. *J. Phys. Chem. B* **117**, 7771–7782 (2013).

[399] Galvin, C. J., Dimitriou, M. D., Satija, S. K. & Genzer, J. Swelling of polyelectrolyte and polyzwitterion brushes by humid vapors. *J. Am. Chem. Soc.* **136**, 12737–12745 (2014).

[400] Yuan, W. *et al.* The edge- and basal-plane-specific electrochemistry of a single-layer graphene sheet. *Sci. Rep.* **3**, 2248 (2013).

[401] Kavan, L., Yum, J. H. & Gratzel, M. Optically transparent cathode for dye-sensitized solar cells based on graphene nanoplatelets. *ACS Nano* **5**, 165–172 (2011).

[402] Roy-Mayhew, J. D., Bozym, D. J., Punckt, C. & Aksay, I. A. Functionalized graphene as a catalytic counter electrode in dye-sensitized solar cells. *ACS Nano* **4**, 6203–6211 (2010).

[403] Ramasamy, E., Lee, W. J., Lee, D. Y. & Song, J. S. Nanocarbon counterelectrode for dye sensitized solar cells. *Appl. Phys. Lett.* **90**, 173103 (2007).

[404] Yang, N., Zhai, J., Wang, D., Chen, Y. & Jiang, L. Two-dimensional graphene bridges enhanced photoinduced charge transport in dye-sensitized solar cells. *ACS Nano* **4**, 887–894 (2010).

[405] Wan, L. *et al.* Room-temperature fabrication of graphene films on variable substrates and its use as counter electrodes for dye-sensitized solar cells. *Solid State Sci.* **13**, 468–475 (2011).

[406] Dodoo-Arhin, D. *et al.* Inkjet-printed graphene electrodes for dye-sensitized solar cells. *Carbon* **105**, 33–41 (2016).

[407] Hardin, B. E., Snaith, H. J. & McGehee, M. D. The renaissance of dye-sensitized solar cells. *Nat. Photonics* **6**, 162–169 (2012).

[408] Calogero, G., Bartolotta, A., Di Marco, G., Di Carlo, A. & Bonaccorso, F. Vegetable-based dye-sensitized solar cells. *Chem. Soc. Rev.* **44**, 3244–3294 (2015).

[409] O'Regan, B. & Grätzel, M. A low-cost, high-efficiency solar cell based on dye-sensitized colloidal TiO_2 films. *Nature* **353**, 737–740 (1991).

[410] Gratzel, M. Photoelectrochemical cells. *Nature* **414**, 338–344 (2001).

[411] Bisquert, J., Cahen, D., Hodes, G., Rhle, S. & Zaban, A. Physical chemical principles of photovoltaic conversion with nanoparticulate, mesoporous dye-sensitized solar cells. *J. Phys. Chem. B* **108**, 8106–8118 (2004).

[412] Calogero, G. *et al.* Anthocyanins and betalains as light-harvesting pigments for dye-sensitized solar cells. *Sol. Energy* **86**, 1563–1575 (2012).

[413] Hao, S., Wu, J., Huang, Y. & Lin, J. Natural dyes as photosensitizers for dye-sensitized solar cell. *Sol. Energy* **80**, 209–214 (2006).

[414] Matthews, D., Infelta, P. & Grtzel, M. Calculation of the photocurrent-potential characteristic for regenerative, sensitized semiconductor electrodes. *Sol. Energy Mater. Sol. Cells* **44**, 119–155 (1996).

[415] Tennakone, K., Kumara, G., Kumarasinghe, A., Sirimanne, P. & Wijayantha, K. Efficient photosensitization of nanocrystalline TiO_2 films by tannins and related phenolic substances. *J. Photochem. Photobiol. A Chem.* **94**, 217–220 (1996).

[416] Amao, Y. & Komori, T. Bio-photovoltaic conversion device using chlorine-e6 derived from chlorophyll from Spirulina adsorbed on a nanocrystalline TiO_2 film electrode. *Biosens. Bioelectron.* **19**, 843–847 (2004).

[417] POLO, A. & MURAKAMIIHA, N. Blue sensitizers for solar cells: Natural dyes from Calafate and Jaboticaba. *Sol. Energy Mater. Sol. Cells* **90**, 1936–1944 (2006).

[418] Garcia, C. G., Polo, A. S. & Murakami Iha, N. Y. Fruit extracts and ruthenium polypyridinic dyes for sensitization of TiO_2 in photoelectrochemical solar cells. *J. Photochem. Photobiol. A Chem.* **160**, 87–91 (2003).

[419] Papageorgiou, N. Counter-electrode function in nanocrystalline photoelectrochemical cell configurations. *Coord. Chem. Rev.* **248**, 1421–1446 (2004).

[420] SMESTAD, G., BIGNOZZI, C. & ARGAZZI, R. Testing of dye sensitized TiO_2 solar cells I: Experimental photocurrent output and conversion efficiencies. *Sol. Energy Mater. Sol. Cells* **32**, 259–272 (1994).

[421] Fang, X. *et al.* Effect of the thickness of the Pt film coated on a counter electrode on the performance of a dye-sensitized solar cell. *J. Electroanal. Chem.* **570**, 257–263 (2004).

[422] Yu, Y.-J. *et al.* Tuning the graphene work function by electric field effect. *Nano Lett.* **9**, 3430–3434 (2009). 0909.0020.

[423] Woodward, R. I. *et al.* Tunable Q-switched fiber laser based on saturable edge-state absorption in few-layer molybdenum disulfide (MoS_2). *Opt. Express* **22**, 31113 (2014).

[424] Zhang, M. *et al.* Solution processed MoS_2-PVA composite for sub-bandgap mode-locking of a wideband tunable ultrafast Er:fiber laser. *Nano Res.* **8**, 1522–1534 (2015).

[425] Woodward, R. I. *et al.* Wideband saturable absorption in few-layer molybdenum diselenide ($MoSe_2$) for Q-switching Yb-, Er- and Tm-doped fiber lasers. *Opt. Express* **23**, 20051 (2015).

[426] Zhang, M. *et al.* Yb- and Er-doped fiber laser Q-switched with an optically uniform, broadband WS_2 saturable absorber. *Sci. Rep.* **5**, 17482 (2015).

[427] Howe, R. C. T. *et al.* Surfactant-aided exfoliation of molybdenum disulfide for ultrafast pulse generation through edge-state saturable absorption. *Phys. Status Solidi B* **253**, 911–917 (2016).

[428] Beal, A. R., Knights, J. C. & Liang, W. Y. Transmission spectra of some transition metal dichalcogenides. II. Group VIA: trigonal prismatic coordination. *J. Phys. C Solid State Phys.* **5**, 3540–3551 (1972).

[429] Li, Y. *et al.* Measurement of the optical dielectric function of monolayer transition-metal dichalcogenides: MoS_2, $MoSe_2$, WS_2, and WSe_2. *Phys. Rev. B* **90**, 205422 (2014).

[430] O'Neill, A., Khan, U. & Coleman, J. N. Preparation of high concentration dispersions of exfoliated MoS_2 with increased flake size. *Chem. Mater.* **24**, 2414–2421 (2012).

[431] Gutiérrez, H. R. *et al.* Extraordinary room-temperature photoluminescence in triangular WS_2 monolayers. *Nano Lett.* **13**, 3447–3454 (2013).

[432] Berkdemir, A. *et al.* Identification of individual and few layers of WS_2 using Raman Spectroscopy. *Sci. Rep.* **3**, 1755 (2013).

[433] Flick, E. W. *Industrial solvents handbook* (William Andrew, 1998), 5th edn.

[434] Chen, S. *et al.* Broadband optical and microwave nonlinear response in topological insulator. *Opt. Mater. Express* **4**, 587 (2014).

[435] Garmire, E. Resonant optical nonlinearities in semiconductors. *IEEE J. Sel. Top. Quantum Electron.* **6**, 1094–1110 (2000).

[436] Sheik-Bahae, M., Said, A., Wei, T.-H., Hagan, D. & Van Stryland, E. Sensitive measurement of optical nonlinearities using a single beam. *IEEE J. Quantum Electron.* **26**, 760–769 (1990).

[437] von der Linde, D. Characterization of the noise in continuously operating mode-locked lasers. *Appl. Phys. B* **39**, 201–217 (1986).

[438] Trushin, M., Kelleher, E. J. R. & Hasan, T. Theory of edge-state optical absorption in two-dimensional transition metal dichalcogenide flakes. *Phys. Rev. B* **94**, 155301 (2016).

[439] Hu, G. *et al.* Black phosphorus ink formulation for inkjet printing of optoelectronics and photonics. *Nat. Commun.* **8**, 278 (2017).

[440] Curcio, J. A. & Petty, C. C. The near infrared absorption spectrum of liquid water. *J. Opt. Soc. Am.* **41**, 302 (1951).

[441] Wozniak, B. & Dera, J. Light absorption by water molecules and inorganic substances dissolved in sea water. In *Light Absorpt. Sea Water*, 11–81 (Springer, New York, NY, 2007).

[442] Bohren, C. E. & Wiley, D. R. H. *Absorption and scattering of light by small particles* (Wiley-VCH Verlag GmbH, Weinheim, Germany, 1998).

[443] Friedlander, S. K. S. K. *Smoke, dust, and haze: Fundamentals of aerosol dynamics* (Oxford University Press, Oxford, UK, 2000).

[444] Brent, J. R. *et al.* Production of few-layer phosphorene by liquid exfoliation of black phosphorus. *Chem. Commun.* **50**, 13338–13341 (2014).

[445] Sabri, S. S. *et al.* Graphene field effect transistors with parylene gate dielectric. *Appl. Phys. Lett.* **95**, 242104 (2009).

[446] Chua, L.-L. *et al.* General observation of n-type field-effect behaviour in organic semiconductors. *Nature* **434**, 194–199 (2005).

[447] Sotor, J. *et al.* Ultrafast thulium-doped fiber laser mode locked with black phosphorus. *Opt. Lett.* **40**, 3885 (2015).

[448] Li, D. *et al.* Polarization and thickness dependent absorption properties of black phosphorus: New saturable absorber for ultrafast pulse generation. *Sci. Rep.* **5**, 15899 (2015).

[449] Qin, Z. *et al.* Mid-infrared mode-locked pulse generation with multilayer black phosphorus as saturable absorber. *Opt. Lett.* **41**, 56 (2016).

[450] Hisyam, M. B., Rusdi, M. F. M., Latiff, A. A. & Harun, S. W. Generation of Mode-Locked Ytterbium doped fiber ring laser using few-layer black phosphorus as a saturable absorber. *IEEE J. Sel. Top. Quantum Electron.* **23**, 39–43 (2017).

[451] Ismail, E. I., Kadir, N. A., Latiff, A. A., Ahmad, H. & Harun, S. W. Black phosphorus crystal as a saturable absorber for both a Q-switched and mode-locked erbium-doped fiber laser. *RSC Adv.* **6**, 72692–72697 (2016).

[452] Lee, D., Park, K., Debnath, P. C., Kim, I. & Song, Y.-W. Thermal damage suppression of a black phosphorus saturable absorber for high-power operation of pulsed fiber lasers. *Nanotechnology* **27**, 365203 (2016).

[453] Song, Y. *et al.* Vector soliton fiber laser passively mode locked by few layer black phosphorus-based optical saturable absorber. *Opt. Express* **24**, 25933 (2016).

[454] Mao, D. *et al.* Stable high-power saturable absorber based on polymer-black-phosphorus films. *Opt. Commun.* (2016).

[455] Li, J. *et al.* Black phosphorus: a two-dimension saturable absorption material for mid-infrared Q-switched and mode-locked fiber lasers. *Sci. Rep.* **6**, 30361 (2016).

[456] Luo, Z.-C. *et al.* Microfiber-based few-layer black phosphorus saturable absorber for ultra-fast fiber laser. *Opt. Express* **23**, 20030–20039 (2015).

[457] Park, K. *et al.* Black phosphorus saturable absorber for ultrafast mode-locked pulse laser via evanescent field interaction. *Ann. Phys.* **527**, 770–776 (2015).

[458] Yu, H., Zheng, X., Yin, K., Cheng, X. & Jiang, T. Thulium/holmium-doped fiber laser passively mode locked by black phosphorus nanoplatelets-based saturable absorber. *Appl. Opt.* **54**, 10290 (2015).

[459] Chen, Y. *et al.* Optically driven black phosphorus as a saturable absorber for mode-locked laser pulse generation. *Opt. Eng.* **55**, 081317 (2016).

[460] Chen, Y., Chen, S., Liu, J., Gao, Y. & Zhang, W. Sub-300 femtosecond soliton tunable fiber laser with all-anomalous dispersion passively mode locked by black phosphorus. *Opt. Express* **24**, 13316 (2016).

[461] Guo, Q. *et al.* Black phosphorus mid-infrared photodetectors with high gain. *Nano Lett.* **16**, 4648–4655 (2016).

[462] Yuan, H. *et al.* Polarization-sensitive broadband photodetector using a black phosphorus vertical p-n junction. *Nat. Nanotechnol.* **10**, 707–713 (2015).

[463] Yu, T. *et al.* Graphene coupled with silicon quantum dots for high-rerformance bulk-silicon-based Schottky-junction photodetectors. *Adv. Mater.* **28**, 4912–4919 (2016).

[464] An, X., Liu, F., Jung, Y. J. & Kar, S. Tunable graphene-silicon heterojunctions for ultrasensitive photodetection. *Nano Lett.* **13**, 909–916 (2013).

[465] Amirmazlaghani, M., Raissi, F., Habibpour, O., Vukusic, J. & Stake, J. Graphene-Si Schottky IR detector. *IEEE J. Quantum Electron.* **49**, 589–594 (2013).

[466] Goykhman, I. *et al.* On-chip integrated, silicon-graphene plasmonic Schottky photodetector with high responsivity and avalanche photogain. *Nano Lett.* **16**, 3005–3013 (2016).

[467] Liu, Y. *et al.* Planar carbon nanotube-graphene hybrid films for high-performance broadband photodetectors. *Nat. Commun.* **6**, 8589 (2015).

[468] Konstantatos, G. *et al.* Hybrid graphene-quantum dot phototransistors with ultrahigh gain. *Nat. Nanotechnol.* **7**, 363–368 (2012).

[469] Buscema, M. *et al.* Fast and broadband photoresponse of few-layer black phosphorus field-effect transistors. *Nano Lett.* **14**, 3347–3352 (2014).

[470] Viti, L. *et al.* Black phosphorus terahertz photodetectors. *Adv. Mater.* **27**, 5567–5572 (2015).

[471] Deng, Y. *et al.* Black phosphorus-monolayer MoS_2 van der Waals heterojunction p-n diode. *ACS Nano* **8**, 8292–8299 (2014).

[472] Ye, L., Li, H., Chen, Z. & Xu, J. Near-infrared photodetector based on MoS_2 /black phosphorus heterojunction. *ACS Photonics* **3**, 692–699 (2016).

[473] Choi, K.-H., Yoo, J., Lee, C. K. & Lee, S.-Y. All-inkjet-printed, solid-state flexible supercapacitors on paper. *Energy Environ. Sci.* **9**, 2812–2821 (2016).

[474] Secor, E. B. & Hersam, M. C. Emerging carbon and post-carbon nanomaterial inks for printed electronics. *J. Phys. Chem. Lett.* **6**, 620–626 (2015).

[475] Jang, B. Z. & Zhamu, A. Nano graphene platelet-based conductive inks and printing process (2011).

[476] Chen, J.-H. *et al.* Printed graphene circuits. *Adv. Mater.* **19**, 3623–3627 (2007).

[477] Stankovich, S. *et al.* Graphene-based composite materials. *Nature* **442**, 282–286 (2006).

[478] Jang, B. Z., Zhamu, A. & Guo, J. Mass production of nano-scaled platelets and products (2010).

[479] Hu, G. *et al.* Nanoplatelet dispersions, methods for their production and uses thereof (2017).

[480] Thostenson, E. T., Ren, Z. & Chou, T.-W. Advances in the science and technology of carbon nanotubes and their composites: A review. *Compos. Sci. Technol.* **61**, 1899–1912 (2001).

[481] Chand, S. Carbon fibers for composites. *J. Mater. Sci.* **35**, 1303–1313 (2000).

[482] Liu, Y. & Kumar, S. Polymer/carbon nanotube nano composite fibers - a review. *ACS Appl. Mater. Interfaces* **6**, 6069–6087 (2014).

[483] Guo, J., Song, L., Zhamu, A. & Jang, B. Z. Nano-scaled graphene plate-reinforced composite materials and method of producing same (2010).

[484] Jang, B. Z., Zhamu, A. & Guo, J. Process for producing nano-scaled platelets and nanocompsites (2008).

[485] Jang, B. Z. & Zhamu, A. Method of producing nano-scaled graphene and inorganic platelets and their nanocomposites (2012).

[486] Jang, B. Z., Zhamu, A., Guo, J. & Song, L. Hybrid fiber tows containning both nano-fillers and continuous fibers, hybrid composites, and their production processes (2008).